Simulation of the Martian diffuse auroral emissions and photochemistry induced by solar energetic particles

Yuki Nakamura

Yuki Nakamura. Simulation of the Martian diffuse auroral emissions and photochemistry induced by solar energetic particles. Astrophysics [astro-ph]. Sorbonne Université; Tōhoku Gakuin Daigaku (Sendai, Japon), 2023. English. NNT : 2023SORUS026 . tel-04909572

HAL Id: tel-04909572
https://theses.hal.science/tel-04909572v1

Sorbonne Université

Ecole Doctorale Astronomie et Astrophysique d'Île-de-France
Laboratoire Atmosphères, Milieux, Observations Spatiales (LATMOS)

Simulation of the Martian diffuse auroral emissions and photochemistry induced by solar energetic particles

Par Yuki NAKAMURA

Thèse de doctorat en Astronomie et Astrophysique

Dirigée par François LEBLANC et Naoki TERADA

Présentée et soutenue publiquement le 23 Janvier 2023

Devant un jury composé de :

1. LEBLANC, François, Directeur de Recherche au CNRS, Co-directeur de thèse
2. KATOH, Yuto, Professeur de Tohoku University, Président du jury
3. FONTAINE, Dominique, Directrice de Recherche au CNRS, Examinateur
4. GÉRARD, Jean-Claude, Professeur de Liège Université, Rapporteur
5. TERADA, Naoki, Professeur de Tohoku University, Co-directeur de thèse
6. HOSOKAWA, Keisuke, Professeur de The University of Electro-Communications, Rapporteur

Doctoral thesis

Simulation of the Martian diffuse auroral emissions and photochemistry induced by solar energetic particles

（太陽高エネルギー粒子が引き起こす火星のディフューズオーローラと
大気光化学反応の数値シミュレーション研究）

Yuki NAKAMURA
（中村　勇貴）

Department of Geophysics
Graduate School of Science
Tohoku University

Thesis Committee Members

Professor Naoki Terada (Co-supervisor, Chair, Tohoku University)
Dr. François Leblanc (Co-supervisor, LATMOS, CNRS)
Professor Jean-Claude Gérard (Liège Université)
Professor Keisuke Hosokawa (The University of Electro-Communications)
Dr. Dominique Fontaine (LPP, CNRS)
Professor Yuto Katoh (Tohoku University)

2022

Abstract

The impacts of solar energetic particles (SEPs) on the atmospheric composition on present-day Mars have been investigated using newly developed Monte Carlo and photochemical models. We validate our Monte Carlo model by comparing it with the Martian diffuse auroral emission observations. Our simulations highlight that SEP protons are the main source of the low-altitude peak emission and succeed in reproducing the observed peak altitude and shape of the diffuse auroral emission profiles for the first time. This is a new finding contrary to previous studies, which considered only SEP electrons. Our three-dimensional Monte Carlo simulations for the CO_2^+ ultraviolet doublet, oxygen 557.7 nm, and oxygen 630.0 nm emission lines find that the morphology of the electron-induced emission is patchy and bright only within the cusp regions, while the proton-induced emission is diffuse without any fine structures. This difference results from the difference in their gyro radii. Our results on the Martian diffuse auroral emissions suggest a significant impact of SEP protons on the Martian atmosphere globally and deeply. We also predicted the changes in atmospheric composition during SEP events on Mars. We find that the depletion of ozone density occurs between 20-60 km due to the enhanced HOx (H, OH, and HO_2) densities induced by the precipitation of 4.6-46 MeV SEP protons. A depletion by 75% of the ozone density at 40 km altitude should occur during SEP events once every 1 year on average. This will be verified by Trace Gas Orbiter mission, which should be able to observe the signatures of the impact of SEP protons on the Martian atmosphere.

Key words: Solar energetic particles, Martian diffuse aurora, Photochemistry

Résumé

Les impacts des particules énergétiques solaires (SEP) sur la composition atmosphérique de la planète Mars actuelle ont été étudiés à l'aide d'un modèle Monte Carlo et d'un modèle photochimique. Nous avons validé notre modèle Monte Carlo en le comparant aux observations de l'émission aurorale diffuse martienne. Nos simulations mettent en évidence que les protons énergétiques sont la source principale du pic d'émission à basse altitude, et réussissent à reproduire l'altitude du pic observé et la forme des profils d'émission aurorale diffuse, contrairement aux études précédentes, qui ne considéraient que les électrons énergétiques. Nos simulations tridimensionnelles Monte Carlo des émissions du doublet ultraviolet CO_2^+, de l'oxygène 557,7 nm et de l'oxygène 630,0 nm montrent que la morphologie de l'émission induite par les électrons est non-uniforme et brillante uniquement dans les régions des champs crustaux, tandis que l'émission induite par les protons est diffuse sans aucune structure fine. Cette différence résulte de la différence de leurs rayons de gyration autour des lignes de champ magnétique. Nos résultats sur les émissions aurorales diffuses martiennes suggèrent un impact significatif des protons énergétiques sur l'atmosphère martienne de manière globale et profonde. Nous avons également prédit les changements de la composition atmosphérique pendant un événement SEP sur Mars. Nous constatons que l'appauvrissement de la densité d'ozone se produit entre 20 et 60 km en raison de l'augmentation de la densité de HOx (H, OH, et HO_2) induite par la précipitation de protons SEP de 4,6 à 46 MeV. Une diminution de 75% de la densité de l'ozone à 40 km d'altitude devrait se produire pendant un événement SEP une fois tous les ans en moyenne. Ceci sera vérifié par la mission Trace Gas Orbiter, qui devrait être capable d'observer les signatures de l'impact des protons SEP sur l'atmosphère martienne.

Mots clés : Particules énergétiques solaires, Aurore diffuse martienne, Photochimie, Simulation Monte Carlo, MAVEN, TGO/NOMAD.

Abstract

The response of the Martian atmosphere to changing conditions of energetic particles and radiation coming from the Sun, i.e., the space weather on Mars, is one of the biggest interests of Martian exploration in order to understand the potential habitability of Mars. The notable feature of Mars' environment in terms of space weather is the absence of a global intrinsic magnetic field (e.g., Leblanc et al., 2002). Earth's magnetosphere plays a significant role in preventing solar wind from precipitating into Earth's atmosphere, while the absence of an intrinsic magnetic field on Mars leads to a direct interaction between the solar wind and the Martian upper atmosphere. The crustal magnetic fields localized in the southern hemisphere act as local shielding against incoming charged particles (e.g., Leblanc et al., 2002; Lillis et al., 2011). Another feature of Mars in terms of space weather is the thin Martian atmosphere. The surface pressure of the Martian atmosphere is 6 mbar, more than 100 times thinner than Earth's atmosphere, allowing energetic particles to penetrate deeper into the atmosphere. Owing to the absence of a global intrinsic magnetic field and thin atmosphere on Mars, solar energetic particles (SEPs), high energy charged particles emitted from the Sun associated with solar flares and coronal mass ejections, can easily precipitate deep into the Martian atmosphere. When SEPs precipitate into planetary atmospheres, they have various effects on the atmosphere. SEPs that precipitate into planetary atmospheres cause ionization, dissociation, and excitation of atmospheric molecules, leading to auroral emissions (e.g., Sandford, 1961; Schneider et al., 2015) and changes in atmospheric composition (e.g., Crutzen et al., 1975; Rusch et al., 1981; Solomon et al., 1981). The impacts of SEPs on Earth's atmosphere have been intensively studied for the past decades, e.g., the depletion of the ozone density has been observed in the polar mesosphere and stratosphere during a large SEP event occurring in October-November 2003, which is known as the Halloween event (e.g., Seppälä et al., 2004; Jackman et al., 2005; Randall et al., 2005). As for Mars, our understanding of the impacts of SEPs on the Martian atmosphere is gradually progressing thanks to the recent discovery of a new type of the Martian aurora, diffuse aurora, detected by the Imaging Ultraviolet Spectrograph (IUVS) instrument onboard the Mars Atmosphere and Volatile Evolution (MAVEN) spacecraft (Schneider et al., 2015). The notable features of the Martian diffuse aurora are the global brightening of ultraviolet (UV) emission spanning across the whole nightside of Mars and the low peak altitude of ~60 km, indicating that SEPs have precipitated globally and deeply into

the Martian atmosphere. Previous models suggested that 100 keV of monoenergetic electron precipitation should have been at the origin of the low altitude (~60 km) peak of the limb emission; however, no model was able to reproduce the observed emission profiles using the observed energetic electron flux spectra (Schneider et al., 2015; Gérard et al., 2017; Haider and Masoom, 2019). Furthermore, there have been no studies investigating the effects of SEPs on the neutral chemical composition in the present-day Martian atmosphere. Understanding the impacts of SEPs on the atmospheric neutral chemistry on Mars is of astrobiological interest because N_2O and HCN, which are known as the precursors of prebiotic chemistry, are expected to be produced during SEP events (e.g., Airapetian et al.,2016). It is now a good opportunity to investigate the impacts of SEPs on the Martian atmosphere because the Nadir and Occultation for MArs Discovery (NOMAD) instrument onboard the ExoMars Trace Gas Orbiter (TGO) spacecraft, a high-sensitivity and high-resolution spectrometer covering the spectral ranges from UV to Infrared (IR) for atmospheric constituents in the Martian atmosphere, has continued observations since 2018 and because large SEP events are expected to hit Mars during the increasing phase of the solar cycle 25.

The goal of this thesis is to clarify the effects of SEPs on the atmospheric neutral composition on present-day Mars. We have newly developed two numerical models to achieve this goal. The first model is Particle TRansport In Planetary atmospheres (PTRIP). PTRIP is a Monte Carlo model solving the transport of electrons, protons, and hydrogen atoms in planetary atmospheres considering inelastic and elastic collisions with atmospheric molecules, which can calculate ionization, dissociation, and excitation rates of atmospheric molecules. In order to solve precisely the collisions of the energetic particles with atmospheric molecules, we choose better adapted elastic cross sections and scattering angle distributions at high energies than previously published Monte Carlo models. We validated PTRIP by comparing it with previous models. For both electron and proton transport, the new elastic cross sections and scattering angle distributions make the elastic scattering more likely to be forward-peaked at higher energies, leading to smaller backscatter probabilities and deeper penetrations into the atmosphere than previously modeled. We also built a new method for converting particle trajectories into a flux of incident and secondary particles as a function of energy and altitude. This method enables us to estimate accurately the collision rates for rare collisions, even when using a small number of incident particles.

The second model is Photochemical and RadiatiOn Transport model for Extensive USe (PROTEUS), which is a one-dimensional photochemical model solving chemical production, loss, and vertical transport of atmospheric species. PROTEUS is a flexible photochemical model that consists of a Python graphical user interface (GUI) and Fortran subroutines, in which users can intuitively select a planet and chemical reactions and can easily implement new chemical reactions. Chemical reactions selected on GUI are automatically analyzed by a string parsing code written in Python, which will be applied to Fortran 90 modules to simulate selected chemical reactions on a selected planet. We present examples of PROTEUS application to the Martian atmosphere and the Jovian ionosphere, which are in good agreement with previous numerical models. PROTEUS can significantly save time for those who need to develop a new photochemical model; they just need to add chemical reactions in the Python code and just select them on GUI to run a new photochemical model. PROTEUS can be easily extended to other planets and satellites, e.g., Venus, Earth, Titan, and exoplanets in the future.

We first validated PTRIP by comparing it with the vertical profiles of the Martian diffuse auroral emission observed by MAVEN/IUVS during two SEP events in December 2014 and September 2017. We aim to reproduce the observed CO_2^+ ultraviolet doublet (UVD) profiles by considering the contribution of energetic protons reaching MeV energies. We used the electron and proton flux spectra observed by the Solar Energetic Particle (SEP) instrument and the Solar Wind Electron Analyzer (SWEA) instrument onboard MAVEN. Our results showed that proton-induced CO_2^+ UVD emission profiles are brighter, narrower in altitude, and have a lower peak altitude than electron-induced CO_2^+ UVD emission profiles. The sum of the electron- and proton-induced CO_2^+ UVD emission profiles displays similar shapes and altitude peaks as those of the observed profiles (Schneider et al., 2015, 2018), and the extension of energy up to 500 keV for electrons and 20 MeV for protons enabled us to obtain emission profiles closer to the observations. However, the calculated intensity is larger than the observed intensity by a factor of 2 during the December 2014 SEP event, a discrepancy that might be explained by SEP shadowing (Lillis et al., 2016), calculation geometry effect, and magnetic mirror effect (Jolitz et al., 2021). Therefore, the contribution of energetic protons to the Martian diffuse auroral emission helps to reconcile the in-situ observations of the SEP electron and proton flux spectra by MAVEN/SEP and SWEA with the emission brightness observed by IUVS (Schneider et al., 2015, 2018) during the two SEP events.

We extended PTRIP to three dimensions to investigate the effects of the crustal magnetic fields in the southern hemisphere of Mars on the transport of SEPs and the Martian diffuse auroral emission. Our results show different morphology for the electron-induced emission and proton-induced emission in the strong crustal field region due to the difference in their gyro radii. The electron-induced CO_2^+ UVD emission is patchy and bright within the cusp regions, while the proton-induced CO_2^+ UVD emission is diffuse without any fine structures. The oxygen 557.7 nm and 630.0 nm emission lines are also investigated, and we found that the oxygen 557.7 nm emission is similar in shape and intensity to the CO_2^+ UVD emission, whereas the oxygen 630.0 nm emission is restricted to the cusp regions, SEP electron precipitation being its main source because proton-induced emission is completely quenched at low altitudes.

The evolution of the atmospheric neutral chemical composition in the Martian atmosphere during a large SEP event was investigated using PTRIP and PROTEUS. Our results show that the ozone density decreases in the altitude range of 20-60 km by a factor of 10 during a Halloween-class SEP event due to the loss of O by an enhanced HO_2 density. The altitude range of 20-60 km in which the depletion of the ozone density occurs corresponds to the penetration of SEP protons with an energy range of 4.6-46 MeV. Variations in the ozone and HOx (OH and HO_2) densities converge in 5 hours during a Halloween-class SEP event, while the NOx (NO and NO_2) density, which has a longer lifetime, is significantly enhanced during the SEP event. The depletion of the ozone density is expected to be detectable by TGO/NOMAD, but not in other species variations. We performed a sensitivity test of ozone variation with respect to the intensity and spectral shape of the SEP proton flux spectrum. We found that a hard spectral slope at low energy and larger break energy results in a large amount of ozone depletion. A 75% depletion of the ozone density at 40 km altitude and an 8-10% depletion of the column ozone density can be expected during SEP events occurring once a year on average based on a statistical analysis of SEP events in 1976-2016. Our model reveals, for the first time, that ozone concentration decreases significantly during a large SEP event in the Martian atmosphere as on Earth, but via different chemical pathways driven by CO_2 ionization and CO recombination catalytic cycle.

In this thesis, we have provided new insights into the impacts of SEPs on the Martian atmosphere, using newly developed numerical models PTRIP and PROTEUS. Our results suggested a significant contribution of SEP protons to the auroral emissions and the variation of the atmospheric chemical composition because they precipitate into the Martian atmosphere globally and deeply. The spatial feature of the Martian diffuse auroral emissions and the changes in the atmospheric chemical composition simulated in the present study will be validated by future observations by MAVEN/IUVS and TGO/NOMAD.

Further validation of PTRIP and PROTEUS models will be planned in the future. The electron density profiles simulated by our models will be compared with the electron density observations made with the radio occultation measurements such as the Radio Occultation Science Experiment (ROSE) instrument onboard MAVEN and the observation of the attenuation of radio waves reflected from the Martian surface. Since PTRIP and PROTEUS are designed for the adaptability to many planetary atmospheres, we will be able to model SEP-induced auroral emissions on Earth and Venus to further validate our models. Validation of PTRIP by comparing it with auroral emission observations on Mars, Earth, and Venus will lead to further improvement of PTRIP and our better understanding of the interaction of SEPs with planetary atmospheres. Our models will be applied to the ancient Martian atmosphere to estimate the concentration of N_2O, HCN, and H_2CO due to the continuous precipitation of SEPs in the past to explore the search for traces of extraterrestrial life on Mars.

Sommaire

La réponse de l'atmosphère martienne aux conditions changeantes des particules énergétiques et des radiations provenant du Soleil, aussi connue sous le nom de météo spatiale à Mars, est l'un des plus grands enjeux de l'exploration martienne afin de comprendre l'habitabilité passée potentielle de Mars. La caractéristique notable de l'environnement de Mars en termes d'interaction avec notre étoile est l'absence de champ magnétique intrinsèque global (Leblanc et al., 2002). La magnétosphère terrestre joue un rôle important en empêchant le vent solaire de se précipiter directement dans l'atmosphère terrestre, alors que l'absence de champ magnétique intrinsèque sur Mars conduit à une interaction directe entre le vent solaire et la haute atmosphère martienne. Les champs magnétiques crustaux localisés dans l'hémisphère sud agissent comme un bouclier local contre les particules chargées entrantes (Leblanc et al., 2002 ; Lillis et al., 2011). Une autre caractéristique de Mars en termes d'interaction avec notre étoile est la minceur de l'atmosphère martienne. La pression de surface de l'atmosphère martienne est de 6 mbar, soit plus de 100 fois moins que l'atmosphère terrestre, ce qui permet aux particules énergétiques de pénétrer plus profondément dans l'atmosphère. En raison de l'absence d'un champ magnétique intrinsèque global et de la minceur de l'atmosphère martienne, les particules énergétiques solaires (PES), des particules chargées de haute énergie émises par le Soleil et associées aux éruptions solaires et aux éjections de masse coronale, peuvent facilement précipiter dans l'atmosphère martienne. Lorsque les PES précipitent dans l'atmosphère d'une planète, elles ont divers effets sur celle-ci. Ces particules précipitantes provoquent l'ionisation, la dissociation et l'excitation des molécules atmosphériques, ce qui entraîne des émissions aurorales (Sandford, 1961 ; Schneider et al., 2015) et des changements dans la composition de l'atmosphère (Crutzen et al., 1975 ; Rusch et al., 1981 ; Solomon et al., 1981). Les impacts des SEP sur l'atmosphère terrestre ont été intensivement étudiés au cours des dernières décennies. L'appauvrissement de la densité d'ozone a ainsi été observé dans la mésosphère et la stratosphère polaires lors d'un grand événement SEP survenu en octobre-novembre 2003, connu sous le nom d'événement Halloween (par exemple, Seppälä et al., 2004 ; Jackman et al., 2005 ; Randall et al., 2005). En ce qui concerne Mars, notre compréhension des impacts des PES sur l'atmosphère martienne a fortement progressé grâce à la découverte récente d'un nouveau type d'aurore martienne, l'aurore diffuse, détectée par l'instrument IUVS (Imaging Ultraviolet Spectrograph) à bord de MAVEN (Mars Atmosphere and Volatile Evolution)

(Schneider et al., 2015). Les caractéristiques d’une aurore diffuse martienne sont une distribution très étendue de l'émission ultraviolette (UV) sur toute la face nocturne de Mars et la faible altitude du maximum de l’émission autour ~60 km, ce qui indique que les PES précipitent globalement et profondément dans l'atmosphère martienne. Des modèles antérieurs ont suggéré que la précipitation d'électrons mono-énergétiques de 100 keV aurait dû être à l'origine du maximum d’émission à ~60 km. Pourtant, aucun modèle n'a pu reproduire les profils d'émission observés à l'aide des spectres de flux d'électrons énergétiques observés (Schneider et al., 2015 ; Gérard et al., 2017 ; Haider et Masoom, 2019). En outre, aucune étude n'a étudié les effets des PES sur la composition chimique neutre de l'atmosphère martienne actuelle. La compréhension des impacts des PES sur la chimie neutre atmosphérique sur Mars présente un intérêt astrobiologique car on s'attend à ce que N_2O et HCN, qui sont connus comme les précurseurs de la chimie prébiotique, soient produits pendant de tels événements (Airapetian et al.,2016). L'instrument Nadir and Occultation for MArs Discovery (NOMAD) à bord de la sonde ExoMars Trace Gas Orbiter (TGO), un spectromètre à haute sensibilité et haute résolution couvrant les domaines spectraux de l'UV à l'infrarouge (IR) pour les constituants atmosphériques de l'atmosphère martienne, a commencé ses observations en 2018 et devrait pouvoir apporter des observations originales sur cette question, notamment puisque des événements énergétiques solaires intenses devraient se multiplier pendant la phase croissante du cycle solaire 25.

Le but de cette thèse est de clarifier les effets des PES sur la composition neutre de l'atmosphère de Mars. Nous avons récemment développé deux modèles numériques pour atteindre cet objectif. Le premier modèle est Particle TRansport In Planetary atmospheres (PTRIP). PTRIP est un modèle de Monte Carlo qui résout le transport des électrons, des protons et des atomes d'hydrogène dans les atmosphères planétaires en tenant compte des collisions inélastiques et élastiques avec les molécules atmosphériques, ce qui permet de calculer les taux d'ionisation, de dissociation et d'excitation des molécules atmosphériques. Afin de résoudre précisément les collisions des particules énergétiques avec les molécules atmosphériques, des sections élastiques et des distributions d'angles de diffusion à haute énergie mieux adaptées au cas Martien ont été intégré. Nous avons validé PTRIP en le comparant aux modèles précédents. Pour le transport des électrons et des protons, les nouvelles sections élastiques et distributions des angles de diffusion conduisent à des probabilités de rétrodiffusion plus faibles et des pénétrations plus profondes dans l'atmosphère que celles modélisées précédemment. Nous avons également élaboré une nouvelle méthode pour convertir les trajectoires des particules en un flux de particules incidentes et secondaires en fonction de l'énergie et de l'altitude. Cette méthode nous permet d'estimer avec précision les taux de collision même en utilisant un petit nombre de particules incidentes.

Le deuxième modèle est Photochemical and RadiatiOn Transport model for Extensive USe (PROTEUS), qui est un modèle photochimique unidimensionnel résolvant la production chimique, la perte et le transport vertical des espèces atmosphériques. PROTEUS est un modèle photochimique flexible qui se compose d'une interface utilisateur graphique (GUI) Python et de sous-programmes Fortran, dans lesquels les utilisateurs peuvent sélectionner une planète et des réactions chimiques et peuvent facilement implémenter de nouvelles réactions chimiques. Les réactions chimiques sélectionnées sur l'interface graphique sont automatiquement analysées par un code d'analyse écrit en Python, qui sera appliqué aux modules Fortran 90 pour simuler les réactions chimiques sélectionnées sur la planète choisie. Nous présentons des exemples d'application de PROTEUS à l'atmosphère martienne et à l'ionosphère jovienne, qui sont en bon accord avec les modèles numériques précédents. PROTEUS peut faire gagner beaucoup de temps à ceux qui ont besoin de développer un nouveau modèle photochimique ; il leur suffit d'ajouter des réactions chimiques dans le code Python et de les sélectionner dans l'interface graphique pour exécuter un nouveau modèle photochimique. PROTEUS peut être facilement étendu à d'autres planètes et satellites, par exemple Vénus, la Terre, Titan, et des exoplanètes dans le futur.

Nous avons d'abord validé PTRIP en le comparant aux profils verticaux de l'émission aurorale diffuse martienne observée par MAVEN/IUVS lors de deux événements PES en décembre 2014 et septembre 2017. Nous avons cherché à reproduire les profils observés du doublet ultraviolet (UVD) CO_2^+ en considérant la contribution des protons énergétiques atteignant des énergies de l'ordre du MeV. Nous avons utilisé les spectres de flux d'électrons et de protons observés par l'instrument Solar Energetic Particle (SEP) et l'instrument Solar Wind Electron Analyzer (SWEA) à bord de MAVEN. Nos résultats ont montré que les profils d'émission de CO_2^+ UVD induits par les protons sont plus lumineux, plus étroits en altitude, et atteignent un maximum à une altitude plus basse que les profils d'émission de CO_2^+ UVD induits par les électrons. La somme des profils d'émission CO_2^+ UVD induits par les électrons et par les protons présente une variation en altitude similaire à ceux des profils observés (Schneider et al., 2015, 2018). La prise en compte des flux précipitants jusqu'à 500 keV pour les électrons et 20 MeV pour les protons nous a permis d'obtenir des profils d'émission plus proches des observations. Cependant, l'intensité calculée est plus grande que l'intensité observée d'un facteur 2 pendant l'événement PES de décembre 2014, une différence qui pourrait être expliquée par l'effet de la planète sur la propagation de ces particules (Lillis et al., 2016), l'effet de géométrie du calcul et l'effet miroir magnétique (Jolitz et al., 2021). Par conséquent, la contribution des protons énergétiques à l'émission aurorale diffuse martienne permet de réconcilier les observations in-situ de flux d'électrons et de protons énergétiques mesurés par MAVEN/SEP et SWEA avec le profil de l'émission observée par IUVS (Schneider et al., 2015, 2018) pendant ces deux événements.

Nous avons étendu PTRIP à trois dimensions pour étudier les effets des champs magnétiques crustaux dans l'hémisphère sud de Mars sur le transport des PES et l'émission aurorale diffuse martienne. Nos résultats montrent une morphologie différente pour l'émission induite par les électrons et l'émission induite par les protons dans la région de forte intensité du champ crustal en raison de la différence de leurs rayons de gyration autour des lignes de champs magnétiques. L'émission CO_2^+ UVD induite par les électrons est non uniforme et brillante dans les régions de lignes de champ ouverte, tandis que l'émission CO_2^+ UVD induite par les protons est diffuse et sans aucune structure fine. Les lignes d'émission de l'oxygène à 557,7 nm et 630,0 nm ont également été étudiées, et nous avons constaté que l'émission de l'oxygène à 557,7 nm est similaire en forme et en intensité à l'émission de CO_2^+ UVD, tandis que l'émission de l'oxygène à 630,0 nm est limitée aux régions de lignes de champ ouverte, la précipitation d'électrons SEP y étant la source principale car l'émission induite par les protons est complètement éteinte à basse altitude.

L'évolution de la composition chimique neutre de l'atmosphère martienne pendant un grand événement PES a été étudiée à l'aide de PTRIP et PROTEUS. Nos résultats montrent que la densité d'ozone diminue dans la gamme d'altitude de 20-60 km d'un facteur 10 pendant un événement PES de classe Halloween en raison de la perte de O par réaction avec HO_2 dont la densité a augmenté La plage d'altitude de 20 à 60 km dans laquelle se produit l'appauvrissement de la densité d'ozone correspond à la pénétration des protons avec une plage d'énergie de 4,6 à 46 MeV. Les variations des densités d'ozone et de HOx (OH et HO_2) convergent en 5 heures après le début d'événement PES de type Halloween, alors que la densité de NOx (NO et NO_2), qui a une durée de vie plus longue, est significativement augmentée pendant tout l'événement PES. L'appauvrissement de la densité d'ozone devrait être détectable par TGO/NOMAD, mais pas les variations des autres espèces. Nous avons effectué un test de sensibilité de la variation de l'ozone par rapport à l'intensité et à la forme spectrale du spectre du flux de protons. Nous avons trouvé qu'une pente spectrale dure à basse énergie et une énergie de rupture plus grande résulte en une grande quantité d'appauvrissement de l'ozone. Un appauvrissement de 75% de la densité d'ozone à 40 km d'altitude et un appauvrissement de 8-10% de la densité colonne d'ozone peuvent être induites pendant les événements PES se produisant une fois par an en moyenne, sur la base d'une analyse statistique des événements PES de 1976-2016. Notre modèle révèle, pour la première fois, que la concentration d'ozone diminue significativement pendant un grand événement PES dans l'atmosphère martienne comme sur Terre, mais via des voies chimiques différentes contrôlées par l'ionisation du CO_2 et le cycle catalytique de recombinaison du CO.

Dans cette thèse, nous avons fourni de nouvelles informations sur les impacts des PES sur l'atmosphère martienne, en utilisant les modèles numériques récemment développés PTRIP et PROTEUS. Nos résultats suggèrent une contribution significative des protons aux émissions aurorales et à la variation de la composition chimique de l'atmosphère, car ils précipitent dans l'atmosphère martienne de manière globale et profonde. La caractéristique spatiale des émissions aurorales diffuses martiennes et les changements de la composition chimique de l'atmosphère simulés dans la présente étude seront validés par les observations futures de MAVEN/IUVS et TGO/NOMAD.

Une validation supplémentaire des modèles PTRIP et PROTEUS est prévue. Les profils de densité électronique simulés par nos modèles seront comparés aux observations de densité électronique réalisées avec les mesures de radio-occultation telles que l'instrument Radio Occultation Science Experiment (ROSE) à bord de MAVEN et l'observation de l'atténuation des ondes radio réfléchies par la surface martienne. Puisque PTRIP et PROTEUS sont conçus pour s'adapter à de nombreuses atmosphères planétaires, nous serons en mesure de modéliser les émissions aurorales induites par les PES sur Terre et Vénus. La validation de PTRIP en le comparant aux observations d'émissions aurorales sur Mars, la Terre et Vénus permettra d'améliorer encore PTRIP et de mieux comprendre l'interaction des PES avec les atmosphères planétaires. Nos modèles seront également appliqués à l'ancienne atmosphère martienne pour estimer la concentration de N_2O, HCN, et H_2CO due à la précipitation continue de PESs au cours de l’histoire de Mars et pouvoir ainsi explorer une chimie potentiellement à l’origine d’une extraterrestre sur Mars.

Acknowledgments

I would like to express my deep and sincere gratitude to my two supervisors, Prof. Naoki Terada at Tohoku University and Dr. François Leblanc at Sorbonne Université, for giving me this precious opportunity to engage in this work and to study abroad. They taught me plasma physics, numerical techniques, the Martian environment, and how to think, explain and present my work logically. Everything I have learned from you has become the foundation of my research.

I am grateful to Prof. Yasumasa Kasaba, Prof. Yuto Katoh, Prof. Takahiro Obara, Dr. Takeshi Sakanoi, Dr. Fuminori Tsuchiya, Dr. Hiroaki Misawa, Dr. Masato Kagitani, Dr. Atsushi Kumamoto, Dr. Isao Murata, and Dr. Takeshi Kuroda for their helpful advice and comments at seminars in Tohoku University.

I would like to express my sincere thanks to Dr. Hiromu Nakagawa for giving me fruitful advice, kind encouragement throughout my work, and delightful moments at Tohoku University.

I am grateful to Dr. Shotaro Sakai for his helpful advice in developing a Monte Carlo model and for meaningful discussions regarding the Martian aurorae, magnetosphere, and ionosphere.

I would like to thank Mr. Shungo Koyama, Dr. Tatsuya Yoshida, Dr. Kaori Terada, and Mr. Hiroki Karyu for their contributions to developing a photochemical model.

I would like to extend my gratitude to Dr. Ryuho Kataoka and Ms. Kiyoka Murase for providing many inspirations regarding space weather, and for involving me in the auroraXcosmic project.

I am grateful to Ms. Sayano Hiruba for providing the MAVEN particle flux and ephemeris datasets and for meaningful discussions regarding Martian ozone.

I would like to express my deep gratitude to Prof. Jean-Claude Gérard and Dr. Lauriane Soret for their invaluable suggestions and discussions in Liège. The precious time I spent with you in Liège is one of my most cherished memories in my research life.

I would like to express my deep thanks to Prof. Nick Schneider and Prof. Syed Aftab Haider for fruitful discussions regarding the Martian aurorae and for providing meaningful suggestions.

I am grateful to Dr. Ali Rahmati for providing the MAVEN/SEP flux data during the September 2017 solar event.

I would like to express my sincere gratitude to Dr. Ann Carine Vandaele, Dr. Shohei Aoki, Dr. Lori Neary, Dr. Arianna Piccialli, and Dr. Yannick Willame for meaningful suggestions in discussing detectability with TGO/NOMAD.

I would like to express my deep thanks to the rest of the members of my jury, Dr. Dominique Fontaine and Prof. Keisuke Hosokawa.

My special thanks go to my colleague, Ms. Nao Yoshida, and all members of the Planetary Atmosphere laboratory at Tohoku University for spending delightful time with me and for the help in my daily life. My thanks also go to Ms. Miyako Tanno for her administrative support.

I am grateful to Mr. Adrien Finance, Dr. Marie Bouillon, and all members of LATMOS for welcoming me warmly in Paris. My sincere thanks go to Dr. Dominique Delcourt and Dr. Jean-Yves Chaufray for their support in carrying out my work in France.

This work is supported by the International Joint Graduate Program in Earth and Environmental Sciences (GP-EES). I am deeply grateful to GP-EES and its secretary, Ms. Shinobu Okuyama, for her administrative support. This work is also supported by the Japan Society for the Promotion of Science (JSPS).

I would like to express my heartfelt gratitude to my fiancée Aoi Motoyama for her heartwarming words of encouragement and constant support. I accomplished this work because you always stayed close to me with your love.

Finally, my deepest gratitude goes to my parents and sister, Keiichi Nakamura, Kumiko Nakamura, and Yuka Mori, for their constant support and encouragement throughout my life.

Yuki Nakamura
Paris
25 November 2022

Contents

Published paper reprint

List of Figures

List of Tables

Chapter 1

General introduction

1.1 Basic characteristics of Mars' environment

Earth's neighbor Mars, the fourth planet in our solar system, has attracted human interest over the past centuries because of its similarities and differences with Earth. The remarkable similarity between the two planets stems from the possibility that Mars may once have possessed a thick warm atmosphere and liquid water on its surface, indicated by geological evidence such as valley networks on the Martian surface (e.g., Craddock and Howard, 2002). Mars is thus one of the most intriguing planets to search for extraterrestrial life. Contrary to its potential habitability in the past, the environment of present-day Mars is different from that of Earth. The average surface pressure is 6 mbar consisting mainly of 95% CO_2 and 3% N_2 with a mean surface temperature of ~210 K (Williams, 2021), making it impossible to have liquid water on Mars' surface. The differences between Mars' past and present-day atmospheres highlight the fact that Mars should have experienced a dramatic climate change and lost its atmosphere and water to the ground and/or to the interplanetary space on a geological timescale (e.g., Carr, 1987). Recent observations of the isotopic ratio in the Martian atmosphere have suggested that Mars has lost most of its atmosphere into space (e.g., Jakosky, 1991; Jakosky and Jones, 1994; Jakosky et al., 2017) possibly due to intense solar activity in the past (e.g., Terada et al., 2009; Amerstorfer et al., 2017). Thus, how vulnerable the Martian atmosphere is to space weather is one of the biggest interests of the Martian exploration.

The notable feature of Mars' environment in terms of space weather is the absence of a global intrinsic magnetic field (e.g., Leblanc et al., 2002). Earth's magnetosphere plays a significant role in preventing solar wind from penetrating into Earth's atmosphere, while the absence of an intrinsic magnetic field on Mars leads to the direct interaction between the solar wind and the Martian upper atmosphere. The Martian ionosphere acts as a conductive obstacle to incoming solar wind plasma, leading to a formation of an induced magnetosphere (e.g., Michel, 1971;

Intriligator and Smith, 1979). The deceleration of the supersonic solar wind plasma to subsonic leads to the pileup of the interplanetary magnetic field lines in the dayside bow shock and magnetosheath, becoming a major obstacle against incoming charged particles (e.g., Leblanc et al., 2002) (see Figure 1.1). Another feature of Mars' environment in terms of space weather is the crustal magnetic field localized in the southern hemisphere. The Magnetometer and Electron Reflectometer (MAG/ER) instrument on board Mars Global Surveyor (MGS) has revealed the presence of crustal magnetic fields localized in the southern hemisphere of Mars (e.g., Acuña et al., 2001; Connerney et al., 2005). The crustal magnetic field is especially strong near the latitude of 50°S and the east longitude of 180°E with a maximum strength of about 200 nT at 400 km altitude (Acuña et al., 2001). The crustal magnetic fields act as local shielding for incoming charged particles (e.g., Leblanc et al., 2002; Lillis et al., 2011).

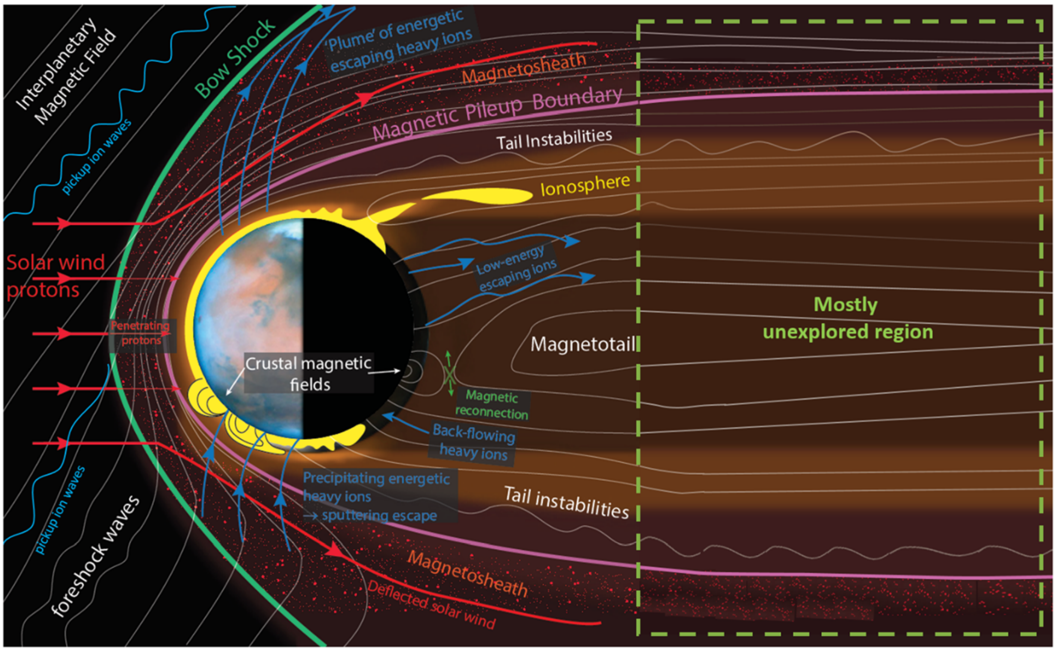

Figure 1.1 Schematic illustration of the space environment around Mars. The left side is facing sunward. Figure is adapted from Sánchez-Cano et al. (2021).

1.2 Solar energetic particles (SEPs)

When an eruptive event, such as a solar flare and a coronal mass ejection (CME), occurs on the Sun, an enormous amount of energy is released into the interplanetary space as electromagnetic radiation, solar wind plasma, and energetic particles. All these energies cause disturbances in the planetary environment; solar X-rays induce increased ionization in the upper atmosphere causing irregularities in the wireless communication systems (e.g., Lanzerotti, 2017), the solar wind induces geomagnetic storms around Earth (e.g., Tsurutani et al., 1988) and enhanced atmospheric escape on unmagnetized planets such as Mars (e.g., Terada et al., 2009; Jakosky et al. 2015). Energetic particles penetrate deep into the atmosphere becoming a radiation hazard for life (e.g., Kataoka et al., 2015; Hassler et al., 2018; Ehresmann et al., 2018). The energetic particles accelerated near the Sun are called solar energetic particles (SEPs).

SEPs are high-energy charged particles emitted into the interplanetary space from the Sun, which consist mainly of protons and electrons with energies ranging from a few keV to a few GeV (Reames, 2021). There are two types of SEP events, impulsive SEP events and gradual SEP events. The impulsive SEP events are related to acceleration by magnetic reconnections in solar flares (e.g., Mann, 2015) and the gradual SEP events are related to acceleration at shock waves driven by CMEs (e.g., Cane et al., 1988; Desai and Giacalone, 2016). The impulsive SEP events are electron-rich, occur 1,000 times per year at solar maximum, and typically last several hours, whereas the gradual SEP events are proton-rich, occur 10 times per year at solar maximum, and typically last several days (e.g., Reames, 1999; Reames, 1995; Desai and Giacalone, 2016). Gradual SEP events are of great interest in terms of the influences on planetary atmospheres due to their long duration and large intensities even though they are less frequent.

When SEPs precipitate into planetary atmospheres, they have various effects on the atmosphere. SEPs that precipitate into planetary atmospheres cause ionization, dissociation, and excitation of atmospheric molecules, leading to auroral emissions (e.g., Sandford, 1961; Schneider et al., 2015) and changes in atmospheric composition (e.g., Crutzen et al., 1975; Rusch et al., 1981; Solomon et al., 1981), which will be addressed in the following chapters.

1.3 SEP effects on the atmosphere of Earth

Owing to the global intrinsic magnetic field, SEP effects on Earth's atmosphere are significant especially in the polar cap region. Precipitation of SEP protons into the polar cap region induces increased electron density at low altitudes, leading to the absorption of high-frequency radio waves, which is referred to as the polar cap absorption events (PCAs) (e.g., Reid and Collins, 1959). With PCAs, auroral emissions are observed in the polar cap region, called the polar-glow aurora (Sandford, 1961, 1962). Polar-glow aurorae are characterized by diffuse emissions of N_2^+ first negative bands around 400 nm and H_β emission at 486.1 nm over the whole nightside polar cap region without a significant increase in oxygen emissions at 557.7 nm (Sandford, 1961, 1963). The weak brightness of oxygen 557.7 nm emission and the great Doppler broadening of the H_β emission line indicate that the penetration of very energetic protons (~ MeV) into low altitudes is at the origin of the polar-glow aurora (Sandford, 1963).

The depletion of the ozone density is of special interest during SEP events, because ozone is an essential molecule for protecting life from ultraviolet radiation. SEP protons ionize and dissociate atmospheric molecules producing atomic nitrogen and molecular oxygen ions, leading to the formation of odd nitrogen NOx (N, NO, and NO_2) and odd hydrogen HOx (H, OH, and HO_2) (e.g., Crutzen et al., 1975; Rusch et al., 1981; Solomon et al., 1981). The increased NOx and HOx destroy ozone through the following catalytic reaction cycles (e.g., Crutzen et al., 1970).

$$\mathrm{NO} + \mathrm{O_3} \rightarrow \mathrm{NO_2} + \mathrm{O_2} \tag{R1.1}$$

$$\mathrm{NO_2} + \mathrm{O} \rightarrow \mathrm{NO} + \mathrm{O_2} \tag{R1.2}$$

$$\text{Net: } \mathrm{O} + \mathrm{O_3} \rightarrow \mathrm{O_2} + \mathrm{O_2} \tag{R1.3}$$

$$\mathrm{OH} + \mathrm{O} \rightarrow \mathrm{H} + \mathrm{O_2} \tag{R1.4}$$

$$\mathrm{H} + \mathrm{O_3} \rightarrow \mathrm{OH} + \mathrm{O_2} \tag{R1.5}$$

$$\text{Net: } \mathrm{O} + \mathrm{O_3} \rightarrow \mathrm{O_2} + \mathrm{O_2} \tag{R1.6}$$

The depletion of the ozone density has been observed during several SEP events (e.g., McPeters and Jackman, 1985). Especially, ozone depletion during large solar storms in October-November 2003, which was one of the largest SEP events in the past decades known as the Halloween event, has been intensively studied (e.g., Seppälä et al., 2004; Jackman et al., 2005; Randall et al., 2005). During the Halloween event, the NOAA 16 SBUV/2 satellite observed a decrease of ozone density by 40% at 0.5 hPa atmospheric pressure level (~ 55 km) in the southern polar region from 27 October through 1 November (see Figure 1.2).

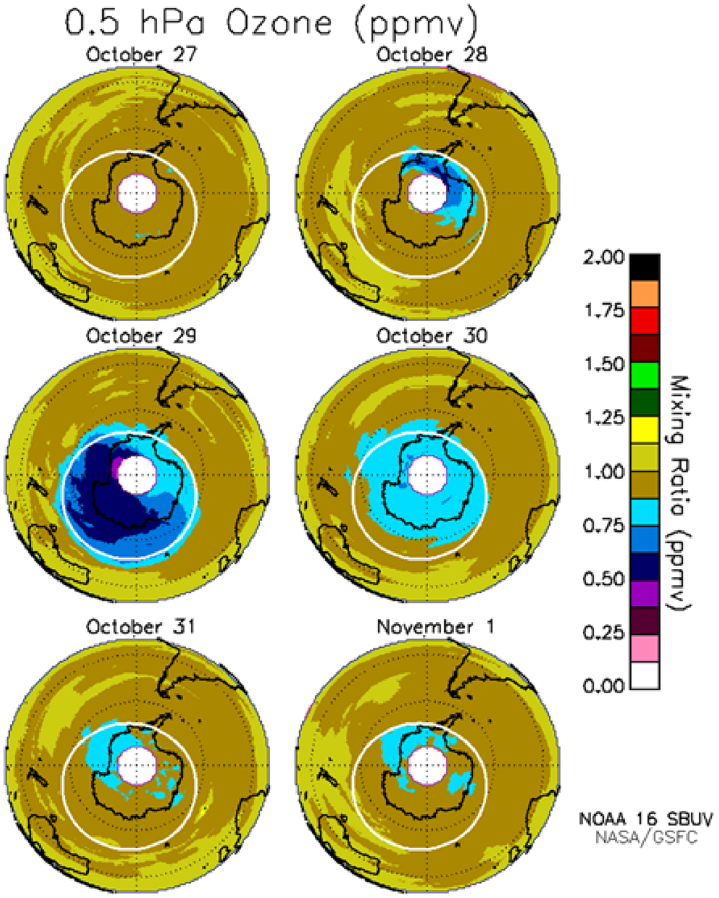

Figure 1.2 Variation of ozone mixing ratio at the atmospheric pressure level of 0.5 hPa in the southern hemisphere polar region during the October-November 2003 SEP event. Figure is adapted from Jackman et al. (2005).

The Global Ozone Monitoring by Occultation of Stars (GOMOS) instrument measured ozone and NO_2 densities during this SEP event and found a strong anti-correlation between the ozone and NO_2 column densities (Seppälä et al., 2004) (see Figure 1.3). The decrease of the ozone density and the enhancement of the NO_2 density were not expected from the FinRose-CTM model without considering SEP effects. The effects of SEPs lasted several months after the Halloween event due to the downward transport of NOx in the polar vortex in winter (e.g., Seppälä et al., 2004; Randall et al., 2005; Krivolutsky et al., 2015).

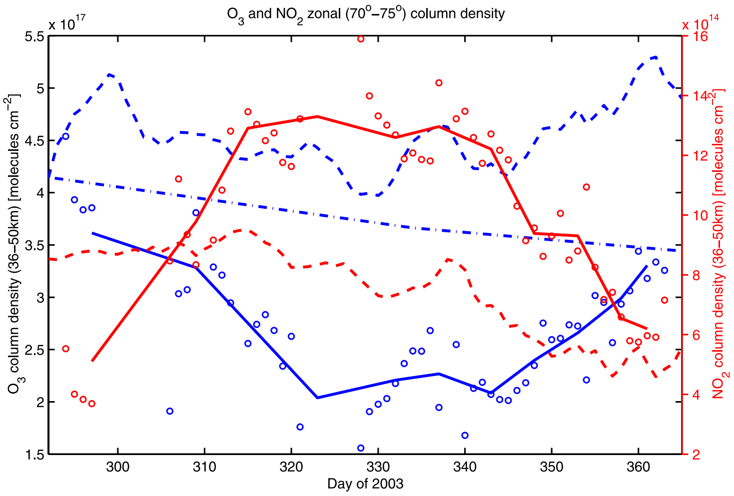

Figure 1.3 Column densities of O_3 (blue) and NO_2 (red) obtained from GOMOS daily zonal average profiles in the latitude range of 70-75 °S and in the altitude range of 36-50 km. The circles are the daily values, and the solid curves are the 5-day mean values. The dashed curves are calculated from the FinRose-CTM model without SEP effects. The dash-dot line is the ozone climatology (Paul et al., 1998). Figure is adapted from Seppälä et al. (2004).

1.4 SEP effects on the atmosphere of Mars

As mentioned above, SEPs cause auroral emissions and ozone depletion in Earth's polar cap region. How do SEPs affect the Martian atmosphere?

The insufficient magnetic field shielding and the thin Martian atmosphere lead to global and deep precipitation of SEPs into the Martian atmosphere. Numerical simulations by Leblanc et al. (2002) showed that SEP protons with energy greater than tens of keV can penetrate the bow shock of the induced magnetosphere without losing energy and that these particles can precipitate even into the nightside, leading to global impacts of SEPs on the Martian atmosphere.

One of the consequences of the precipitation of SEPs into the Martian atmosphere is diffuse aurora. In order to characterize the SEP-induced diffuse auroral emissions on Mars, let me introduce all the three types of aurorae that have been identified on Mars. The first one is the discrete aurora, which was first detected by the Spectroscopy for the Investigation of the Characteristics of the Atmosphere of Mars (SPICAM) instrument on board the Mars Express (MEx) spacecraft in the strong crustal field region in the southern hemisphere (Bertaux et al., 2005). The main feature of the Martian discrete aurora is patchy emissions localized in time and in the cusp region of the crustal magnetic field (Bertaux et al., 2005; Leblanc et al., 2008; Gérard et al., 2015). The CO_2^+ ultraviolet doublet (UVD) at 288.3 and 289.6 nm, CO Cameron bands between 180 and 240 nm, CO Fourth Positive systems between 135 and 170 nm, and OI emissions at 130.4 nm and 297 nm have been observed so far (Soret et al., 2016; Lillis et al., 2022). The discrete aurora is believed to be caused by the precipitation of accelerated suprathermal electrons into the nightside cusp region originating at the magnetosheath and magnetotail (e.g., Brain et al., 2006, 2007). Recent observations made with the Imaging Ultraviolet Spectrograph (IUVS) instrument on board the Mars Atmosphere and Volatile Evolution (MAVEN) spacecraft and by the Emirates Mars Ultraviolet Spectrometer (EMUS) instrument on board the Emirates Mars Mission (EMM) revealed that the discrete aurora occurs more frequently, and it can be seen also in the northern hemisphere region with a weak or absent crustal magnetic field (Soret et al., 2021; Schneider et al., 2021; Lillis et al., 2022).

The second type of aurora is the proton aurora, which was first detected by IUVS (Deighan et al., 2018). The Martian proton aurora results from the precipitation of hydrogen energetic neutral atoms (H-ENAs) and protons into the Martian upper atmosphere (Deighan et al., 2018; Hughes et al., 2019). Solar wind protons collide with the Martian hydrogen corona extending beyond the bow shock becoming H-ENAs via charge exchange collisions, and they are allowed to go through the bow shock and to precipitate into the Martian atmosphere on the dayside, producing proton aurorae (Deighan et al., 2018; Hughes et al., 2019). The main feature of the Martian proton aurora is the brightening of the Lyman-α emissions on the dayside and the seasonal dependence of the occurrence rate and emission intensity. The occurrence rate and emission intensity of the Martian proton aurora are highest during the southern summer solstice because the inflation of the Martian atmosphere leads to the enhancement of the hydrogen corona densities during this season and the solar wind proton flux peaks near the perihelion (Hughes et al., 2019).

The third type is the diffuse aurora, which was first detected by IUVS during the SEP event in December 2014 (Schneider et al., 2015). Since an enhancement of the ultraviolet (UV) emissions on the nightside of Mars has been observed in correlation with a SEP event, the Martian diffuse aurora is believed to be caused by the precipitation of SEPs into Mars' nightside atmosphere (Schneider et al., 2015, 2018). The main features of the Martian diffuse aurora are the global enhancement of the UV emissions spanning across the whole nightside of Mars (see Figure 1.4) and its peak at low altitudes around 60 km (see Figure 1.5) (Schneider et al., 2015, 2018), indicating that SEPs precipitate into the Martian atmosphere globally and deeply. The spectra of the Martian diffuse aurora are dominated by CO_2^+ UVD and CO Cameron bands (Schneider et al., 2015, 2018; Gérard et al., 2017) (see Figure 1.5). The Martian diffuse aurorae have been observed so far during three SEP events in December 2014, March 2015, and September 2017 (Schneider et al., 2015, 2018; Jakosky et al., 2015). It has been proposed that the origin of the Martian diffuse auroral emissions is the precipitation of 100 keV SEP electrons along magnetic field lines draped around Mars (Schneider et al., 2015, 2018; Gérard et al., 2017; Haider and Masoom, 2019). However, no model has been able to reproduce the limb emission profiles observed by IUVS using the SEP electron flux observed simultaneously by MAVEN/SEP instrument. Previous models indicated that SEP electrons with an energy of around 100 keV can reach altitudes around 60 km (Schneider et al., 2015; Gérard et al., 2017; Haider and Masoom, 2019), however, the simulated peak altitude was more than 30 km higher than the observed peak altitude due to the larger contribution of the low energy electrons of the observed energy spectrum of the SEP electrons (Haider and Masoom, 2019). Such a conclusion leads to the following question: Could SEP protons be at the origin of the profile of the Martian diffuse auroral emission? The temporal variations of the auroral emission intensity and those of the SEP electron and proton fluxes did not clearly show that the diffuse auroral emission is produced by SEP electrons or/and protons (Schneider et al., 2018). Numerical simulations by Jolitz et al. (2017) suggested that protons with energy larger than ~ MeV can reach altitudes below 80 km, however, the contribution of SEP protons to the Martian diffuse aurora has not been evaluated so far.

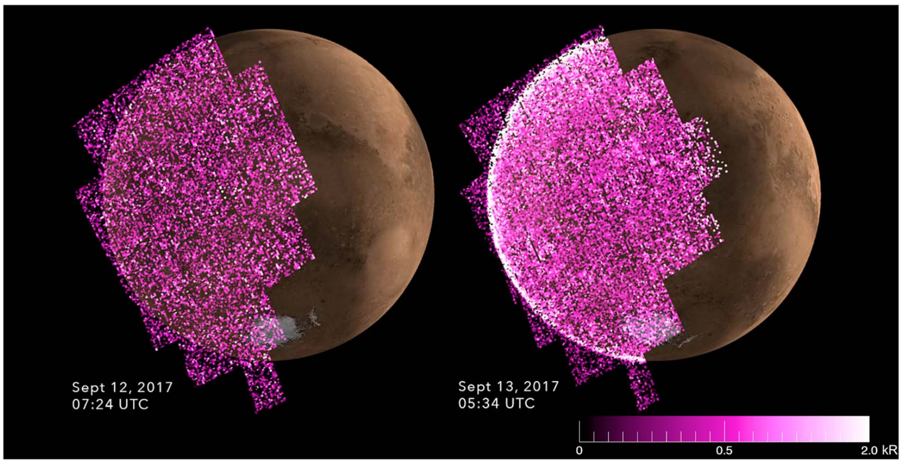

Figure 1.4 Global image of the emission intensity in the midultraviolet wavelength range corresponding to the CO Cameron bands during the September 2017 SEP event observed by IUVS. Images obtained (left) at the start of the SEP event on orbit 5726 and (right) at the peak of the SEP event on orbit 5731. The right panel represents the enhancement of the emission intensity across the whole nightside compared with the left panel. Adapted from Schneider et al. (2018).

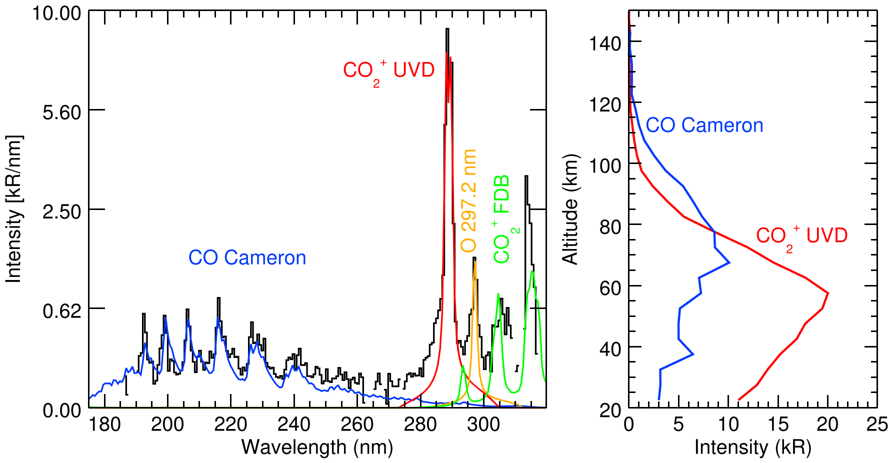

Figure 1.5 (left) Limb emission spectrum during orbit 5730. (right) Vertical profiles of the CO Cameron bands and CO_2^+ ultraviolet doublet (UVD) emissions during orbit 5730. Adapted from Schneider et al. (2018).

Enhancement of the electron density in the Martian atmosphere due to SEP precipitation leads to a disappearance of radar signals reflected from the Martian surface, called a "radar blackout" (e.g., Morgan et al., 2006; Espley et al., 2007; Harada et al., 2018; Sánchez-Cano et al., 2019; Lester et al., 2022), similar to the PCAs in Earth's polar cap region. There have been several radar sounding instruments on board the spacecraft orbiting Mars, the Mars Advanced Radar for Subsurface and Ionosphere Sounding (MARSIS) instrument on board MEx and the Shallow Radar (SHARAD) instrument on board the Mars Reconnaissance Orbiter (MRO) spacecraft, to probe the Martian ionosphere, surface, and subsurface layers. The increase of the electron density at low altitudes below 100 km due to the precipitation of SEPs causes the attenuation of high-frequency (HF) radio waves at low altitudes where the electron-neutral collision frequency is equal to the frequency of the radar instruments (Sánchez-Cano et al., 2019), leading to a partial or at worst complete absorption of the radio waves reflected from the surface. Since the radar blackouts can be observed even in the region where the solar zenith angle is greater than 90°, the radar blackouts are not caused by solar X-rays but by SEPs that can directly impinge into Mars' nightside atmosphere (Morgan et al., 2006). During the September 2017 SEP event, MARSIS recorded radar blackouts for 10 consecutive days and SHARAD recorded them for 3 days both on the dayside and nightside, indicating that the enhancement of the electron density occurs on a global scale (Sánchez-Cano et al., 2019). Sheel et al. (2012) simulated the impacts of SEP protons on the Martian ionospheric composition and found that electron density can be significantly enhanced below 100 km altitude due to precipitation of SEP protons, leading to an attenuation larger than >13 dB of the HF waves in agreement with the MARSIS observations.

Another question now arises: Does neutral chemical composition in the Martian atmosphere change during SEP events? In contrast to Earth, there have been no studies that investigated the effects of SEPs on the neutral chemical composition in present-day Mars' atmosphere. Understanding the effects of SEPs on the atmospheric chemistry on Mars is of astrobiological interest since SEPs are considered as one of the energy sources for prebiotic chemistry on early Mars (e.g., Lingam et al., 2018). There are several energy sources for the prebiotic chemistry, such as the solar UV flux, shock heating by meteoroids, lightning, crustal radioactivity, volcanoes, and SEPs. As mentioned earlier, currently gradual SEP events occur only 10 times per year, so SEP events are not expected to have a significant impact on the planetary environment on a geological timescale. However, flare observations of solar type G stars by Kepler mission suggested that our Sun should have been much more active, and Carrington-type SEP event, regarded as the largest SEP event reported so far, could have hit the planetary atmospheres 1 event per day 4 billion years ago (e.g., Shibayama et al., 2013; Lingam et al., 2018). Laboratory experiments suggested that high-energy protons (~3 MeV) have the highest efficiency in the synthesis of amino acids compared with other energy sources (Kobayashi et al., 1990). Owing to the frequent SEP events in the past and the highest efficiency in the production of amino acids, SEPs are therefore considered as one of the key energy sources for prebiotic chemistry on early Mars (Lingam et al., 2018).

Adams et al. (2021) suggested that the dissociation of nitrogen molecules in the early Martian atmosphere due to SEPs and lightning leads to the production of N_2O and HCN, both of which are known as the precursors of prebiotic chemistry. N_2O is a precursor for the production of HCN, and HCN is a precursor for the abiotic synthesis of amino acids and nucleic acids (e.g., Patel et al., 2015). Since N_2O is a strong greenhouse gas with a global warming potential 298 times larger than CO_2, the production of N_2O due to frequent SEP events in the past could solve the "faint-young Sun paradox" (Airapetian et al., 2016) and could have warmed the ancient Mars' atmosphere.

Understanding SEP impacts on the present-day Martian atmosphere is thus at first needed to investigate how SEPs played a role in prebiotic chemistry in the ancient atmosphere and to explore potential life on Mars.

ExoMars Trace Gas Orbiter (TGO) carries the Nadir and Occultation for MArs Discovery (NOMAD) instrument, a high-sensitivity and high-resolution spectrometer covering the spectral ranges from UV to infrared (IR) for atmospheric constituents (including CO_2, CO, H_2O, NO_2, N_2O, O_3, CH_4, C_2H_2, C_2H_4, C_2H_6, H_2CO, HCN, OCS, SO_2, HCl, HO_2, and H_2S) in the Martian atmosphere (Vandaele et al., 2015). TGO/NOMAD has started the observation of the Martian atmosphere since April 2018. There have been no large SEP events hitting Mars since its start of operation due to the solar minimum period, however, large SEP events are expected to hit Mars from now on during the increasing phase of the solar cycle 25.

1.5 Purposes of this thesis

The goal of this thesis is to clarify the effects of SEPs on the atmospheric neutral composition on present-day Mars. In order to achieve this goal, two numerical models have been newly developed. The first one is Particle TRansport In Planetary atmospheres (PTRIP), a Monte Carlo model solving the transport and collisions of energetic electrons, protons, and hydrogen atoms in planetary atmospheres to calculate ionization, dissociation, and excitation rates of atmospheric molecules during SEP events, which will be described in Chapter 2. The second one is Photochemical and RadiatiOn Transport model for Extensive USe (PROTEUS), a one-dimensional photochemical model solving photochemical reactions and vertical diffusions of atmospheric constituents to investigate the changes in atmospheric composition during SEP events, which will be described in Chapter 3. The specific objectives of this thesis are; (1) to validate PTRIP by comparing it with the Martian diffuse auroral emission profiles observed by MAVEN/IUVS, which will be described in Chapter 4, (2) to clarify the effects of the crustal magnetic fields in the southern hemisphere on the transport of SEPs and the production of the Martian diffuse auroral emissions, which will be described in Chapter 5, and (3) to predict the changes in atmospheric neutral composition on present-day Mars during SEP events and to evaluate their detectability by TGO/NOMAD for future observations, which will be described in Chapter 6. Finally, I will conclude this thesis and will provide some future perspectives in Chapter 7.

Chapter 2

Particle TRansport In Planetary atmospheres (PTRIP)

The Particle TRansport In Planetary atmospheres, PTRIP, is a Monte Carlo model that is designed to calculate the transport and collisions of electrons, protons, and hydrogen atoms that precipitate into planetary atmospheres and to determine the associated ionization, dissociation, and excitation rates. The key assumptions in PTRIP are as follows: (1) atmospheric particles are at rest with respect to incident particles, (2) each incident particle is independent and does not collide or interact with other incident particles, and (3) initial incident angles with respect to the atmosphere are isotropically distributed over one hemisphere directed vertically downward. PTRIP solves the three velocity components of the particle but takes into account only the trajectory of the particle along the altitude (PTRIP will be extended to three dimensions in space in Chapter 5). In Chapter 2, the methodology for solving the transport and collisions of particles is described in detail.

2.1 Equations

PTRIP solves the equation of motion for each incident particle as follows:

$$m\frac{d\boldsymbol{v}}{dt} = q\left(\boldsymbol{v} \times \boldsymbol{B}(\boldsymbol{l}) + \boldsymbol{E}(\boldsymbol{l})\right) \quad , \tag{2.1}$$

where m, $\boldsymbol{v}$, and q are the mass, velocity vector, and the charge of the incident particle, respectively, and $\boldsymbol{B}(\boldsymbol{l})$ and $\boldsymbol{E}(\boldsymbol{l})$ are the magnetic field and electric field vectors at the particle location $\boldsymbol{l}$, respectively.

In PTRIP, a random number is used to determine whether there is a collision at each time step for each incident particle. The collision probability P_c for a particle traveling along a distance Δl is expressed as:

$$P_c = 1 - \exp\left[-\sum_s n_s(\boldsymbol{l})\, \sigma_s^T(E)\, \Delta l \right] \quad , \tag{2.2}$$

where $n_s(\boldsymbol{l})$ is the number density of the sth atmospheric species at the particle location $\boldsymbol{l}$, $\sigma_s^T(E)$ is the total collisional cross section of the sth atmospheric species for particle energy E, and $\Delta l = |v\Delta t|$, where v is the absolute velocity of the particle and Δt is the time step size. A collision occurs if a random number determined from a uniform distribution in a range [0, 1] is less than P_c. Since P_c is the sum of the probabilities for n collisions during Δt (n = 1, 2, 3, …), the accuracy of the collision probability depends on Δt. Δt is determined so that the number of collisions not taken into account during Δt is less than 0.01, which requires P_c to be less than 0.1 (Vahedi and Surrendra, 1995). If a collision occurs, another random number is used to determine the type of collision so that the probability of each type of collision is weighted by the ratio of the frequency of each type of collision to the total collision frequency (Vahedi and Surrendra, 1995).

Several inputs are required by PTRIP. Regarding the incident particles, we need to define the initial type (electron or proton), the initial energy, and the number of incident particles. The number of incident particles at each incident energy is selected to be 1000. Regarding the atmospheric species and their interactions with the incident particles, we need to define the atmospheric neutral density profiles, the inelastic and elastic cross sections, energy loss, scattering angle distributions, and the produced secondary electron energy.

2.2 Cross sections, energy loss, and scattering angle

PTRIP takes into account the elastic and inelastic cross sections of impacting electrons, protons, and hydrogen atoms with atmospheric species. First, we describe the elastic and inelastic cross sections due to electron impacts. We calculate the total elastic cross sections of CO_2, CO, N_2, O_2, and O by the formula of Yalcin et al. (2006), which is applicable to 1 keV - 1 MeV. Below 1 keV, we use the total elastic cross section of CO_2 recommended by Itikawa (2002), of CO recommended by Itikawa (2015), of N_2 recommended by Itikawa (2006), of O_2 recommended by Itikawa (2009), and of O in Porter and Jump (1978) and Porter et al. (1987). The analytic fits of the differential ionization cross sections of CO_2 are taken from Bhardwaj and Jain (2009), including the production of 4 excited states ($X^2\Pi_g$, $A^2\Pi_u$, $B^2\Sigma_u^+$, and $C^2\Sigma_g^+$), dissociative ionization, and double ionization. The analytic fits of the differential ionization cross sections of N_2, O_2, and O are taken from Jackman et al. (1977). The accuracy of the energetic electron transport model depends on the accuracy of the ionization cross section of CO_2 because energetic electrons lose energy mostly by ionizing collisions with CO_2. The total ionization cross section of CO_2 used in PTRIP is $\sim 3.0 \times 10^{-22}$ m^2 at 100 keV, which agrees well with the observed value of $\sim 3.2 \times 10^{-22}$ m^2 at 100 keV by Rieke and Prepejchal (1972). The analytic fits of the differential excitation cross sections of CO_2 are taken from Bhardwaj and Jain (2009). The fundamental three vibrational excitations of CO_2, (010), (100), and (001), within the energy range of 1.5 eV to 30 eV are taken from Itikawa (2002).

Second, we describe the elastic and inelastic cross sections due to proton impacts. The differential screened Rutherford cross section for the elastic scattering of protons by atoms without correction for relativistic effects can be expressed as:

$$\frac{d\sigma}{d\Omega}(E,\theta) = \left(\frac{Ze}{8\pi\varepsilon_0 E}\right)^2 \frac{1}{(1-\cos\theta+2\eta)^2} \quad , \tag{2.3}$$

where Ω is the solid angle, Z is the atomic number of the target particle, e is the elementary charge, ε_0 is the permittivity in space, E is the incident proton energy in eV, θ is the scattering angle, and η is the screening parameter. Derivation of the screened Rutherford cross section is given in Appendix A. The screening parameter η is expressed as (Nigam et al., 1959):

$$\eta = \frac{1}{4}\left(1.12\frac{\lambda}{2\pi a}\right)^2 \quad , \tag{2.4}$$

where λ is the de Broglie wavelength ($\lambda = h/p$, h is the Planck constant and p is the momentum of a proton) and a is the Fermi radius of the atom ($a = 0.885 a_0 Z^{-1/3}$, a_0 is the Bohr radius a_0 = 5.29×10^{-11} m). The total elastic cross section can be expressed by integrating Equation (2.3) over the solid angle Ω:

$$\sigma(E) = \left(\frac{Ze}{8\pi\varepsilon_0 E}\right)^2 \frac{\pi}{\eta(1+\eta)} \tag{2.5}$$

For the study of proton transport in a planetary atmosphere, the differential and total elastic cross sections from Kallio and Barabash (2001) have been widely used in many models (e.g., Fang et al., 2013; Jolitz et al., 2017) and are based on the observation of hydrogen atom-impact elastic cross sections up to 5 keV (Newman et al., 1986; Noël and Prölss, 1993). The observed differential elastic cross section of 5.34 MeV proton impacts on carbon atoms at a scattering angle of 60 degrees is 3.2×10^{-30} m^2 sr^{-1} (Shute et al., 1962); however, the differential elastic cross section from Kallio and Barabash (2001) for incident 5.34 MeV proton at a scattering angle of 60 degrees is 8.2×10^{-27} m^2 sr^{-1}, which is calculated by the formula described in Kallio and Barabash (2001); this value is 3 orders of magnitude larger than the observed value reported by Shute et al. (1962). The differential elastic cross section of carbon for an incident 5.34 MeV proton at the scattering angle of 60 degrees calculated by Equation (2.3) is 2.6×10^{-30} m^2 sr^{-1}, which is in good agreement with the observed differential elastic cross section from Shute et al. (1962).

The analytic fits of the differential ionization cross section of CO_2 due to proton impacts are taken from Rudd et al. (1983), including the production of 4 excited states ($X^2\Pi_g$, $A^2\Pi_u$, $B^2\Sigma_u^+$, and $C^2\Sigma_g^+$). The analytic fits of the differential ionization cross sections of CO, N_2, and O_2 are also taken from Rudd et al. (1983). The total ionization cross section of O is taken from Basu et al. (1987) for above 2 keV and from Haider et al. (2002) for below 2 keV. The analytic fits of the differential charge exchange cross sections of CO_2 above 10 keV are taken from Rudd et al. (1983), including the production of 4 excited states ($X^2\Pi_g$, $A^2\Pi_u$, $B^2\Sigma_u^+$, and $C^2\Sigma_g^+$). The total charge exchange cross section of CO_2 below 10 keV is taken from Haider et al. (2002), and the branching ratio is assumed to be the one for a 10 keV proton in Rudd et al. (1983). The analytic fits of the differential charge exchange cross sections of CO, N_2, and O_2 are taken from Rudd et al. (1983). The total charge exchange cross section of O is taken from Basu et al. (1987) for above 1 keV and Haider et al. (2002) for below 1 keV.

Finally, we describe the elastic and inelastic cross sections due to hydrogen atom impacts. The total elastic cross sections are calculated by the formula of Noël and Prölss (1993), and the parameters for this formula are taken from Kallio and Barabash (2001). Since there is almost no information on the hydrogen atom-impact inelastic cross sections of CO_2, we approximated these cross sections. The total ionization and electron stripping cross sections of CO_2 are assumed to be identical to the hydrogen atom-impact total ionization and electron stripping cross section of O_2, as in many previous studies (e.g., Kallio and Barabash, 2001; Jolitz et al., 2017). The total ionization and electron stripping cross sections of O_2 are taken from Basu et al. (1987) for above 1 keV and from Haider et al. (2002) for below 1 keV. The branching ratio of $CO_2^+(B^2\Sigma_u^+)$ to total CO_2 ionization is assumed to be 0.1, which is identical to the branching ratio due to proton impacts

(Rudd et al., 1983). The total ionization and electron stripping cross sections of CO are also assumed to be identical to those of O_2. The total ionization and electron stripping cross sections of N_2 are taken from Kozelov and Ivanov (1992). The total ionization cross section of O is taken from Basu et al. (1987) for above 2 keV and Haider et al. (2002) for below 2 keV, and the electron stripping cross section of O is taken from Basu et al. (1987) for above 10 keV and from Haider et al. (2002) for below 10 keV. The cross section of CO_2 with hydrogen atoms leading to Lyman-α emission is taken from Haider et al. (2002).

If a collision occurs, the energy loss, scattering angle, and secondary electron energy are calculated for each type of collision. If a collision is elastic, the scattering angle and energy loss are calculated. The scattering angle distribution of electrons is taken from Porter et al. (1987) at low energy (CO_2: below 500 eV, CO: below 800 eV, O_2: below 500 eV, N_2: below 1 keV, and O: below 1 keV) and calculated by the formula of Yalcin et al. (2006) above these energies. The scattering angle of electrons is calculated randomly by using these scattering angle distributions (e.g., Solomon, 2001). The scattering angle of protons can be randomly calculated by using the differential elastic cross section in Equation (2.3). The scattering angle distribution of hydrogen atoms is calculated by the formula of Noël and Prölss (1993), and the parameters for this formula are taken from Kallio and Barabash (2001). The scattering angle of hydrogen atoms is calculated randomly by using this scattering angle distribution (Noël and Prölss, 1993). Energy loss in elastic collision is calculated by solving equations of energy and momentum conservation in a binary collision.

If a collision is inelastic, incident particles lose a fixed amount of energy equal to the energy threshold for ionization, excitation, charge exchange, electron stripping, and Lyman-α. Threshold energies are taken from the references of cross sections as already explained in the previous section. In all inelastic collisions, the scattering angle is assumed to be 0 with the assumption of strong forward-peaked scattering (Solomon, 2001). If a collision leads to ionization, the incident particle also loses the amount of energy associated with the produced secondary electron, which will be described in the next section.

2.3 Secondary electron production

Secondary electron energy due to an electron impact is randomly calculated by the formula of Green and Sawada (1972) and Jackman et al. (1977). The secondary electron energy due to a proton impact is randomly calculated by the formula of Solomon (2001). The secondary electron energy due to a hydrogen atom impact is also calculated by this method. If a collision leads to electron stripping from a hydrogen atom, the calculated secondary electron energy is in the rest frame of the hydrogen atom, which is then converted to the energy in the rest frame of the atmosphere. All the produced secondary electrons are added to the simulation. Electrons lose energy to thermal electrons via Coulomb collisions. The energy transfer rate from incident electrons to thermal electrons is calculated by the formula of Swartz et al. (1971).

2.4 Method for converting trajectories into flux

The collision rate as a function of altitude z for the jth collision type (e.g. ionization rate) of the sth atmospheric species in an SEP event, $P_s^j(z)$, can be calculated by integrating the collision rate of the incident flux of 1 cm^{-2} s^{-1} for incident energy E_0 as a function of altitude $p_s^j(z, E_0)$ weighted by the energy flux spectrum $f(E_0)$ cm^{-2} s^{-1}:

$$P_s^j(z) = \int f(E_0)\, p_s^j(z, E_0)\, dE_0 \tag{2.6}$$

In the Monte Carlo model, the collision rate $p_s^j(z, E_0)$ can be calculated by counting the number of collisions leading to ionization with atmospheric particles in a given cell; however, this counting method is noisy at high altitudes where the collision frequency is small, and minor types of collisions that do not occur frequently. We convert the trajectories of all the particles into a flux and mean pitch angle of the incident particles as a function of altitude and energy. The ionization rate can then be calculated by using the flux, mean pitch angle, neutral density, and collisional cross section. The flux and mean pitch angle are determined at each altitude z ($0 \leq z \leq 500$ km with 1 km resolution) and energy grid E ($15 \leq E \leq E_0$ eV, logarithmically spaced with 10 energy bins in one digit). The collision rate of the jth collision type of the sth atmospheric species within a cell of $[z, z + \Delta z]$×$[E, E + \Delta E]$ of the incident energy E_0 with the incident flux at the top of the model of 1 cm^{-2} s^{-1}, $p_s^j(z, E_0)$ cm^{-3} s^{-1}, can be expressed by using the flux as:

$$p_s^j(z, E_0) = n_s(z) \int_0^{E_0} \sigma_s^j(E) \left[\frac{\phi^+(z, E, E_0)}{\bar{\mu}^+(z, E, E_0)} + \frac{\phi^-(z, E, E_0)}{\bar{\mu}^-(z, E, E_0)} \right] dE \quad , \tag{2.7}$$

where $n_s(z)$ is the number density of the sth atmospheric species at the altitude grid of z, $\sigma_s^j(E)$ is the cross section of the jth collision type of the sth atmospheric species at the energy grid of E, $\phi^+(z, E, E_0)$ and $\phi^-(z, E, E_0)$ are upward and downward fluxes with the incident flux of the incident energy E_0 at the top of the model of 1 cm^{-2} s^{-1} within a cell of $[z, z + \Delta z] \times [E, E + \Delta E]$, respectively, and $\bar{\mu}^+(z, E, E_0)$ and $\bar{\mu}^-(z, E, E_0)$ are the mean cosine pitch angles of upward and downward moving particles within a cell $[z, z + \Delta z] \times [E, E + \Delta E]$ for incident energy E_0, respectively.

We constructed a method of converting all particle trajectories into fluxes in the following flow: (1) converting the trajectory of a single particle into a flux and (2) taking the average of all the fluxes converted from each particle's trajectory. In Figure 2.1a, the red line illustrates the trajectory of a single particle in the altitude-energy frame. To convert the trajectory into flux, one particle is injected (red dot in Figure 2.1a) per second, and all the particles follow the same trajectory. The flux is always 1 cm^{-2} s^{-1} at every point of the trajectory. In Figure 2.1b, the initial downward flux at the cell $[z, z + \Delta z] \times [E, E + \Delta E]$ is 1 cm^{-2} s^{-1} if a particle enters the cell $[z, z + \Delta z] \times [E, E + \Delta E]$ with negative vertical velocity, and vice versa. For better understanding, another example of a trajectory is shown in Figure 2.1c. The initial flux 1 cm^{-2} s^{-1} works well when a particle crosses the whole cell without being backscattered (an enlarged view of a cell in Figure 2.1g). The initial flux overestimates the flux if a particle does not cross the whole cell without being backscattered (e.g., a cell with a blue frame in Figure 2.1b and an enlarged view of a cell in Figure 2.1h), and underestimates the flux if it returns to the cell (e.g., a cell with a blue frame in Figure 2.1c and an enlarged view of a cell in Figure 2.1i) and if it is frequently backscattered within the cell (e.g., an enlarged view of a cell in Figure 2.1j), respectively. The overestimation and underestimation of the initial flux can be improved by multiplying the flux of 1 cm^{-2} s^{-1} by the ratio between the vertical length L traveled by the particle within the cell, and the vertical cell size Δz, $L/\Delta z$. The vertical length L within the cell can be calculated numerically by $L = \sum |v_{z_i}| \Delta t_i$ within the cell, where v_{z_i} is the vertical velocity of the ith particle and Δt_i is a time step size (Figure 2.1d). For example, for the downward flux, L is calculated numerically by summing $|v_{z_i}| \Delta t_i$ at each time step within the cell only if the particle moves downward ($v_{z_i} < 0$). If a particle crosses the whole cell and is not backscattered into this cell, the flux is kept at 1 cm^{-2} s^{-1} (Figure 2.1g: L is the length of a vertical purple bar). If a particle does not cross the whole cell without being backscattered, the flux is then less than 1 cm^{-2} s^{-1} (e.g., a cell with a blue frame in Figure 2.1e, and an enlarged view of a cell in Figure 2.1h: L is the length of a vertical purple bar). If a particle re-enters the cell or if it is frequently backscattered within the cell, the flux is then more than 1 cm^{-2} s^{-1} (e.g., a cell with a blue frame in Figure 2.1f, and an enlarged view of a cell in Figure 2.1i and 2.1j: L is the sum of the length of vertical purple bars).

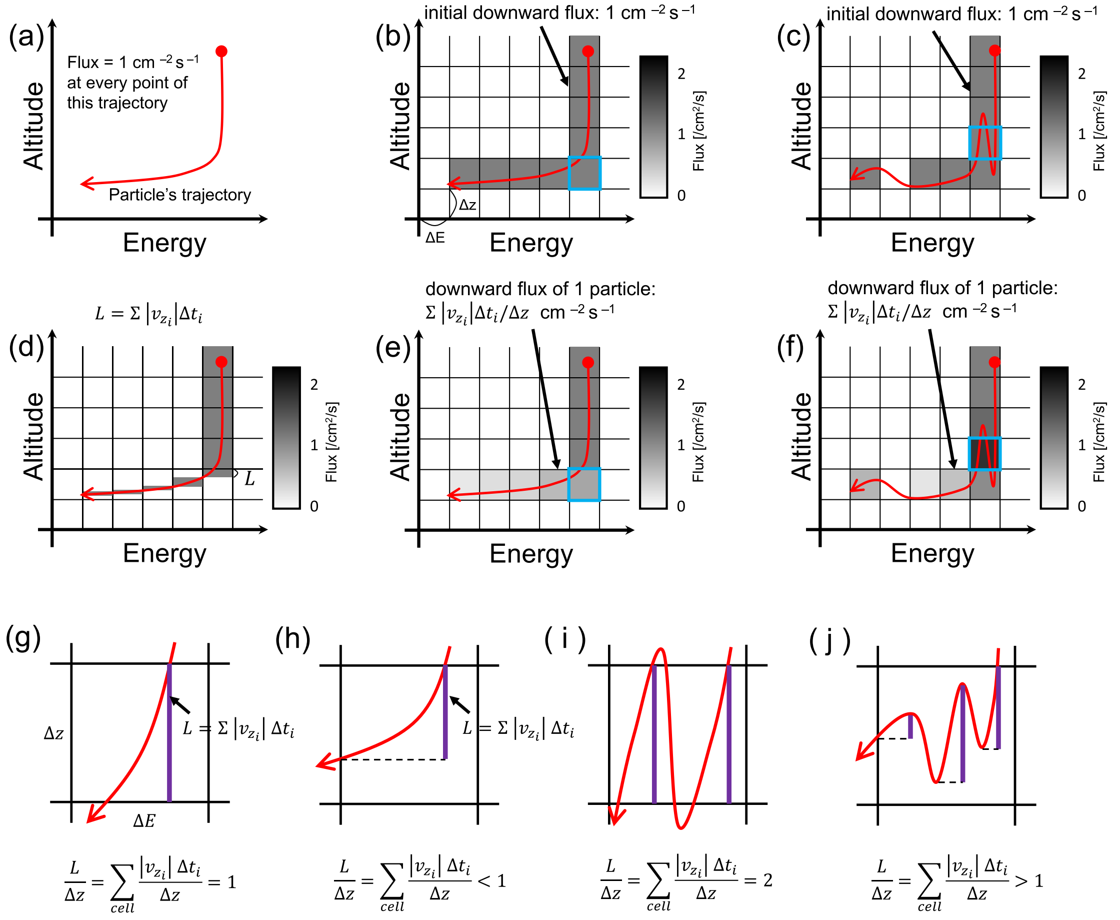

Figure 2.1 Schematic illustration of the method of converting the trajectory of a single particle (red lines) into a flux (see text for details). (g-j) The vertical purple bars represent the vertical length that traveled by a downward moving particle within the cell. Figure is adapted from Nakamura et al. (2022a).

Finally, this flux of a single incident particle is calculated for each of the N incident particles, and taking average of all the converted fluxes yields the expressions of the upward and downward fluxes at each cell, corresponding to the flux of 1 cm^{-2} s^{-1} at the top of the atmosphere (Figure 2.1e and 2.1f). The upward and downward fluxes for an initial energy E_0 with the model topside incident flux of 1 cm^{-2} s^{-1} ($\phi^+(z,E,E_0)$ and $\phi^-(z,E,E_0)$, respectively) are expressed as:

$$\phi^+(z,E,E_0) = \frac{1}{N}\sum_{i=1}^{N}\sum_{\substack{z<z_i\le z+\Delta z\\ E<E_i\le E+\Delta E\\ v_{z_i}\ge 0}} \frac{|v_{z_i}|\Delta t_i}{\Delta z} \tag{2.8}$$

$$\phi^-(z,E,E_0) = \frac{1}{N}\sum_{i=1}^{N}\sum_{\substack{z<z_i\le z+\Delta z\\ E<E_i\le E+\Delta E\\ v_{z_i}<0}} \frac{|v_{z_i}|\Delta t_i}{\Delta z} \tag{2.9}$$

The upward and downward mean cosine pitch angles ($\bar{\mu}^+(z,E,E_0)$ and $\bar{\mu}^-(z,E,E_0)$) at the cell $[z, z+\Delta z]\times[E, E+\Delta E]$ are calculated as:

$$\bar{\mu}^+(z,E,E_0) = \left(\sum_{i=1}^{N}\sum_{\substack{z<z_i\le z+\Delta z\\ E<E_i\le E+\Delta E\\ v_{z_i}\ge 0}} |\cos\theta_i|\Delta t_i\right)\Bigg/\left(\sum_{i=1}^{N}\sum_{\substack{z<z_i\le z+\Delta z\\ E<E_i\le E+\Delta E\\ v_{z_i}\ge 0}} \Delta t_i\right), \tag{2.10}$$

$$\bar{\mu}^-(z,E,E_0) = \left(\sum_{i=1}^{N}\sum_{\substack{z<z_i\le z+\Delta z\\ E<E_i\le E+\Delta E\\ v_{z_i}<0}} |\cos\theta_i|\Delta t_i\right)\Bigg/\left(\sum_{i=1}^{N}\sum_{\substack{z<z_i\le z+\Delta z\\ E<E_i\le E+\Delta E\\ v_{z_i}<0}} \Delta t_i\right), \tag{2.11}$$

where $\cos\theta_i = v_{z_i}/v_i$. Examples of the calculated upward and downward fluxes, and the mean cosine pitch angles are shown in Figures B.1-B.5 in Appendix B. A comparison of the two methods of deriving the ionization rate, counting the number of ionization collisions and using the converted fluxes (Equations (2.7-2.11)), are shown in Figure 2.2. The ionization rate calculated by the method using the converted fluxes is in very good agreement with the counting method. The accuracy of the converted flux depends on the timestep. The distance that a particle travels within one timestep should be kept as being less than 1% of the vertical grid size.

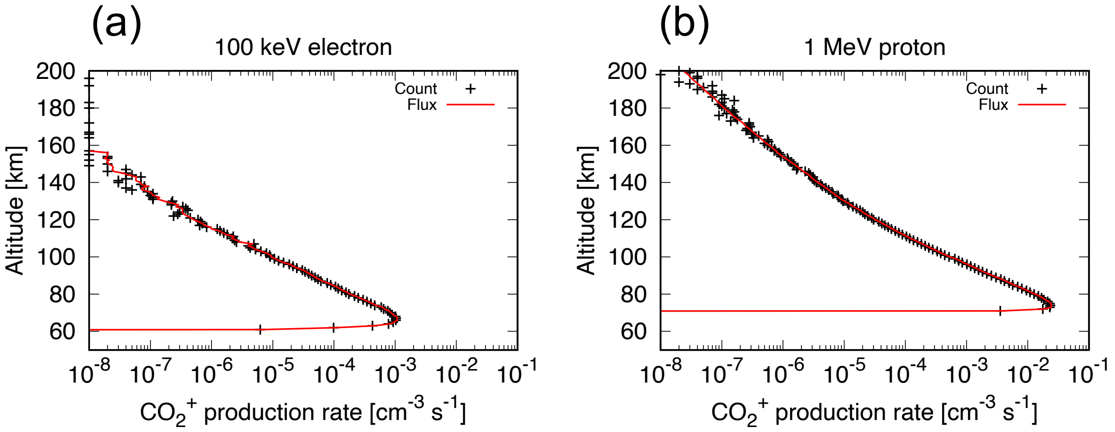

Figure 2.2 Comparison of the production rate of CO_2^+ calculated by using the method of counting (black dots) and the method using the flux, mean cosine pitch angle, and neutral density (red solid curves). (a) Incident 100 keV electrons and (b) 1 MeV protons are injected.

2.5 Energy conservation under magnetic fields

The accuracy of the 4th order Runge-Kutta method under a magnetic field strongly depends on the timestep size. The timestep size is set in order to be always less than 1% of the orbital period of the gyration motion. The variation of the energy of an incident 100 eV electron within a magnetic field strength of 100 nT is shown in Figure 2.3. In this simulation, collisions with atmospheric molecules are ignored and only the equation of motion is solved. After 10^6 timesteps (10^4 orbits of the gyration motion), an incident 100 eV electron loses less than 0.1% of its energy. Since incident particles are suppressed from the simulation less than 10^7 timesteps (corresponding to ~1% loss of energy) due to the energy loss or exiting the atmosphere, our choice of the timestep size is enough accurate for our purpose to investigate the collisions with atmospheric molecules.

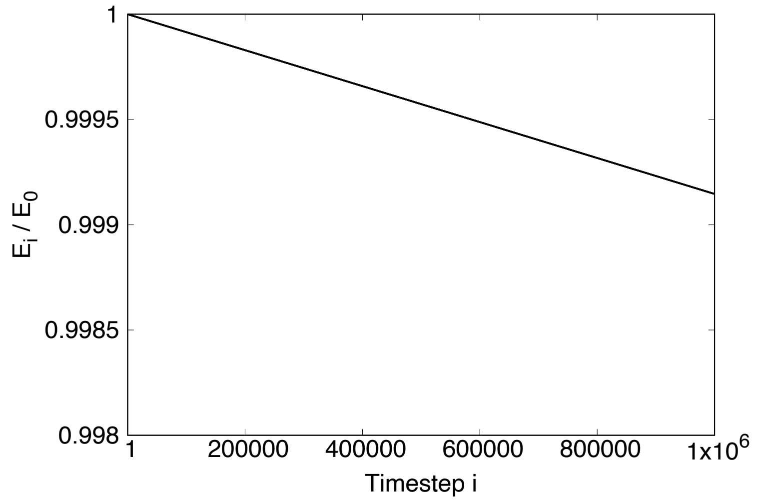

Figure 2.3 Variation of the energy of an electron with an incident energy 100 eV in a uniform magnetic field of 100 nT. The horizontal axis is the number of timesteps and the vertical axis is the ratio of the electron energy at each timestep to the initial energy. 100 timesteps correspond to one gyration.

2.6 Validation

Since the numerical codes of PTRIP were newly developed, we first compare our model of electron transport with Gérard et al. (2017). The altitude profile of CO_2 is taken from Gérard et al. (2017). For simplicity, we ignore other species of the atmosphere in this test calculation. Our model uses the scattering angle distributions for elastic scattering with the CO_2 of Porter et al. (1987) for below 500 eV and that of Yalcin et al. (2006) for above 500 eV. Since Gérard et al. (2017) used the value of Porter et al. (1987) even at high energies, we performed validation calculations for two cases: (1) case 1 used the Porter et al. (1987) scattering angle distribution at all energies, and (2) case 2 used the Porter et al. (1987) value for below 500 eV and the Yalcin et al. (2006) value for above 500 eV. The electron flux at the top of the model is 1 mW m^{-2} for all incident energies, which is set to be the same as Gérard et al. (2017). The incident angle is isotropically distributed.

Figures 2.4a and 2.4b show the calculated $CO_2^+(B^2\Sigma_u^+)$ production rate for the two cases, and Figures 2.4c and 2.4d show the calculated limb intensity of CO_2^+ UVD for the two cases. In case 1, the production rate of $CO_2^+(B^2\Sigma_u^+)$ and the limb intensity of CO_2^+ UVD are the largest at 2 keV and decrease with incident energy above 2 keV. This trend is also visible in the Gérard et al. (2017) value. The peak limb intensity of CO_2^+ UVD in case 1 is 30 kR at 2 keV and 10 kR at 100 keV, which is in good agreement with Gérard et al. (2017). In case 2, the production rate of $CO_2^+(B^2\Sigma_u^+)$ and the limb intensity of CO_2^+ UVD are almost constant above 500 eV. The production rate of $CO_2^+(B^2\Sigma_u^+)$ at 100 keV in case 1 is 4 times smaller than that in case 2. The penetration altitude of electrons in case 1 is higher than that in case 2. The difference between the two cases comes from the different scattering angle distributions. Figure 2.5 shows the backscattering probability of electrons at each incident energy for the two cases. In case 1, the backscattering probability increases with incident energy above 500 eV and reaches ~80% at 100 keV. In case 2, the backscattering probability is almost constant at ~ 30% above 2 keV. In case 1, since the same scattering angle distribution is used above 500 eV, electrons with higher energy have more chances to change direction because they experience more elastic collisions. In case 2, since scattering becomes more forward-peaked at high energy, the backscattering probability does not increase at high energy. The production rate of $CO_2^+(B^2\Sigma_u^+)$ and limb intensity of CO_2^+ UVD in case 1 at high energy are smaller than those in case 2 because electrons are more likely to be backscattered before they lose energy via ionization. There remains a discrepancy in the penetration altitude of electrons between case 1 and Gérard et al. (2017); the possible reasons are the different total elastic cross section and ionization cross section used in the two models. However, the penetration altitude of electrons during the December 2014 SEP event in our calculation (in case 2) is consistent with Haider and Masoom (2019), as explained in Section 4.2.

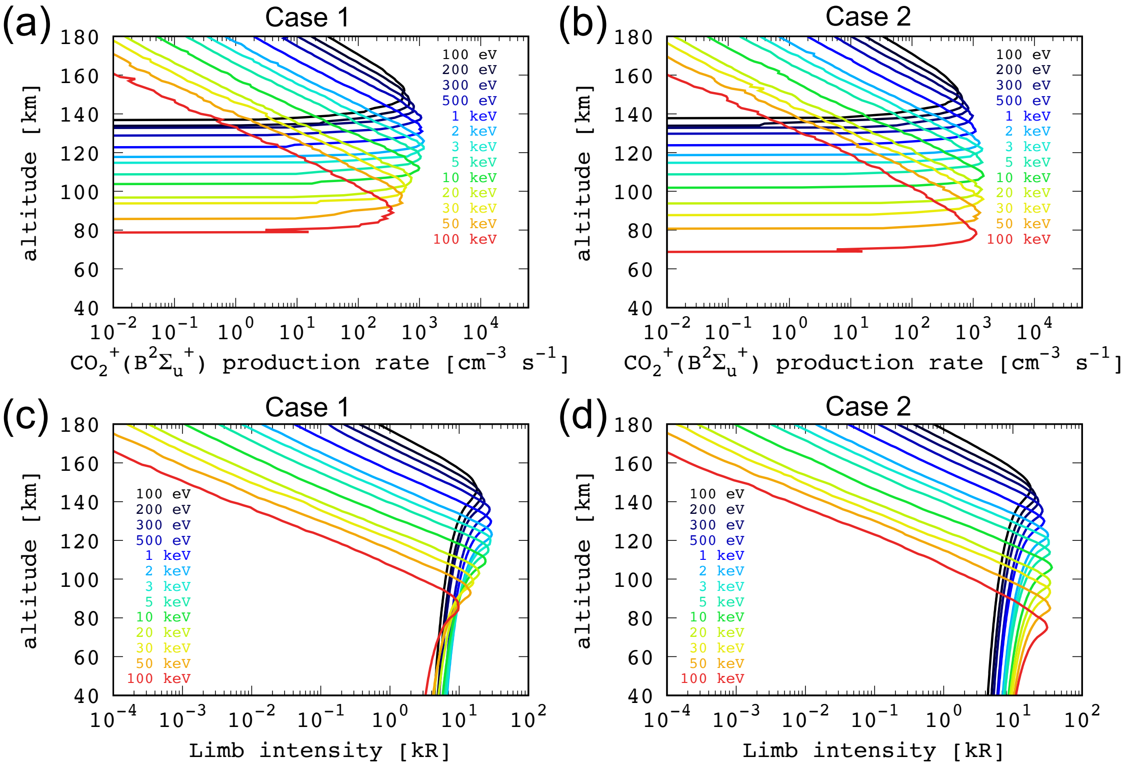

Figure 2.4 (a, b) Production rate of $CO_2^+(B^2\Sigma_u^+)$ due to electron impacts for each incident electron energy in case 1 and case 2. Case 1 uses the elastic scattering angle distribution of Porter et al. (1987) for all energies, and case 2 uses Porter et al. (1987) below 500 eV and Yalcin et al. (2006) above 500 eV. (c, d) Limb intensity profile of CO_2^+ UVD in case 1 and case 2, respectively. The model topside incident electron flux is 1 mW m^{-2} at each incident energy for the two cases. Figure is adapted from Nakamura et al. (2022a).

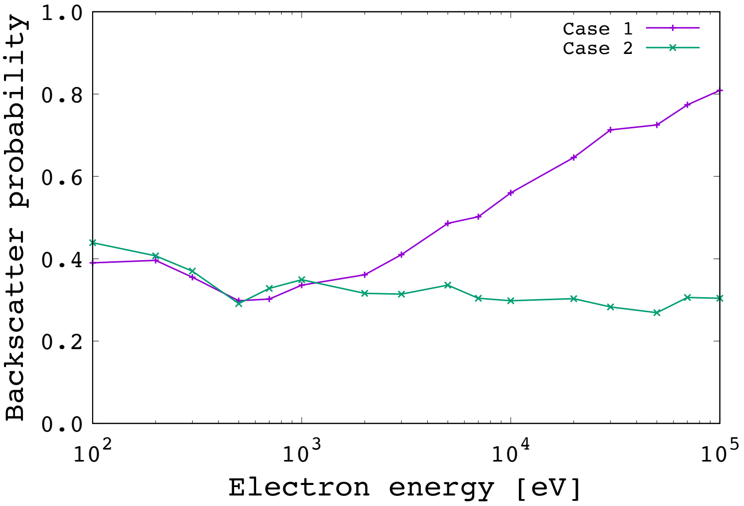

Figure 2.5 Backscattering probability of different incident electron energies in case 1 and case 2. Figure is adapted from Nakamura et al. (2022a).

Our model of proton and hydrogen atom transport is also compared with previous models. Several models have been proposed for proton and hydrogen atom transport in the Martian atmosphere: a model of fast neutral hydrogen atoms (hereafter called KB01) (Kallio and Barabash, 2001), the Stopping and Range of Ions in Matter model (hereafter called SRIM) (Leblanc et al., 2002), and the Atmospheric Scattering of Protons and Energetic Neutrals (hereafter called ASPEN) (Jolitz et al., 2017). KB01, SRIM, and ASPEN were previously compared in Leblanc et al. (2002) and Jolitz et al. (2017) using the test calculation of incident 800 eV neutral hydrogen atoms. One thousand hydrogen atoms of 800 eV were isotropically injected into the Martian atmosphere. Our model predicts that 27% of the energy is deposited into ionization, which agrees with KB01 (27%) and ASPEN (26%). We found that 26% and 24% of energy is deposited into electron stripping and Lyman-α emission, respectively, which agree with KB01 (26% and 30%, respectively). We found that 19% of the energy was deposited into direct neutral heating via elastic collisions, which is in close agreement with KB01 (14%), SRIM (16%), and ASPEN (13%). Our model found that 57% of hydrogen atoms were backscattered, which agrees with KB01 (58%) and is larger than ASPEN (32%) and SRIM (10%).

For proton transport, our model uses the differential and the total elastic cross sections described in Equations (2.3) and (2.5), while ASPEN used the differential and the total elastic cross sections from KB01, and it predicted that the backscattering probability of protons increases with incident energy above 100 keV, reaching more than 60% at 5 MeV. Since they used the scattering angle distribution from KB01 that does not depend on the proton energy, higher energy protons experience so many elastic collisions that they are more likely to change their directions, leading to a high backscattering probability. We tested the proton backscattering probability for two cases: case A used the same differential and total elastic cross section of protons and hydrogen atoms as KB01, and case B used the differential and total elastic cross section of protons described in Equations (2.3) and (2.5) and those of hydrogen atoms from KB01. The backscatter probabilities of different incident proton energies in the two cases are shown in Figure 2.6. In case A, the backscattering probability of protons increases with incident proton energy above 200 keV and reaches more than 60% at 5 MeV, which is in close agreement with ASPEN. In case B, the backscattering probability is close to that in case A below 100 keV, but it decreases with incident proton energy and reaches nearly 0% at 5 MeV because the scattering becomes more likely to be forward-peaked at higher energy. As described in Section 2.2, since KB01 overestimated the differential elastic cross section of MeV protons by a few orders of magnitude at large scattering angles, case A significantly overestimated the backscattering probability, which leads to the underestimation of the ionization rate at low altitudes where MeV protons deposit energy into the atmosphere.

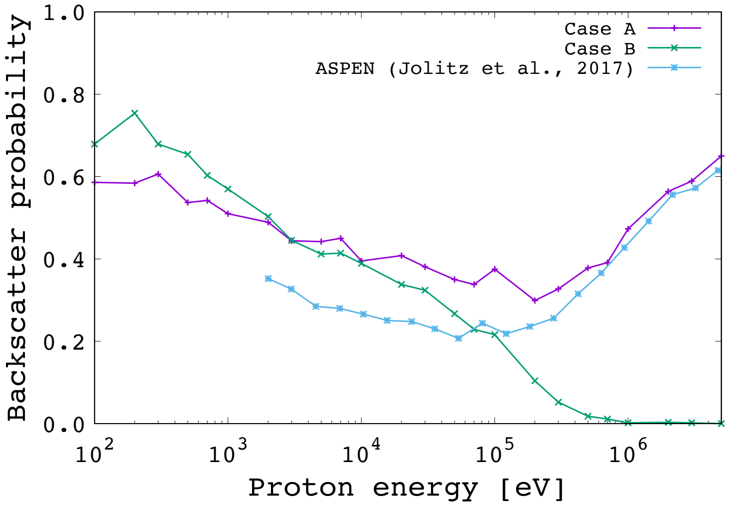

Figure 2.6 Backscattering probability of different incident proton energies in case A and case B. Case A uses the differential cross section and the total elastic cross section from KB01 and case B uses the screened Rutherford elastic cross section. Figure is adapted from Nakamura et al. (2022a).

2.7 Chapter summary

A Monte Carlo model, Particle TRansport In Planetary atmospheres (PTRIP), has been newly developed to solve the transport of energetic electrons, protons, and hydrogen atoms in planetary atmospheres. In order to solve precisely the collisions of the energetic particles with atmospheric molecules, we choose better adapted elastic cross sections and scattering angle distributions at high energy than previously published Monte Carlo models. We validated PTRIP by comparing it with previous models. For both electron and proton transport, the new elastic cross sections and scattering angle distributions make the elastic scattering more likely to be forward-peaked at higher energy, leading to smaller backscatter probabilities and deeper penetrations into the atmosphere than previously modeled. We also built a new method for converting particle trajectories into a flux of incident and secondary particles as a function of energy and altitude. This method enables us to estimate accurately the collision rates at high altitudes where collisions are rare and collision rates of small cross sections, even when using a small number of incident particles.

Chapter 3

Photochemical and RadiatiOn Transport model for Extensive USe (PROTEUS)

Photochemical models are essential for investigating the vertical chemical structure of planetary atmospheres and their evolution throughout the history of the planets. They solve continuity-transport equations considering the production and loss of each atmospheric species by numerous chemical reactions including photolysis. So far, plenty of photochemical models have been developed for various planetary atmospheres (e.g., Kasting et al., 1979; Nair et al., 1994; Kim and Fox, 1994; Fox and Sung, 2001; Krasnopolsky, 2009; Krasnopolsky, 2012; Chaffin et al., 2017). As the mass and spectral resolutions of measurements for detecting chemical species in planetary atmospheres increase and the theory of chemical kinetic systems become more complex, the need for photochemical models with hundreds or thousands of chemical reactions increases.

There are roughly three approaches to develop a numerical code for solving a lot of chemical reactions (Damian et al., 2002). The first approach is a hard-coding approach, in which the developer analyzes the chemical reactions, derives all the production and loss rate terms for each chemical species, and codes them into a program by hand. This approach is easy to develop when the number of chemical reactions is smaller than a hundred, however, it takes a lot of time to develop a code when the number of reactions becomes larger than hundreds or more. It is also difficult to add new chemical reactions into an already hard-coded program.

The second approach is a totally integrated approach, in which the chemical reactions are listed in a specific file in a certain format, and they are parsed by a program and stored in a memory when it is run. This approach is flexible in adding new chemical reactions after the development of the core program, and easy to deal with hundreds of chemical reactions without developer's manual derivation. This approach was used in the Atmos model in Fortran language for instance, which was originally developed by Kasting et al. (1979), updated by Zahnle et al. (2006), and recently described in Arney et al. (2016). Recently an integrated Martian photochemical model was developed by Chaffin et al. (2017) in Julia language with a more flexible way of describing reactions and rate coefficients.

The third approach is a preprocessing approach, in which the chemical reactions are listed in a specific file like the totally integrated approach but are parsed by a preprocessor to generate a hard-coded program in a high-level language such as Fortran or C language (Damian et al., 2002). This approach is also flexible in implementing hundreds of chemical reactions and is as efficient as the hard-coding approach. This approach was used in the kinetic preprocessor (KPP) originally developed by Damian et al. (2002), which has been widely used for chemical kinetic models for Earth's atmosphere.

In this chapter, we present a new integrated photochemical model named Photochemical and RadiatiOn Transport model for Extensive USe (PROTEUS), with a totally integrated approach. PROTEUS couples Python and Fortran modules, which is designed for adaptability to many planetary atmospheres, for flexibility to deal with thousands of or more chemical reactions with high efficiency, and for intuitive operation with a graphical user interface (GUI). A Python GUI program integrates a list of chemical reactions, GUI functions controlling the behavior of GUI operation, and a string parsing function analyzing chemical reactions that output a Fortran 90 module. Fortran 90 modules solve differential equations numerically. Chemical reactions are written in a simple and flexible string format in the Python GUI program, making it easy to add new chemical reactions into the Python GUI program. The feature of PROTEUS that the Python GUI program outputs a Fortran 90 module is similar to the preprocessing approach, leading to high efficiency, however, the Fortran modules in PROTEUS are not hard-coded but are rather generic.

PROTEUS has been newly developed and independent of other photochemical models or KPPs that have been developed so far.

3.1 Governing equations

PROTEUS is a one-dimensional photochemical model that solves a system of continuity equations for each species as follows:

$$\frac{\partial n_i}{\partial t} = P_i - L_i - \frac{\partial \Phi_i}{\partial z} \quad , \tag{3.1}$$

where n_i is the number density of ith species, P_i is the production rate of ith species, L_i is the loss rate of ith species, z is the altitude and Φ_i is the vertical flux of ith species. The vertical flux Φ_i for both neutral and ionized species can be expressed as follows:

$$\begin{aligned}\Phi_i = &-n_i D_i \left(\frac{1}{n_i}\frac{\partial n_i}{\partial z} + \frac{1}{H_i} + \frac{q_i}{q_e}\frac{T_e/T_i}{P_e}\frac{\partial P_e}{\partial z} + \frac{1+\alpha_i}{T_i}\frac{\partial T_i}{\partial z} \right) \\ &- n_i \quad \left(\frac{1}{n_i}\frac{dn_i}{dz} + \frac{1}{H} + \frac{1}{T}\frac{dT}{dz} \right)\end{aligned} \quad , \tag{3.2}$$

where D_i is the binary diffusion coefficient between ith species and the background atmosphere, H_i=$k_B T_i/m_i g$ is the scale height of ith species, m_i is the mass of ith species, k_B is the Boltzmann constant, g is the gravitational acceleration, q_i is the charge of ith species, q_e is the elementary charge, T_e and T_i are the temperatures of electrons and ith species, respectively, P_e=$n_e k_B T_e$ is the electron pressure, n_e is the electron number density, α_i is the thermal diffusion coefficient, is the eddy diffusion coefficient, H=$k_B T/mg$ is the mean scale height of the background atmosphere, m is the mean molecular mass of the atmosphere, and T is the neutral temperature. The temperature profiles are assumed to be stationary in time. The third term in Equation (3.2) is the ambipolar diffusion term, which is applied only to charged species. The altitude-dependent gravitational acceleration g is calculated by using the mass and radius of the planet.

PROTEUS is basically a one-dimensional photochemical model and currently does not solve horizontal transportation but considers the rotation of a planet as options to obtain a simplified global distribution. PROTEUS has four options for the simulation geometry: (1) one-dimensional simulation at a given latitude at noon, (2) two-dimensional simulation at noon at each latitude from the north pole to the south pole, (3) two-dimensional simulation at a given latitude with rotation, and (4) three-dimensional simulation at all latitudes with rotation. The three-dimensional simulation has already been applied by Nakamura et al. (2022b) for the Jovian ionosphere.

3.2 Radiative transfer

PROTEUS uses the EUVAC model (Richards et al., 1994) for the reference irradiance spectrum of the solar extreme ultraviolet (EUV) flux to calculate the photoionization rates of atmospheric species. The EUVAC model provides the solar EUV flux in 37 wavelength bins ranging from 5 nm to 105 nm. The EUVAC model requires the input of F10.7 value and its 81 days running average value. For calculating the photodissociation rates of atmospheric species, we use the reference irradiance spectrum of the solar flux in the wavelength range 0.05-2499.5 nm taken from Woods et al. (2009). Adopting the solar flux taken from the EUVAC model and Woods et al. (2009), the radiative transfer is solved by considering the absorption of the solar irradiation by atmospheric species. In PROTEUS, users can flexibly change the wavelength bin size for the solar irradiance of Woods et al. (2009) and absorption/dissociation cross sections of chemical species. The solar flux and cross section data can be provided in any wavelength bins, which are automatically interpolated and binned to the wavelength bin given by the user. The automatic binning algorithm is especially useful when users need high resolution wavelength bins in a limited wavelength range. For example, if users need to resolve the Schumann-Runge bands of the oxygen molecule, the user can set a 0.01 nm resolution at 176-192.6 nm and 1 nm at other wavelength range, which reduce the computational cost in solving radiation transfer and dissociation rate of atmospheric species even fully resolving the structured Schumann-Runge bands of the oxygen molecule. An example of the automatic binning algorithm applied to the Schmann-Runge bands of O_2 molecule in several wavelength resolutions is shown in Figure 3.1. This algorithm is also useful for resolving a slight difference in absorption cross sections between isotopes (Yoshida, T. et al., 2022 submitted).

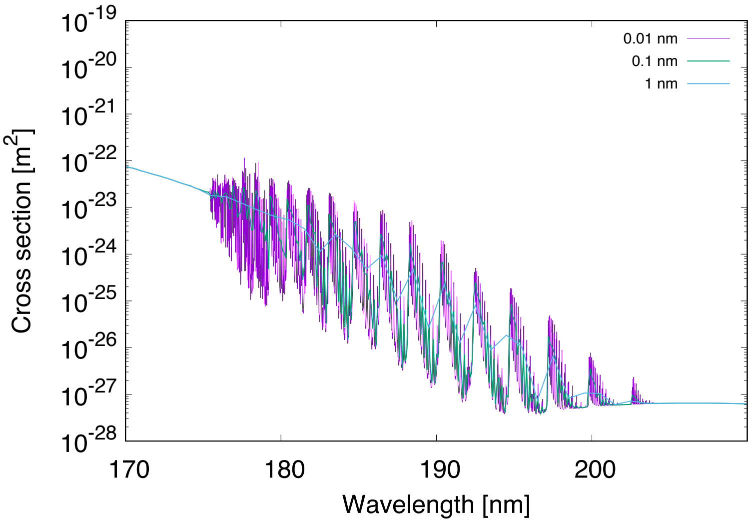

Figure 3.1 Example of the automatic binning algorithm for the Schumann-Runge bands of O_2 photo-absorption cross section. The purple curve is the cross section calculated with a 0.01 nm resolution, the green curve is calculated with a 0.1 nm resolution, and the cyan curve is calculated with a 1 nm resolution.

The reference solar irradiance spectra are then divided by the square of the heliocentric distance r of the planet in AU. The distance r between the planet and the Sun at a given solar longitude L_s is given by

$$r = r_m \frac{1 - e^2}{1 + e\cos\left(L_s - L_{s,P}\right)} \quad , \tag{3.3}$$

where r_m is the mean heliocentric distance in AU between the planet and the Sun, e is the eccentricity of the planetary orbit, and $L_{s,P}$ is the solar longitude at perihelion. The solar zenith angle at latitude θ and an hour angle η is given by

$$\cos\chi = \sin\theta\sin\delta + \cos\theta\cos\delta\cos\eta \quad , \tag{3.4}$$

where δ is solar declination. δ and η are given by

$$\sin\delta = \sin\varepsilon\sin L_s \quad , \tag{3.5}$$

$$\eta = \frac{2\pi t_L}{T_p} \quad , \tag{3.6}$$

where ε is the tilt angle of the rotational axis, t_L is the time in second measured from the local noon, and T_p is the rotational period of the planet.

3.3 Numerical method

We referred to the numerical method for solving the system of continuity equations for the photochemical model described in Catling and Kasting (2017) with some corrections. The vertical flux in Equation (3.2) can be re-written as follows:

$$\Phi_i = -(\quad + D_i)\frac{\partial n_i}{\partial z} - \zeta_i n_i \tag{3.7}$$

$$\zeta_i = D_i\left(\frac{1}{H_i} + \frac{q_i}{e}\frac{T_e/T_i}{P_e}\frac{\partial P_e}{\partial z} + \frac{1+\alpha_i}{T_i}\frac{\partial T_i}{\partial z}\right) + \quad \left(\frac{1}{H} + \frac{1}{T}\frac{dT}{dz}\right) \tag{3.8}$$

In order to solve the system of differential equations (Equation (3.1)), we define the density and temperature at the mid-point of the vertical grid and the vertical flux at the boundary of vertical grid as shown in Figure 3.2.

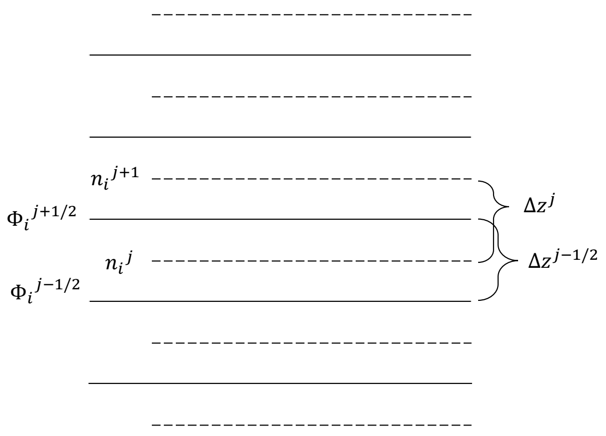

Figure 3.2 Indexing of vertical grids for density and vertical flux.

Then the spatial derivative of the vertical flux in the finite differentiation method is expressed as follows:

$$\left.\frac{\partial \Phi_i}{\partial z}\right|_j = \frac{\Phi_i{}^{j+1/2} - \Phi_i{}^{j-1/2}}{\Delta z^{j-1/2}} \quad , \tag{3.9}$$

where values denoted as the vertical grid index j are defined at the mid-points of the vertical grid, and values denoted as the vertical grid indices $j+1/2$ and $j-1/2$ are defined at boundary of the vertical grid. The vertical fluxes at the mid-point of vertical grids are expressed as:

$$\Phi_i^{j+1/2} = -\left({}^{j+1/2} + D_i^{j+1/2}\right)\frac{n_i^{j+1} - n_i^{j}}{\Delta z^{j}} - \zeta_i^{j+1/2} n_i^{j+1/2} \quad , \tag{3.10}$$

$$\Phi_i^{j-1/2} = -\left({}^{j-1/2} + D_i^{j-1/2}\right)\frac{n_i^{j} - n_i^{j-1}}{\Delta z^{j-1}} - \zeta_i^{j-1/2} n_i^{j-1/2} \quad , \tag{3.11}$$

where

$$\begin{aligned}\zeta_i^{j+1/2} &= D_i^{j+1/2}\left(\frac{1}{H_i^{j+1/2}} + \frac{q_i}{e}\frac{T_e^{j+1/2}/T_i^{j+1/2}}{P_e^{j+1/2}}\frac{P_e^{j+1} - P_e^{j}}{\Delta z^{j}} + \frac{1+\alpha_i}{T_i^{j+1/2}}\frac{T_i^{j+1} - T_i^{j}}{\Delta z^{j}}\right)\\ &+ {}^{j+1/2}\left(\frac{1}{H^{j+1/2}} + \frac{1}{T^{j+1/2}}\frac{T^{j+1} - T^{j}}{\Delta z^{j}}\right)\end{aligned} \tag{3.12}$$

$$\begin{aligned}\zeta_i^{j-1/2} &= D_i^{j-1/2}\left(\frac{1}{H_i^{j-1/2}} + \frac{q_i}{e}\frac{T_e^{j-1/2}/T_i^{j-1/2}}{P_e^{j-1/2}}\frac{P_e^{j} - P_e^{j-1}}{\Delta z^{j-1}} + \frac{1+\alpha_i}{T_i^{j-1/2}}\frac{T_i^{j} - T_i^{j-1}}{\Delta z^{j-1}}\right)\\ &+ {}^{j-1/2}\left(\frac{1}{H^{j-1/2}} + \frac{1}{T^{j-1/2}}\frac{T^{j} - T^{j-1}}{\Delta z^{j-1}}\right)\end{aligned} \tag{3.13}$$

Values at the boundary of vertical grids were calculated by averaging the values at the mid-points of vertical grids next to it, i.e., $n_i^{j+1/2} = \left(n_i^{j+1} + n_i^{j}\right)/2$ for example. Then the spatial derivative of the vertical flux can be described as a following finite differential equation:

$$\begin{aligned}\left.\frac{\partial \Phi_i}{\partial z}\right|_j &= \frac{\Phi_i^{j+1/2} - \Phi_i^{j-1/2}}{\Delta z^{j-1/2}}\\ &= \left[-\frac{{}^{j+1/2} + D_i^{j+1/2}}{\Delta z^{j-1/2}\Delta z^{j}} - \frac{\zeta_i^{j+1/2}}{2\Delta z^{j-1/2}}\right] n_i^{j+1}\\ &+ \left[\frac{{}^{j+1/2} + D_i^{j+1/2}}{\Delta z^{j-1/2}\Delta z^{j}} - \frac{\zeta_i^{j+1/2}}{2\Delta z^{j-1/2}} + \frac{{}^{j-1/2} + D_i^{j-1/2}}{\Delta z^{j-1/2}\Delta z^{j-1}} + \frac{\zeta_i^{j-1/2}}{2\Delta z^{j-1/2}}\right] n_i^{j}\\ &+ \left[-\frac{{}^{j-1/2} + D_i^{j-1/2}}{\Delta z^{j-1/2}\Delta z^{j-1}} + \frac{\zeta_i^{j-1/2}}{2\Delta z^{j-1/2}}\right] n_i^{j-1}\end{aligned} \tag{3.14}$$

However, this formulation would result in a mismatch in which the density moved from the vertical grid j to $j+1$ through the grid boundary $j+1/2$ is different when viewed from the vertical grid j and $j+1$, respectively, if the vertical grid size Δz is not uniform but altitude-dependent. The density moved from the vertical grid j to $j+1$ when viewed from the grid j is expressed as follows:

$$\left.\frac{\partial \Phi_i}{\partial z}\right|_j^{j\to j+1} = \left[\frac{{}^{j+1/2} + D_i{}^{j+1/2}}{\Delta z^{j-1/2}\Delta z^{j}} - \frac{\zeta_i{}^{j+1/2}}{2\Delta z^{j-1/2}}\right] n_i{}^{j} \tag{3.15}$$

The density moved from the vertical grid j to $j+1$ when viewed from the grid $j+1$ is expressed as follows:

$$\left.\frac{\partial \Phi_i}{\partial z}\right|_{j+1}^{j\to j+1} = \left[\frac{{}^{j+1/2} + D_i{}^{j+1/2}}{\Delta z^{j+1/2}\Delta z^{j}} - \frac{\zeta_i{}^{j+1/2}}{2\Delta z^{j+1/2}}\right] n_i{}^{j} \tag{3.16}$$

Thus, those values differ when $\Delta z^{j+1/2}$ is not equal to $\Delta z^{j-1/2}$. This mismatch also occurs between the vertical grid $j-1$ and j. Equation (3.14) is then be re-written to conserve the transport of density between vertical grids as follows:

$$\begin{aligned}\left.\frac{\partial \Phi_i}{\partial z}\right|_j = &\left[-\frac{{}^{j+1/2} + D_i{}^{j+1/2}}{\Delta z^{j}\Delta z^{j}} - \frac{\zeta_i{}^{j+1/2}}{2\Delta z^{j}}\right] n_i{}^{j+1}\\ &+ \left[\frac{{}^{j+1/2} + D_i{}^{j+1/2}}{\Delta z^{j}\Delta z^{j}} - \frac{\zeta_i{}^{j+1/2}}{2\Delta z^{j}} + \frac{{}^{j-1/2} + D_i{}^{j-1/2}}{\Delta z^{j-1}\Delta z^{j-1}} + \frac{\zeta_i{}^{j-1/2}}{2\Delta z^{j-1}}\right] n_i{}^{j}\\ &+ \left[-\frac{{}^{j-1/2} + D_i{}^{j-1/2}}{\Delta z^{j-1}\Delta z^{j-1}} + \frac{\zeta_i{}^{j-1/2}}{2\Delta z^{j-1}}\right] n_i{}^{j-1}\end{aligned} \tag{3.17}$$

Note that all the simulations were performed with the uniform vertical grid size in this thesis.

Substituting the finite differential equation (Equation (3.17)) for the partial differential equation (Equation (3.1)) yields the following ordinary differential equation:

$$\frac{dn_i{}^{j}}{dt} = \mathcal{A}_i{}^{j} n_i{}^{j+1} + \mathcal{B}_i{}^{j} n_i{}^{j} + \mathcal{C}_i{}^{j} n_i{}^{j-1} + \mathcal{D}_i{}^{j} \quad , \tag{3.18}$$

where $\mathcal{A}_i{}^{j}$, $\mathcal{B}_i{}^{j}$, $\mathcal{C}_i{}^{j}$, and $\mathcal{D}_i{}^{j}$ are expressed as follows except for lower and upper boundaries:

$$
\begin{aligned}
\mathcal{A}_i{}^j &= \frac{{}^{j+1/2} + D_i{}^{j+1/2}}{\Delta z^j \Delta z^j} + \frac{\zeta_i{}^{j+1/2}}{2\Delta z^j} \\
\mathcal{B}_i{}^j &= -\frac{{}^{j+1/2} + D_i{}^{j+1/2}}{\Delta z^j \Delta z^j} + \frac{\zeta_i{}^{j+1/2}}{2\Delta z^j} - \frac{{}^{j-1/2} + D_i{}^{j-1/2}}{\Delta z^{j-1} \Delta z^{j-1}} - \frac{\zeta_i{}^{j-1/2}}{2\Delta z^{j-1}} \\
\mathcal{C}_i{}^j &= \frac{{}^{j-1/2} + D_i{}^{j-1/2}}{\Delta z^{j-1} \Delta z^{j-1}} - \frac{\zeta_i{}^{j-1/2}}{2\Delta z^{j-1}} \\
\mathcal{D}_i{}^j &= P_i{}^j - L_i{}^j
\end{aligned}
\qquad (3.19)
$$

At lower boundary, $\mathcal{A}_i{}^1$, $\mathcal{B}_i{}^1$, $\mathcal{C}_i{}^1$, and $\mathcal{D}_i{}^1$ are expressed as follows:

$$
\begin{aligned}
\mathcal{A}_i{}^1 &= \frac{{}^{3/2} + D_i{}^{3/2}}{\Delta z^1 \Delta z^1} + \frac{\zeta_i{}^{3/2}}{2\Delta z^1} \\
\mathcal{B}_i{}^1 &= -\frac{{}^{3/2} + D_i{}^{3/2}}{\Delta z^1 \Delta z^1} + \frac{\zeta_i{}^{3/2}}{2\Delta z^1} + \frac{v_i{}^1}{\Delta z^1} \\
\mathcal{C}_i{}^1 &= 0 \\
\mathcal{D}_i{}^1 &= P_i{}^1 - L_i{}^1 + \frac{\Phi_i{}^1}{\Delta z^1}
\end{aligned}
\quad , \qquad (3.20)
$$

where $v_i{}^1$ and $\Phi_i{}^1$ are fixed velocity and flux of ith species at the lower boundary. Either $v_i{}^1$ or $\Phi_i{}^1$ is given for each ith species as a lower boundary condition, or they are set to zero if not needed. Note that the velocity and flux with positive values at lower boundary conditions direct vertically upward. At upper boundary, $\mathcal{A}_i{}^J$, $\mathcal{B}_i{}^J$, $\mathcal{C}_i{}^J$, and $\mathcal{D}_i{}^J$ are expressed as follows:

$$
\begin{aligned}
\mathcal{A}_i{}^J &= 0 \\
\mathcal{B}_i{}^J &= -\frac{{}^{J-1/2} + D_i{}^{J-1/2}}{\Delta z^{J-1} \Delta z^{J-1}} - \frac{\zeta_i{}^{J-1/2}}{2\Delta z^{J-1}} - \frac{v_i{}^J}{\Delta z^J} \\
\mathcal{C}_i{}^J &= \frac{{}^{J-1/2} + D_i{}^{J-1/2}}{\Delta z^{J-1} \Delta z^{J-1}} - \frac{\zeta_i{}^{J-1/2}}{2\Delta z^{J-1}} \\
\mathcal{D}_i{}^J &= P_i{}^J - L_i{}^J - \frac{\Phi_i{}^J}{\Delta z^J}
\end{aligned}
\quad , \qquad (3.21)
$$

where J is the index of vertical grid at upper boundary, and $v_i{}^J$ and $\Phi_i{}^J$ are fixed velocity and flux of ith species at upper boundary escaping the atmosphere. Either $v_i{}^J$ or $\Phi_i{}^J$ is given for each ith species as an upper boundary condition, or they are set to zero if not needed. Note that the velocity and flux with positive values at upper boundary conditions also direct vertically upward.

Renumbering the indices of the equations is useful to solve this system of differential equation numerically (Catling and Kasting, 2017). Assuming that the number of chemical species is I, x_k is defined as follows:

$$x_k = n_i{}^j; \quad k = i + (j-1)I \quad (i = 1,2,\ldots,I;\ j = 1,2,\ldots,J) \tag{3.22}$$

Thus, the system of ordinary differential equation (Equation (3.18)) can be re-written as the vector form as follows:

$$\frac{d\boldsymbol{x}}{dt} = \boldsymbol{F}(\boldsymbol{x}) \tag{3.23}$$

Forward difference approximation was applied to the time derivative on the left-hand side.

$$\frac{d\boldsymbol{x}}{dt} \backsimeq \frac{\boldsymbol{x}^{n+1} - \boldsymbol{x}^n}{\Delta t} \quad , \tag{3.24}$$

$$\therefore \frac{\boldsymbol{x}^{n+1} - \boldsymbol{x}^n}{\Delta t} = \boldsymbol{F}(\boldsymbol{x}) \quad , \tag{3.25}$$

The basic equations are stiff equations in which some of the variables such as number densities of short-lived species change more quickly than others. Thus, PROTEUS applied an implicit method solving the differential equations by evaluating the function $\boldsymbol{F}$ at the forward time step.

$$\boldsymbol{x}^{n+1} = \boldsymbol{x}^n + \boldsymbol{F}(\boldsymbol{x}^{n+1})\Delta t \tag{3.26}$$

The function $\boldsymbol{F}(\boldsymbol{x}^{n+1})$ evaluated at the forward time step can be approximated by a following first order Taylor series:

$$\begin{aligned} \boldsymbol{F}(\boldsymbol{x}^{n+1}) &= \boldsymbol{F}(\boldsymbol{x}^n) + \left.\frac{\partial \boldsymbol{F}}{\partial \boldsymbol{x}}\right|_n (\boldsymbol{x}^{n+1} - \boldsymbol{x}^n) \\ &= \boldsymbol{F}(\boldsymbol{x}^n) + \boldsymbol{\mathcal{J}}(\boldsymbol{x}^{n+1} - \boldsymbol{x}^n) \end{aligned} \quad , \tag{3.27}$$

where $\boldsymbol{\mathcal{J}}$ is the Jacobian matrix defined as follows:

$$\boldsymbol{\mathcal{J}} \equiv \left.\frac{\partial \boldsymbol{F}}{\partial \boldsymbol{x}}\right|_n = \begin{pmatrix} \frac{\partial F_1}{\partial x_1} & \frac{\partial F_1}{\partial x_2} & \cdots & \frac{\partial F_1}{\partial x_N} \\ \frac{\partial F_2}{\partial x_1} & \frac{\partial F_2}{\partial x_2} & \cdots & \frac{\partial F_2}{\partial x_N} \\ \vdots & \vdots & \ddots & \vdots \\ \frac{\partial F_N}{\partial x_1} & \frac{\partial F_N}{\partial x_2} & \cdots & \frac{\partial F_N}{\partial x_N} \end{pmatrix} \tag{3.28}$$

By defining $\Delta\boldsymbol{x} = \boldsymbol{x}^{n+1} - \boldsymbol{x}^n$, Equation (3.27) can be described as follows:

$$\Delta\boldsymbol{x} = [\,\boldsymbol{F}(\boldsymbol{x}^n) + \boldsymbol{\mathcal{J}}\Delta\boldsymbol{x}]\Delta t \tag{3.29}$$

Thus, $\Delta\boldsymbol{x}$ can be solved as follows:

$$\left(\frac{\mathbb{I}}{\Delta t} - \boldsymbol{\mathcal{J}}\right)\Delta\boldsymbol{x} = \boldsymbol{F}(\boldsymbol{x}^n) \quad , \tag{3.30}$$

$$\therefore \Delta\boldsymbol{x} = \left(\frac{\mathbb{I}}{\Delta t} - \boldsymbol{\mathcal{J}}\right)^{\boldsymbol{-1}} \boldsymbol{F}(\boldsymbol{x}^n) \quad , \tag{3.31}$$

where $\mathbb{I}$ is the $N \times N$ unit matrix with $N = I \times J$.

Here we survey the form of the Jacobian matrix $\boldsymbol{\mathcal{J}}$. $\boldsymbol{\mathcal{J}}$ can be divided into two components $\boldsymbol{\mathcal{J}} = \boldsymbol{\mathcal{J}}^c + \boldsymbol{\mathcal{J}}^t$, where $\boldsymbol{\mathcal{J}}^c$ is related to chemical production and loss term (called as chemical Jacobian) and $\boldsymbol{\mathcal{J}}^t$ is related to vertical transport equation (called as transport Jacobian). Submatrix of $\boldsymbol{\mathcal{J}}^c$ at a certain vertical grid (a gray square in Equation (3.32)) is independent of $\boldsymbol{x}^n$ at any different vertical grids and $\boldsymbol{\mathcal{J}}^t$ is independent of other species. The chemical Jacobian $\boldsymbol{\mathcal{J}}^c$ has a following form:

$$\mathcal{J}^c = \tag{3.32}$$

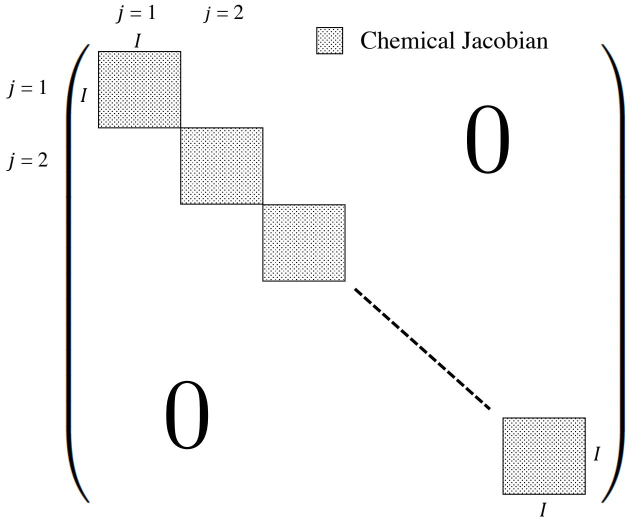

Each meshed square is the chemical Jacobian components at each vertical grid, which is independent of $\mathcal{A}_i{}^j$, $\mathcal{B}_i{}^j$, and $\mathcal{C}_i{}^j$. The transport Jacobian $\mathcal{J}^t$ has the following form.

$$\mathcal{J}^t = \tag{3.33}$$

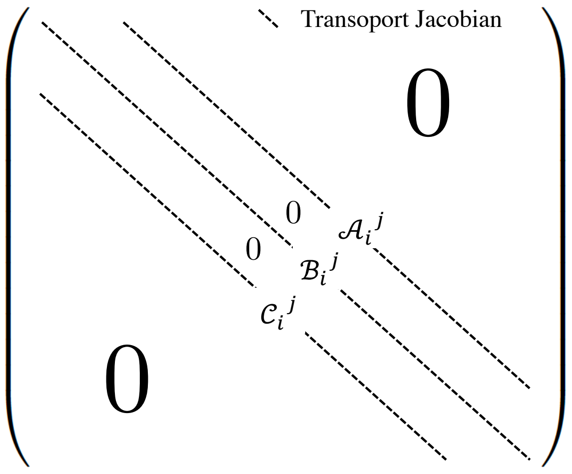

Therefore, the Jacobian matrix has a following form.

$$\mathcal{J} = \mathcal{J}^c + \mathcal{J}^t = \tag{3.34}$$

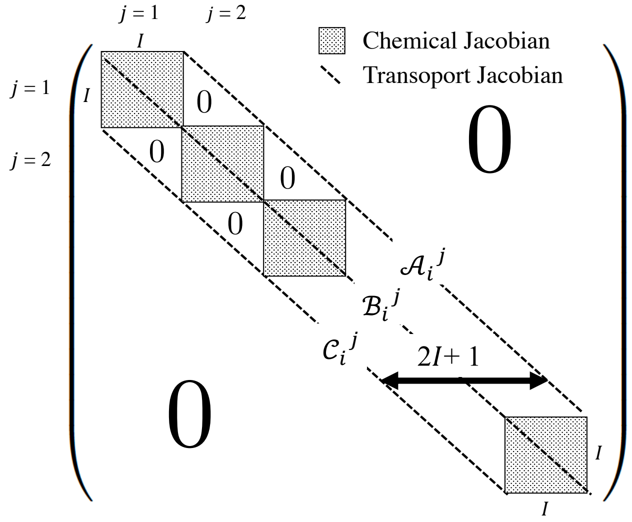

The Jacobian matrix is thus a sparse banded matrix with a bandwidth of $2I$+1, where I is the number of chemical species. In numerical code, the Jacobian matrix is stored in a variable with a dimension ($2I$+1, $I \times J$) in order to save the memory size and to reduce the computational cost of calculating the inverse matrix $(\mathbb{I}/\Delta t - \mathcal{J})^{-\mathbf{1}}$ using a LU decomposition method.

Finally, the density at the next time step can be obtained by adding $\Delta \boldsymbol{x}$ to the current density $\boldsymbol{x}^n$.

$$\boldsymbol{x}^{n+1} = \boldsymbol{x}^n + \Delta \boldsymbol{x} \tag{3.35}$$

The time step size Δt is set to 10^{-8} sec at first, which is then allowed to increase at a given rate when the change in all the species at all the vertical grids becomes lower than 10%.

3.4 Structure of PROTEUS

PROTEUS consists of a Python GUI program and Fortran 90 modules. The Python GUI program contains a list of chemical reactions for each planet, string parsing functions that parse the reactions and reaction rate coefficients selected in GUI, and GUI functions that control the behavior of GUI. Python language was adopted because of its flexibility in parsing strings and its capability in operating GUI. Since Python language is not efficient for numerical calculation, Fortran language was adopted to solve differential equations numerically. The structure of PROTEUS is illustrated in Figure 3.3. Chemical reactions listed in the Python file are first read by GUI functions (arrow 1 in Figure 3.3). Then, users select reactions on GUI (arrows 2 in Figure 3.3), which will be analyzed by string parsing functions (arrow 3 in Figure 3.3) to output a Fortran

90 module named “v_in.f90” and data files (in directories “PLJ_list” and “settings”) including information of the selected chemical reactions (arrow 4 in Figure 3.3). The Fortran 90 module “v__in.f90” is the only module that includes information on chemical reactions, and other Fortran 90 modules are independent of chemical reactions to be used in the simulation. Datafiles of initial density profiles and temperature profiles are read by “v__in.f90” (arrow 5 in Figure 3.3). The selected reactions, settings such as temperature profile and initial density profiles are applied to the Fortran 90 model when the main Fortran 90 routine “e__main.f90” call subroutines in “v__in.f90” (arrow 6 in Figure 3.3). Users can then run the Fortran model by compiling all the Fortran 90 modules (indicated as “7” in Figure 3.3).

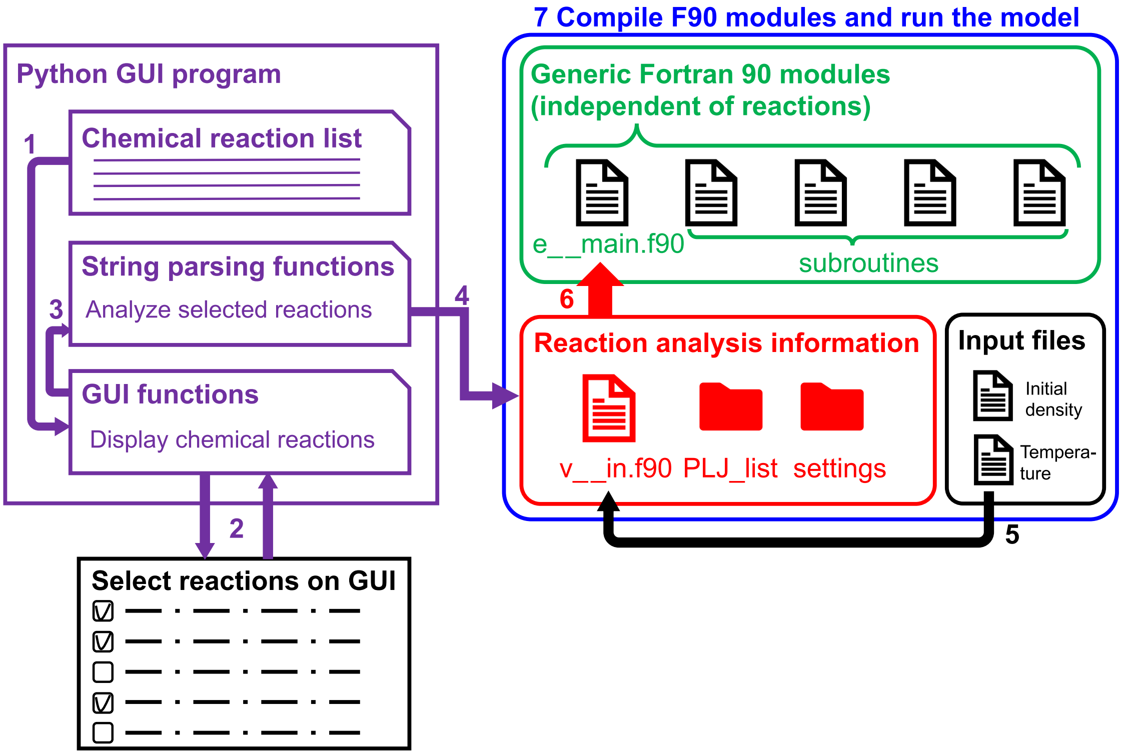

Figure 3.3 Schematic illustration of the structure of PROTEUS.

The structure of the Fortran codes is illustrated in Figure 3.4. It should be noted that each Fortran 90 file contains several modules with distinct functions, but only the Fortran 90 file is indicated for simplicity. The main routine “e__main.f90” consists of three parts, (1) initialization, (2) calculation, and (3) finalization. The description of each part and each Fortran 90 file are as follows.

(1) All variables are defined in “v__tdec.f90”. Information on the chemical reactions, boundary conditions, and calculation settings are defined in “v__in.f90”. Physical constants and parameters of the planetary orbit are given in “c__prm.f90”. Production rates calculated by other models (e.g., ionization rate calculated by PTRIP (described in Chapter 2) and a meteoroid ablation model (Nakamura et al., 2022b)) can be input in “p__Mars.f90” and “p__Jupiter.f90”. The solar EUV flux is calculated by the EUVAC model and the absorption and ionization cross sections are defined in “p__EUVAC.f90”. The solar flux of Woods et al. (2009) is defined and absorption and dissociation cross sections are calculated in ”p__UV.f90”.

(2) The radiative transfer is solved and the optical depth is calculated in “p__photochem_opticaldepth.f90”. Ionization and dissociation rates, reaction rate coefficients, and production and loss rates of each species are calculated in “p__photochem_rate.f90”. The vertical diffusion flux is calculated in “p__photochem_transport.f90”. The eddy and binary diffusion coefficients are defined in “p__eddy_diffusion.f90” and “p__molecular_diffusion.f90”, respectively. “p__photochem_scheme.f90” calculates the Jacobian matrix and advances the timestep using the implicit method.

(3) At last, “p__io.f90” outputs the calculated simulation results.

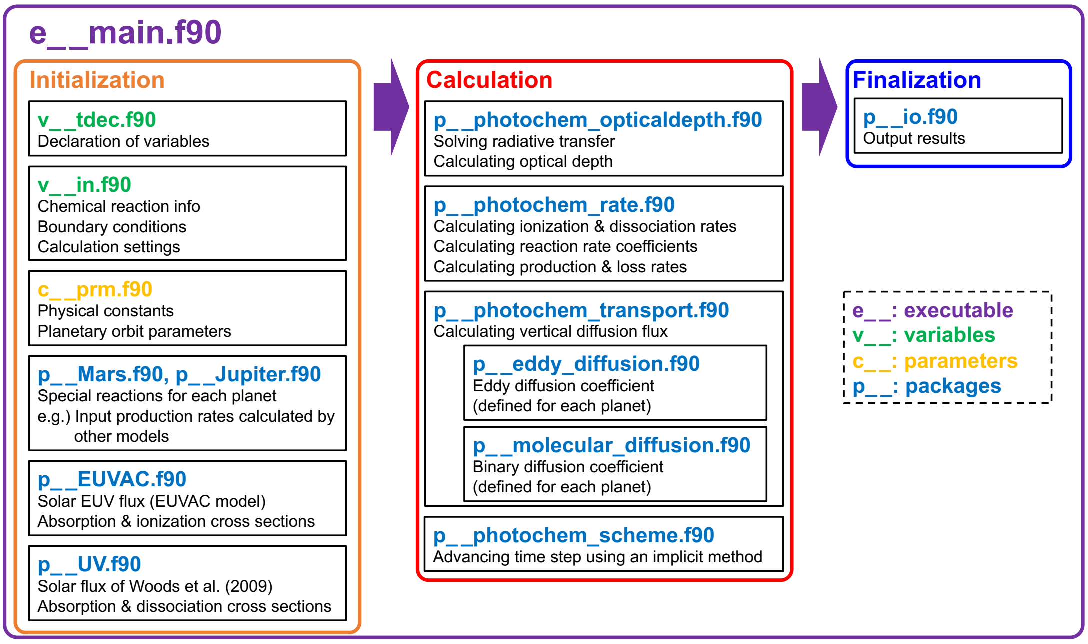

Figure 3.4 Schematic illustration of the structure of Fortran codes.

3.5 Graphical user interface

The Python GUI program uses the tkinter package, a standard library of Python to use the Tcl/Tk GUI toolkit (https://docs.python.org/3/library/tkinter.html). The Python GUI allows users to easily and intuitively select a planet and chemical reactions of interest, and run the simulation. An example of GUI is shown in Figure 3.5, and the operation of GUI is as follows. Once the user runs the Python GUI program, one can select a planet as indicated ("1" in the upper panel of Figure 3.5). After selecting a planet, one can create a new project directory, or select or rename a project directory that still exists as indicated ("2" in the upper panel of Figure 3.5). Then the chemical reaction list for the selected planet appears in the window (the lower panel of Figure 3.5). Chemical reactions and their rate coefficients written in the Python GUI program are automatically converted into Unicode and displayed, making them easy to read. One can select or clear reactions by clicking on the checkbox at each reaction ("3" in the lower panel of Figure 3.5). By inserting chemical species, a reference, or a label into a search box, only related reactions appear in the window. One can set upper and lower boundary conditions, initial density profiles, vertical grid size, and other calculation settings such as the dimension of the simulation, season, latitude, integration time, and maximum time step size ("4" in the lower panel of Figure 3.5). After all the settings are done, one can press "Output f90 module", then the following files are generated in the selected project directory: a Fortran 90 module named "v__in.f90", setting files stored in the directory "settings", and information about production and loss reactions of each chemical species, rate coefficient labels, and Jacobian matrix analyzed by the string parsing function stored in the directory "PLJ_list". The list of chemical species, the number of chemical species, indices, mass, and charge of each chemical species are automatically determined and written in "v__in.f90" at this time. Those text files are read by the Fortran 90 module "v__in.f90". One can also output those files, compile, and run the Fortran codes by pressing "Output f90 module & Run model", which requires the installation of an open source software CMake into the user's computer ("5" in the lower panel of Figure 3.5). All the settings and selected reactions are saved, and users can use the same settings and selected reactions the next time they run GUI. At the end of the simulation, users can quickly plot the density profiles by pressing the "Plot setting" button ("6" in the lower panel of Figure 3.5).

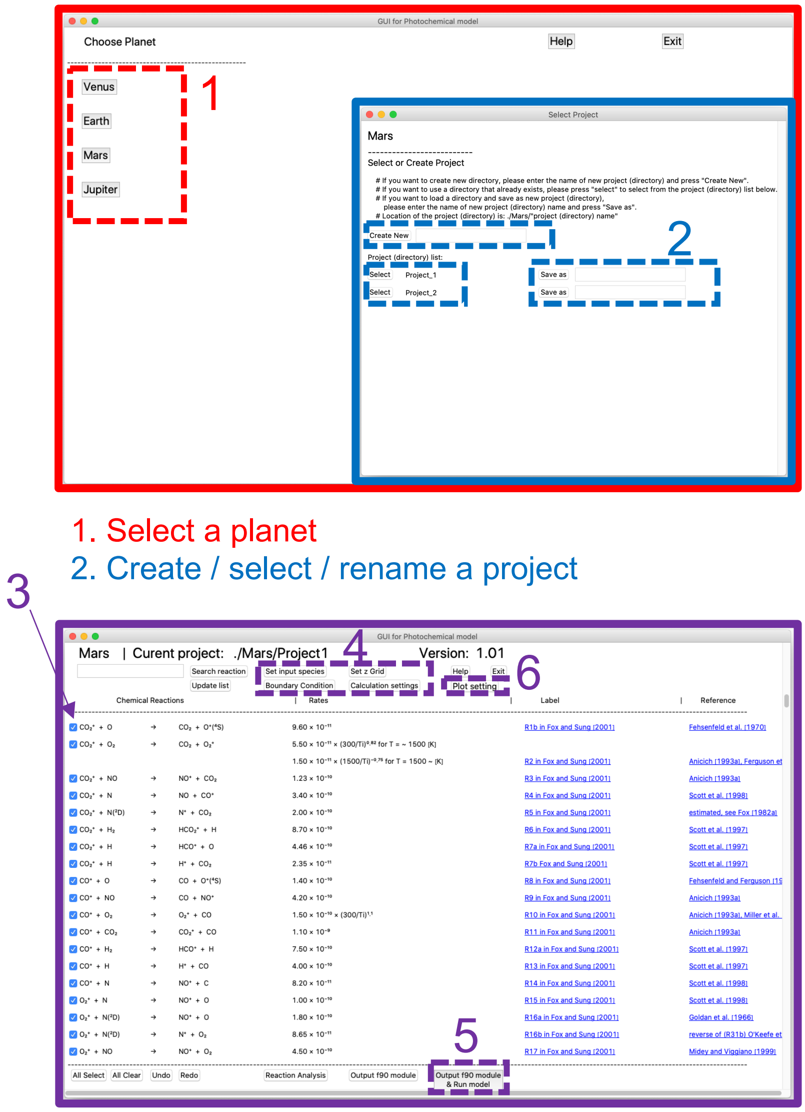

Mars

Select or Create Project

\# If you want to create new directory, please enter the name of new project (directory) and press "Create New".
\# If you want to use a directory that already exists, please press "select" to select from the project (directory) list below.
\# If you want to load a directory and save as new project (directory),
please enter the name of new project (directory) name and press "Save as".
\# Location of the project (directory) is: ./Mars/"project (directory) name"

Project (directory) list:
Project_1
Project_2

1. Select a planet
2. Create / select / rename a project

Mars | Curent project: ./Mars/Project1 Version: 1.01

Chemical Reactions			Rates	Label	Reference
☑ $CO_2^+ + O$	→	$CO_2 + O^+(^4S)$	9.60×10^{-11}	R1b in Fox and Sung [2001]	Fehsenfeld et al. [1970]
☑ $CO_2^+ + O_2$	→	$CO_2 + O_2^+$	$5.50 \times 10^{-11} \times (300/Ti)^{0.82}$ for T = ~ 1500 [K] $1.50 \times 10^{-11} \times (1500/Ti)^{-0.75}$ for T = 1500 ~ [K]	R2 in Fox and Sung [2001]	Anicich [1993a], Ferguson et
☑ $CO_2^+ + NO$	→	$NO^+ + CO_2$	1.23×10^{-10}	R3 in Fox and Sung [2001]	Anicich [1993a]
☑ $CO_2^+ + N$	→	$NO + CO^+$	3.40×10^{-10}	R4 in Fox and Sung [2001]	Scott et al. [1998]
☑ $CO_2^+ + N(^2D)$	→	$N^+ + CO_2$	2.00×10^{-10}	R5 in Fox and Sung [2001]	estimated, see Fox [1982a]
☑ $CO_2^+ + H_2$	→	$HCO_2^+ + H$	8.70×10^{-10}	R6 in Fox and Sung [2001]	Scott et al. [1997]
☑ $CO_2^+ + H$	→	$HCO^+ + O$	4.46×10^{-10}	R7a in Fox and Sung [2001]	Scott et al. [1997]
☑ $CO_2^+ + H$	→	$H^+ + CO_2$	2.35×10^{-11}	R7b Fox and Sung [2001]	Scott et al. [1997]
☑ $CO^+ + O$	→	$CO + O^+(^4S)$	1.40×10^{-10}	R8 in Fox and Sung [2001]	Fehsenfeld and Ferguson [19
☑ $CO^+ + NO$	→	$CO + NO^+$	4.20×10^{-10}	R9 in Fox and Sung [2001]	Anicich [1993a]
☑ $CO^+ + O_2$	→	$O_2^+ + CO$	$1.50 \times 10^{-10} \times (300/Ti)^{1.1}$	R10 in Fox and Sung [2001]	Anicich [1993a], Miller et al.
☑ $CO^+ + CO_2$	→	$CO_2^+ + CO$	1.10×10^{-9}	R11 in Fox and Sung [2001]	Anicich [1993a]
☑ $CO^+ + H_2$	→	$HCO^+ + H$	7.50×10^{-10}	R12a in Fox and Sung [2001]	Scott et al. [1997]
☑ $CO^+ + H$	→	$H^+ + CO$	4.00×10^{-10}	R13 in Fox and Sung [2001]	Scott et al. [1997]
☑ $CO^+ + N$	→	$NO^+ + C$	8.20×10^{-11}	R14 in Fox and Sung [2001]	Scott et al. [1998]
☑ $O_2^+ + N$	→	$NO^+ + O$	1.00×10^{-10}	R15 in Fox and Sung [2001]	Scott et al. [1998]
☑ $O_2^+ + N(^2D)$	→	$NO^+ + O$	1.80×10^{-10}	R16a in Fox and Sung [2001]	Goldan et al. [1966]
☑ $O_2^+ + N(^2D)$	→	$N^+ + O_2$	8.65×10^{-11}	R16b in Fox and Sung [2001]	reverse of (R31b) O'Keefe et
☑ $O_2^+ + NO$	→	$NO^+ + O_2$	4.50×10^{-10}	R17 in Fox and Sung [2001]	Midey and Viggiano [1999]

3. Select chemical reactions
4. Set initial density profile data, boundary conditions, vertical grid, and calculation settings
5. Output F90 modules and run the model
6. Plot density profiles after the simulation

Figure 3.5 Overview of GUI and instruction of the operation.

3.6 Format of chemical reaction list

The main feature of PROTEUS is the simple format of chemical reaction list in the Python GUI program and on the GUI. Format of chemical reaction list in the Python GUI program and some examples are illustrated in Figure 3.6.

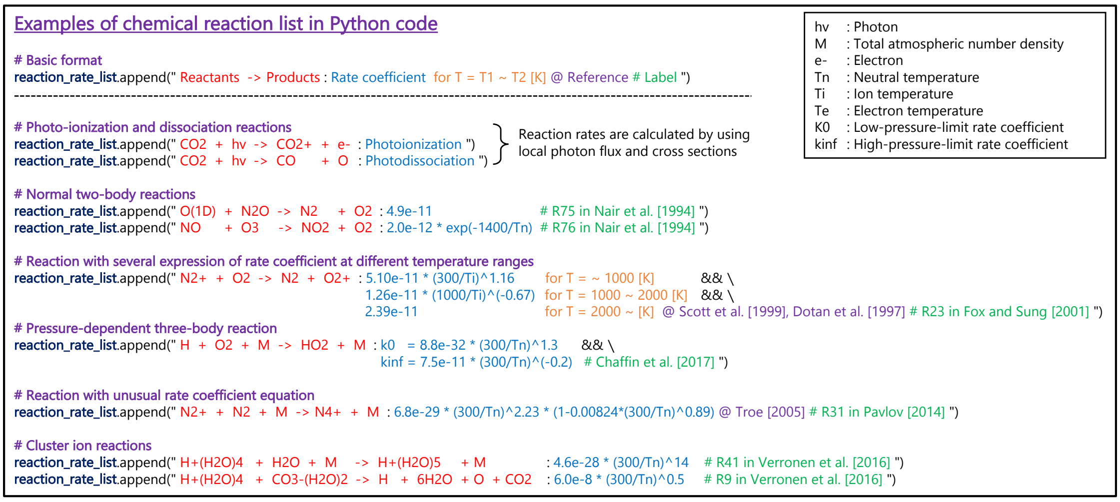

Examples of chemical reaction list in Python code

```
# Basic format
reaction_rate_list.append(" Reactants  -> Products : Rate coefficient  for T = T1 ~ T2 [K] @ Reference # Label ")
-------------------------------------------------------------------------------------------------------------------------------

# Photo-ionization and dissociation reactions
reaction_rate_list.append(" CO2  +  hv  ->  CO2+  +  e-  : Photoionization ")
reaction_rate_list.append(" CO2  +  hv  ->  CO     +  O  : Photodissociation ")

# Normal two-body reactions
reaction_rate_list.append(" O(1D)  +  N2O  ->  N2    +  O2  : 4.9e-11                   # R75 in Nair et al. [1994] ")
reaction_rate_list.append(" NO     +  O3   ->  NO2  +  O2  : 2.0e-12 * exp(-1400/Tn)  # R76 in Nair et al. [1994] ")

# Reaction with several expression of rate coefficient at different temperature ranges
reaction_rate_list.append(" N2+  +  O2  ->  N2  +  O2+  : 5.10e-11 * (300/Ti)^1.16       for T = ~ 1000 [K]          && \
                                                          1.26e-11 * (1000/Ti)^(-0.67)  for T = 1000 ~ 2000 [K]   && \
                                                          2.39e-11                      for T = 2000 ~ [K]  @ Scott et al. [1999], Dotan et al. [1997] # R23 in Fox and Sung [2001] ")
# Pressure-dependent three-body reaction
reaction_rate_list.append(" H  +  O2  +  M  ->  HO2  +  M  : k0   = 8.8e-32 * (300/Tn)^1.3      && \
                                                             kinf = 7.5e-11 * (300/Tn)^(-0.2)   # Chaffin et al. [2017] ")

# Reaction with unusual rate coefficient equation
reaction_rate_list.append(" N2+  +  N2  +  M  -> N4+  +  M  : 6.8e-29 * (300/Tn)^2.23 * (1-0.00824*(300/Tn)^0.89) @ Troe [2005] # R31 in Pavlov [2014] ")

# Cluster ion reactions
reaction_rate_list.append(" H+(H2O)4   +  H2O  +  M    ->  H+(H2O)5    + M             : 4.6e-28 * (300/Tn)^14    # R41 in Verronen et al. [2016] ")
reaction_rate_list.append(" H+(H2O)4   +  CO3-(H2O)2  ->  H   +  6H2O  + O  + CO2   : 6.0e-8 * (300/Tn)^0.5    # R9 in Verronen et al. [2016] ")
```

Reaction rates are calculated by using local photon flux and cross sections

hv : Photon
M : Total atmospheric number density
e- : Electron
Tn : Neutral temperature
Ti : Ion temperature
Te : Electron temperature
K0 : Low-pressure-limit rate coefficient
kinf : High-pressure-limit rate coefficient

Figure 3.6 Format of the chemical reaction list in the Python GUI program.

Any reactions and their rate coefficients are described in the following string format in the Python GUI program. A chemical reaction and its rate coefficient are separated by a colon ":", and the left- and right-hand sides of the reaction are separated by an arrow "->". Chemical species can be written simply as a string. For instance, ionized species "N_2^+", "CO_2^+", and "$H^+(H_2O)_4$" are simply described as "N2+", "CO2+", and "H+(H2O)4", respectively, and electron is described as "e-". Isotope species such as "$^{13}CO_2$" can be written as "^13CO2". Each chemical species and an addition operator "+" or an arrow "->" should be separated by at least one space. PROTEUS also deals with three-body reactions with the expression "M" describing the total atmospheric number density. Temperature-dependent rate coefficient equation can be simply described as a string in infix notation. Addition operator "+", subtraction operator "-", multiplication operator "*", division operator "/", exponentiation operator "^" or "**", exponential function "exp()", square root function "sqr ()", neutral, ion and electron temperatures "Tn", "Ti", and "Te", respectively, altitude in km "h", decimal fraction values such as "1.1 ", integer values such as "300", and values in E notation such as "4.9e-11" can be used in the rate coefficient equation. If there is a temperature range T_1-T_2 [K] in which the rate coefficient is valid, one can describe the temperature range by "for T = T_1 ~ T_2 [ ]".

Reactions and their rate coefficients selected on GUI are parsed by the string parsing functions in the Python GUI program. The index for each chemical species is automatically determined by the string parsing function, and the mass and charge of each chemical species are also automatically identified by the string parsing function. The string of each species is automatically divided into constituent elements and mass is calculated by the sum of the mass of all the elements, and the charge is calculated by counting the number of "+" and "-" in the string of each species. The string parsing function analyzes which reaction produces or loses each chemical species. The rate coefficient expressions written in infix notation are first separated into tokens. Then the order of tokens in infix notation is converted into reverse Polish notation (i.e., postfix notation) and automatically labeled. The Fortran 90 modules calculate the reaction rate coefficient using the labeled tokens arranged in reverse Polish notation. This method allows PROTEUS to process a variety of expressions of temperature- and altitude-dependent rate coefficients (as seen in Figure 3.6) at high computational speed. All the information needed to calculate the production rate, loss rate, and the Jacobian matrix is output as text files, which will be read by Fortran 90 module to apply the information about the selected chemical reactions. The number of chemical species and reactions, mass and charge of chemical species, rate coefficient of each reaction, and contribution of each reaction to production/loss of each species are automatically applied to Fortran 90 modules by reading those text files. Those features make PROTEUS a flexible photochemical model that can be applied to many planetary atmospheres with a different set of chemical reactions.

3.7 Application to planetary atmospheres and validation

3.7.1 Application to the Martian atmosphere

For the application to the Martian atmosphere, parameters of Mars and its orbit are implemented into PROTEUS; The mean distance between Mars and the Sun is r_m=1.524 AU, the eccentricity is e= 0.0934, the solar longitude at perihelion is $L_{s,P}$=250°, the tilt angle of the rotational axis is ε=25.2°, the rotational period is T_p=88775 sec, the mass of Mars is 6.417×10^{23} kg, and the mean radius of Mars is 3389.5 km (Patel et al., 2002; Williams, 2021).

The cross sections implemented into PROTEUS for the application to Mars are as follows. Ionization cross sections of CO_2, CO, O_2, N_2, and O are taken from Schunk and Nagy (2009). Absorption cross sections and quantum yields for calculating dissociation rates of atmospheric molecules are listed in Table C.1 and displayed in Figures C.1 and C.2 in Appendix C. In order to validate PROTEUS, it was compared with the one-dimensional Martian photochemical model by

Chaffin et al. (2017) (hereafter called as C17 model), using the same chemical reactions and their rate coefficients, boundary conditions, temperature and water vapor profiles, and binary and eddy diffusion coefficient profiles. The neutral density profiles simulated by PROTEUS and C17 models are shown in Figure 3.7. PROTEUS and C17 models are in good agreement except for small differences for O_3, OH, HO_2, and H_2O_2. Those differences could be due to the difference in the photo-absorption and dissociation cross sections used in the two models.

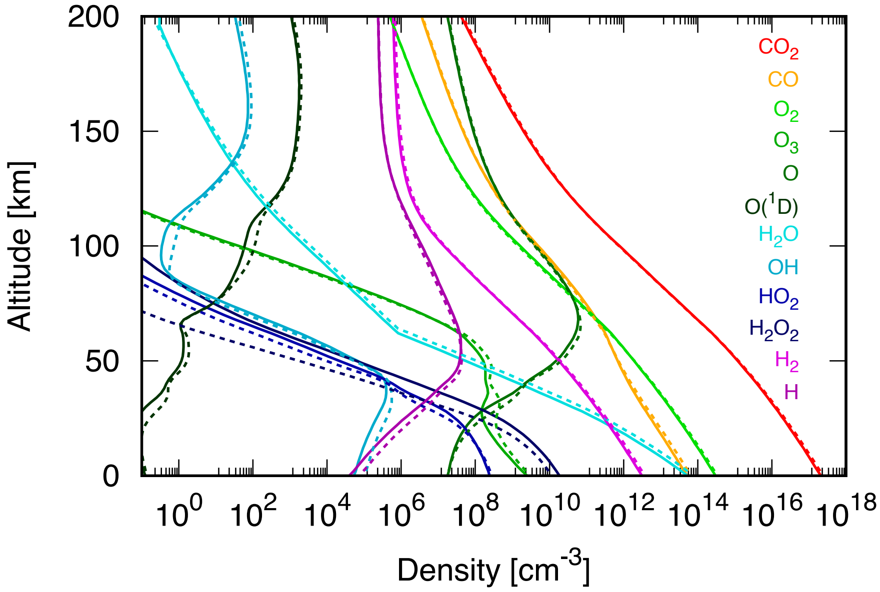

Figure 3.7 Vertical profiles of neutral density simulated by PROTEUS (solid) and one-dimensional Martian photochemical model by Chaffin et al. (2017) (dashed). The same boundary conditions, chemical reactions and their rate coefficient, binary and eddy diffusion coefficients, and temperature profile, were used in both simulations for validation.

3.7.2 Application to the Jovian ionosphere

For the application to the Jovian atmosphere, parameters of Jupiter and its orbit are implemented into PROTEUS; The mean distance between Jupiter and the Sun is r_m=5.2 AU, the eccentricity e, the solar longitude at perihelion $L_{s,P}$, and tilt angle of the rotational axis ε are set to zero for simplicity, the rotational period is assumed to be the System III period related to the period of radio burst T_p= 35729.71 sec, the mass of Jupiter is 1.898×10^{27} kg, and the equatorial radius of Jupiter is 71492 km (Williams, 2021; Russell et al., 2001).

Ionization cross sections of hydrogen molecule and atom, helium atom, hydrocarbon molecules (CH_4, C_2H_2, C_2H_4, and C_2H_6), and metallic atoms (Fe, Mg, Si, and Na) implemented into PROTEUS for the application to the Jovian ionosphere are found in Appendix of Nakamura et al. (2022b) and references therein.

PROTEUS has recently been applied to the Jovian ionosphere by Nakamura et al. (2022b). Chemical reactions regarding hydrocarbon ion chemistry used in the simulation are described in Nakamura et al. (2022b). Ion density profiles calculated by PROTEUS with 218 reactions are shown in Figure 3.8. Simulated ion density profiles are in good agreement with Kim and Fox (1994), as discussed in Nakamura et al. (2022b). Slight differences seen in the shape of profiles of hydrocarbon ions could result from the difference in the initial density profiles of hydrocarbon molecules, which are not indicated in Kim and Fox (1994).

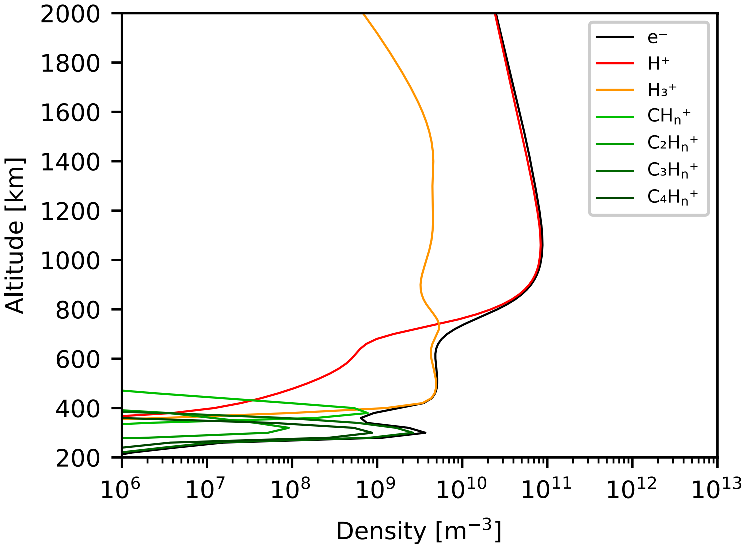

Figure 3.8 Ion density profiles of the Jovian ionosphere simulated by PROTEUS. Profiles are the same as Figure 3a in Nakamura et al. (2022b) that used PROTEUS.

3.8 Chapter summary

We have newly developed a flexible one-dimensional photochemical model named PROTEUS, which consists of a Python GUI program and Fortran 90 modules. Chemical reactions can be easily implemented into Python code as a simple string format, and users can intuitively select a planet and chemical reactions to be considered in their calculation on GUI. Chemical reactions selected on GUI are automatically analyzed by a string parsing code written in Python, which will be applied to Fortran 90 modules to simulate selected chemical reactions on a selected planet. This chapter presents examples of PROTEUS application to the Martian atmosphere and the Jovian ionosphere, which are in good agreement with previous numerical models. PROTEUS can significantly save time for those who need to develop a new photochemical model; they just need to add chemical reactions in the Python code and just select them on GUI to run a new photochemical model. PROTEUS can be easily extended to other planets and satellites, e.g., Venus, Earth, Titan, and exoplanets in the future.

Chapter 4

Contribution of MeV protons to the Martian diffuse aurora

Solar energetic particles (SEPs) can easily penetrate deep into the Martian atmosphere owing to insufficient magnetospheric and atmospheric shielding of Mars (Leblanc et al., 2002). Penetration of SEPs into the Martian atmosphere leads to increased ionization, heating of the atmosphere, and alteration of the atmospheric chemistry (Leblanc et al., 2002; Jolitz et al. 2017; Haider and Masoom, 2019; Gérard et al., 2017; Lingam et al., 2018). One of the consequences of the interaction of SEPs with the Martian atmosphere is the production of auroral emissions (Schneider et al., 2015).

There are three types of aurorae that have been identified on Mars: discrete aurora, proton aurora, and diffuse aurora. The discrete aurora was first detected by Mars Express in the crustal magnetic field region (Bertaux et al., 2005) and is believed to be caused by the acceleration of electrons due to the electric potential along open magnetic field lines (Brain et al., 2006). The discrete aurora is characterized by a strongly localized patch-like morphology of the emissions and a peak altitude of approximately 120 km, which indicates that precipitation of a few keV electrons causes the discrete aurora (e.g., Bertaux et al., 2005). The proton aurora was first detected by the Mars Atmosphere and Volatile EvolutioN (MAVEN) spacecraft on the dayside of Mars (Deighan et al., 2018; Ritter et al., 2018). Proton aurorae are produced by solar wind protons that are neutralized by charge exchange with exospheric hydrogen atoms outside Mars' induced magnetosphere. They travel without losing energy to the atmosphere, where they collide with Mars' main atmospheric constituent, CO_2, become excited, and produce Lyman-α emissions. These proton aurorae are visible preferentially during the dayside southern summer solstice (near the solar longitude (Ls), which is 270° when the Mars hydrogen exosphere is the densest) and display a brightness profile peaking at an altitude of approximately 120 km (Hughes et al., 2019).

Recently, MAVEN discovered a new type of aurora, namely, diffuse aurora, that spans the Mars nightside and results from the interaction of SEPs with the Martian atmosphere (Schneider et al., 2015, 2018). This new type of aurora on Mars is characterized by global brightening and by its low peak altitude of ~60 km, which indicates that more energetic particles are deposited deep in the Martian atmosphere than previously observed. Previous models suggested that 100 keV of monoenergetic electron precipitation should have been at the origin of the low altitude (~60 km) peak of the limb emission; however, no model was able to reproduce the observed emission profiles by using the observed energetic electron flux spectra (Schneider et al., 2015; Gérard et al., 2017; Haider and Masoom, 2019). Previous auroral emission models did not take into account the contribution of MeV proton precipitation, although MeV protons can penetrate down to ~70 km altitude as well (Jolitz et al., 2017). Observations of SEP electron and ion fluxes with the Solar Energetic Particle instrument during the aurorae observed by Imaging UltraViolet Spectrograph (IUVS) instruments onboard MAVEN suggested that both electron and proton energetic populations could have been at the origin of the diffuse aurora (Schneider et al., 2018).

In this chapter, we aim to evaluate the contribution of SEP protons to the Martian diffuse aurora emissions and validate PTRIP by comparing it with MAVEN/IUVS observations. PTRIP was used to calculate the limb intensity profile of the CO_2^+ ultraviolet doublet (UVD) emission produced by precipitating electrons and protons with energies ranging from 100 eV to 100 keV and from 50 keV to 5 MeV, respectively, as observed by MAVEN during the December 2014 SEP event and September 2017 SEP event. We ignore the effects of the electric and magnetic fields on the particle trajectory in this chapter for simplicity, and simulations were performed in one dimension for space and three dimensions for velocity.

4.1 MAVEN/SEP and SWEA measurements

The instruments used to constrain the electron and proton fluxes are the Solar Energetic Particle (SEP) and Solar Wind Electron Analyzer (SWEA) onboard MAVEN.

The MAVEN/SEP instrument consists of two sensors: SEP1 and SEP2. Each sensor consists of a pair of double-ended solid-state telescopes to measure 20-1000 keV electrons and 20-6000 keV ions in four orthogonal directions with a field of view of 42°×31° (Larson et al., 2015). The directions are labeled '1F', '1R', '2F', and '2R', where '1' and '2' denote the MAVEN/SEP instrument sensors (SEP1 and SEP2, respectively), and 'F' and 'R' denote the 'forward' FOV and 'reverse' FOV, respectively (Larson et al., 2015). The MAVEN/SEP instrument data used in this chapter correspond to Level 2 data provided by Planetary Data System (PDS) (Larson et al., MAVEN SEP Calibrated Data Product Bundle, https://pds-ppi.igpp.ucla.edu/search/view/?f=yes&id=pds://PPI/maven.sep.calibrated/data/spec).

The SWEA instrument is a symmetric, hemispheric electrostatic analyzer designed to measure the energy and angular distributions of solar wind electrons and ionospheric photoelectrons in the Martian environment (Mitchell et al., 2016). The instruments measure electron fluxes in the energy range of 3 eV - 4.6 keV (Mitchell et al., 2016). The SWEA instrument data used in this chapter correspond to Level 2 data provided by PDS (Mitchell et al., MAVEN SWEA Calibrated Data Bundle, https://pds-ppi.igpp.ucla.edu/search/view/?f=yes&id=pds://PPI/maven.swea.calibrated).

Note that we assume isotropic pitch angle distribution of electrons and protons obtained by MAVEN/SEP and SWEA. For electrons, we used MAVEN/SEP electrons > 30 keV and SWEA < 5 keV, with interpolation between those values. For protons, we used MAVEN/SEP ions > 50 keV because the sensitivity of the MAVEN/SEP ion is low below 50 keV.

We used the median value of the electron and proton fluxes obtained by MAVEN/SEP and SWEA instruments of orbit 437 for the December 2014 SEP event. Orbit 437 was chosen because the observed auroral emission was the brightest (Schneider et al., 2015). The channel of MAVEN/SEP was selected as 1F; the electron and proton fluxes of MAVEN/SEP were used only when MAVEN/SEP attenuator was open. The electron and proton flux spectra for the December 2014 SEP event used in this chapter are shown in Figure 4.2a.

So far, the September 2017 SEP event has been the strongest solar energetic particle event detected by MAVEN/SEP on Mars. The high fluxes of energetic electrons and ions during this event caused the instrument mechanical attenuator to automatically close in order to reduce the detected flux of particles and prevent saturation of the instrument. However, the flux of the highest energy particles (above a few MeV) that can penetrate the instrument housing (and the attenuator) was strong enough to contribute to a significant portion of the differential energy flux measured by MAVEN/SEP at the range of energies that are typically associated with particles that can be stopped by the attenuator. The level of background is less severe for the time periods when the MAVEN/SEP attenuators were open so it was possible to apply fitting procedures in order to remove this background present in the data. We fit a series of theoretical ion and electron spectra to the measurements in all of the MAVEN/SEP energy channels, including coincidence events that are mainly caused by penetrating particles. In our fitting, we use a realistic model of the instrument geometric factor and find the ion and electron spectra that produce the best match with the measurements. The results are shown in Figure 4.1. The electron and proton flux spectra for the September 2017 SEP event used in this study are shown in Figure 4.2b. Note that since the electron and proton fluxes used for the September 2017 SEP event were taken from the timing just before the flux peak and auroral emission peak, the resulting modeled auroral emission intensity should be small compared with the IUVS observation reported by Schneider et al. (2018). For this event, we do not focus on the absolute auroral emission intensity but on the relative intensity of electron- and proton-induced emissions and on the shapes of the auroral emission profiles.

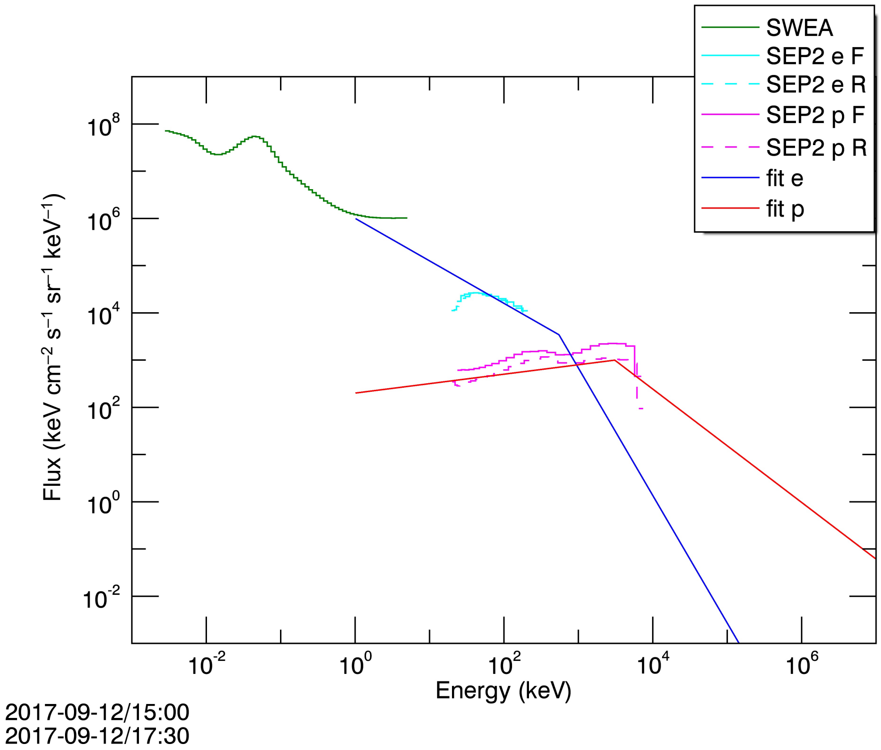

Figure 4.1 Electron and proton fluxes measured by MAVEN/SEP and SWEA from 15:00UT to 17:30UT on 12 September 2017. The green line shows the electron flux observed by SWEA. The cyan solid and dashed lines show the electron fluxes observed by the SEP2 sensor in the forward and in the reverse directions, respectively. The violet solid and dashed lines show the proton fluxes observed by the SEP2 sensor in the forward and in the reversed directions, respectively. The blue solid line is the fit used in the simulation for the electron fluxes and the red solid line is that for the proton fluxes. Figure is adapted from Nakamura et al. (2022a).

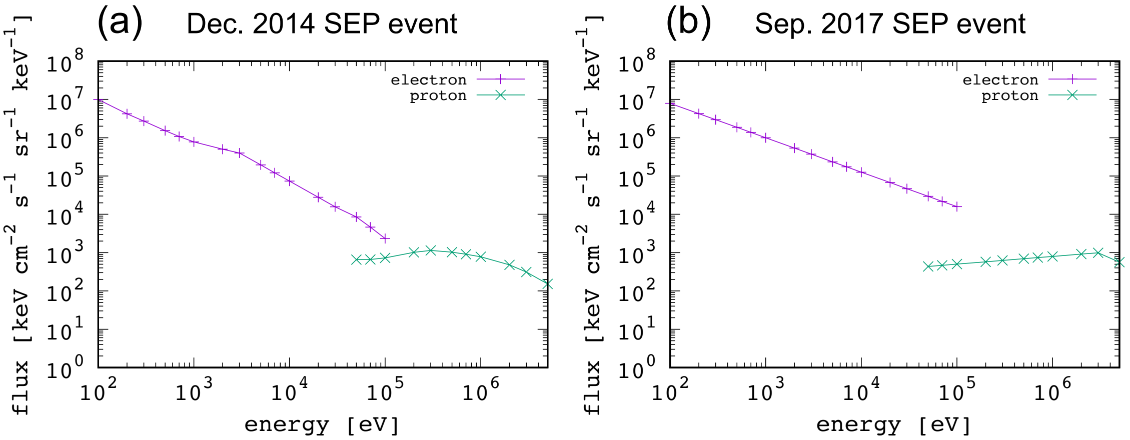

Figure 4.2 (a, b) Electron and proton fluxes for the December 2014 SEP event and the September 2017 SEP event that were used in the simulation, respectively. Figure is adapted from Nakamura et al. (2022a).

4.2 Production rate of $CO_2^+(B^2\Sigma_u^+)$

In this study, we use the atmospheric density profiles for the 5 main species (CO_2, CO, N_2, O_2, and O) from the nightside of the northern hemisphere as calculated by the Mars Climate Database (MCD) version 5.3 (Millour et al., 2018). CO_2 is the most important constituent in this study because we focus on the ionization of CO_2 to generate CO_2^+ UVD emissions. Figure 4.3 shows the atmospheric neutral density profiles used in this chapter for the December 2014 SEP event and the September 2017 SEP event. The solar longitude (Ls) was 255° (near perihelion) on 20 December 2014 and 60° (near aphelion) on 13 September 2017, corresponding to the season of atmospheric inflation and contraction on Mars, respectively (e.g., Forget et al., 2009). The solar activity and the dust load are set to be average. The latitude and local time are set to be 35°N and 00:00, respectively, to match the IUVS observation geometry when the diffuse aurora profile was obtained (Schneider et al., 2015). The CO_2 number densities at an altitude of 80 km were 8.5×10^{19} m^{-3} on 20 December 2014 and 3.1×10^{19} m^{-3} on 13 September 2017, respectively.

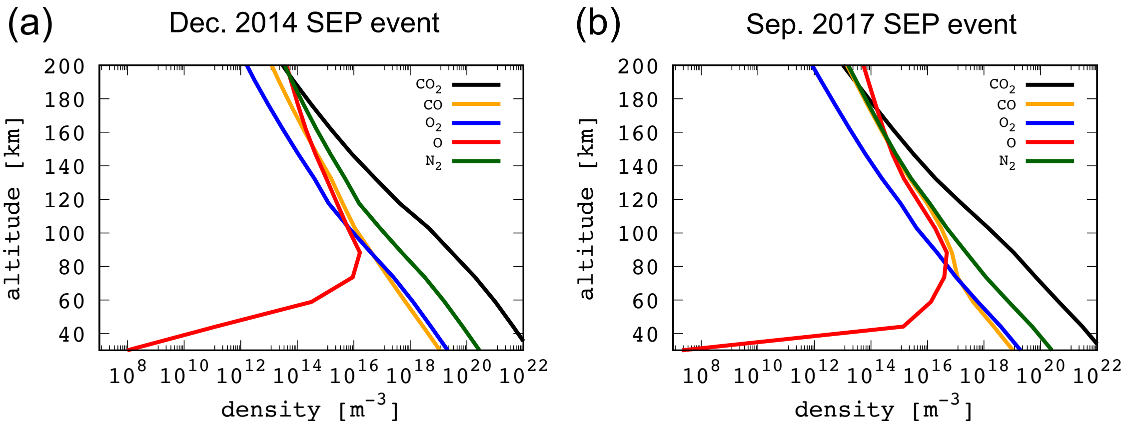

Figure 4.3 (a) Atmospheric density profile on 20 December 2014 and (b) atmospheric density profile on 13 September 2017 used in the Monte Carlo simulations. These density profiles were calculated by Mars Climate Database. Figure is adapted from Nakamura et al. (2022a).

The focus of this chapter is to derive the limb intensity profile of CO_2^+ UVD emissions. CO_2^+ UVD is emitted by the transition of CO_2^+ from the $B^2\Sigma_u^+$ state to the ground state $X^2\Pi_g$. The transition from $CO_2^+(B^2\Sigma_u^+)$ has another branch of transition to the $A^2\Pi_u$ state. We considered the branching ratio of the reaction leading to CO_2^+ UVD emission to be equal to 0.5 (Fox and Dalgarno, 1979a; Bhardwaj and Jain, 2013; Haider and Masoom, 2019). The CO_2^+ UVD volume emission rate is identical to the production rate of $CO_2^+(B^2\Sigma_u^+)$ multiplied by the branching ratio of 0.5. The limb intensity profile of the CO_2^+ UVD volume emission rate, which can be directly compared to the observations by MAVEN/IUVS, is then calculated by integrating the CO_2^+ UVD volume emission rate along the line of sight in the limb geometry.

Figure 4.4 represents the calculated production rate of $CO_2^+(B^2\Sigma_u^+)$ with an incident flux of 1 cm^{-2} s^{-1} at each incident energy of electrons and protons at the top of the model on 20 December 2014 and on 13 September 2017. The penetration altitude of electrons in our calculation was compared with Haider and Masoom (2019). They calculated the ionization rate during the December 2014 SEP event and found that the ionization rate by 100 keV electrons peaks at an altitude of 75 km. The peak altitude of the ionization rate by 100 keV electrons is 75 km in our model, which is precisely consistent with Haider and Masoom (2019). For protons, the penetration altitude of 5 MeV protons is approximately 55-65 km, which is approximately 10-20 km lower than Jolitz et al. (2017). A possible reason for the discrepancy between our model and Jolitz et al. (2017) is the different atmospheric density profiles, which are not described in Jolitz et al. (2017). Different scattering angle distributions in the elastic collision can also explain this discrepancy with Jolitz et al. (2017) because the smaller differential elastic cross section at a large scattering angle used in PTRIP implies a smaller deviation of the protons when traveling radially and therefore a deeper penetration. The penetration altitude at each incident energy is approximately 10 km lower for the September 2017 SEP event than for the December 2014 SEP event due to the seasonal atmospheric contraction on Mars.

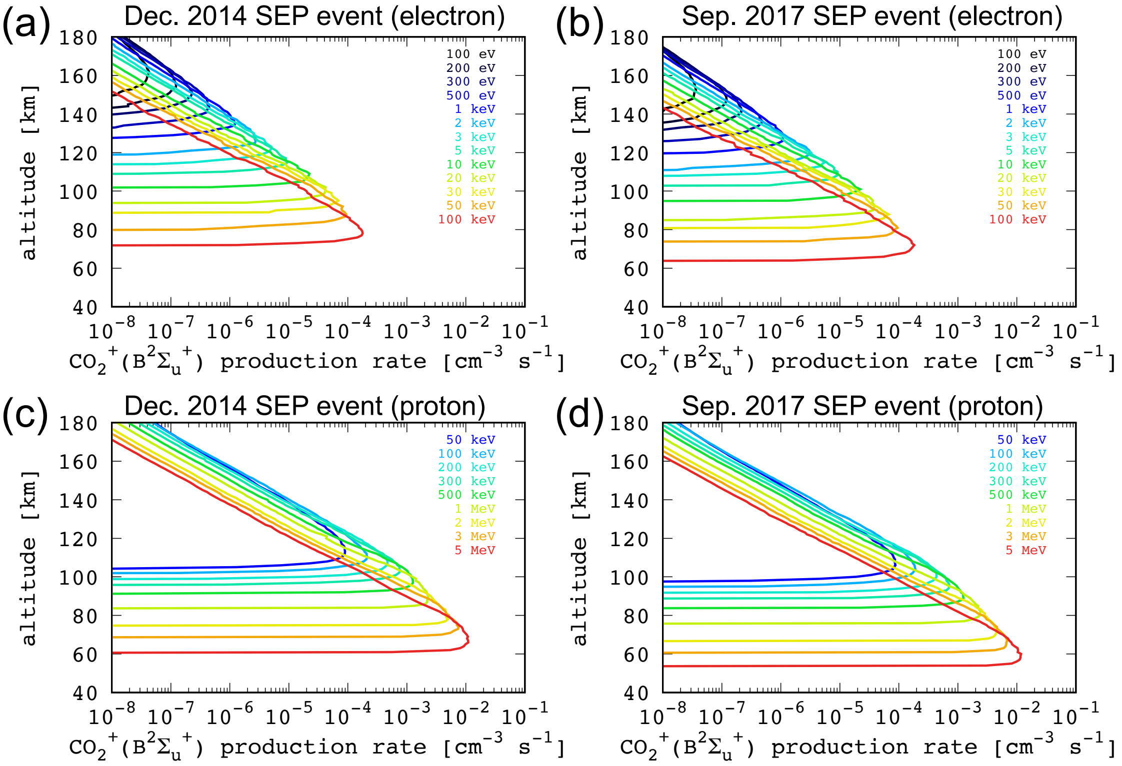

Figure 4.4 (a, b) Production rate of $CO_2^+(B^2\Sigma_u^+)$ with an incident flux of 1 cm^{-2} s^{-1} for each incident energy of electrons at the top of the model during the December 2014 SEP event and the September 2017 event, respectively, and (c, d) those of protons during the December 2014 SEP event and the September 2017 SEP event, respectively. Note that not all incident energies in the model are shown here to make the figure easier to read. Figure is adapted from Nakamura et al. (2022a).

Figure 4.5 shows the calculated production rate of $CO_2^+(B^2\Sigma_u^+)$ for each incident energy of electrons and protons during the December 2014 SEP event and the September 2017 SEP event according to Equation (2.5) by using the production rate with an incident flux of 1 cm^{-2} s^{-1} at each incident energy (Figure 4.4) and electron and proton fluxes observed by MAVEN (Figure 4.2). A comparison of the total production rate of $CO_2^+(B^2\Sigma_u^+)$ between incident electrons and protons during these two SEP events is shown in Figure 4.5. During the December 2014 SEP event, the largest contribution to the production rate of $CO_2^+(B^2\Sigma_u^+)$ due to electron impact occurs at an altitude of approximately 110 km, corresponding to incident 3-10 keV electrons (Figure 4.5a). The largest contribution to the production rate of $CO_2^+(B^2\Sigma_u^+)$ due to proton and hydrogen atom impacts occurs at 80 km altitude by incident 2 MeV protons (Figure 4.5c). The production rates of $CO_2^+(B^2\Sigma_u^+)$ by electrons and protons both have a peak value of 10 cm^{-3} s^{-1} during this SEP event. During the September 2017 SEP event, the largest contribution to the production rate of $CO_2^+(B^2\Sigma_u^+)$ due to electron impact occurs at 70 km altitude by incident 100 keV electrons. The largest contribution to the production rate of $CO_2^+(B^2\Sigma_u^+)$ due to proton and hydrogen atom impacts occurs at 70 km altitude by incident 3 MeV protons. The production rates of $CO_2^+(B^2\Sigma_u^+)$ by electrons and protons have peak values of 20 cm^{-3} s^{-1} and 40 cm^{-3} s^{-1}, respectively. For both SEP events, the production rate of $CO_2^+(B^2\Sigma_u^+)$ is dominated by proton impacts below 100 km altitude and by electron impacts above 100 km. It is noted that the limitation of the energy range of PTRIP could affect our simulation of the September 2017 SEP event. The production rate of $CO_2^+(B^2\Sigma_u^+)$ due to the precipitation of both electrons and protons increases with an incident energy up to near the upper limit of the energy range of the calculation. A higher energy than considered in our model would increase the $CO_2^+(B^2\Sigma_u^+)$ production rate at lower altitudes, which could result in a lower peak altitude and a larger peak production rate than that shown in Figure 4.6. The incident energy of protons is limited to above 50 keV due to the observational limitation of MAVEN/SEP. Protons below 50 keV could contribute to the production of $CO_2^+(B^2\Sigma_u^+)$ at altitudes above ~110 km, but their contribution can simply be speculated to be less than 1/100 of the peak value due to MeV protons according to Figure 4.5.

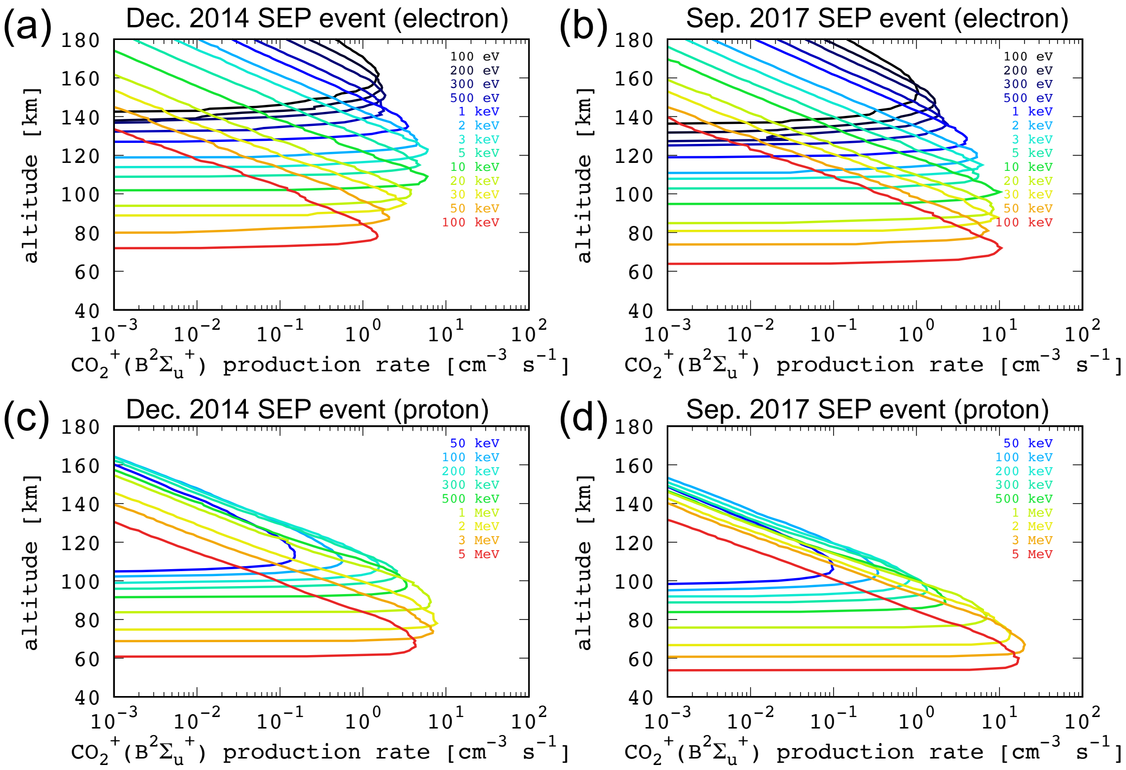

Figure 4.5 (a, b) Production rate of $CO_2^+(B^2\Sigma_u^+)$ due to precipitation of electrons during the December 2014 SEP event and the September 2017 event, respectively, and (c, d) those of protons during the December 2014 SEP event and the September 2017 SEP event, respectively. These production rates are calculated by using the energy flux observed by MAVEN/SEP and SWEA. Note that not all incident energies in the model are shown here to make the figure easier to read. Figure is adapted from Nakamura et al. (2022a).

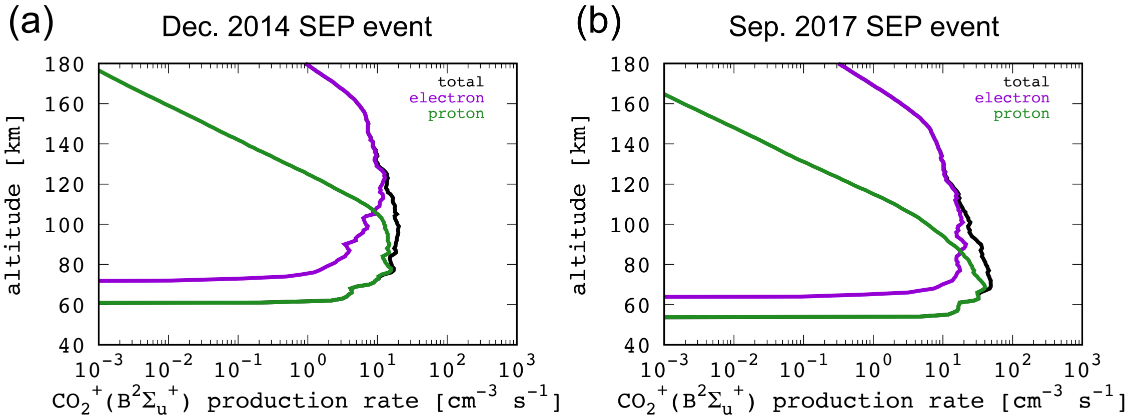

Figure 4.6 (a, b) Total production rate of $CO_2^+(B^2\Sigma_u^+)$ (black) and the contribution of impacting electrons (purple) and protons (green) during the December 2014 SEP event and the September 2017 SEP event, respectively. Figure is adapted from Nakamura et al. (2022a).

4.3 Limb emission profile of CO_2^+ ultraviolet doublet

The limb intensity profile of CO_2^+ UVD emissions is calculated by integrating the volume emission rate of CO_2^+ UVD along the line of sight in the limb geometry. As mentioned in Section 4.2, the volume emission rate of CO_2^+ UVD is estimated by multiplying the production rate of $CO_2^+(B^2\Sigma_u^+)$ by 0.5. Figure 4.7 shows the limb intensity profiles of CO_2^+ UVD for each incident energy of electrons and protons during the December 2014 SEP event and the September 2017 SEP event.

During the December 2014 SEP event, electron-induced CO_2^+ UVD emissions are largest at approximately 110 km with an intensity of 1 kR, produced essentially by 3-10 keV electrons. As suggested by previous models of diffuse aurora during the December 2014 SEP event (Schneider et al., 2015; Gérard et al., 2017; Haider and Masoom, 2019), 100 keV electrons reasonably produce CO_2^+ UVD emissions at low altitudes (70-80 km), as observed by MAVEN; however, the total electron-induced emissions do not peak at low altitudes because low-energy electrons produce brighter emissions at higher altitudes. While electron-induced CO_2^+ UVD emission peaks at a high altitude of ~110 km, proton-induced CO_2^+ UVD emission peaks at a low altitude of ~80 km with an intensity of 1 kR due to 2 MeV protons.

During the September 2017 SEP event, electron-induced CO_2^+ UVD emissions are largest at approximately 70 km with an intensity of 1 kR due to 100 keV electrons. Proton-induced CO_2^+ UVD emission peaks at low altitudes of ~65 km with an intensity of 2 kR due to 3 MeV protons. For both SEP events, the electron-induced CO_2^+ UVD emission profile covers an altitude range between 60 and 140 km, while the proton-induced CO_2^+ UVD emission profile has a narrower altitude range (between 60 and 100 km) owing to the difference in the electron and proton spectral shapes as shown in Figure 4.2.

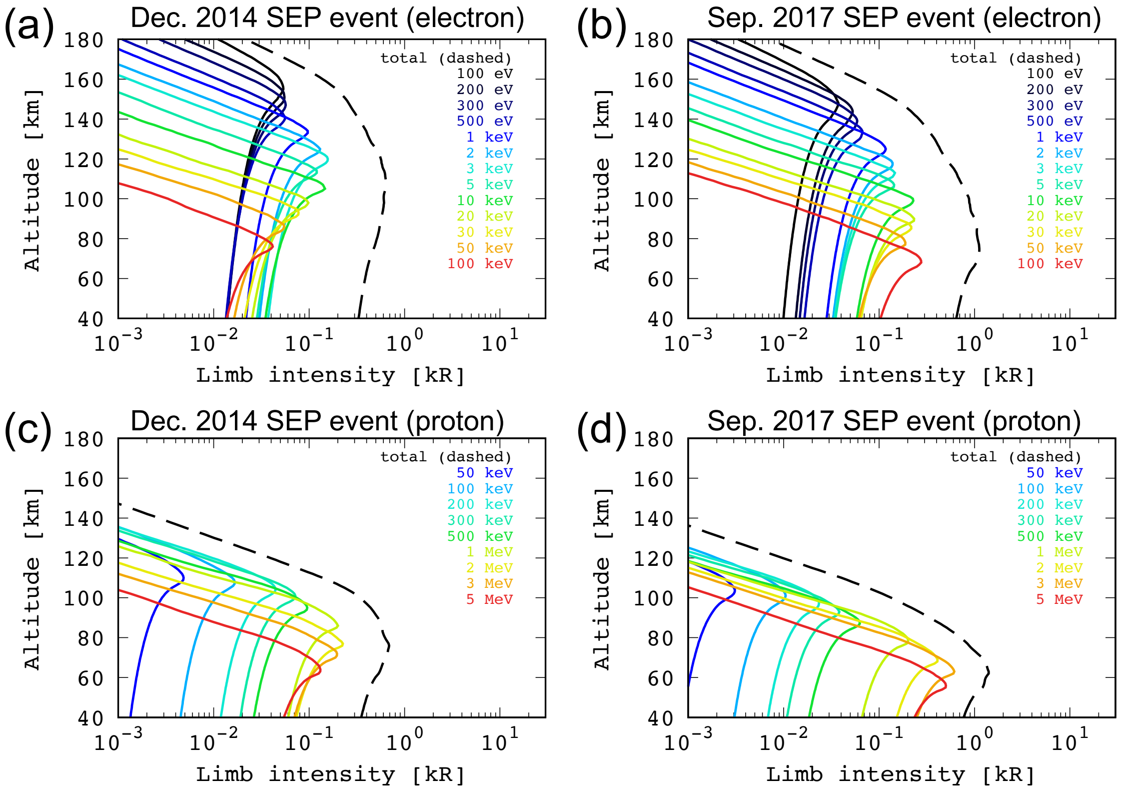

Figure 4.7 (a, b) Limb intensity of CO_2^+ UVD due to precipitation of electrons for differential incident energies during the December 2014 SEP event and the September 2017 SEP event, respectively, and (c, d) those of protons during the December 2014 SEP event and the September 2017 SEP event, respectively. Note that not all incident energies in the model are shown here to make the figure easier to read. Figure is adapted from Nakamura et al. (2022a).

We compared our model results with the observations of CO_2^+ UVD limb intensity obtained by Schneider et al. (2015) and Schneider et al. (2018) for the December 2014 SEP event and the

September 2017 SEP event, respectively. Figure 4.8a shows the calculated limb intensity profiles of CO_2^+ UVD emissions and the observed profile during the December 2014 SEP event. The calculated total CO_2^+ UVD limb intensity is 2 times larger than the observation. Our calculated altitude profile peaks at 76 km, which is very close to the observed peak at ~70 km. Figure 4.8b shows the calculated limb intensity profiles of CO_2^+ UVD emissions and the observed profile during the September 2017 SEP event. Since we used the electron and proton flux at the time before the flux peak and auroral emission peak, the calculated limb profiles were multiplied by a factor of 8 to match the observed emission intensity. Our calculated altitude profile peaks at 68 km, which is 10 km higher than the observation.

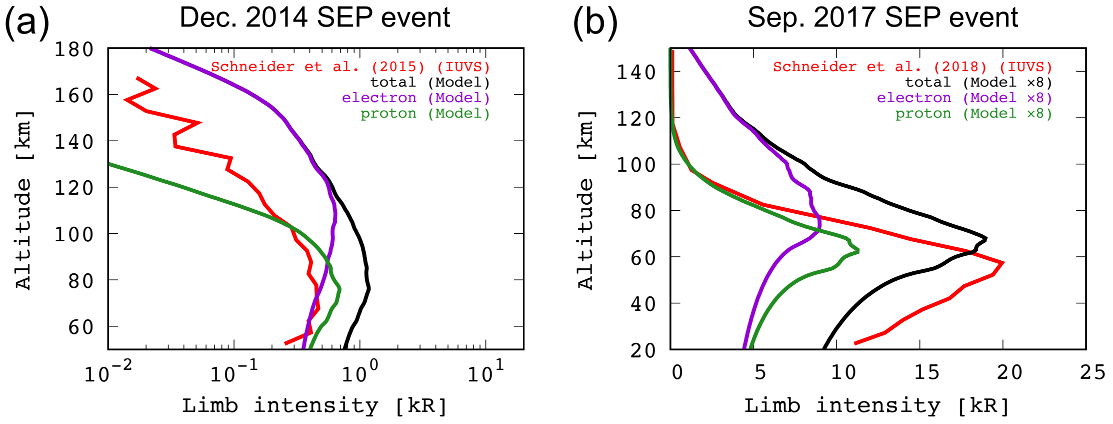

Figure 4.8 (a, b) Total limb intensity of CO_2^+ UVD (black) and contribution of impacting electrons (purple) and protons (green) during the December 2014 SEP event and the September 2017 SEP event, respectively. Observed profiles are taken from Schneider et al. (2015) and Schneider et al. (2018) in the December 2014 SEP event and the September 2017 SEP event, respectively. Note that the calculated limb profiles for the September 2017 SEP event were multiplied by a factor of 8 to match the observed emission intensity. Figure is adapted from Nakamura et al. (2022a).

4.4 Extrapolation of the energy range

Even if we found a good agreement between observations and simulations (Figure 4.8), there are several limits when comparing modeled with observed profiles. The results displayed in Figure 4.8 depend first on the cross sections and an ionizing branching ratio of the H-CO_2 collision. Since we assumed that most of the cross sections for H-CO_2 used are identical to the cross sections for

H-O_2 collisions, our calculations might be impacted by this assumption. Another aspect that may have affected our calculations is that we assumed the branching ratio of $CO_2^+(B^2\Sigma_u^+)$ to the total CO_2 ionization due to hydrogen atom impacts to be 0.1. Since MeV protons hardly experience charge exchange collisions until they lose energy to below 100 keV due to the smaller charge exchange cross sections compared with ionization cross sections leading to small contributions of hydrogen atom-impact ionization to the total ionization rates, the uncertainty in the H-CO_2 collision cross sections can be regarded as negligible.

As already mentioned in Section 4.2, the upper limit of the energy range considered in PTRIP could limit our capability to compare the results of our simulation to the IUVS observations. Extrapolating the cross sections and the electron and proton fluxes considered in this chapter allows us to provide a first estimate of the potential contributions to the emission due to electrons above 100 keV and protons above 5 MeV. For the December 2014 SEP event, since the electron and proton fluxes observed by MAVEN/SEP are limited below 200 keV and 6 MeV, respectively, we simply extrapolated the electron flux above 200 keV and proton flux above 6 MeV logarithmically to estimate the contribution of energetic electrons up to 500 keV and energetic protons up to 20 MeV. For the September 2017 SEP event, fitting results of the electron and proton fluxes shown in Figure 4.1 was used to estimate the contribution of energetic electrons up to 500 keV and energetic protons up to 20 MeV. The extrapolated electron and proton fluxes during the two SEP events are shown in Figure 4.9.

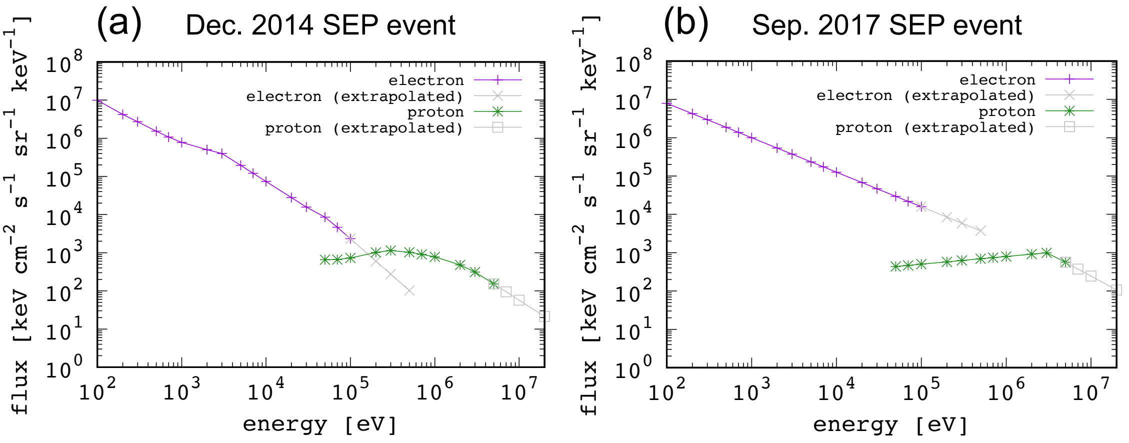

Figure 4.9 (a, b) Electron and proton fluxes for the December 2014 SEP event and the September 2017 SEP event, respectively, with energy ranges extrapolated up to 500 keV for electrons and 20 MeV for protons.

The ionization collisional cross sections due to electron and proton impacts are extrapolated as follows. For electrons, the ionization cross section is known to exhibit the asymptotic relation up to 100 keV as $(\mathrm{E}) \propto \mathrm{E}^{-1}\ \mathrm{n}(\mathrm{E})$, which is expected by the Born approximation, but it deviates from this behavior above 100 keV (Rieke and Prepejchal, 1972). We used the ionization cross section of CO_2 due to electron impacts above 100 keV from Kumar et al. (2010), which agrees very well with the experimental cross section from Rieke and Prepejchal (1972). For protons, since the asymptotic relation of the ionization cross section is expected to hold even at around 100 MeV (Porter et al., 1976), we simply apply the analytic expression of ionization cross sections of Rudd et al. (1983) up to 20 MeV.

Figure 4.10 shows the limb intensity profiles of CO_2^+ UVD for each incident energy of electrons up to 500 keV and protons up to 20 MeV during the December 2014 SEP event and the September 2017 SEP event. During the December 2014 SEP event, the contribution of electrons above 100 keV is comparatively small, while the contribution of protons above 5 MeV is comparable to the peak value. During the September 2017 SEP event, the contributions of both electrons above 500 keV and protons above 5 MeV are comparable to the peak value. A comparison between our model results with energy extension and the IUVS observations is shown in Figure 4.11. Note that the calculated limb profiles for the September 2017 SEP event were multiplied by a factor of 6 to match the observed emission intensity. During the December 2014 SEP event, the shapes, the peak altitude, and the intensity of CO_2^+ UVD limb profiles do not largely change even if we take into account the contribution of more energetic electrons and protons. During the September 2017 SEP event, the calculated limb intensity profile changed below 70 km altitude and it peaks at 55 km, which is in good agreement with the IUVS observation.

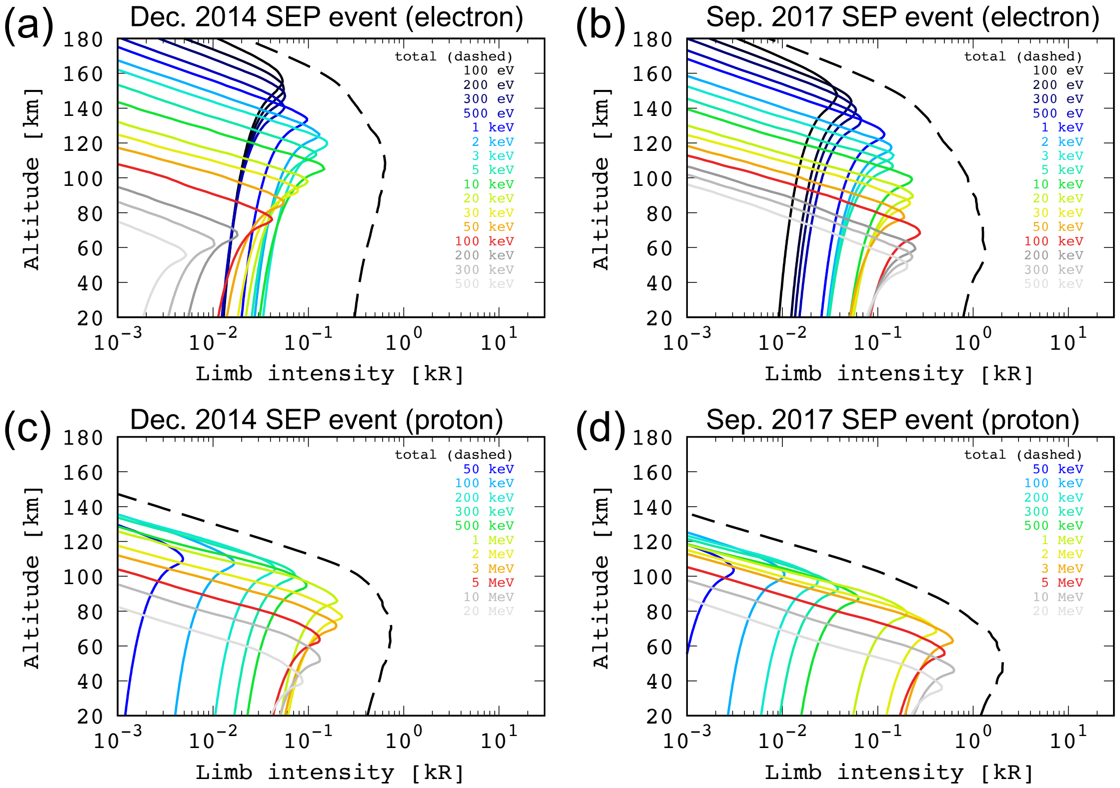

Figure 4.10 (a, b) Limb intensity of CO_2^+ UVD due to precipitation of electrons for differential incident energies during the December 2014 SEP event and the September 2017 SEP event, respectively, and (c, d) those of protons during the December 2014 SEP event and the September 2017 SEP event, respectively. Electron and proton energy ranges are extended to 500 keV and 20 MeV, respectively. Note that not all incident energies in the model are shown here to make the figure easier to read. Figure is adapted from Nakamura et al. (2022a).

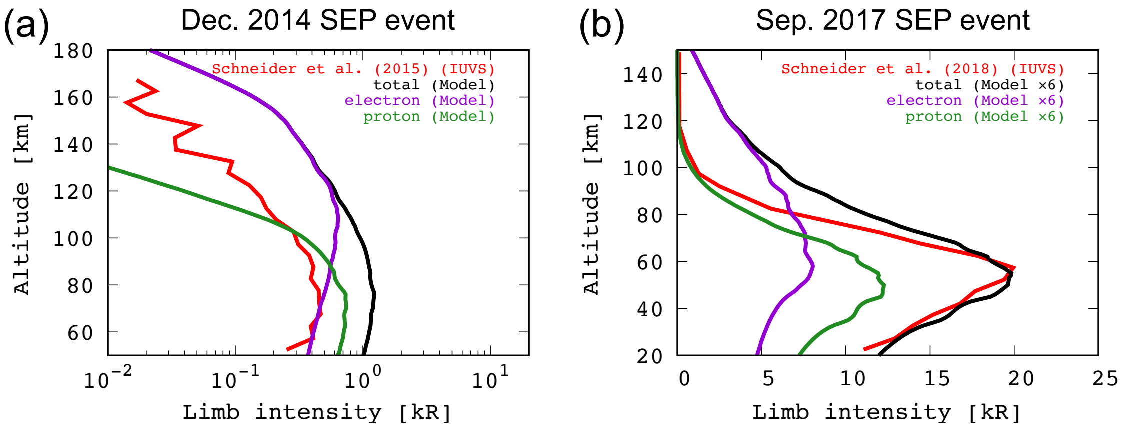

Figure 4.11 (a, b) Contribution of the impacting electrons up to 500 keV (purple) and protons up to 20 MeV (green) to the CO_2^+ UVD limb intensity, and the total limb intensity of CO_2^+ UVD (black) during the December 2014 SEP event and the September 2017 SEP event, respectively. Observed profiles are taken from Schneider et al. (2015) and Schneider et al. (2018) in the December 2014 SEP event and the September 2017 SEP event, respectively. Note that the calculated limb profiles for the September 2017 SEP event were multiplied by a factor of 6 to match the observed emission intensity. Figure is adapted from Nakamura et al. (2022a).

The penetration altitude of incident particles strongly depends on the neutral atmospheric temperature. The Martian atmosphere is known to exhibit large variability with respect to season, latitude, and local time (e.g., Forget et al., 2009). A different atmospheric temperature would impact, as a first order, the altitude profile of the emission brightness. Since we obtained rather good agreement between the simulated altitude profile of the emission brightness and the observed profile for the two SEP events, our choice of atmospheric density profiles for both events was close to the real atmospheric conditions at that time.

We did not take into account the effects of the magnetic field. Electrons are expected to be guided to the regions of open magnetic field lines, and they are unlikely to penetrate into closed field line regions (Lillis et al., 2011; Jolitz et al., 2021). Proton penetration to low altitudes is also expected to be depleted in regions of strong crustal magnetic fields (Leblanc et al., 2002). Due to the different gyro radii of electrons and protons, different sensitivities to the magnetic field strength and configuration are expected (Bisikalo et al., 2017).

4.5 Possible explanation for the overestimation

We provide possible explanations for the overestimate of the modeled CO_2^+ UVD limb intensity compared to IUVS observations during the December 2014 SEP event. Since the SEP-induced CO_2^+ UVD emission peaks at low altitudes, CO_2^+ UVD could have been absorbed by the Martian atmosphere if there is an absorber of CO_2^+ UVD. Ozone has a strong absorption line around the wavelength of CO_2^+ UVD ~289 nm (see Figure C.1). The absorption cross section of ozone at 289 nm is about 10^{-22} m^2 (Gröller et al., 2018) and the maximum density of ozone is 10^{15} m^{-3} above an altitude of 50 km (Lebonnois et al., 2006). Integrating the optical depth along the line of sight over a distance of 1000 km using the above cross section and density of ozone yields an upper limit of the optical depth of 0.1 at 289 nm, which is insufficient to absorb CO_2^+ UVD emission by the Martian atmosphere above an altitude of 50 km.

SEP shadowing by Mars could reduce the SEP ion flux on the nightside of Mars. The Martian Radiation Environment Experiment (MARIE) measurements onboard Mars Odyssey found that the count rate of SEP ions (20-200 MeV) near Mars showed modulation during solar events in October 2002 (Luhmann et al., 2007). They showed that the modulation of the SEP ion flux near Mars resulted from the shadowing of the SEP ion flux and the orientation of the interplanetary magnetic field (IMF). Lillis et al. (2016) reported the anisotropy of SEP ions near Mars, which was suggested to be caused by shadowing by Mars and the configuration of the magnetic field. Since the location and the timing of the observation of electron and proton fluxes made by MAVEN/SEP and SWEA were not precisely the same as the observations of the auroral emission made by IUVS, SEP shadowing might have reduced fluxes at the origin of IUVS observations. Shadowing of the SEP event by Mars might largely explain the factor of 2 of the difference between the observed emission brightness and the simulated brightness at the SEP event on 20 December 2014. Another aspect that might reduce the model emission rate is the calculation geometry. Our calculation used the plane-parallel atmosphere, but if we apply a spherical atmosphere, MeV protons with pitch angles larger than 60 degrees at an altitude of 500 km do not penetrate deep into the atmosphere but go through the upper atmosphere and exit the atmosphere because of their large gyro radii, which are on the order of the planetary radius. The geometric effect is effective for only protons with energies larger than MeV, so the emission rate due to these protons could be reduced by a factor reaching ~2. For electrons, only a few percent of the SEP electrons can reach the atmosphere due to the magnetic mirror effect (Jolitz et al., 2021), which might also be applicable to low-energy protons.

4.6 Chapter summary

Previous studies were not able to reproduce the observed SEP-induced CO_2^+ UVD auroral emission profiles with precipitating energetic electrons considering the electron energy flux spectrum during SEP events observed by MAVEN (Schneider et al., 2015; Gérard et al., 2017; Haider and Masoom, 2019). This chapter aimed to reproduce the observed CO_2^+ UVD profiles by taking into account the contribution of energetic protons reaching MeV energies. We developed a Monte Carlo model, PTRIP, which solves the transport of electrons, protons, and hydrogen atoms through the Martian atmosphere. PTRIP is used to investigate the contribution of electron- and proton-induced CO_2^+ UVD emissions by using the electron and proton flux spectra observed by MAVEN. Our results showed that proton-induced CO_2^+ UVD emission profiles are brighter, narrower in altitude, and have a lower peak altitude than electron-induced CO_2^+ UVD emission profiles. The sum of the electron- and proton-induced CO_2^+ UVD emission profiles displays similar shapes and altitude peaks as those of the observed profiles (Schneider et al., 2015, 2018), and the extension of energy up to 500 keV for electrons and 20 MeV for protons enabled us to obtain emission profiles closer to the observations. However, the calculated intensity is larger than the observed intensity by a factor of 2 during the December 2014 SEP event, a discrepancy that might be explained by SEP shadowing (Lillis et al., 2016), calculation geometry effect, and magnetic mirror effect (Jolitz et al., 2021). Therefore, the contribution of energetic protons helps to reconcile the in-situ observations of the SEP electron and proton flux spectra by MAVEN/SEP with the observed emission brightness observed by IUVS (Schneider et al., 2015, 2018) during the two SEP events. This conclusion should be confirmed by considering other SEP events and completed by taking into account other possible effects that can impact the reconstructed emission brightness profiles.

Chapter 5

Three-dimensional simulation of the Martian diffuse auroral emission

In Chapter 4, we performed Monte Carlo simulations without magnetic fields in one dimension for space and in three dimensions for velocity using PTRIP, and we have shown that both SEP electrons and protons contributed to the Martian diffuse auroral emission, with higher altitude emissions by SEP electrons and lower altitude peak emission by SEP protons. In Chapter 5, we investigate the effects of crustal magnetic fields in the southern hemisphere of Mars on the transport of SEPs and on the morphology and intensity of the Martian diffuse auroral emission by performing a three-dimensional simulation using PTRIP. In this chapter, oxygen atom emission lines at 557.7 nm and 630.0 nm are also investigated in addition to the CO_2^+ UVD emission in order to evaluate the visibility of the Martian diffuse auroral emission in the visible wavelength range and to clarify whether the contribution of SEP electrons and protons can be separated by viewing several emission lines.

5.1 Application of PTRIP to three-dimensional simulation

5.1.1 Crustal magnetic field

The crustal magnetic field vector was calculated by a potential function using 90th-order spherical harmonics with coefficients taken from Cain et al. (2003), which is based on the magnetic field vector data obtained by Mars Global Surveyor. The vertical component of the crustal magnetic field at 100 km altitude is shown in Figure 5.1. Particles were uniformly and isotropically injected into the region within the area limited by the green lines in Figure 5.1 (30°S ~ 70°S latitude and 160°E ~ 200°E longitude) where the crustal magnetic field strength is the strongest. The initial altitude was set to 450 km and particles that reach an altitude above 500 km were removed from the simulation domain. This 50 km margin from the initial altitude allows us to track the bouncing motion of electrons between cusps of crustal magnetic fields. In this chapter, electric fields are ignored for simplicity which is acceptable considering the energy ranges of the SEPs simulated in this work.

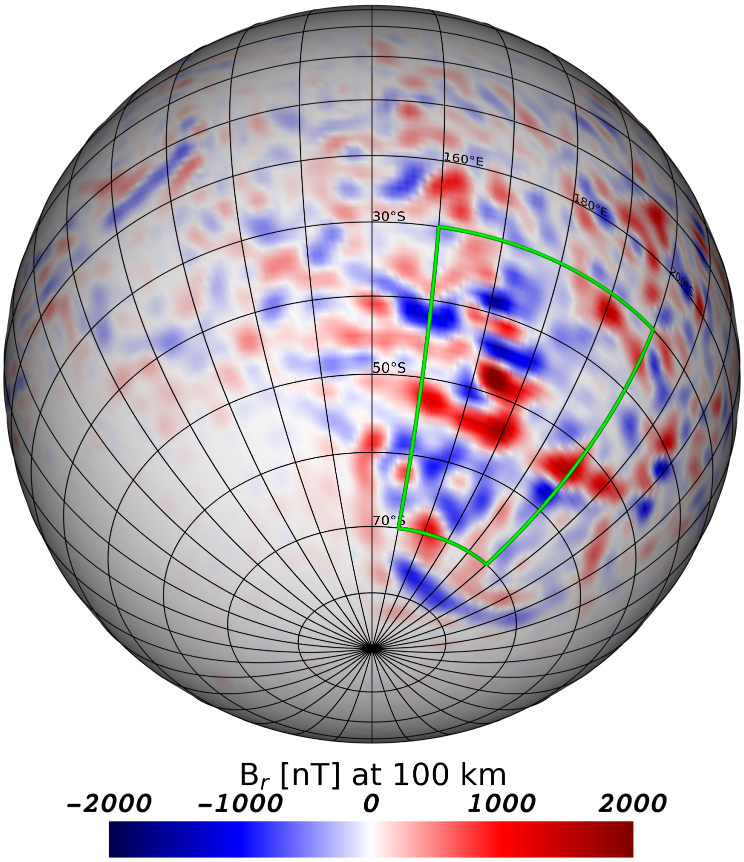

Figure 5.1 The vertical component of the Martian crustal magnetic field at 100 km altitude calculated using the 90th-order spherical harmonics in Cain et al. (2003). The area indicated by the green lines is the region where particles are injected in the simulation.

Since calculating the magnetic field vector using the 90th-order spherical harmonics at every timestep requires high computational cost, the magnetic field vector is calculated in advance with a horizontal resolution of 1° and a vertical resolution of 1 km, and then interpolated at the location of the particle using a volume-weighted interpolation.

5.1.2 Cubed sphere grid

A spherical grid system is needed to create a map of the number of collisions in the atmosphere surrounding Mars. The latitude-longitude grid system is widely used because of its simplicity, but this grid system has a problem because the surface area of individual cells can vary by more than one order of magnitude between polar and equatorial regions when latitude- and longitude-angle intervals are given uniformly. The large difference in the cell surface areas results in a large statistical error in the Monte Carlo simulation in small area cells, and a large horizontal resolution is not able to resolve the structure of the localized crustal magnetic field morphology on Mars. Thus, a cubed sphere grid system (e.g., Ronchi et al., 1996) has been implemented into PTRIP, which is generated by projecting a cubic grid onto a spherical surface and has a quite uniform surface area of cells and horizontal resolution. In this study, a cubed sphere grid of 72,600 cells horizontally is applied to cover the entire Mars (1,952 cells horizontally for the area indicated in green in Figure 5.1), with a horizontal resolution of 32.6-52.5 km and a small deviation in the cell surface area of up to 13% (Figure 5.2), both of which satisfy the above requirements. The vertical grid is defined in an altitude range of 0-500 km with a vertical resolution of 5 km. The generation of a cubed sphere grid and the localization method are explained in Appendix D.

The number of collisions counted by PTRIP in each cell at each energy bin is then normalized to one incident particle per 1 cm^{-2}. Suppose N incident particles are injected into a region (30°S-70°S, 160°E-200°E) of surface area . The number of collisions ${}_j^{i,h}(E_0)$ of the jth collision type at altitude grid cell h due to incident particle with energy E_0 is counted within the ith horizontal grid cell of a surface area $\Delta\ {}^{i}$. The number of collisions ${}_j^{i,h}(E_0)$ per cm^{-2} unit is ${}_j^{i,h}(E_0)/\Delta\ {}^{i}$. Then the normalized number of collisions ${}_j^{i,h}(E_0)$ of the jth collision type within an ith horizontal grid cell is expressed as:

$$ {}_j^{i,h}(E_0) = \frac{{}_j^{i,h}(E_0)}{\Delta\ {}^{i}} \frac{\ }{N} \tag{5.2} $$

In this chapter, N is set to 10,000 at each energy bin. The collision rate $P_j^{i,h}$ of the jth collision type at altitude grid h within the ith horizontal cell for an incident particle flux $f(E_0)$ can be written as:

$$ P_j^{i,h} = \int f(E_0)\ {}_j^{i,h}(E_0)\, dE_0 \quad , \tag{5.3} $$

where the integration range of E_0 is 100 eV ~ 100 keV for electrons and 46 keV ~ 6.8 MeV for protons.

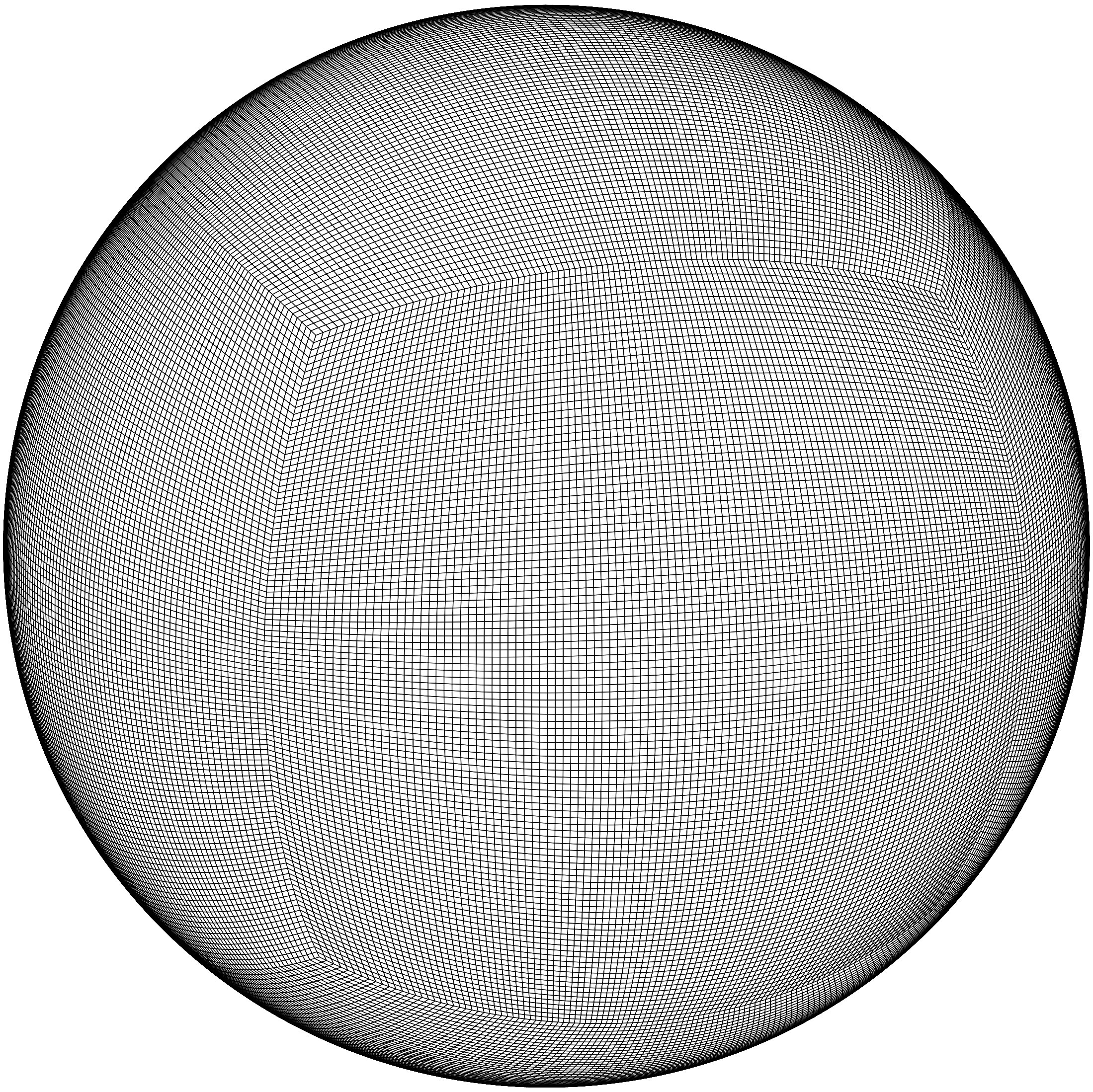

Figure 5.2 Cubed sphere grid system that consists of 72,600 cells horizontally used in the simulation. Horizontal resolution between adjacent vertices ranges 32.6-52.5 km on the Martian surface and a maximum difference of cell surface area is 13% from the mean.

5.1.3 Reduced calculation for secondary electron transport

As described in Chapter 2, PTRIP tracks all the secondary electrons produced in the atmosphere by ionizing collisions between primary SEPs and atmospheric molecules and by electron stripping reactions between hydrogen atoms and atmospheric molecules. Since the three-dimensional Monte Carlo simulation requires a large number of incident particles, it requires enormous calculation costs to track all the secondary electrons. In order to take into account the transport of secondary electrons in the three-dimensional simulation, we developed a reduced calculation method for secondary electrons. The important approximation here is that the secondary electrons are solved in advance in three dimensions in velocity and one dimension in space, without magnetic fields.

The number of collisions ${}_j^h$ of the jth collision type due to secondary electrons at the altitude grid cell h can be estimated as follows:

$${}_j^h = \sum_{\eta} \sum_{\varepsilon} {}_{\eta,\varepsilon} \mathscr{k}_j^{\eta,\varepsilon,h} \quad , \tag{5.4}$$

where ${}_{\eta,\varepsilon}$ is the number of secondary electrons produced within the ηth vertical grid cell and the εth energy bin, $\mathscr{k}_j^{\eta,\varepsilon,h}$ is the number of collisions of the jth collision type within the hth altitude grid cell due to secondary electrons produced within the ηth vertical grid cell and the εth energy bin. It should be noted that the energy bin here is independent of the energy bin of the incident particles, and the energy bin here is logarithmically distributed by dividing one digit into 24 bins. $\mathscr{k}_j^{\eta,\varepsilon,h}$ were calculated in advance by injecting 1,000 electrons at the vertical grid cell η and at the energy bin ε isotropically and normalized on a per-one-electron basis. The performance of this reduced count method for secondary electrons is shown in Figure 5.3. The production rate of CO_2^+ estimated by the reduced count method obtained a good agreement with the production rate of CO_2^+ when all the secondary electrons were tracked after their production described in Chapter 2. In the three-dimensional simulation, the number of collisions ${}_j^{i,h}$ within the ith horizontal grid cell and the hth vertical grid cell can be estimated by using the number of secondary electrons ${}_{\eta,\varepsilon}^{i}$ produced within the ith horizontal grid cell as follows:

$${}_j^{i,h} = \sum_{\eta} \sum_{\varepsilon} {}_{\eta,\varepsilon}^{i} \mathscr{k}_j^{\eta,\varepsilon,h} \tag{5.5}$$

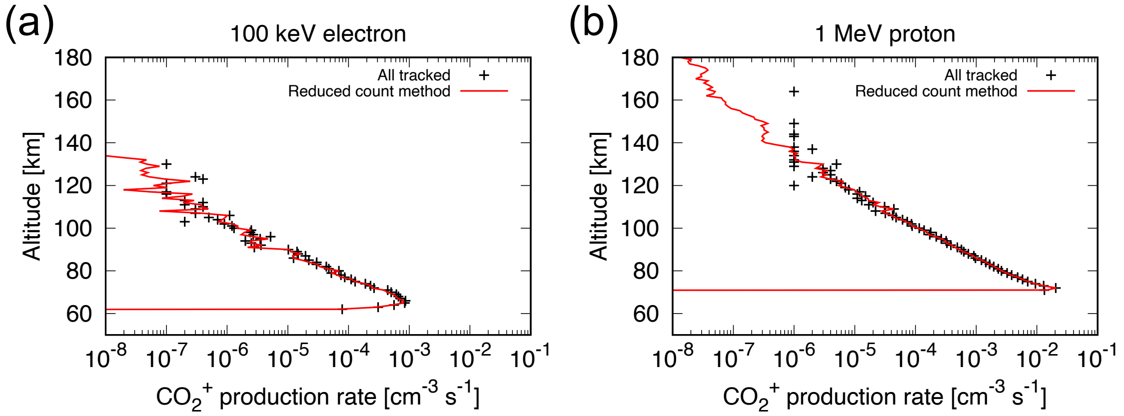

Figure 5.3 Comparison of the production rate of CO_2^+ only due to secondary electrons between the case that all the secondary electrons produced were tracked and the reduced count method. The black points represent the production rate of CO_2^+ when all the secondary electrons were tracked after their production, and the red curves represent the production rate estimated by the reduced count method. (a) One hundred of incident 100 keV electrons and (b) ten incident 1 MeV protons were injected with incident angles of 0 degree. Electric and magnetic fields were ignored in this simulation.

This reduced count method for secondary electrons ignores electric and magnetic fields for the transport of secondary electrons. Figures 5.4a and 5.4b shows the calculated flux of secondary electrons of 28.7 eV produced at 120 km altitude and Figures 5.4c and 5.4d shows those produced at 150 km altitude. It should be noted that the energy gaps seen in the secondary electron fluxes were due to the loss of discrete energy corresponding to the threshold energy of ionization, dissociation, and excitation of atmospheric molecules. 28.7 eV electrons produced at 120 km altitude lose all the energy just around the produced altitude, while 28.7 eV electrons produced at 150 km altitude travel in the atmosphere, and some of them escape the atmosphere. The motion of secondary electrons produced below 120 km altitude is not affected by magnetic fields because of the short mean free path, while the motion of secondary electrons produced above 150 km altitude should be affected by magnetic fields due to the long mean free path. All the simulations in this chapter ignored magnetic fields in the transport of secondary electrons, which would result in uncertainty in the auroral emissions above 150 km. This uncertainty is negligible for SEP protons at all energy and SEP electrons above 2 keV because the ionization by electrons and protons at such energy is negligible above 150 km. It is not negligible for SEP electrons with energy below 1 keV because of their contribution to ionization above 150 km. The electron-induced auroral emission profiles above 150 km altitude should be therefore interpreted cautiously.

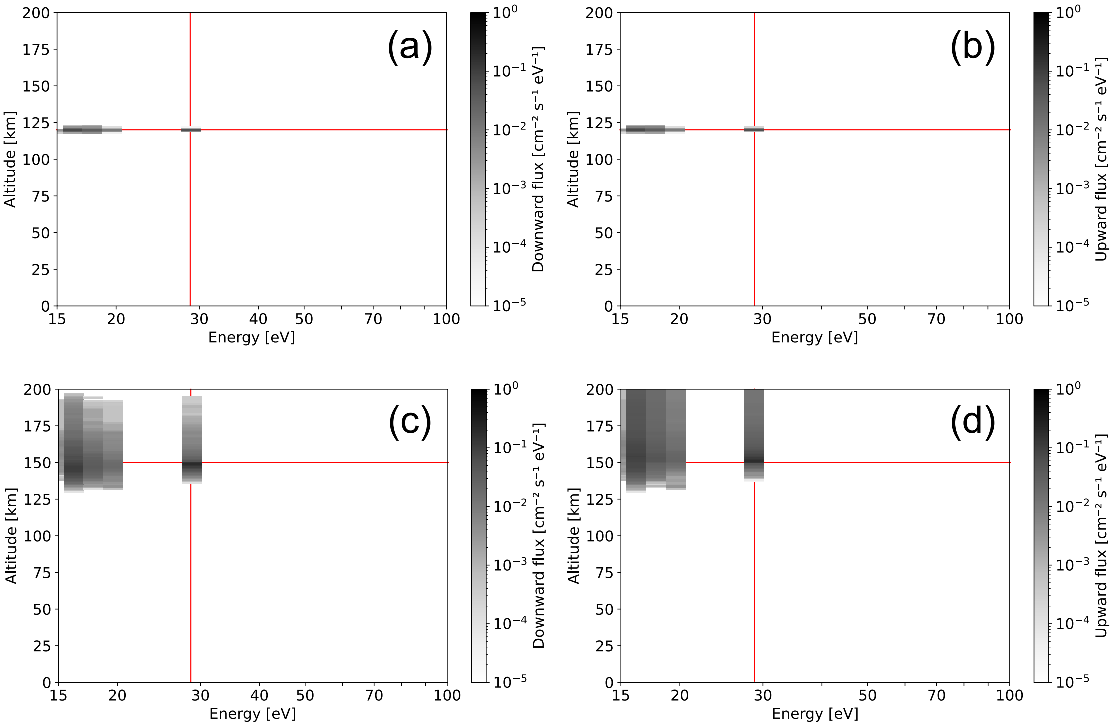

Figure 5.4 (a, b) Downward and upward fluxes of 28.7 eV secondary electrons produced at 120 km altitude, respectively, and (c, d) downward and upward fluxes of 28.7 eV secondary electrons produced at 150 km altitude, respectively. The red horizontal and vertical lines indicate the altitude and energy at which secondary electrons are produced.

5.1.4 Oxygen atom emission lines

Since the dissociation cross sections for the production of $O(^1S)$ and $O(^1D)$ due to proton-CO_2 impact are unknown, only emissions due to secondary electrons are taken into account for the SEP proton-induced emissions, which could be therefore considered as a lower limit.

The mechanism of the production of oxygen 557.7 nm emission is as follows. $O(^1S)$ is produced by electron impacts on CO_2 (R5.1). $O(^1S)$ de-excites to $O(^1D)$ to produce 557.7 nm emissions (R5.2). The emission is quenched by the collisions with ambient CO_2 (R5.3 and R5.4).

$$\mathrm{CO_2} + \mathrm{e}^* \rightarrow \mathrm{O}(^1\mathrm{S}) + \mathrm{CO} + \mathrm{e}^* \quad , \qquad \text{(R5.1)}$$

$$\mathrm{O}(^1\mathrm{S}) \xrightarrow{A_{5577}} \mathrm{O}(^1\mathrm{D}) + h\nu\ (557.7\ \mathrm{n}\quad) \quad , \qquad \text{(R5.2)}$$

$$\mathrm{O(^1S)} + \mathrm{CO_2} \overset{k_1}{\rightarrow} \mathrm{O(^1D)} + \mathrm{CO_2} \quad , \tag{R5.3}$$

$$\mathrm{O(^1S)} + \mathrm{CO_2} \overset{k_2}{\rightarrow} \mathrm{O(^3P)} + \mathrm{CO_2} \quad , \tag{R5.4}$$

where e* denotes impacting electrons, $_{5577}$=1.215 s^{-1} is the Einstein coefficient of the transition (R5.2) (Itikawa and Ichimura, 1990), k_1=2.02×10^{-11}exp(-1327/T) cm^3 s^{-1} and k_2=1.19×10^{-11}exp(-1327/T) cm^3 s^{-1} are the reaction rate coefficients of the reactions (R5.3) and (R5.4) (Capetanakis et al., 1993), respectively, T is the neutral temperature. The volume emission rate of the oxygen 557.7 nm emission $_{5577}$ can be calculated as follows:

$$_{5577} = \left(\frac{_{5577}}{_{1\mathrm{S}} + (k_1 + k_2)[\mathrm{CO_2}]}\right) P_{1\mathrm{S}} \quad , \tag{5.6}$$

where $P_{1\mathrm{S}}$ is the production rate of O(^{1}S) due to electron impacts, $_{1\mathrm{S}}$=1.291 s^{-1} is the sum of the Einstein coefficients of all the transitions from the O(^{1}S) state (Itikawa and Ichimura, 1990), and $[\mathrm{CO_2}]$ is the number density of CO$_2$ in cm^{-3}. The dissociation cross section of the O(^{1}S) production due to the electron-CO$_2$ collision (R5.1) was taken from Shirai et al. (2001).

The mechanism of the production of the oxygen 630.0 nm emission is as follows. O(^{1}D) is produced by electron impacts on CO$_2$ (R5.5) or by the transition from O(^{1}S) (R5.2). O(^{1}D) de-excites to O(^{3}P$_0$) to produce 630.0 nm emissions (R5.6). The emission is quenched by the collisions with ambient CO$_2$ (R5.7).

$$\mathrm{CO_2} + \mathrm{e^*} \rightarrow \mathrm{O(^1D)} + \mathrm{CO} + \mathrm{e^*} \quad , \tag{R5.5}$$

$$\mathrm{O(^1D)} \xrightarrow{A_{6300}} \mathrm{O(^3P_0)} + h\nu\ (\ 30.0\ \mathrm{n}\ \ ) \quad , \tag{R5.6}$$

$$\mathrm{O(^1D)} + \mathrm{CO_2} \overset{k_3}{\rightarrow} \mathrm{O(^3P_{0-2})} + \mathrm{CO_2} \quad , \tag{R5.7}$$

where $_{6300}$=5.627×10^{-3} s^{-1} is the Einstein coefficient of the transition (R5.6) (Itikawa and Ichimura, 1990), and k_3=7.5×10^{-11}exp(115/T) cm^3 s^{-1} is the reaction rate coefficients of the reaction (R5.7) (Burkholder et al., 2019). The volume emission rate of the oxygen 630.0 nm emission $_{6300}$ can be calculated as follows:

$$_{6300} = \left(\frac{_{5577} + k_1[\mathrm{CO_2}]}{_{1\mathrm{S}} + (k_1 + k_2)[\mathrm{CO_2}]} \times \frac{_{6300}}{_{1\mathrm{D}} + k_3[\mathrm{CO_2}]}\right) P_{1\mathrm{S}} + \left(\frac{_{6300}}{_{1\mathrm{D}} + k_3[\mathrm{CO_2}]}\right) P_{1\mathrm{D}} \quad , \tag{5.7}$$

where $P_{1\mathrm{D}}$ is the production rate of O(^{1}D) due to electron impacts, $_{1\mathrm{D}}$=7.446×10^{-3} s^{-1} is the sum of the Einstein coefficients of all the transitions from O(^{1}D) state (Itikawa and Ichimura, 1990). The first term represents the emission from O(^{1}D) cascaded from the O(^{1}S) state and the second term represents the emission from O(^{1}D) produced directly by electron impacts.

The dissociation cross section for the production of O(^{1}D) due to the electron-CO_2 collision (R5.5) was estimated as follows. Parameters for the analytic expression of electron impact cross sections of CO_2 for discrete states are summarized in Table 1 of Sawada et al. (1972) based on the semiempirical analytic expression for those cross sections of Strickland and Green (1969), which referred to the generalized oscillator strength experiment by Lassettre and Shiloff (1965). According to Fox and Dalgarno (1979b), the 9.3 eV electronic state corresponds to the production of O(^{1}D). Sawada et al. (1972) pointed out the discrepancy in the total inelastic cross section between Strickland and Green (1969) and Hake and Phelps (1967). Jackman et al. (1977) multiplied the cross sections of all the electronic states of Sawada et al. (1972) by a factor of 2.6 to solve the discrepancy, which resulted in an energy per ion pair closer to the experimental values. Therefore, in this chapter, we regarded the cross section of the 9.3 eV electronic state in Sawada et al. (1972) multiplied by 2.6 as a cross section for the production of O(^{1}D) by electron-CO_2 collisions.

5.2 Spatial distribution of the Martian diffuse aurora

In this chapter, we used the atmospheric density profiles and the incident fluxes of SEP electrons and protons during the September 2017 SEP event for which the global images of the Martian diffuse aurora were obtained with the IUVS instrument onboard MAVEN. The vertical density profiles of CO_2, CO, O_2, N_2, and O during the September 2017 SEP event were calculated by the Mars Climate Database (MCD) version 5.3 (Millour et al., 2018). The incident fluxes of SEP electrons and protons were taken from Figure 4.9b in Chapter 4. Since SEP electron and proton fluxes in Figure 4.9b were taken just before the rapid increase of the SEP flux in order to avoid cross contamination between channels of MAVEN/SEP, the SEP flux intensities were multiplied by 6 to match the observed intensity of the CO_2^+ UVD limb emission as discussed in Section 4.4. The energy range of the SEP electrons was 100 eV - 100 keV and that of the SEP protons was 46 keV - 6.8 MeV. The atmospheric density profiles and the incident SEP fluxes used in the simulation are shown in Figure 5.5.

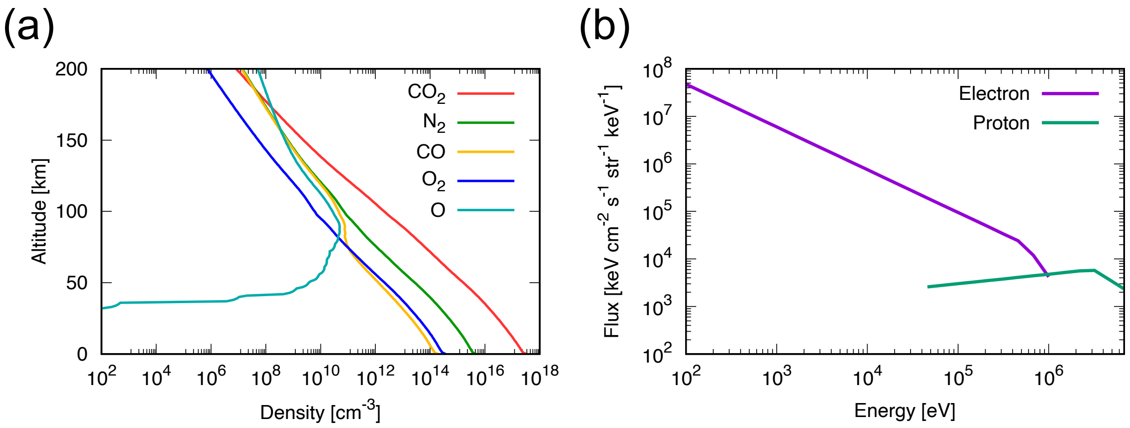

Figure 5.5 (a) Atmospheric density profiles and (b) SEP electron and proton fluxes during the September 2017 SEP event used in the simulation. The SEP electron and proton fluxes were taken from Figure 4.2b in Chapter 4 and multiplied by a factor of 6 to match the observed CO_2^+ UVD limb intensity profile.

The height-integrated column emission brightness distribution of the CO_2^+ UVD emission simulated by PTRIP is shown in Figure 5.6. Electron-induced emissions are strongly localized within the cusp regions of the crustal magnetic fields with a patchy morphology, while proton-induced emissions are not localized with a diffuse morphology. The diffuse aurora is the sum of the proton-induced diffuse emission and the electron-induced patchy emission (Figure 5.7c). The mean and maximum brightness intensity of the emissions at the cusp and closed field regions are summarized in Table 5.1. The closed field region is defined as the region where SEP electrons cannot penetrate below 200 km altitude, as illustrated in Figure 5.9. The mean brightness intensities of the electron- and proton-induced CO_2^+ UVD emissions at the cusp regions are 0.37 and 0.42 kR, respectively, and the maximum brightness intensities are 5.66 and 0.88 kR, respectively. The mean and maximum brightness intensities of the proton-induced CO_2^+ UVD emission at the closed field regions are 0.41 and 0.79 kR, respectively.

The height-integrated column emission brightness distribution of the oxygen 557.7 nm emission simulated by PTRIP is shown in Figure 5.7. The morphology of the emissions is similar to the CO_2^+ UVD emission; electron-induced emissions are patchy at the cusp regions and proton-induced emissions are diffuse. The mean brightness intensities of the electron- and proton-induced oxygen 557.7 nm emissions at the cusp regions are 0.15 and 0.10 kR, respectively, and the maximum brightness intensities are 2.21 and 0.21 kR, respectively. The mean and maximum brightness intensities of the proton-induced oxygen 557.7 nm emission at the closed field regions are 0.10 and 0.19 kR, which were comparable to the cusp regions. Our result that the oxygen 557.7 nm emission intensity is comparable to the CO_2^+ UVD emission intensity is consistent with a one-dimensional simulation of the Martian diffuse auroral emission by Gérard et al. (2017).

The height-integrated column emission brightness distribution of the oxygen 630.0 nm emission simulated by PTRIP is shown in Figure 5.8. The electron-induced oxygen 630.0 nm emission is patchy at the cusp regions like the other emission lines, while the proton-induced oxygen 630.0 nm emission is diffuse with a brightness significantly lower. The morphology of the oxygen 630.0 nm emission is patchy in the cusp regions being largely dominated by the emissions due to the precipitation of SEP electrons. The mean brightness intensities of the electron- and proton-induced oxygen 630.0 nm emissions at the cusp regions are 2.8 and 1.7×10^{-3} R, respectively, and the maximum brightness intensities are 63 and 2.4×10^{-3} R, respectively. The mean and maximum brightness intensities of the proton-induced oxygen 630.0 nm emission at the closed field regions are 1.4×10^{-3} and 2.2×10^{-3} R, which are comparable to the cusp regions.

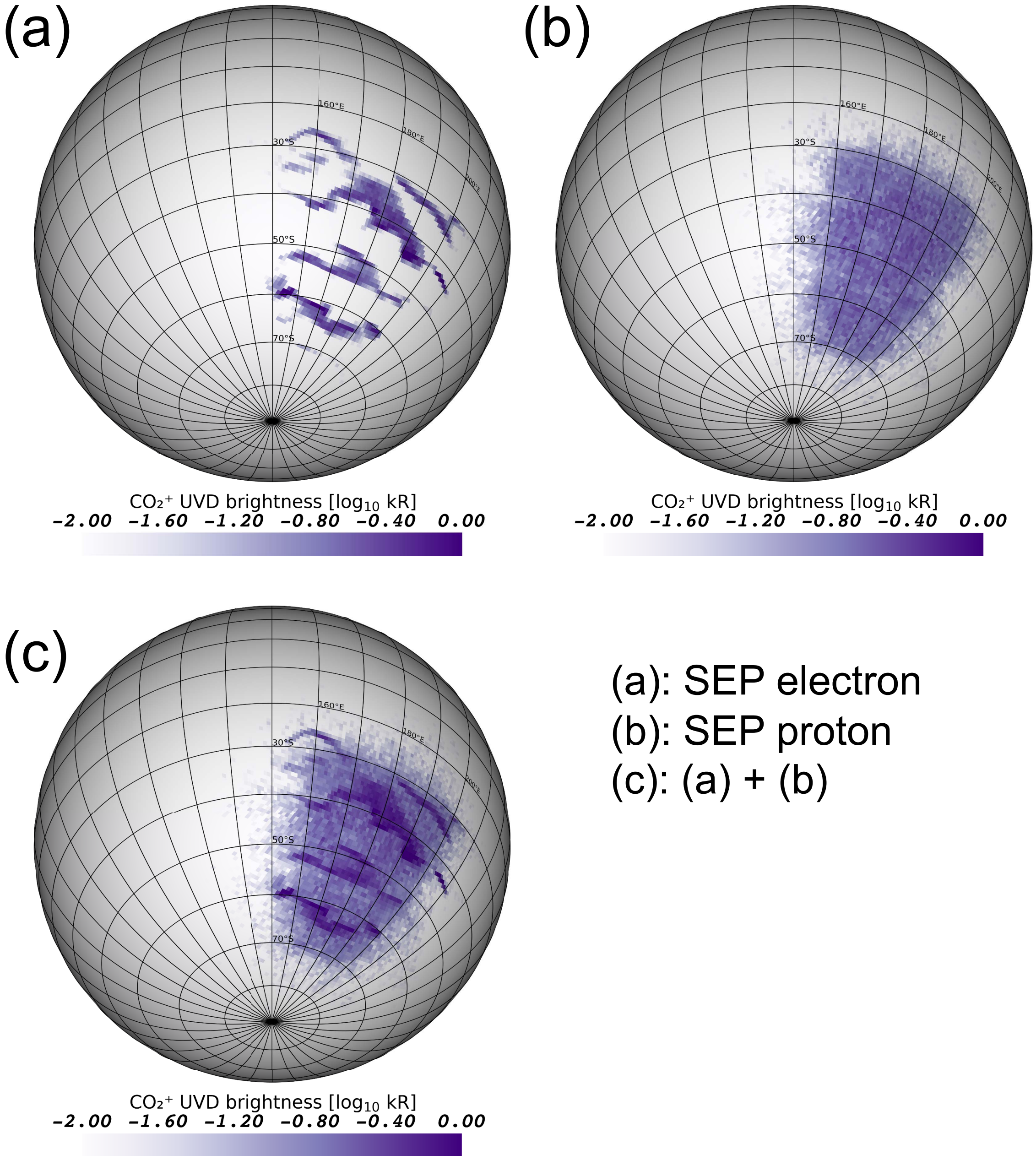

Figure 5.6 Simulated distribution of column intensity of CO_2^+ UVD emission brightness. SEPs are injected into a region of the strong crustal magnetic field region in the southern hemisphere (30°S-70°S, 160°E-200°E). (a) Emission due to precipitation of the SEP electrons with energy ranging 100 eV-100keV. (b) Emission due to precipitation of the SEP protons with energy ranging 46 keV-4.6 MeV. (c) Sum of (a) and (b).

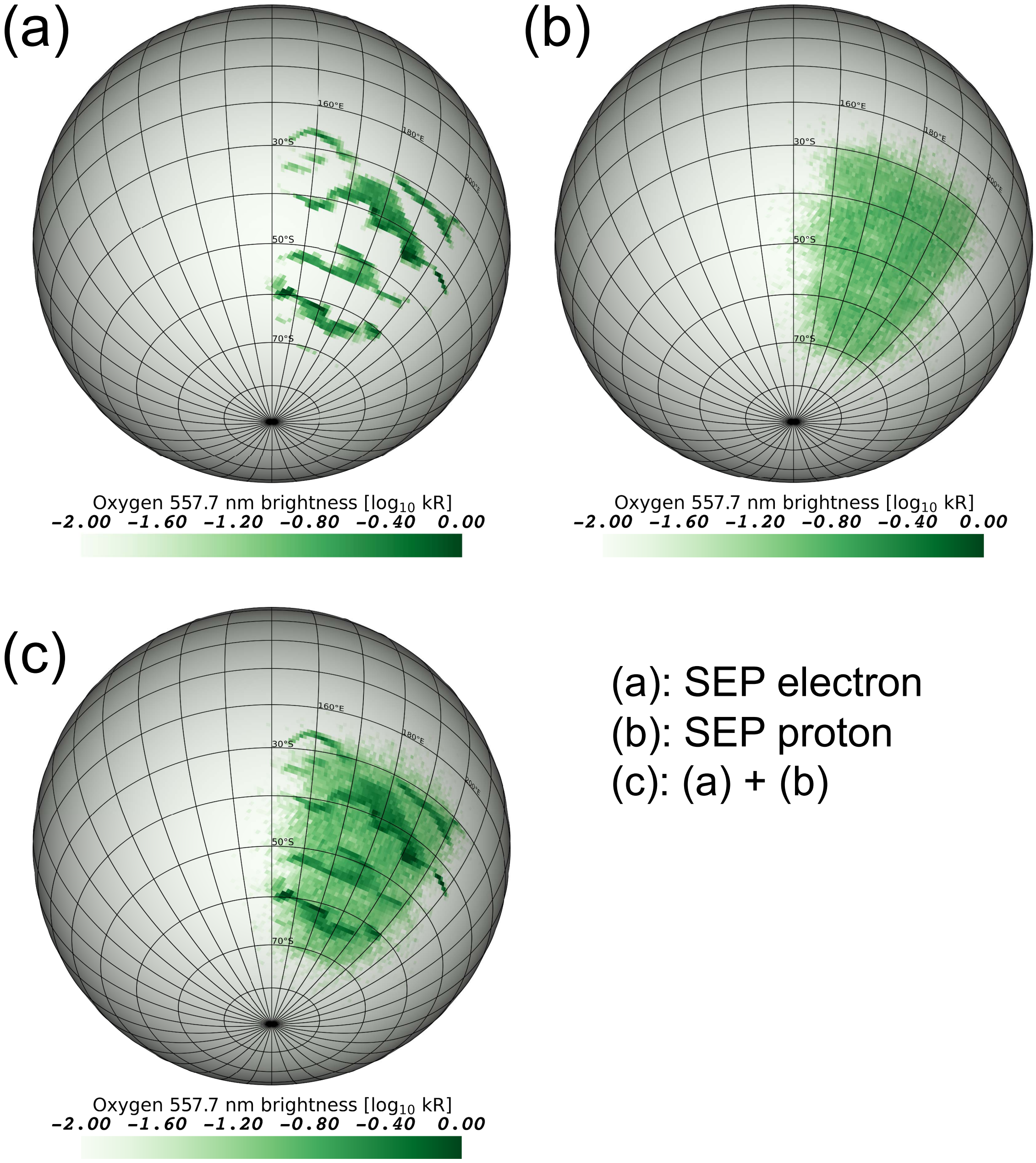

Figure 5.7 Same as Figure 5.6, but for oxygen atom 557.7 nm emission.

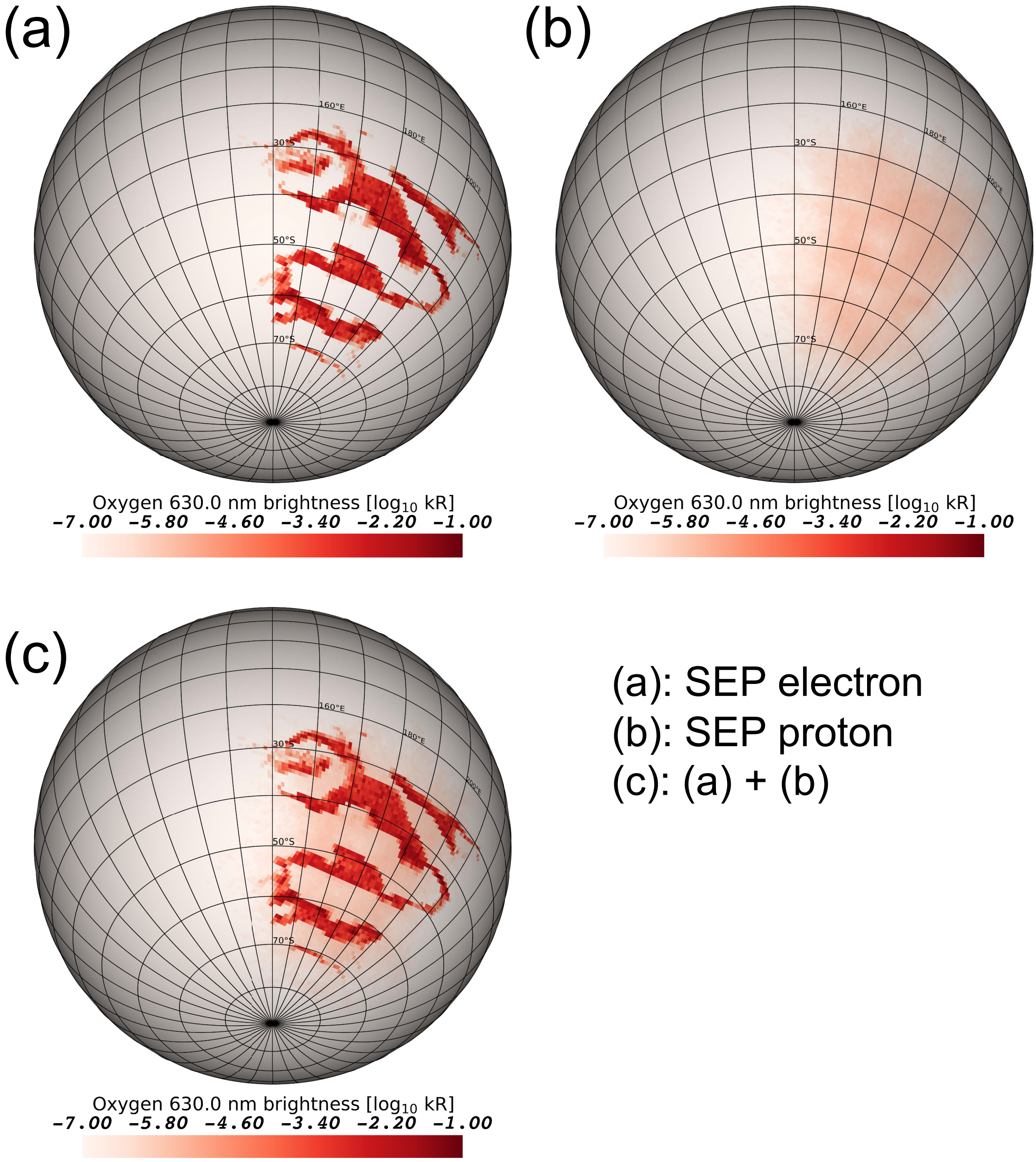

Figure 5.8 Same as Figure 5.6, but for oxygen atom 630.0 nm emission.

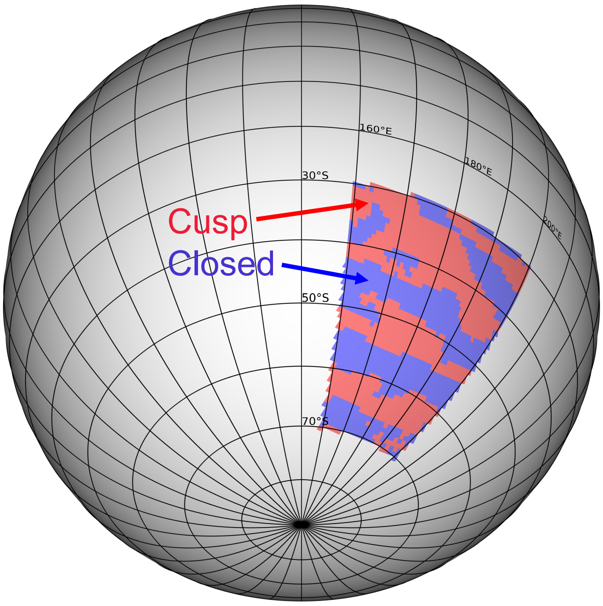

Figure 5.9 The red and blue areas represent the cusp and closed field regions, respectively. The closed field region is defined as the region where SEP electrons cannot penetrate below 200 km altitude.

Table 5.1 Mean and maximum brightness intensity (in the unit of kR) of the CO_2^+ UVD, oxygen 557.7 nm, and 630.0 nm emissions at the cusp and closed field regions.

Brightness [kR]	CO_2^+ UVD		O 557.7 nm		O 630.0 nm	
	Electron	Proton	Electron	Proton	Electron	Proton
Cusp (mean)	0.37	0.42	0.15	0.10	0.0028	1.7×10^{-6}
Cusp (max)	5.66	0.88	2.21	0.21	0.063	2.4×10^{-6}
Closed (mean)	–	0.41	–	0.10	–	1.4×10^{-6}
Closed (max)	–	0.79	–	0.19	–	2.2×10^{-6}

The mean vertical profiles of the CO_2^+ UVD, oxygen 557.7 nm, and 630.0 nm emissions in the cusp and closed field regions are shown in Figure 5.10. Since the closed field region is defined as the region where SEP electrons cannot penetrate below 200 km altitude, the electron-induced emissions in the closed field region are not indicated in Figure 5.10. The total emission profiles in the closed field regions are identical to the proton-induced emissions at the same regions. Proton-induced emission profiles for all emission lines are almost the same between the cusp and closed field regions. The vertical profile of the summed volume emission rate is broadly distributed in altitude in the cusp regions and was narrowly distributed in altitude in the closed field lines regions. The difference in the vertical profiles of the total volume emission rate between the cusp and closed field regions is attributable only to the presence or absence of the contribution from the SEP electrons. The shape of the vertical profile of the volume emission rate of CO_2^+ UVD in the cusp regions is almost identical to the one-dimensional simulation of the $CO_2^+(B^2\Sigma_u^+)$ production in the absence of magnetic fields during the same event shown in Figure 4.6b. The shape of the vertical volume emission profiles of the oxygen 557.7 nm emission is almost the same as the CO_2^+ UVD profiles. The volume emission rate profiles of the oxygen 630.0 nm are significantly reduced below 180 km altitude. The difference in the shape of the volume emission rate profiles of oxygen atom emissions is due to the different effects of the quenching. The vertical profiles of the emission efficiency taking into account the quenching effect are shown in Figure 5.11. The oxygen 557.7 nm emission has a radiative lifetime of about 0.77 sec (Itikawa and Ichimura, 1990) and the emission efficiency falls significantly below 80 km altitude, while the emission efficiency of the oxygen 630.0 nm falls rapidly below 200 km altitude due to the long radiative lifetime of about 130 sec (Itikawa and Ichimura, 1990). As a comparison, the CO_2^+ UVD emission has a much shorter radiative lifetime of 1.26×10^{-7} sec (Herran et al., 1983) and quenching does not play a role. The oxygen 557.7 nm emission is partially quenched below 80 km altitude but not completely, while the oxygen 630.0 nm emission is almost completely quenched below 150 km altitude. Due to the efficient quenching of the oxygen 630.0 nm emission and the difference in the altitude penetration between the SEP electrons and protons, only proton-induced emission is completely quenched whereas electron-induced emission by low-energy electron precipitation is still a significant contribution as seen in Figure 4.5b. As mentioned earlier, electron-induced emission above 150 km altitude should be affected by the uncertainty due to the treatment of secondary electrons neglecting the effect of the magnetic field on their transport, especially for the oxygen 630.0 nm emission.

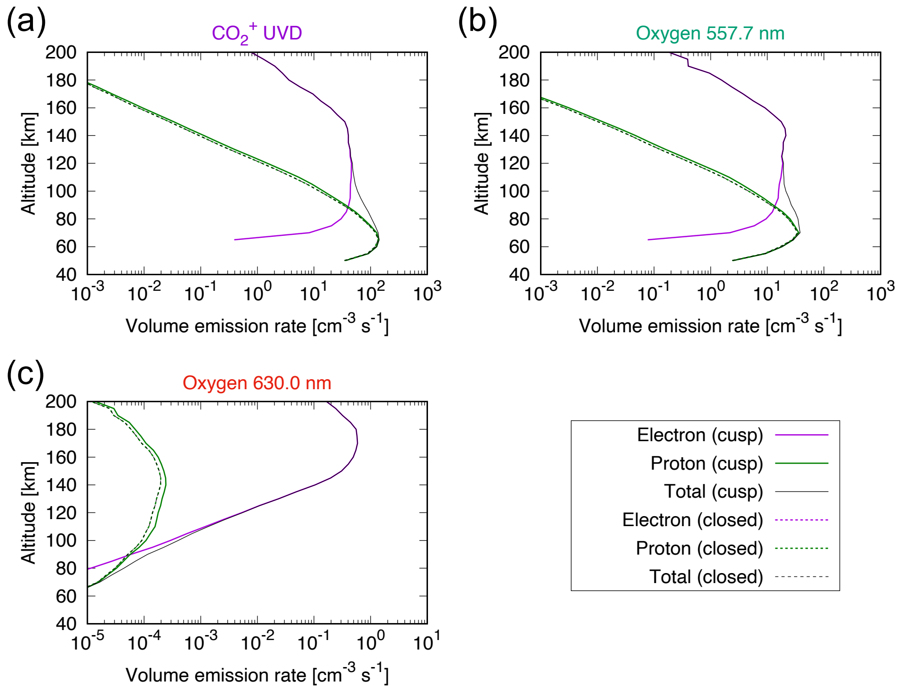

Figure 5.10 (a-c) Mean volume emission rate profiles of CO_2^+ UVD, oxygen 557.7 nm, and 630.0 nm, respectively. The purple and green lines are electron- and proton-induced emissions, respectively, and the black lines are the sum of the electron- and proton-induced emissions. The solid and dashed curves represent the profiles averaged in the cusp and closed field regions, respectively. No electron-induced emission in the closed field regions in all the figures by definition of the closed region.

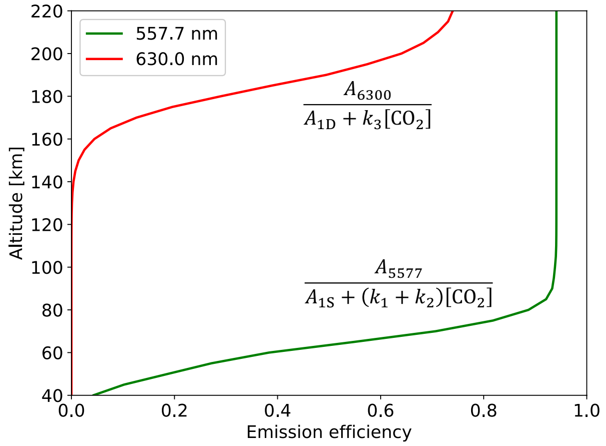

Figure 5.11 Emission efficiency for oxygen emissions at 557.7 nm (green curve) from O(^{1}S) and 630.0 nm (red curve) from O(^{1}D).

5.3 Discussion

The difference in the morphology of the auroral emissions results from the difference in the gyro radius of the SEP electrons and protons. Trajectories of 100 keV electrons and 4.6 MeV protons are shown in Figure 5.12. Those two energies were selected in Figure 5.12 because ionization rates peak at around those two energies during the September 2017 SEP event. As seen in Figure 5.12, the motion of 100 keV electrons is strongly affected by the crustal magnetic fields so they precipitate only into the cusp regions, while the motion of 4.6 MeV protons is not affected by the crustal magnetic fields and their precipitation into the atmosphere is not localized. Assuming a magnetic field strength of 100 nT, the gyro radius of a 100 keV electron is 10 km, smaller than the structure of the crustal magnetic field configuration, while that of a 4.6 MeV proton is 3,000 km, comparable to the radius of Mars. The green and white trajectories represent particles that reach altitudes below 100 km and those that travel only above 100 km, respectively. Here the threshold altitude of 100 km is chosen because the typical lowest altitudes reached by a 100 keV electron and a 4.6 MeV proton are below 100 km without magnetic fields (Figure 4.4). About 80% of the 100 keV electrons do not reach altitudes below 100 km due to the magnetic mirror effect, while only about 30% of the 4.6 MeV protons do not reach altitudes below 100 km because the large incident angle and their large gyro radii allow them to exit the spherical atmosphere without exciting atmospheric molecules, as discussed in Chapter 4. Even though most SEP electrons are backscattered to space due to the magnetic mirror effect, electron-induced emissions are bright in the cusp regions and the vertical profiles in the cusp regions are almost the same as the simulation without magnetic fields in Chapter 4 (Figure 4.6b). The origin of the electron-induced emission brightness in the cusp regions is that the magnetic mirror effect is compensated by the focusing of the incident particles in the cusp regions. Since we injected particles isotropically into the strong crustal magnetic field region from 450 km altitude, the focusing of the particles in the cusp regions compensates for the backscattering of the particles due to the magnetic mirror effect. This is the same phenomenon for the SEP proton flux conservation on Earth between the polar cap cusp region and the Lagrangian point L_1 (Bornebusch et al., 2010). It should be noted that the fraction of particles that precipitate into the cusp regions strongly depends on the initial pitch angle distribution of the SEP electrons. It should also be noted that the emission intensity strongly depends on the incident SEP electron flux at the initial altitude of 450 km. Jolitz et al. (2021) pointed out that only 3% of the SEP electrons reach the exobase of Mars across the bow shock of the induced magnetosphere. Our simulation assumes a uniform SEP electron flux over the strong crustal magnetic field region, which is clearly an overestimate of the flux reaching such altitude. Further improvement of our simulation will take into account the electromagnetic environment of the induced magnetosphere.

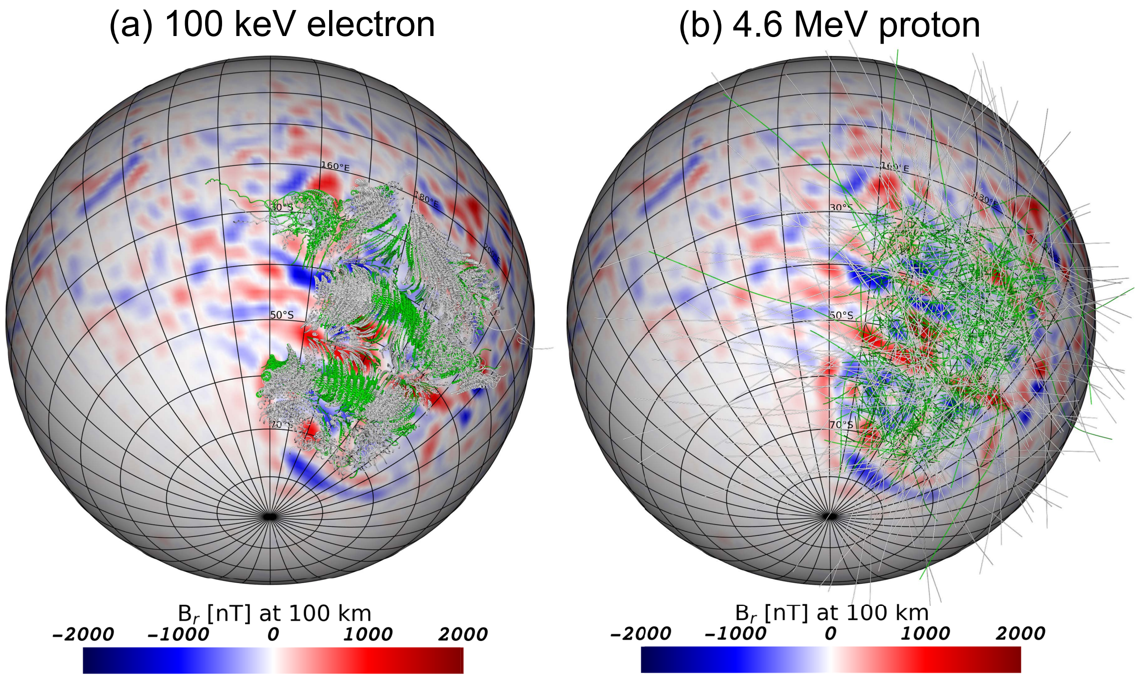

Figure 5.12 (a, b) Trajectories of 100 keV electrons and 4.6 MeV protons, respectively. Trajectories of 1,000 particles are shown in each panel. The color map displays the vertical component of the crustal magnetic field strength at 100 km altitude. The green and white trajectories represent particles that reached altitudes below 100 km or those that did not reach altitudes below 100 km, respectively.

During the September 2017 SEP event, MAVEN/IUVS reported diffuse CO Cameron band emission from the nightside of Mars during orbit number 5731 without apparent fine structure (see Figure 1.4 in Chapter 1). But, during orbit number 5738, MAVEN/IUVS observed patchy discrete-like emissions in the cusp regions (Schneider et al., 2018). Our simulation suggests both diffuse and patchy morphology at the same time. It should be noted that there have been only 2 global images of the Martian diffuse aurora published so far, and further analyses of the global image of the Martian diffuse aurora during SEP events should be needed to confirm our hypothesis.

In Chapters 4 and 5, we have shown that SEP protons with energies above MeV are key drivers to generate the low peak altitude of the limb emission and the globally diffuse morphology of the Martian diffuse auroral emissions. Why the Lyman-α emission as evidence of the proton precipitation into the Martian atmosphere, has not been observed during SEP events (Schneider et al., 2018) remains to be explained. The first possible explanation is the absorption by the Martian atmosphere. Previous observation and modeling of the so-called ‘proton aurora’ on Mars, not related to SEP protons but by the penetration of solar wind protons via charge exchange, showed that the Lyman-α emission below 130 km altitude can be absorbed by the Martian atmosphere (Hughes et al., 2019; Gérard et al., 2019). Since our simulation showed that the SEP protons have an impact on the Martian atmosphere only below 100 km due to the hard-spectral slope of the energy spectrum of SEP proton flux, the Lyman-α emission could have been partially or completely absorbed by the Martian atmosphere. A second possible explanation is the low efficiency of the charge exchange reaction for MeV protons. Proton-induced Lyman-α emission is produced when protons experience charge exchange reactions with atmospheric molecules, or hydrogen atoms experience inelastic collisions with atmospheric molecules. Since the charge exchange cross section due to proton impact is much smaller than the ionization cross section due to proton impact with energies above 100 keV, the probability of a charge exchange reaction for MeV protons is extremely small, which could result in a dim Lyman-α emission due to the precipitation of MeV protons into the Martian atmosphere.

5.4 Chapter summary

We performed a three-dimensional simulation with PTRIP to investigate the effects of the crustal magnetic fields in the southern hemisphere of Mars on the Martian diffuse auroral emission. Our results show different morphology for the electron-induced emission and proton-induced emission in the strong crustal field region due to the difference in their gyro radii. The electron-induced CO_2^+ UVD emission is patchy and bright in the cusp regions, while the proton-induced CO_2^+ UVD emission is diffuse without any fine structures. We also simulated oxygen 557.7 nm and 630.0 nm emission lines and found that the oxygen 557.7 nm emission is similar in shape and intensity to the CO_2^+ UVD emission, whereas the oxygen 630.0 nm emission is restricted to the cusp regions, SEP electron precipitation being its main source because proton-induced emission is completely quenched at low altitudes.

Chapter 6

Numerical prediction of changes in atmospheric chemical compositions during solar energetic particle events on Mars

Solar energetic particles (SEPs) ionize, dissociate, and excite the atmospheric molecules when they precipitate into a planetary atmosphere, leading to changes in ion and neutral chemical compositions. The effects of SEPs on the chemical composition in the terrestrial atmosphere have been intensively studied for decades. For instance, the SEP events of late October and early November 2003, known as the Halloween event, induced a depletion of the ozone density by up to 40% and an enhancement of the odd hydrogen (HOx) and the odd nitrogen (NOx) in the polar mesosphere and stratosphere (e.g., Seppälä et al., 2004; Jackman et al., 2005; Randall et al., 2005). Precipitating energetic particles dissociate nitrogen molecules producing N and $N(^2D)$ in the atmosphere, the latter of which reacts with O_2 becoming NO (Crutzen et al., 1975; Rusch et al., 1981). Precipitating energetic particles ionize O_2 producing O_2^+ in the atmosphere, which reacts with ambient water vapor to produce water cluster ions, and thus H and OH via recombination of the cluster ions with electrons (Solomon et al., 1981). The produced HOx and NOx catalytically destroy ozone in the polar mesosphere during SEP events. Such an effect was confirmed by the observed anti-correlation between HOx/NOx and ozone concentrations during SEP events (e.g., Crutzen et al., 1975; Seppälä et al., 2004; Jackman et al., 2005; Verkhoglyadova et al., 2015).

The impacts of SEPs on the Martian atmosphere are not local as in the Earth's atmosphere but global due to the absence of a strong global magnetic field on Mars. The imaging ultraviolet spectrograph (IUVS) instrument on board the Mars Atmosphere and Volatile EvolutioN (MAVEN) spacecraft has observed ultraviolet diffuse auroral emissions spanned across the whole night side of Mars during SEP events (Schneider et al., 2015, 2018). Recent model studies revealed that the diffuse aurora is caused by the precipitation of SEP electrons (Schneider et al., 2015; Gérard et al., 2017; Haider and Masoom, 2019) and SEP protons (see Chapter 4). In Chapter 4, we have succeeded in reproducing the observed low altitude peak of the diffuse auroral emission profiles by taking into account the contribution of SEP protons, indicating that SEP protons have a significant impact on the lower atmosphere of Mars.

In contrast to Earth, there have been no studies of the effects of SEPs on the neutral chemical composition of the Martian present-day atmosphere. In this chapter, we used a Monte Carlo model, Particle TRansport In Planetary atmospheres (PTRIP) described in Chapter 2, to calculate the vertical profiles of the ionization and dissociation rates of atmospheric molecules during a SEP event. We also used a one-dimensional photochemical model, Photochemical and RadiatiOn Transport model for Extensive USe (PROTEUS) described in Chapter 3, to investigate the changes in atmospheric chemical composition during the SEP event. Our target species are ozone, HOx, and NOx, since the high-resolution spectroscopy Nadir and Occultation for MArs Discovery (NOMAD) instrument on board the Trace Gas Orbiter (TGO) spacecraft has a high sensitivity to these three species. We also describe formaldehyde (H_2CO) and nitrous oxide (N_2O), which are of astrobiological interest because they are important for the prebiotic synthesis of amino acid and nucleic acid (e.g., Airapetian et al., 2016; Lingam et al., 2018).

6.1 Model descriptions

PTRIP is a Monte Carlo model that solves the transport of energetic electrons, protons, and hydrogen atoms in planetary atmospheres and calculates the ionization, dissociation, and excitation rates of atmospheric molecules. PTRIP solves the equation of motion for each incident particle and takes into account all possible collisions between each incident particle and the atmospheric molecules. Collision type, energy loss, scattering angle, and energy of the secondary electrons are randomly determined at each timestep using cross sections, scattering angle distribution, and secondary electron energy spectrum. In this chapter, only SEP protons are injected into the Martian atmosphere because SEP protons have been shown to be the dominant ionization source at low altitudes as described in Chapters 4 and 5. One thousand particles were injected for each incident energy with incident angles isotropically distributed over the downward hemisphere. Electric fields and magnetic fields were ignored because the motion of protons with energy above MeV is not affected by the electromagnetic environment of Mars.

The atmospheric density profiles used in this chapter are shown in Figure 6.1. The vertical profile of the neutral temperature was taken from Chaffin et al. (2017) standard case with an exobase temperature of 240 K and a surface temperature of 210 K. The number density of CO_2 on the surface corresponds to a surface pressure of 6.7 mbar. The volume mixing ratio of N_2 at the surface was set to 1.9 % (Mahaffy et al., 2013). The vertical profiles of the CO_2 and N_2 densities were calculated by considering vertical eddy diffusion and binary diffusion using PROTEUS with boundary conditions on the surface number densities. As for the vertical profile of water vapor, the relative humidity below the tropopause was fixed at 22% and the same volume mixing ratio of water vapor was used above the tropopause as did in Koyama et al. (2021).

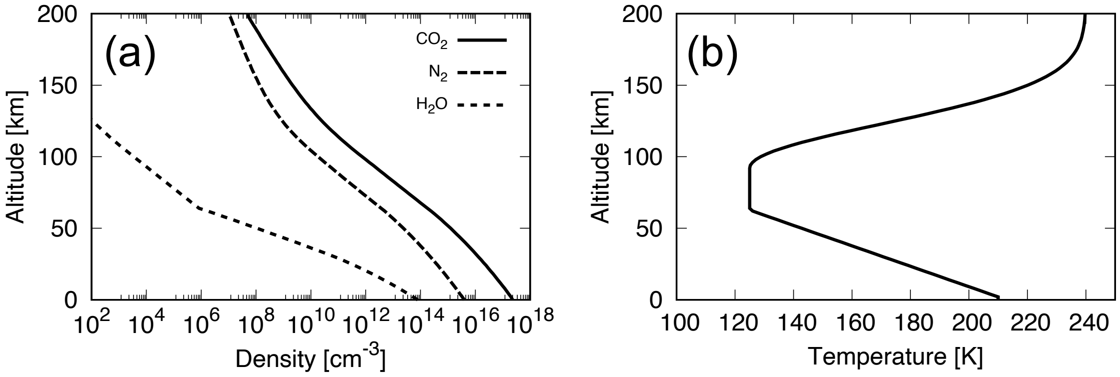

Figure 6.1 Vertical profiles of (a) number densities of CO_2, N_2, and H_2O, and (b) neutral temperature used in the simulation.

In order to investigate the impact of SEP protons on atmospheric chemistry especially at low altitudes, protons with energy from 1 MeV to 220 MeV were taken into account. The incident proton flux at the top of the atmosphere was taken from the SEP event that occurred on 28 October 2003 at Earth, for which an ozone depletion was observed in the Earth's polar mesosphere, as a representative of an extremely large SEP event (hereafter called as a Halloween-class SEP event). In terms of proton flux intensity, a Halloween-class SEP event occurs once every 10 years on average (Birch and Bromage, 2022; Kataoka, 2020). The energy spectrum of the SEP proton flux dJ/dE is known to have a double power-law shape (e.g., Mewaldt et al., 2005; Desai et al., 2016) with fitting equations by Band et al. (1993) expressed as:

$$\frac{dJ}{dE} = CE^{-\gamma_a}\exp\left(-\frac{E}{E_B}\right) \quad \text{for } E \le (\gamma_b - \gamma_a)E_B \quad , \qquad (6.1)$$

$$\frac{dJ}{dE} = CE^{-\gamma_b}[(\gamma_b - \gamma_a)E_B]^{\gamma_b - \gamma_a} \exp(\gamma_b - \gamma_a) \quad \text{for } E \ge (\gamma_b - \gamma_a)E_B \quad , \qquad (6.2)$$

where C is the normalization constant same on the two energy ranges, E is the proton energy in MeV, γ_a and γ_b are the power-law slope at low and high energy, respectively, E_B is the break energy in MeV at which the power-law slope changes from γ_a to γ_b. The parameters C, E_B, γ_a and γ_b (hereafter called as Band parameters) for the SEP event on 28 October 2003 are E_B=27.4 MeV, γ_a=1.04 and γ_b=4.57, and C=5,050 cm^{-2} s^{-1} sr^{-1} MeV^{-1} obtained by dividing the time-integrated flux by the duration of the event 33 hours (Mewaldt et al., 2005) and was divided by a factor of 1.5^2 to scale to the Mars orbit at 1.5 AU. It should be noted that the acceleration of protons by the shock waves propagating from the Earth's orbit to the Mars' orbit is ignored for simplicity. The incident proton flux used in the simulation for this event is shown in Figure 6.2.

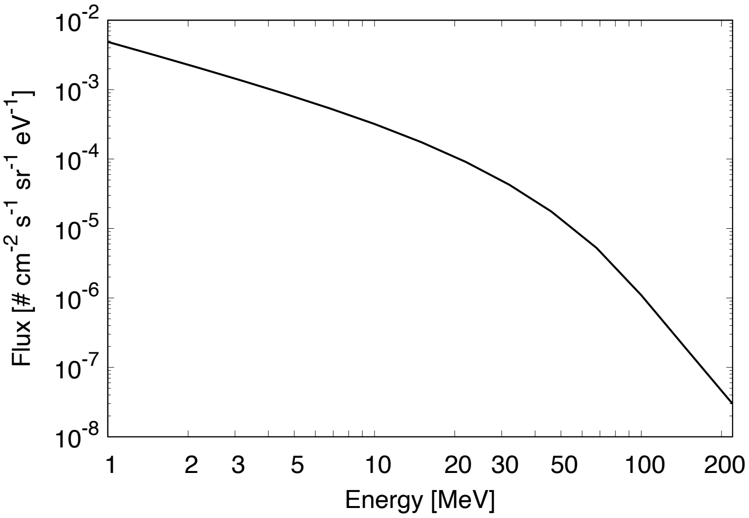

Figure 6.2 Energy spectrum of the SEP proton flux during the 28 October 2003 SEP event scaled to the Mars' position at 1.5 AU.

As the incident proton energy increases especially above 10 MeV, the number of secondary electrons produced in the atmosphere via ionizing collisions becomes massive. To reduce the computational cost when taking into account the contribution of the secondary electrons, we have developed a method to calculate the normalized secondary electron flux in energy-altitude (E-z) grids, which is then multiplied by the number of secondary electrons produced within each E-z grid cell. This reduced flux method is different from the reduced count method described in Chapter 5. As seen in Figure 6.3, this reduced flux method also precisely obtains the same ionization profiles with much less computational cost than the simulation tracing all the secondary electrons.

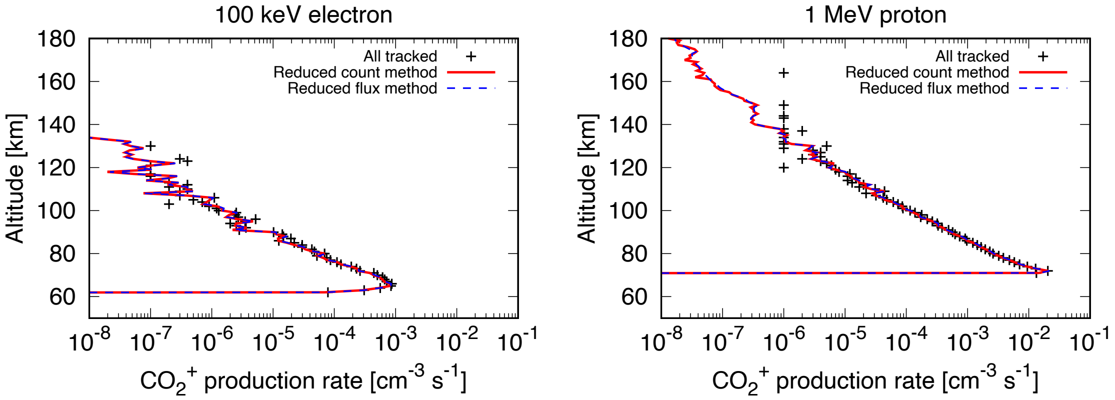

Figure 6.3 Comparison of the production rate of CO_2^+ only due to secondary electrons between the case that all the secondary electrons produced were tracked and the reduced count method. The black points represent the production rate of CO_2^+ when all the secondary electrons were tracked after their production, the red curves represent the production rate estimated by the reduced count method described in Chapter 5, and the blue dashed curves represent the production rate estimated by the reduced flux method. (a) One hundred of incident 100 keV electrons and (b) ten incident 1 MeV protons were injected with incident angles of 0 degree. Electric and magnetic fields were ignored in this simulation.

The accuracy of the proton-impact ionization and elastic cross sections determine the accuracy of the simulation. All the collisional cross sections for protons, hydrogen atoms, and secondary electrons in this chapter are the same as in Chapter 2. The analytic equation of the proton-impact ionization cross sections of CO_2 and N_2 fitted by Rudd et al. (1983) based on the experimental data within the energy range from 5 keV to 4 MeV was applied up to 220 MeV, and the theoretical screened Rutherford elastic cross section described in Section 2.2 was also applied up to 220 MeV. Figure 6.4a shows the production rate of CO_2^+ at each incident proton energy using the incident proton flux displayed in Figure 6.2. PTRIP predicted that protons with energy below 100 MeV lose all their energy before reaching the surface, whereas protons with energy larger than 150 MeV can reach the surface. Such a result is consistent with previous simulations of SEP proton penetration in the Martian atmosphere (Guo et al., 2018) performed with the GEANT4-based Monte Carlo model PLANETCOSMICS (Desorgher et al. 2006). Comparison with PLANETCOSMICS showed that the cross sections chosen in this chapter are valid at high energy so that PTRIP is able to solve the transport of protons up to 220 MeV in the Martian atmosphere. The calculated vertical profiles of the production rates of CO_2^+ and N_2^+ are shown in Figure 6.4b.

It is noted that the bumpy structure seen in the production rate profiles of CO_2^+ and N_2^+ stems from the selection of discrete incident energy bins. Contrary to the terrestrial atmosphere, most of the proton energy leads to the ionization of the Martian CO_2 molecules and the production rate of N_2^+ is two orders of magnitudes smaller than that of CO_2^+. The production rates of atomic nitrogen N and N(^{2}D), which are important precursors for NOx chemistry, were estimated by multiplying the production rate of N_2^+ with the following relative abundance, N_2^+:N^+:N:N(^{2}D) = 1:0.22:0.73:0.95 based on the 200 eV electron impact cross sections which were used as a proxy for the production by high energy particle in Krasnopolsky (2009).

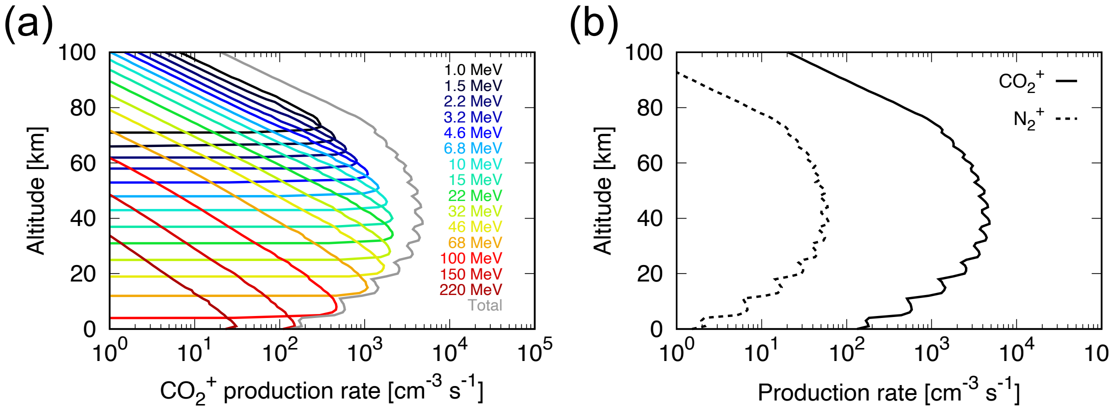

Figure 6.4 (a) Production rate of CO_2^+ calculated by PTRIP at each incident energy using the SEP proton flux of a Halloween-class SEP event. (b) Vertical profiles of the CO_2^+ and N_2^+ production rates calculated by PTRIP.

PROTEUS is a one-dimensional photochemical model that solves a system of continuity equations for chemical production, loss, and vertical diffusion (Equations (3.1) and (3.2) in Chapter 3). The temperature profiles of the electrons and all of the other species were assumed to be the same as the neutral temperature. The vertical profiles of the binary diffusion coefficient were taken from Hunten et al. (1973) and the vertical profile of the eddy diffusion was taken from Krasnopolsky (1993). The thermal diffusion coefficient for H and H_2 were taken from Hunten et al. (1973) and those for other species were set to zero.

We have implemented 490 chemical reactions for 34 neutral and 48 charged species into PROTEUS; the ionization rate by galactic cosmic ray was taken from Molina-Cuberos et al. (2001), the C-, H-, and O-bearing neutral chemistry was taken from Chaffin et al. (2017), chemical reactions related to formaldehyde were taken from Pinto et al. (1980), the N-bearing neutral chemistry was taken from Nair et al. (1994), the ionospheric chemistry was taken from

Fox and Sung (2001), Mukundan et al. (2020), and Anicich (1993), the CO_2-bearing cluster ion chemistry was taken from Molina-Cuberos et al. (2001), and the water cluster ion chemistry was taken from Verronen et al. (2016) and Pavlov (2014). The reaction rate coefficient for the reaction $N(^4S) + CO_2 \rightarrow NO + CO$ is still unknown, and the reaction speed is known to be very slow since this reaction does not conserve spin angular momentum (Rawlins and Kaufman, 1976). Fox and Sung (2001) used a rate coefficient for this reaction equal to 1.7×10^{-16} cm^3 s^{-1} as a standard model in the Venusian atmosphere, which was estimated as an upper limit by Brown and Winkler (1970) and Herron and Huie (1968). There are several experimental studies for the upper limit of this reaction rate, however, they are controversial. Avramenko and Krasnen'kov (1967) obtained a temperature-dependent rate coefficient for this reaction as $3.2\times10^{-13}\exp(-1711/T)$ cm^3 s^{-1} in the temperature range 291-523 K, which gives a rate coefficient of 1.0×10^{-15} cm^3 s^{-1} at a temperature of 300 K. Rawlins and Kaufman (1976) estimated an upper limit of 1.0×10^{-19} cm^3 s^{-1} at temperature 300 K. Fernandez et al. (1998) tried to measure the rate coefficient of this reaction, however, they did not observe any reactions and they estimated an upper limit of 1.1×10^{-17} cm^3 s^{-1} at 285 K. In this chapter, the rate coefficient for this reaction was set to 1.0×10^{-19} cm^3 s^{-1} estimated as upper limit by Rawlins and Kaufman (1976). The chemical reactions used in this chapter are listed in Table E.1 in Appendix E. The upper boundary of PROTEUS was set to 200 km altitude and the lower boundary was the surface. At the upper boundary, the escape fluxes of H and H_2 were calculated as Jeans escape and that of O was fixed at 1.2×10^8 cm^{-2} s^{-1} (Chaffin et al., 2017).

The solar extreme ultraviolet (EUV) flux was calculated by the EUVAC model (Richards et al., 1994) with an F10.7 value of 140 for a moderate solar condition. The solar flux between 0.5 and 1000 nm used to calculate the dissociation rates of atmospheric molecules was taken from Woods et al. (2009). The model takes into account the radiative transfer and the absorption by atmospheric species. Detailed information about the absorption and dissociation cross sections is given in Table C.1 in Appendix C. All the simulations in this study were performed at the subsolar point.

In this chapter, we first ran the model for only neutral species without SEP inputs in order to obtain a converged solution for the neutral species. Since the chemical and transport time scales of ions are around several hours (e.g., Cravens et al., 2017), we then ran the model for both neutral and ionized species without SEP inputs for 10 simulated days in order to reach a quasi-steady state density profile of ions. The quasi-steady state density profiles for all the species were used as initial profiles to investigate the SEP effects. The production rates of CO_2^+, N_2^+, N^+, N, and $N(^2D)$ were calculated by PTRIP and used as inputs into PROTEUS. We ran the model with SEP inputs for 1 simulated day (24 hours) to investigate the change in density profiles during the SEP event. The SEP event was assumed to last 24 hours and the proton flux intensity and its spectral shape were assumed to be constant during that duration. After that duration, we ran PROTEUS for 10 simulated days (240 hours) assuming no SEP inputs in order to examine the recovery phase.

6.2 Changes in the ion density profiles

The ion density profiles in the quasi-steady state calculated by PROTEUS without SEP inputs are shown in Figure 6.5a. There are two ionospheric peaks, one formed by the irradiation of solar EUV flux above 75 km altitude and a second ionospheric peak formed by galactic cosmic rays below 75 km altitude. The dominant ion is O_2^+ above 75 km while water cluster ions dominate below 75 km. Below 50 km altitude, the densities of negative ions become larger than the electron density due to the attachment of electrons to atmospheric molecules and subsequent negative ion chemistry. The simulated ion density profiles in the quasi-steady state are in good agreement with previous numerical models of the lower ionosphere by Molina-Cuberos et al. (2001) and Haider et al. (2009).

Figure 6.5b displays the calculated ion density profiles 1 day after the onset of the SEP event. Ion and electron densities are significantly increased below 100 km altitude, while there is no change above 100 km. It should be noted that the contribution of the SEP electrons was ignored in this study, which is the dominant ionization source at higher altitudes during SEP events (see Figure 4.6 in Chapter 4). Below 100 km altitude, O_2^+ is the dominant ion in the altitude range from 50 to 100 km and water cluster ions are the dominant ions below 50 km. The electron density below 75 km is enhanced by 2-3 orders of magnitudes and it reaches 10^5 cm^{-3} in the altitude range from 50 to 75 km. Such an increase in electron density at low altitudes during SEP events could lead to the absorption of radio emissions from spacecraft and cause the disappearance of surface echo of radar instruments (e.g., Morgan et al., 2005; Espley et al., 2007; Sheel et al., 2012; Harada et al., 2018; Sanchez-Cano et al., 2019; Lester et al., 2022). Our results showed that the contribution of SEP protons to the ion profiles is greater than that of galactic cosmic rays during a large SEP event, which is consistent with the previous model's conclusion regarding the SEP effects on the ionosphere of Mars (Sheel et al., 2012).

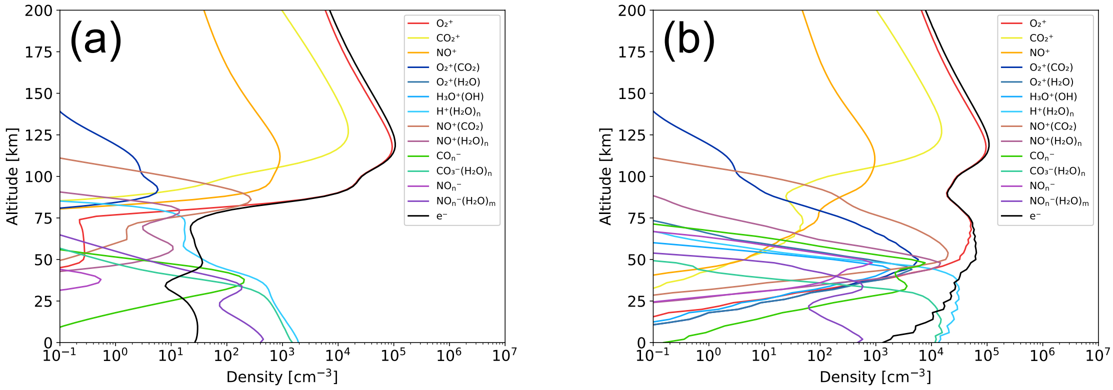

Figure 6.5 Vertical profiles of the ion species calculated by PROTEUS. (a) Before the SEP event and (b) 1 day after the onset of the SEP event.

The temporal variation of the electron density profile during the SEP event is shown in Figure 6.6a and after the SEP event in Figure 6.6b. The time scales of increase and decrease of the electron density during and after the SEP event are both about 10-100 sec and the electron density profile recovers to the pre-SEP state in 1,000 sec after the end of the SEP event. The chemical loss time scale of electrons can explain this temporal variation. The reaction rate coefficient for the recombination of O_2^+ with electrons is 7×10^{-8} cm^3 s^{-1} and that of water cluster ions is about 5×10^{-6} cm^3 s^{-1} assuming that the electron temperature is the same as the neutral temperature of about 130 K. Assuming that electron density is 10^5 cm^{-3}, the loss time scale of electrons is about 140 sec above 50 km at which altitude O_2^+ dominates the ion density profiles and is 2 sec below 50 km at which altitude water cluster ions dominates the ion density profiles. Our results show that the electron density is sensitive to the temporal variation of the SEP proton flux due to the short lifetime of ions and electrons at such low altitudes.

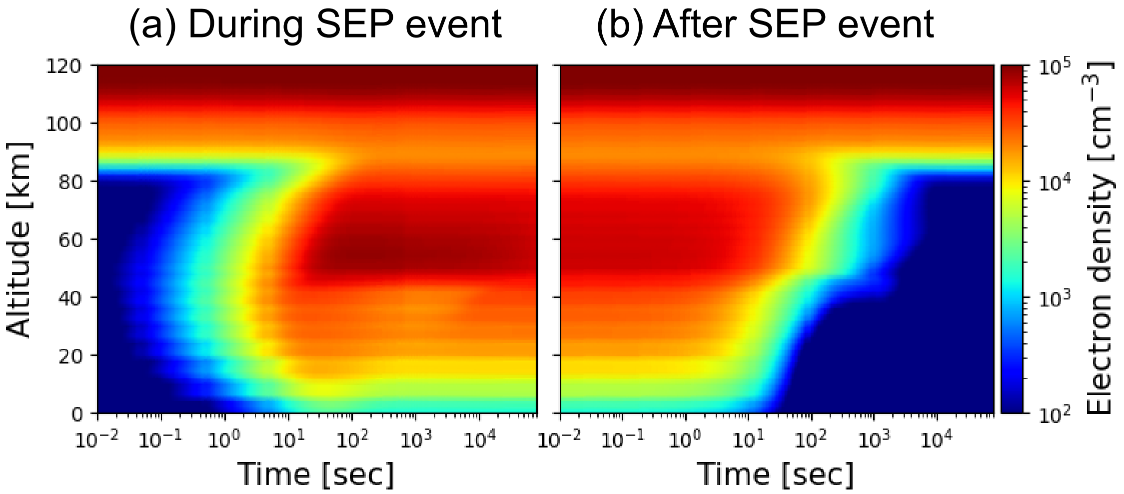

Figure 6.6 (a, b) Temporal variations of the electron density profile during the SEP event and after the end of the SEP event, respectively. Horizontal axes are the time from the onset of the SEP event and the time from the end of the SEP event, respectively.

6.3 Changes in the neutral density profiles

Figure 6.7a shows the vertical profiles of ozone, HOx (OH + HO_2), and NOx (NO + NO_2), before the SEP event, 1 day after the onset of the SEP event, 1 day after the end of the SEP event, and 10 days after the end of the SEP event, calculated by PROTEUS using all the 490 chemical reactions. An enhancement of the HOx density is observed in the altitude range of 20-60 km with a factor 10 maximum enhancement occurring at 40 km. Depletion of the ozone density was confirmed in the altitude range of 20-60 km with a factor 10 maximum decrease occurring at 40 km. The altitude range at which a HOx enhancement and an ozone depletion are observed corresponds to the maximum penetration depth of 4.6-46 MeV protons in the Martian atmosphere as shown in Figure 6.4. An enhancement of the NOx density is observed in the altitude range of 20-100 km with a factor 100 maximum change occurring at 50 km. During the recovery phase, the effect of the SEP on the HOx and ozone densities are still obvious 1 day after the end of the SEP event and almost vanishes 10 days after the end of the SEP event. The effect of the SEP on the NOx density still remains even 10 days after the end of the SEP event due to the long chemical time scales of N and NO (~10^4-10^5 sec at high altitudes). NO molecules move to lower altitudes, maintaining or increasing the NOx density over time, as seen in Figure 6.7a below 40 km altitude.

In order to clarify whether HOx or NOx contribute to the depletion of the ozone density, we perform another simulation using reactions excluding all the nitrogen-related ones. Figure 6.7b shows the vertical profiles of ozone and HOx simulated using 227 reactions without all the nitrogen-related ones at the four timings as in Figure 6.7a. The contribution of NOx to the variation of ozone is negligibly small. The depletion of ozone can be attributed to the enhancement of HOx during the SEP event, not to NOx.

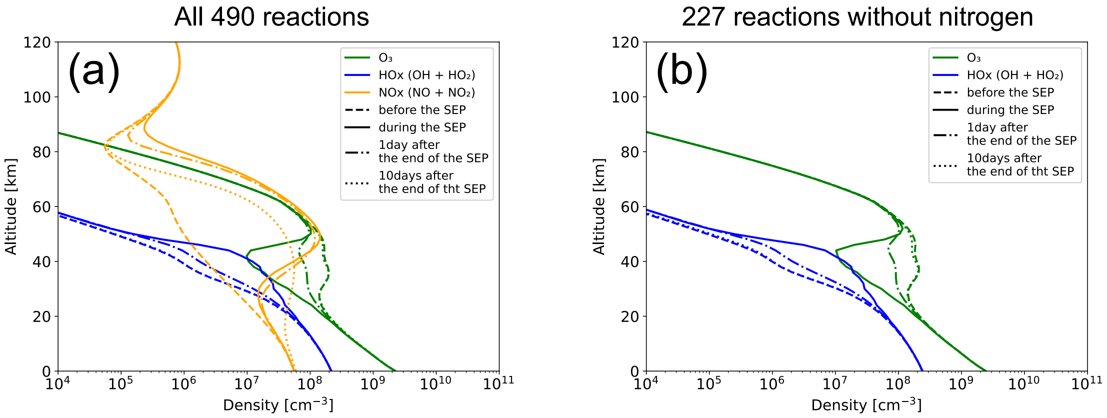

Figure 6.7 Vertical profiles of O_3, HOx ($OH + HO_2$), and NOx ($NO + NO_2$) simulated by PROTEUS. (a) Profiles calculated using all the 490 reactions and (b) profiles calculated using 227 reactions without all the nitrogen-related reactions. Different lines represent the profiles at different timings for each species, before the SEP event (denoted as “before the SEP”), 1 day after the onset of the SEP event (denoted as “during the SEP”), 1 day after the end of the SEP event (denoted as “1 day after the end of the SEP”), and 10 days after the end of the SEP event (denoted as “10 days after the end of the SEP”).

The temporal variation of the O, O_3, H, OH, and HO_2 densities at 40 km altitude where the variation of ozone is the largest is shown in Figure 6.8. The density of these species converged in 5 hours due to short chemical timescales, indicating that the duration of the SEP event does not affect the amount of change in density of these species. The temporal variation of NO at 50 km altitude is also shown in Figure 6.8. The NO density linearly increased during the SEP event, indicating that the amount of change in the NO density strongly depends on the duration of the SEP event.

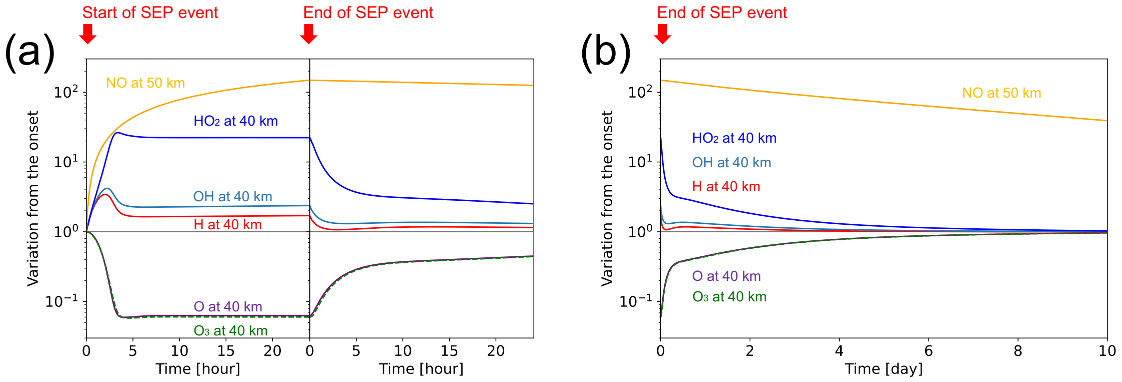

Figure 6.8 (a) Temporal variation of the O, O_3, H, OH, and HO_2 densities at 40 km altitude and the NO density at 50 km from the onset of the SEP event to 1 day after the end of the SEP event. The horizontal axis is the time from the onset of the SEP event on the left panel and the time from the termination of the SEP event on the right panel. The timings of the onset and the end of the SEP event are shown above each panel. (b) Temporal variation of the O, O_3, H, OH, and HO_2 densities at 40 km altitude and the NO density at 50 km from the end of the SEP event to 10 days after.

6.4 Chemical pathways during SEP events

We describe the chemical pathways that occur in the Martian atmosphere during the SEP event, focusing on the reason for the depletion of ozone. The production of HOx during the SEP event starts from the ionization of CO_2 due to proton impact (p^*) and secondary electron impact (e^*).

$$\mathrm{CO_2 + p^* \rightarrow CO_2{}^+ + e^- + p^*} \tag{R6.1}$$

$$\mathrm{CO_2 + e^* \rightarrow CO_2{}^+ + e^- + e^*} \tag{R6.2}$$

The produced CO_2^+ then reacts with the ambient CO_2 and O_2 to become O_2^+. Reactions (R6.3) and (R6.4) are essentially dominant at low altitudes below 80 km because three-body reactions become significant at low altitudes, while those reactions are not efficient in the ionosphere altitudes.

$$\mathrm{CO_2{}^+ + CO_2 + M \rightarrow CO_2{}^+(CO_2) + M} \tag{R6.3}$$

$$\mathrm{CO_2{}^+(CO_2) + O_2 \rightarrow O_2{}^+ + 2CO_2} \tag{R6.4}$$

O_2^+ then reacts with the ambient CO_2 and H_2O molecules to produce water cluster ions $H_3O^+(OH)$, $H^+(H_2O)$, and $H^+(H_2O)_2$ via the following chain reactions. OH radical is produced through the production of $H^+(H_2O)$, and $H^+(H_2O)_2$.

$$\mathrm{O_2}^+ + \mathrm{CO_2} + \mathrm{M} \rightarrow \mathrm{O_2}^+(\mathrm{CO_2}) + \mathrm{M} \quad \text{(R6.5)}$$
$$\mathrm{O_2}^+(\mathrm{CO_2}) + \mathrm{H_2O} \rightarrow \mathrm{O_2}^+(\mathrm{H_2O}) + \mathrm{CO_2} \quad \text{(R6.6)}$$
$$\mathrm{O_2}^+(\mathrm{H_2O}) + \mathrm{H_2O} \rightarrow \mathrm{H_3O^+(OH)} + \mathrm{O_2} \quad \text{(R6.7)}$$
$$\mathrm{O_2}^+(\mathrm{H_2O}) + \mathrm{H_2O} \rightarrow \mathrm{H^+(H_2O)} + \mathrm{OH} + \mathrm{O_2} \quad \text{(R6.8)}$$
$$\mathrm{H_3O^+(OH)} + \mathrm{H_2O} \rightarrow \mathrm{H^+(H_2O)_2} + \mathrm{OH} \quad \text{(R6.9)}$$

$H^+(H_2O)$ and $H^+(H_2O)_2$ then react with the ambient water vapor molecules, which is balanced by the release of H_2O due to impact with ambient atmospheric molecules.

$$\mathrm{H^+(H_2O)_n} + \mathrm{H_2O} + \mathrm{M} \rightarrow \mathrm{H^+(H_2O)_{n+1}} + \mathrm{M} \quad \text{(R6.10)}$$
$$\mathrm{H^+(H_2O)_n} + \mathrm{M} \rightarrow \mathrm{H^+(H_2O)_{n-1}} + \mathrm{H_2O} + \mathrm{M} \quad \text{(R6.11)}$$

Water cluster ions $H_3O^+(OH)$ and $H^+(H_2O)_n$ are finally broken by the recombination with electrons or negative ions (R^-) to produce H and OH in the atmosphere.

$$\mathrm{H_3O^+(OH)} + \mathrm{e^-} \rightarrow \mathrm{H} + \mathrm{OH} + \mathrm{H_2O} \quad \text{(R6.12)}$$
$$\mathrm{H^+(H_2O)_n} + \mathrm{e^-} \rightarrow \mathrm{H} + \mathrm{nH_2O} \quad \text{(R6.13)}$$
$$\mathrm{H_3O^+(OH)} + \mathrm{R^-} \rightarrow \mathrm{H} + \mathrm{OH} + \mathrm{H_2O} + \mathrm{R} \quad \text{(R6.14)}$$
$$\mathrm{H^+(H_2O)_n} + \mathrm{R^-} \rightarrow \mathrm{H} + \mathrm{nH_2O} + \mathrm{R} \quad \text{(R6.15)}$$

Depletion of ozone cannot easily be attributed to the direct reaction with the enhanced H and OH. If either H or OH is the direct reactant to destroy ozone, temporal variation of ozone should coincide with those of H and/or OH considering that the loss time scale of ozone is around 100 seconds. However, as seen in Figure 6.8, the temporal variation of ozone does not coincide with those of H and OH; ozone does not follow the peak shape seen in the H and OH variation 3 hours after the onset of the SEP event. On the other hand, temporal variations of O and O_3 are similar to that of HO_2, and the variation of O_3 is slightly delayed by that of O. According to our simulation, the contribution of the reaction $HO_2 + O_3$ is essentially negligible for the ozone loss and $HO_2 + O$ is the dominant reaction for the loss of O during the SEP event. Therefore, the following scenario is a plausible explanation for the ozone depletion during the SEP event. The increase of the H and OH densities induces the production of HO_2 via the following catalytic cycle of CO recombination.

$$\mathrm{H + O_2 + M \rightarrow HO_2 + M} \quad \text{(R6.16)}$$

$$\mathrm{O + HO_2 \rightarrow OH + O_2} \quad \text{(R6.17)}$$

$$\mathrm{CO + OH + M \rightarrow H + CO_2} \quad \text{(R6.18)}$$

During this catalytic cycle, O is lost by the reaction with HO_2 (R6.17), which results in the decrease of the production rate of ozone by the following main path of ozone production.

$$\mathrm{O + O_2 + M \rightarrow O_3 + M} \quad \text{(R6.19)}$$

The H and OH densities are regulated by the reaction with HO_2, which results in the decrease of H and OH 3 hours after the onset of the SEP event. On the other hand, the HO_2 density does not decrease because HO_2 is mainly removed by the reaction of O + HO_2 and this reaction rate decreases due to the decrease of the O density. This scenario suggests that the depletion of ozone during the SEP event in the Martian atmosphere is different from that in the terrestrial atmosphere, starting with the ionization of CO_2, the depletion of ozone is induced by the decrease of the O density due to an enhanced HO_2 density produced by the catalytic cycle of the CO recombination (R6.16, R6.17, and R6.18).

The duration of the SEP event could affect the variation of the density profiles. As seen in Figure 6.8, the NO density increases in time due to the long chemical timescales of N and NO ($\sim 10^4$-10^5 sec in the altitude range 60-80 km) and the downward motion of N and NO, so that the enhancement of the NO density is sensitive to the duration of the SEP event. Since the enhancement of the HOx density and the decrease of the ozone density reached their converged values in 5 hours, the duration of the SEP event does not affect the amount of variation for those species during the SEP event except if the SEP event lasts less than 5 hours. As seen in Figures 6.9a and 6.9b, since the H density increases in time above 45 km altitude, the duration of the SEP event could affect the amount of the decrease of the ozone density if the SEP event last more than several days because it could affect the downward flux of H after the SEP event.

After the end of the SEP event, the recovery of the ozone density occurs through two consecutive phases. In the first phase, the ozone density rapidly increases for 5 hours as displayed in Figure 6.8. This recovery is purely due to the short lifetime of H, OH, and HO_2, and the short production timescales of O and O_3. Indeed, the lifetime of a chemical species can roughly be estimated by n_i/L_i, those of H, OH, and HO_2 are about 100 sec, 4 sec, and 50 sec at 40 km altitude, respectively. The timescale of production of a chemical species can be estimated by n_i/P_i, and those of O and O_3 are 1000 sec and 500 sec at 40 km altitude, respectively. In the second phase, ozone density slowly recovers to a pre-SEP level on a week timescale. Such a slow recovery phase is due to the downward motion of H atoms from the upper altitudes at which the lifetime of H atom is longer. For instance, the lifetimes of H atom at 60, 70, and 80 km altitudes are 1 hour, 14 hours, and 20 days. The lifetime of H atom rapidly increases with altitude because H atom is mainly lost by a three-body reaction with O_2 (R6.16) and a two-body reaction with O_3, both of which are less efficient at high altitudes where atmospheric density and ozone density rapidly decrease. Figures 6.9c and 6.9d displays the temporal variation of the H density and downward flux after the SEP event. The H density rapidly decreases below 45 km altitude due to its short lifetime, while it slowly decreases above 45 km altitude because of the long lifetime and descent of H atom from the altitudes above. The downward flux of H increases below 70 km after the end of the SEP event, which supplies enough H atom to the lower altitudes to maintain its density. The downward velocity of H atom is around 1 cm s^{-1} (obtained by dividing the flux by the number density), which means that it takes several days for H atoms to move downward from 80 km to 40 km altitudes.

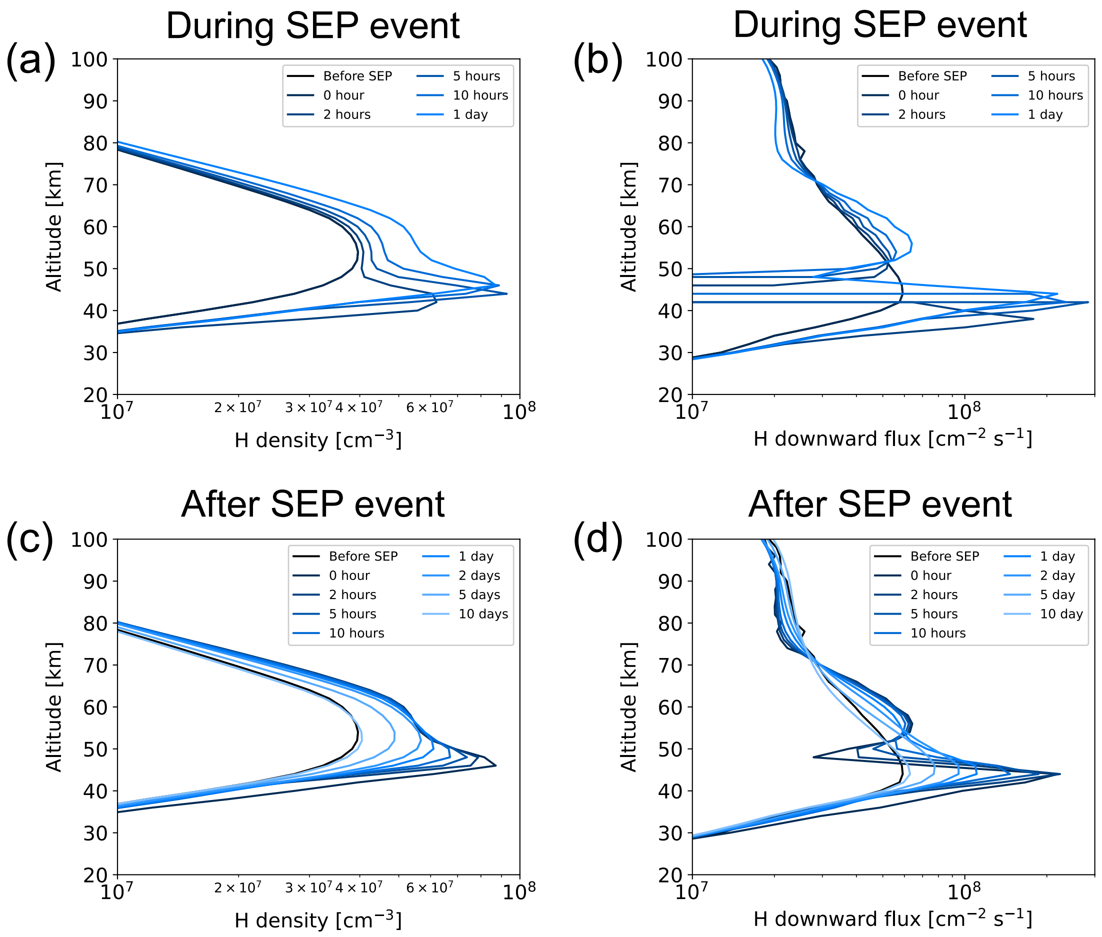

Figure 6.9 (a, b) Simulated vertical profiles of hydrogen atom (H) density and downward flux during the SEP event, respectively. (c, d) Vertical profiles of H density and downward flux after the end of the SEP event, respectively.

6.5 Detectability of changes in chemical composition by TGO/NOMAD

Vertical volume mixing ratio profiles for several species before and at the end of the SEP event are summarized in Figure 6.10. The detection lower limits in the solar occultation (SO) mode of TGO/NOMAD are 1 ppbv for HO_2, 0.1 ppbv for NO_2, 0.001 ppbv for N_2O, and 0.03 ppbv for H_2CO, and the detection limit of TGO/NOMAD ultraviolet and visible spectrometer (UVIS) channel in solar occultation is 0.05 ppbv for O_3 (Vandaele et al., 2015). However, these estimations were performed for clear sky condition (i.e., no aerosols in the atmosphere), which is not representative for most of the cases. The actual detection limits are estimated to be 10 times worse than those values with the presence of a moderate abundance of aerosols (Vandaele et al., 2018). In fact, the detection limit of HCl for clear sky condition was estimated to be 0.03 ppb (Vandaele et al., 2018), however, it is ~0.3 ppb for the actual observations (Aoki et al., 2021). As shown in Figure 6.10, the simulated volume mixing ratios are 10-100 ppbv for O_3, 0.01-1 ppbv for HO_2, 10^{-5}-10^{-1} ppbv for NO_2, 10^{-4}-10^{-3} ppbv for N_2O, and 10^{-15} ppbv for H_2CO within the altitude range where changes induced by the SEP event are significant. The simulated change of the concentration of O_3 is sufficiently above the detection limit of TGO/NOMAD even considering the effects of aerosols. Currently, more than ten vertical profiles can be obtained in a day by the instrument, and the results for the observation of the ozone density by TGO/NOMAD have been published by several papers (Patel et al., 2021; Khayat et al., 2021). Therefore, the depletion of ozone during a Halloween-class SEP event should be detected by TGO/NOMAD. For other species, the simulated changes in the concentration of HO_2 and NO_2 are just at the detection limit of TGO/NOMAD for clear sky condition, so it would be challenging to detect the enhancement of those species during the SEP event due to the small signal-to-noise ratio. As for N_2O and H_2CO, which are important for prebiotic synthesis of amino acid and nucleic acid, the simulated concentrations are far below the detection limit of TGO/NOMAD.

There are several limitations to the comparison between our one-dimensional model and future observations. Our simulations were performed at the subsolar point, while the solar occultation observations are performed near the terminator. Picciali et al. (2021) reported that the ozone density rapidly increases across the terminator of Mars from the dayside to the nightside. Three-dimensional simulation is therefore needed for the direct comparison with solar occultation observations. Furthermore, due to the orbital geometry of TGO spacecraft, the SO observations are performed frequently at high latitudes, where dynamics play an important role in the vertical profile of ozone (Lefèvre et al., 2021). The lack of dynamics in our one-dimensional photochemical model is a major limit in particular at high latitudes. Previous studies have shown that the ozone concentration is known to be strongly anti-correlated with the concentration of water vapor (Lefèvre et al., 2021). Our simulation results should therefore depend on the initial vertical profile of water vapor. Since the goal of our present work is to provide a first prediction of changes in chemical composition during a SEP event in the Martian atmosphere, the effects of dynamics, seasonal variation of water vapor content, and other uncertainties such as seasonal and spatial variation of eddy diffusion coefficient (Yoshida, N. et al., 2022) are out of scope.

We would like to note that our simulation suggests that a SEP event also induces enhancement of the H_2O_2 volume mixing ratio at 20-60 km (e.g., from 0.1 ppbv to 10 ppbv at 40 km altitude, see Figure 6.10). This is not detectable by currently available instruments, however, H_2O_2 has strong absorption lines in the sub-mm range, and future spectroscopic instruments in that spectral range with limb-viewing (e.g., Kasai et al., 2012) may capture the simulated enhancement of H_2O_2.

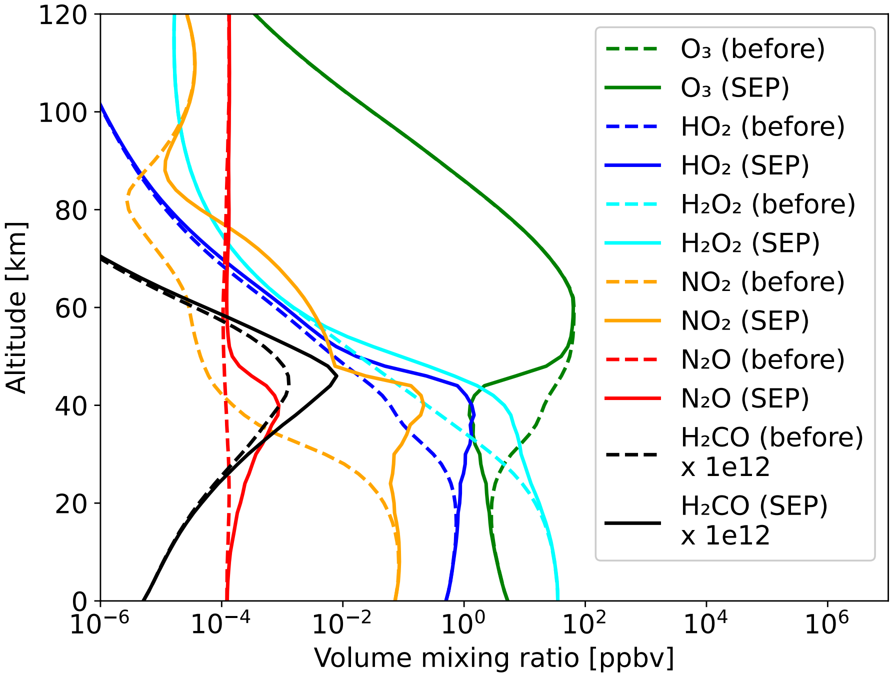

Figure 6.10 Vertical volume mixing ratio profiles for several species before the SEP event (dashed curves) and after the end of the SEP event (solid curves). The mixing ratio of H_2CO is multiplied by a factor of 10^{12}.

6.6 Dependence on the intensity and spectral shape of SEP proton flux

We discuss the effects of the SEP proton flux intensity and its spectral shape on our results. The SEP event that occurred on 28 October 2003 was one of the most intense SEP events on Earth, which would occur once every ten years (Birch and Bromage, 2022; Kataoka, 2020). The only instrument that can measure the absolute intensity of high-energy protons at Mars is the MAVEN/SEP instrument, with an energy range limited to 6 MeV, which limits the accuracy of fitting parameters for the SEP proton flux. We will therefore use the measured proton flux at 1 MeV as a proxy instead of using the normalization constant C in the expression of the proton flux spectrum in Equations (6.1) and (6.2) to expect future SEP events which could cause ozone depletion. Equations (6.1) and (6.2) were therefore re-written by replacing C by the proton flux at 1 MeV $f_{1\mathrm{MeV}}$ in unit cm^{-2} s^{-1} sr^{-1} keV^{-1} as:

$$\frac{dJ}{dE} = f_{1\mathrm{MeV}} E^{-\gamma_a} \exp\left(-\frac{E-1}{E_B}\right) \quad \text{for } E \leq (\gamma_b - \gamma_a)E_B \tag{6.3}$$

$$\frac{dJ}{dE} = f_{1\mathrm{MeV}} E^{-\gamma_b} [(\gamma_b - \gamma_a)E_B]^{\gamma_b - \gamma_a} \exp\left(\gamma_b - \gamma_a + \frac{1}{E_B}\right) \quad \text{for } E \geq (\gamma_b - \gamma_a)E_B \tag{6.4}$$

Statistical analysis of the Band parameters for the SEP proton spectra was given by Desai et al. (2016). They analyzed 46 SEP events for about 16 years from 1998 to 2014 to characterize the variation of the Band parameters among SEP events. They found that the mean values for the low- and high-energy power law slopes γ_a and γ_b were 1.23 and 3.63, respectively. The standard deviation (σ) of γ_a and γ_b were 0.58 and 1.12, respectively. We re-analyzed the distribution of E_B for 44 of 46 events in Desai et al. (2016) at which E_B were determined and found that the 25th, 50th, and 75th percentile values of the break energy E_B were 2.92 MeV, 6.18 MeV, and 12.4 MeV, respectively. We investigated the ozone variation as a function of γ_b and $f_{1\mathrm{MeV}}$ for a value of γ_a=0.65, 1.23, and 1.81 (ranging from mean value minus 1σ to mean value plus 1σ), and E_B of 2.92 MeV, 6.18 MeV, and 12.4 MeV. The $f_{1\mathrm{MeV}}$ value range was set to 0.1-10 cm^{-2} s^{-1} sr^{-1} keV^{-1} according to previous SEP events. The $f_{1\mathrm{MeV}}$ value was equal to 5 cm^{-2} s^{-1} sr^{-1} keV^{-1} during the SEP event on 28 October 2003. During the SEP event in September 2017 on Mars, which was the most intense SEP event observed since MAVEN spacecraft insertion around Mars, the $f_{1\mathrm{MeV}}$ value was equal to 5 cm^{-2} s^{-1} sr^{-1} keV^{-1} if we multiply the SEP proton flux in Figure 4.2 in Chapter 4 by a factor of 6 to match the observed auroral emission intensity (as discussed in Section 4.4) and convert the unit into cm^{-2} s^{-1} sr^{-1} keV^{-1}. During the SEP event in December 2014 on Mars, the $f_{1\mathrm{MeV}}$ value reached 0.8 cm^{-2} s^{-1} sr^{-1} keV^{-1} at peak timing. The range of $f_{1\mathrm{MeV}}$ value of 0.1-10 covers from calm to extreme SEP events.

The results with a slope at low energy γ_a=0.65 are shown in Figure 6.11, those with a slope at low energy γ_a=1.23 are shown in Figure 6.12, and those with a slope at low energy γ_a=1.81 are shown in Figure 6.13. As a whole, a hard-spectral slope at low energy, i.e., a small value of γ_a, a large flux intensity at 1 MeV $f_{1\mathrm{MeV}}$, and a large break energy E_B resulted in a large amount of ozone variation. As already described, since ozone depletion occurs in the altitude range of 20-60 km corresponding to the penetration of protons with energy 4.6-46 MeV, a small value of γ_a with large E_B leads to the largest intensity of proton flux at high energy, leading to a large production of H and OH in the atmosphere. The dependence of the power spectral slope at high energy γ_b varies with E_B. The amount of ozone variation is almost independent of γ_b for large E_B, since the proton flux intensity varies with energy gradually above several times E_B as γ_b

changes, and the proton flux remained the same in the energy range 4.6-46 MeV even as γ_b changed. The qualitative signature of γ_b dependence did not vary with γ_a. The ozone variation does not depend on γ_b and is linearly dependent on E_B if the break energy E_B is larger than 6.18 MeV, near the upper limit of MAVEN/SEP. If the change of slope in the proton flux spectrum does not appear in the MAVEN/SEP flux data during a future SEP event, we can only obtain γ_a and $f_{1\mathrm{MeV}}$, and E_B should be larger than 6 MeV. In this case, we do not have to take care of the power law spectral slope γ_b above the upper energy limit of the instrument. The uncertainty would only be related to the break energy E_B, leading to uncertainty in the ozone variation by several factors. If the break energy E_B can also be determined using the MAVEN/SEP flux data, we then take care of the uncertainty in γ_b, leading to the uncertainty in the ozone variation by several factors. As an example, during the September 2017 SEP event on Mars, γ_a, $f_{1\mathrm{MeV}}$, and E_B were 0.8, 5 $\mathrm{cm}^{-2}\ \mathrm{s}^{-1}\ \mathrm{sr}^{-1}\ \mathrm{keV}^{-1}$, and 3 MeV, respectively (see Figure 4.9b in Chapter 4). Those values were similar to the case of Figures 6.11a and 6.11b, allowing us to estimate the depletion of ozone density to ~50-75% at 40 km altitude and 5-10% in the column, which could sufficiently be detected.

Finally, we discuss the frequency of SEP events that cause ozone depletion. Statistical analysis by Gopalswamy (2018) showed the relationship between the proton flux > 10 MeV and the cumulative distribution of the number of SEP events for 263 SEP events in 1976-2016. Statistical analysis by Kataoka (2020) for 261 SEP events in 1976-2020 obtained almost the same relationship as Gopalswamy (2018). The proton flux > 10 MeV was calculated by integrating the proton flux over energy > 10 MeV for each pair of γ_a, γ_b, $f_{1\mathrm{MeV}}$, and E_B in Figures 6.11-6.13, which was then converted into the frequency of SEP events using the relationship by Gopalswamy (2018). The frequency of SEP events for each pair of those spectral parameters is shown in Figures 6.11-6.13 in red lines. In all cases, a 50% depletion of the ozone density at 40 km and a 4% depletion of the column ozone density would correspond to the frequency of SEP events 2 year^{-1}, a 75% depletion of the ozone density at 40 km and an 8-10% depletion of the column ozone density would correspond to the frequency of SEP events 1 year^{-1}, and a > 90% depletion of the ozone density at 40 km and a 14-16% depletion of the column ozone density would correspond to the frequency of SEP events 0.3 year^{-1}. Since the depletion of the ozone density occurs around 40 km altitude where SEP protons with energy greater than ~10 MeV induce reactions (Figure 6.4a), the depletion of the ozone density is the same for the same proton flux > 10 MeV for each pair of spectral parameters. Therefore, a significant depletion of Mars' atmospheric ozone can occur not only during extreme SEP events such as a Halloween-class SEP event but also even during relatively frequent SEP events at Mars.

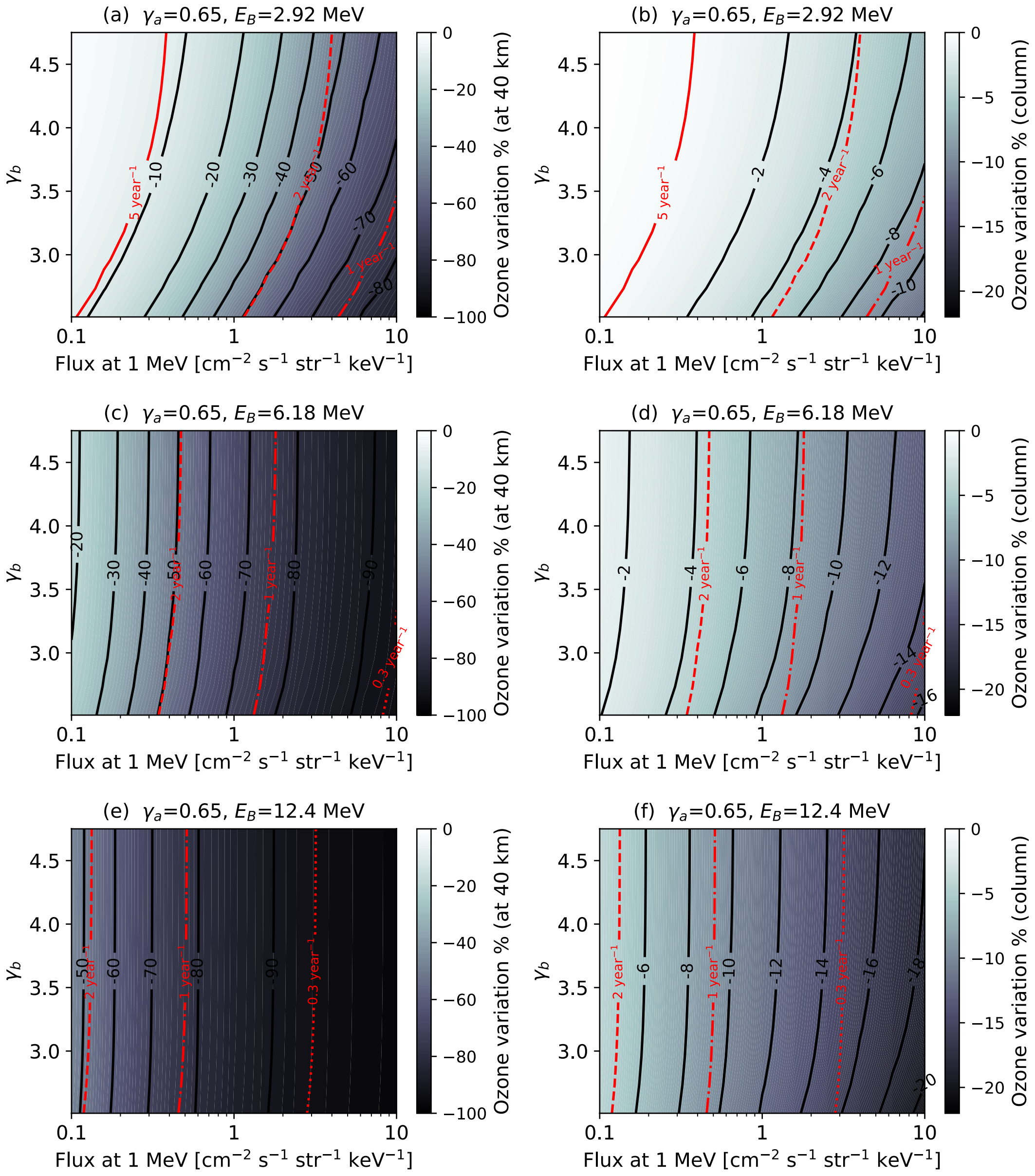

Figure 6.11 Dependence of the ozone density variation on parameters of SEP proton flux spectra. Left panels represent the variation of the ozone density at 40 km altitude and right panels represent the variation of the ozone column density. Vertical axis is the power law spectral slope at high energy γ_b and horizontal axis is the proton flux at 1 MeV. The power law spectral slope at low energy γ_a is 0.65 in all panels. (a, b) The break energy E_B=2.92 MeV, (c, d) E_B=6.18 MeV, and (e, f) E_B=12.4 MeV. The red solid, dashed, dash-dot, and dotted lines represent the frequency of SEP event, 5 year^{-1}, 2 year^{-1}, 1 year^{-1}, and 0.3 year^{-1}, respectively.

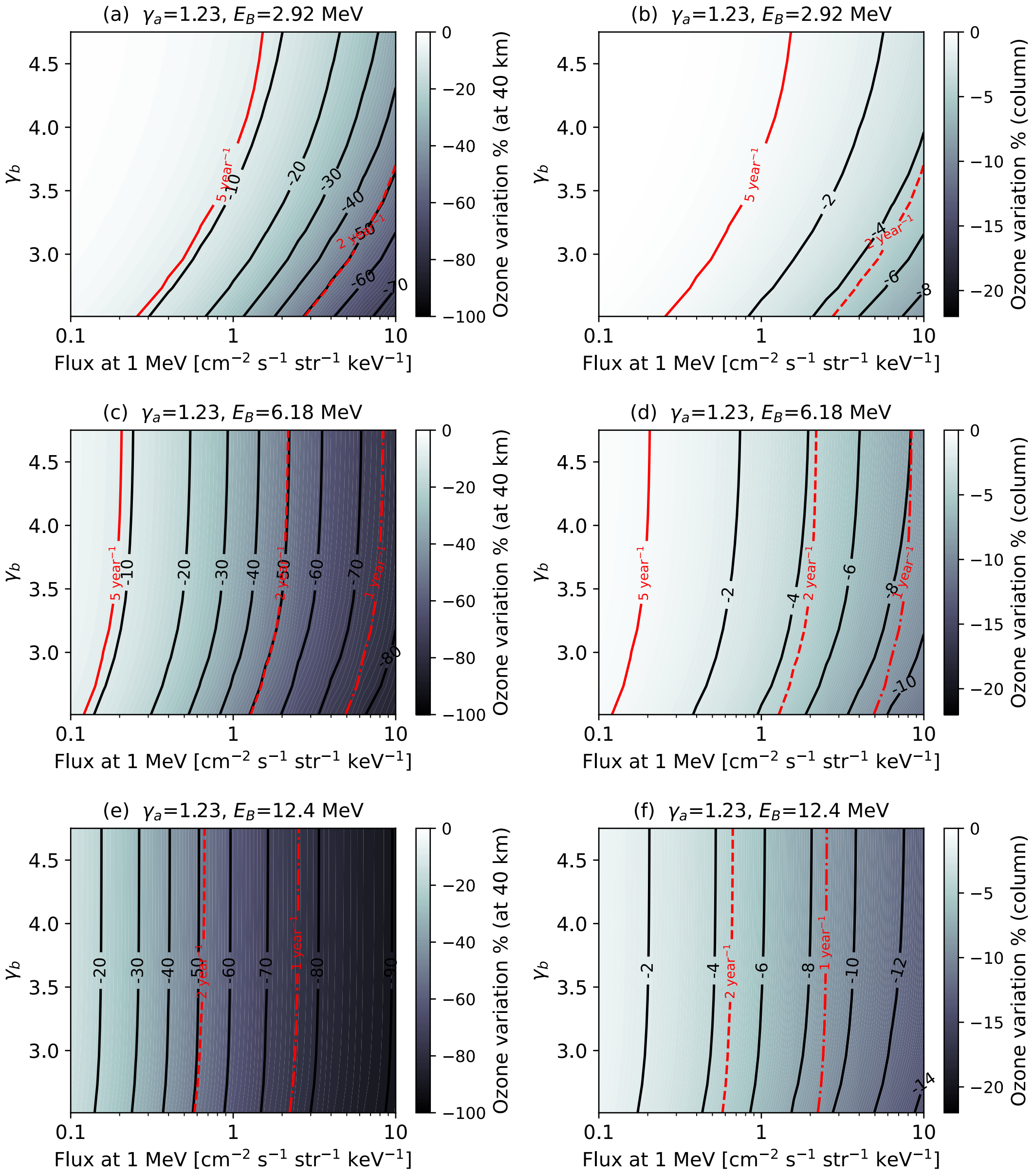

Figure 6.12 Same as Figure 6.11, but for $\gamma_a = 1.23$.

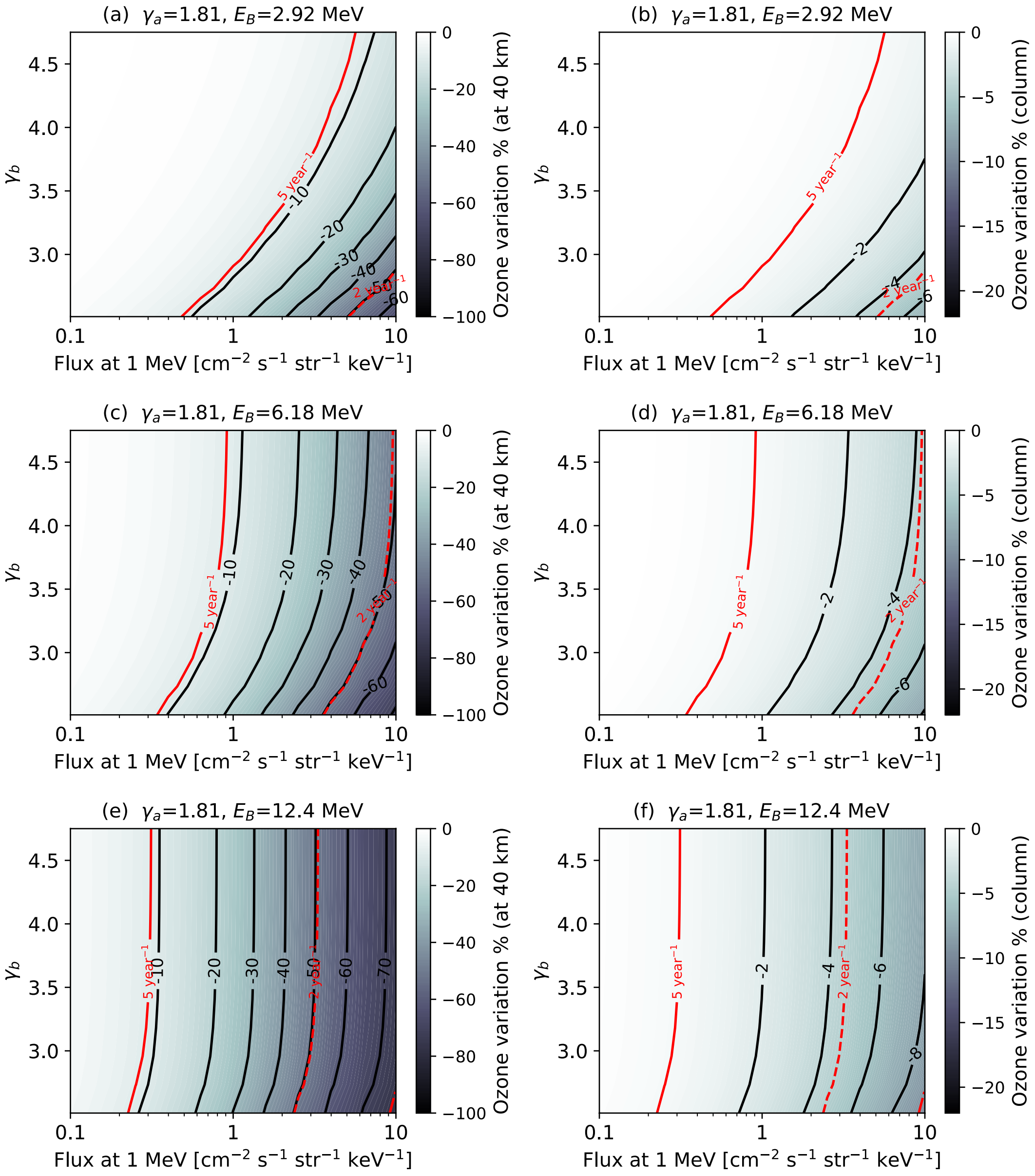

Figure 6.13 Same as Figure 6.11, but for $\gamma_a = 1.81$.

6.7 Chapter summary

We provide the first prediction on the evolution of the atmospheric neutral chemical composition in the Martian atmosphere during a large SEP event by using a Monte Carlo model PTRIP and a one-dimensional photochemical model PROTEUS. Our results show that the ozone density decreases in the altitude range of 20-60 km with a factor 10 maximum enhancement occurring at 40 km during a Halloween-class SEP event due to the loss of O by an enhanced HO_2 density. The altitude range of 20-60 km in which the depletion of the ozone density occurs corresponds to the penetration of SEP protons with an energy range of 4.6-46 MeV. Variations of the ozone and HOx densities converge in 5 hours during a Halloween-class SEP event, while the duration of the SEP event significantly affects the enhancement of the NOx density due to the long lifetime. The depletion of the ozone density is expected to be detectable by TGO/NOMAD, while the variation of other species is not. We perform a sensitivity test of ozone variation with respect to the intensity and spectral shape of the SEP proton flux spectrum. We find that a hard spectral slope at low energy and larger break energy results in a large amount of ozone depletion. A 75% depletion of the ozone density at 40 km altitude and an 8-10% depletion of the column ozone density can be expected during SEP events occurring once a year on average based on a statistical analysis of SEP events in 1976-2016. Our model reveals, for the first time, that ozone concentration can decrease significantly during a large SEP event in the Martian atmosphere as on Earth, but via different chemical pathways driven by CO_2 ionization and CO recombination catalytic cycle. It is now a good opportunity for us to predict the effects of SEPs on neutral chemistry in the Martian atmosphere; the detection of changes in the neutral composition is expected in a few years, since the solar activity is getting active in the increasing phase of the solar cycle 25, and TGO/NOMAD is operating since 2018.

Chapter 7

Conclusions and future perspectives

7.1 Conclusions

In this thesis, we have investigated the Martian diffuse auroral emissions and changes in atmospheric chemical composition induced by the precipitation of SEPs into the Martian atmosphere. In order to carry out this study, we have developed two numerical models. One is a Monte Carlo model described in Chapter 2, Particle TRansport In Planetary atmospheres (PTRIP), which is designed to solve the transport of electrons, protons, and hydrogen atoms in planetary atmospheres in order to calculate the ionization, dissociation, and excitation rates of atmospheric molecules. The other is a one-dimensional photochemical model described in Chapter 3, Photochemical and RadiatiOn Transport model for Extensive USe (PROTEUS), which is designed for adaptability to many planetary atmospheres, for flexibility to deal with thousands of or more chemical reactions with high efficiency, and for intuitive operation with GUI. These two numerical models were validated by comparing them with previous numerical models. The major findings of this thesis using these two numerical models are summarized as follows:

(1) Contribution of SEP protons to the Martian diffuse auroral emission

In Chapter 4, we calculated the limb emission profiles of the CO_2^+ UVD due to the precipitation of SEP electrons and protons using PTRIP for the December 2014 SEP event and the September 2017 SEP event and compared the model results with MAVEN/IUVS observations to validate PTRIP. For simplicity, we ignored electric fields and magnetic fields, and the simulations were performed in three dimensions in velocity and one dimension in space. We used the SEP electron and proton fluxes for the two SEP events observed by MAVEN/SEP and SWEA instruments with energy ranges of 100 eV - 100 keV for electrons and 50 keV - 5 MeV for protons. Our results showed that both SEP electrons and protons contributed to the CO_2^+ UVD emission, with high altitude emission dominated by SEP electrons and low altitude peak emission dominated by SEP protons. We compared the sum of electron- and proton-induced emission profiles calculated by

PTRIP with MAVEN/IUVS observations. For the December 2014 SEP event, the calculated shape of the CO_2^+ UVD limb profiles was similar to the limb emission profile obtained by MAVEN/IUVS and the peak altitude of the emission profile was 76 km in good agreement with MAVEN/IUVS observation, while we overestimated the emission intensity by a factor of 2. For the September 2017 SEP event, the calculated peak altitude was 68 km, which was 10 km higher than MAVEN/IUVS observation. During the September 2017 SEP event, the upper limit of the energy range in PTRIP was one of the reasons for the discrepancy in the peak altitudes between PTRIP and MAVEN/IUVS. Extending the energy range up to 500 keV for electrons and 20 MeV for protons further improved our results. Therefore, we were able to reproduce the shape and peak altitude of the limb emission profiles of CO_2^+ UVD for the two SEP events for the first time. PTRIP was thus validated by comparing it with MAVEN/IUVS observations and we showed that the observed SEP fluxes can explain the observed shapes of the auroral emission profiles. For the December 2014 SEP event, the overestimation of the emission intensity by factor ~2 can be explained by the anisotropy in the incident SEP flux, calculation geometry effect, and the lack of magnetic fields in the simulation.

(2) Three-dimensional simulation of the Martian diffuse auroral emission

In Chapter 5, we extended PTRIP to three dimensions in space and took into account the effects of magnetic fields on the particle trajectory to investigate the effects of the crustal magnetic fields in the southern hemisphere on the transport of SEPs and on the Martian diffuse auroral emissions. We found that the morphology of the electron- and proton-induced emissions are different in the strong crustal magnetic field region due to the difference in gyro radii. The electron-induced CO_2^+ UVD emission is patchy and bright only within the cusp regions, while the proton-induced CO_2^+ UVD emission is diffuse without any fine structures. We also simulated oxygen 557.7 nm and 630.0 nm emissions and found that the oxygen 557.7 nm emission is similar in shape and intensity to the CO_2^+ UVD emission, whereas the oxygen 630.0 nm emission is restricted to the cusp regions, SEP electron precipitation being its main source since proton-induced emission is completely quenched at low altitudes.

(3) Changes in atmospheric chemical composition during SEP events on Mars

In Chapter 6, we investigated the effects of SEPs on the atmospheric composition in the Martian atmosphere using PTRIP and PROTEUS. We found that enhancement of the HOx density and depletion of the ozone density occur in the altitude range 20-60 km corresponding to the penetration of SEP protons with energy 4.6-46 MeV, with a maximum variation by a factor of 10 occurring at 40 km during a Halloween-class SEP event. Variations of the ozone and HOx densities converge in 5 hours during a Halloween-class SEP event due to the short production and loss time scales, while the NOx density continues increasing during the SEP event due to its long lifetime. The depletion of the ozone density can be explained by the following processes. Precipitation of SEP protons produces CO_2^+, which reacts with ambient CO_2 and O_2 to become O_2^+. O_2^+ then reacts with the ambient CO_2 and H_2O molecules to become water cluster ions. The reaction of water cluster ions with the ambient H_2O molecules and the recombination of water cluster ions with electrons and negative ions produce H and OH in the atmosphere. The enhanced H and OH densities lead to the production of HO_2, which reacts with O to cause the decrease of the O density. The decrease of the O density leads to a decrease in the production rate of ozone, leading to the depletion of ozone during SEP events. After the SEP event, the recovery of the ozone density occurs through two distinct phases. First, the ozone density rapidly increases in 5 hours due to the short lifetimes of HOx of about 10-100 s and short production time scales of O and O_3 of about 1000 and 500 s, respectively. Second, the ozone density gradually recovers to a pre-SEP level in one week. The second phase is due to the downward motion of H atom from the upper altitudes at which the lifetime of H atom is longer than several days. We compared our results with the detection limit of TGO/NOMAD. The depletion of the ozone density is expected to be detectable by TGO/NOMAD, while the variations of other species such as HO_2, NO_2, H_2CO, and N_2O are not expected to be detected due to the small abundances below the detection limit of TGO/NOMAD. We investigated the dependence of the ozone density variation on the intensity and the spectral shape of the SEP proton flux spectrum. We found that a hard spectral slope at low energy and large break energy lead to a large amount of ozone depletion. We discussed the frequency of SEP events that cause ozone depletion and found that a 75% depletion of the ozone density at 40 km altitude and an 8-10% depletion of the column ozone density can be expected during SEP events occurring once a year on average.

7.2 Future perspectives

In this thesis, we have provided new insights into the Martian diffuse auroral emissions and photochemistry induced by the precipitation of SEPs. Previous studies looked for the sources of the Martian diffuse auroral emissions as only being due to SEP electrons and were not able to reproduce the observed emission profiles. We took into account the contribution of SEP protons to the Martian diffuse auroral emissions and succeeded in reproducing the observed shapes and peak altitudes of the limb intensity profiles, suggesting a significant contribution from SEP protons to the auroral emission profiles at low altitudes. Our three-dimensional simulation of the Martian diffuse auroral emissions in UV and visible wavelength ranges will be compared with future observations with MAVEN/IUVS and TGO/NOMAD to further validate PTRIP and to improve our understanding of the precipitation of SEPs into the Martian atmosphere. There have been no studies on the effects of SEPs on the atmospheric neutral composition on present-day Mars. We are able to predict the changes in atmospheric neutral composition during SEP events using PTRIP and PROTEUS, which will be compared with future observations with TGO/NOMAD in particular within a few years during the increasing phase of the solar cycle 25.

There are three other future prospects regarding this thesis.

(1) SEP-induced auroral emissions on Earth and Venus

A first future prospect is the modeling of SEP-induced auroral emissions on Earth and Venus. As introduced in Chapter 1, the precipitation of SEP protons into Earth's polar cap region leads to the polar-glow aurora. There are only a few observations and theories of the polar-glow aurora (Sandford, 1961, 1962, 1963; Simmons and Henriksen, 1995), and its understanding has not progressed in the past decades. The auroraXcosmic project is a Japanese new Antarctic observation research project aiming to understand the space weather in Earth's polar cap region. Revisiting the polar-glow aurora by observations and simulations is one of the main objectives of the auroraXcosmic project. Since PTRIP has been developed to investigate the transport of SEPs not only in the Martian atmosphere but also on other planets, PTRIP can be used to estimate the brightness of the polar-glow auroral emissions. The auroraXcosmic project aims to observe the emission of N_2^+ first negative (1NG) bands at 391.4 nm and 427.8 nm during SEP events. PTRIP is able to estimate the volume emission rate of the N_2^+ 1NG bands emissions at 391.4 nm and 427.8 nm by multiplying the volume production rate of N_2^+ by factors 0.0714 and 0.025, respectively (Rees, 1984; McConkey and Latimer, 1965; Gerdjikova and Shepherd, 1987; Ono, 1993).

Venus is also our next target due to its similarity with Mars, i.e., a similar atmospheric composition and the absence of a global intrinsic magnetic field as on Mars. Weak emissions of the oxygen 557.7 nm emission on Venus during two solar storms on 27 December 2010 and 12 December 2013 have been reported by Gray et al. (2021), which is considered to be produced by the precipitation of protons with energy ~100 keV. As described in Chapter 5, PTRIP is able to estimate the brightness of the oxygen 557.7 nm emission, which can be used to evaluate the Venusian green aurora during SEP events and can be compared with observations. Validation of PTRIP by comparing it with auroral emission observations on Mars, Earth, and Venus will lead to further improvement of PTRIP and our better understanding of the interaction of SEPs with planetary atmospheres.

(2) Validation of PTRIP by comparing it with electron density observations

A second future prospect is the validation of PTRIP with electron density observations in the atmosphere during SEP events. There are two approaches for the evaluation of the electron density during SEP events. One is the radio occultation measurements. The Radio Occultation Science Experiment (ROSE) instrument is a radio occultation investigation on board MAVEN to measure vertical profiles of electron density in the Martian ionosphere (Withers et al., 2020). Recently, enhancements of electron density at low altitudes have been observed by MAVEN/ROSE during a SEP event occurring in March 2021 coincided with the enhancements of SEP proton fluxes, but there was no signature of SEP electron populations (Withers et al., 2022). Previous observations were not able to distinguish the contribution of SEP electrons and protons due to their coincident enhancements (Schneider et al., 2018), while the SEP event in March 2021 was the first indication of the atmospheric ionization on the nightside due to SEP protons owing to the absence of SEP electrons. This finding might support our conclusion that SEP protons have significant impacts on the Martian atmosphere at low altitudes. Comparing the vertical profiles of electron density simulated by PTRIP and PROTEUS with MAVEN/ROSE observations will be needed to further validate our models.

The other approach is the attenuation of radio signals by the Martian ionosphere as introduced in Chapter 1. Harada, Nakamura, et al. (to be submitted) analyzed the attenuation of surface echo by MEx/MARSIS during the December 2014 SEP event on Mars and found that there was a frequency-dependent attenuation of the radar signal reflected from the surface. The frequency-dependent attenuation of the radar signal can be used to estimate the altitude-dependent electron density because radio waves are attenuated where the frequency of the radio waves is equal to the electron-neutral collision frequency. Harada, Nakamura, et al. simulated the vertical electron density profiles using PTRIP and PROTEUS at several timings when the frequency-dependent attenuations were observed, and they estimated the attenuation magnitude of radio waves as a function of frequency. Harada, Nakamura, et al. were able to better reproduce the relative temporal variation of the frequency-dependent attenuation magnitude when both SEP electron and proton fluxes were considered than when only SEP electron flux was considered.

(3) Prebiotic chemistry in the ancient Martian atmosphere

A third future application of this thesis is the estimation of the concentration of HCN, N_2O, and H_2CO in the ancient Martian atmosphere due to the continuous precipitation of SEPs. As introduced in Chapter 1, SEPs are one of the key energy sources in producing HCN and N_2O leading to the synthesis of amino acids in primitive atmospheres (e.g., Kobayashi et al., 1990; Airapetian et al., 2016; Lingam et al., 2018). H_2CO is also one of our targets because H_2CO is a precursor of ribose in formose reactions (Butlerow, 1861; Breslow, 1959). Ribose is an essential component of deoxyribonucleic acid (DNA) and ribonucleic acid (RNA). In Chapter 6, we have shown that the densities of NOx and H continuously increase during a SEP event, indicating that significant enhancements of the N_2O and H_2CO densities could be expected under the continuous precipitation of SEPs into the ancient Martian atmosphere. The ancient Martian atmosphere may have been a thick CO_2 atmosphere, which is photochemically unstable leading to a CO-dominant atmosphere (e.g., Koyama et al., 2021), suggesting that the production rate of H_2CO in the ancient Martian atmosphere should have been much higher than that of present-day Mars. We will implement further chemical reactions regarding organic compounds into PROTEUS to investigate the production rate of HCN, N_2O, and H_2CO in the ancient Martian atmosphere. Coupling PROTEUS with Paleo Martian Global Climate Model (PMGCM) combined with a global river model (Kamada et al., 2020, 2021, 2022) will allow us to estimate the global distribution of the concentrations of HCN, N_2O, and H_2CO on the ancient Martian surface. A combination of PROTEUS and PMGCM will also enable us to investigate the greenhouse effect of N_2O in the ancient Martian atmosphere. Our estimate will be used to infer the concentration of amino acids and nucleic acids on the ancient Martian surface thanks to laboratory experiments by Dr. Furukawa at Tohoku University (e.g., Takeuchi, Furukawa, et al., 2020). Such a work will be useful for the search for traces of extraterrestrial life on Mars in future landing missions.

Appendix A

Derivation of screened Rutherford cross section

The number of particles dN that are scattered into a solid angle $d\Omega$ in the unit time can be expressed by using the scattered particle flux j_{sc} as follows:

$$dN = j_{\mathrm{sc}}\, r^2 d\Omega \tag{A.1}$$

Since dN is proportional to the incident particle flux j_{inc}, dN can be re-written as follows:

$$dN = j_{\mathrm{inc}} \frac{d\sigma}{d\Omega} d\Omega \quad , \tag{A.2}$$

where $d\sigma/d\Omega$ is the differential cross section.

The Schrödinger equation for a non-relativistic particle with a mass of m.

$$i\hbar \frac{\partial}{\partial t}\psi(\boldsymbol{r},t) = \left[-\frac{\hbar^2}{2m}\boldsymbol{\nabla}^2 + \quad (\boldsymbol{r})\right]\psi(\boldsymbol{r},t) \quad , \tag{A.3}$$

where i is the imaginary unit, $\hbar$ is the reduced Planck constant, ψ is the wave function, is the time-independent potential of the environment in which the particle exists. Assuming the steady state, the wave function ψ can be expressed as follows by the variable separation.

$$\psi(\boldsymbol{r},t) = f(t)\varphi(\boldsymbol{r}) \tag{A.4}$$

Substituting Equation (A.4) for ψ in Equation (A.3) and dividing both sides of the equation by $\phi(t)\varphi(\boldsymbol{r})$ gives the following equation.

$$\frac{i\hbar}{\phi(t)}\frac{\partial\phi(t)}{\partial t} = \frac{1}{\varphi(\boldsymbol{r})}\left[-\frac{\hbar^2}{2m}\boldsymbol{\nabla}^2\varphi(\boldsymbol{r}) + \quad (\boldsymbol{r})\varphi(\boldsymbol{r})\right] \tag{A.5}$$

Since the left side of Equation (A.5) is a function of time and the right side is a function of space, both sides of Equation (A.5) should be a constant value with a dimension of energy. $\phi(t)$ and $\psi(\boldsymbol{r}, t)$ can be expressed as follows:

$$\phi(t) = \exp\left[-\frac{iEt}{\hbar}\right] \tag{A.6}$$

$$\psi(\boldsymbol{r}, t) = \varphi(\boldsymbol{r})\exp\left[-\frac{iEt}{\hbar}\right] \tag{A.7}$$

Therefore, Equation (A.3) becomes

$$\left[-\frac{\hbar^2}{2m}\boldsymbol{\nabla}^2 + \quad (\boldsymbol{r})\right]\varphi(\boldsymbol{r}) = E\varphi(\boldsymbol{r}) \tag{A.8}$$

Assuming that the boundary condition of the potential $\quad (\boldsymbol{r}) \rightarrow 0$ when $r \rightarrow \infty$, Equation (A.8) should satisfy the following condition.

$$-\frac{\hbar^2}{2m}\boldsymbol{\nabla}^2\varphi(\boldsymbol{r}) = E\varphi(\boldsymbol{r}) \qquad (r \rightarrow \infty) \tag{A.9}$$

Assuming that an incident particle is moving towards the target particle along the $\boldsymbol{e}_z$ direction with a wave vector $\boldsymbol{k} = k\boldsymbol{e}_z$, the solution of Equation (A.7) is a plane wave of the incident particle.

$$\varphi_{\mathrm{inc}}(r) = e^{ikz} \tag{A.10}$$

The other solution of Equation (A.9) is the outward scattered wave due to the interaction of the incident wave with the potential. The scattered wave should have a following form:

$$\varphi_{\mathrm{sc}}(r) = f(\theta)\frac{e^{ikz}}{r} \quad , \tag{A.11}$$

where $f(\theta)$ is the scattering amplitude. Therefore, the boundary condition at $r \to \infty$ becomes

$$\varphi(r) = e^{ikz} + f(\theta)\frac{e^{ikr}}{r} \qquad (r \to \infty) \tag{A.12}$$

In order to obtain the cross section, it is needed to calculate the probability current density described as follows:

$$\begin{aligned} \boldsymbol{j}(\boldsymbol{r}) &= \frac{\hbar}{2mi}(\varphi^* \boldsymbol{\nabla}\varphi - (\boldsymbol{\nabla}\varphi^*)\varphi) \\ &= \frac{1}{m}\mathrm{Re}\left(\varphi^* \frac{\hbar}{i}\boldsymbol{\nabla}\varphi\right) \end{aligned} \tag{A.13}$$

The gradient operator $\boldsymbol{\nabla}$ can be expressed in the polar coordinate with basis vectors $(\boldsymbol{e}_r, \boldsymbol{e}_\theta, \boldsymbol{e}_\phi)$ as follows:

$$\boldsymbol{\nabla} = \boldsymbol{e}_r\frac{\partial}{\partial r} + \boldsymbol{e}_\theta\frac{1}{r}\frac{\partial}{\partial \theta} + \boldsymbol{e}_\phi\frac{1}{r\sin\theta}\frac{\partial}{\partial \phi} \tag{A.14}$$

When $\boldsymbol{\nabla}$ operates to φ expressed as Equation (A.12), it becomes

$$\boldsymbol{\nabla}\varphi = \boldsymbol{e}_z ike^{ikz} + \boldsymbol{e}_r f(\theta)ik\frac{e^{ikr}}{r} + O(r^{-2}) \tag{A.15}$$

$$\therefore \frac{\hbar}{i}\boldsymbol{\nabla}\varphi = \hbar k\left[\boldsymbol{e}_z e^{ikz} + \boldsymbol{e}_r f(\theta)\frac{e^{ikr}}{r} + O(r^{-2})\right] \tag{A.16}$$

Then the boundary condition of the probability current density at $r \to \infty$ becomes

$$\boldsymbol{j}(\boldsymbol{r}) \overset{r\to\infty}{\longrightarrow} \frac{\hbar k}{m}\left[\boldsymbol{e}_z + \boldsymbol{e}_r|f(\theta)|^2\frac{1}{r^2} + (\boldsymbol{e}_z + \boldsymbol{e}_r)\mathrm{Re}\ \left. f(\theta)\frac{e^{ik(r-z)}}{r}\right\} + \cdots\right] \tag{A.17}$$

The first term in Equation (A.17) is current along the $\boldsymbol{e}_z$ direction, which corresponds to the incident particle beam j_{inc}, and the second term is the radially outward current, which corresponds to the scattered particle beam j_{sc}.

$$j_{\mathrm{inc}} = j_z = \frac{\hbar k}{m} \tag{A.18}$$

$$j_{\mathrm{sc}} = j_r = \frac{\hbar k}{m}\frac{|f(\theta)|^2}{r^2} \tag{A.19}$$

Then the number of particles dN that are scattered into a solid angle $d\Omega$ in the unit time is

$$dN = j_{\mathrm{sc}}\, r^2 d\Omega = \frac{\hbar k}{m}|f(\theta)|^2 d\Omega = j_{\mathrm{inc}}|f(\theta)|^2 d\Omega \tag{A.20}$$

By comparing Equation (A.20) with (A.2), the differential cross section $d\sigma/d\Omega$ can be expressed as follows:

$$\frac{d\sigma}{d\Omega} = |f(\theta)|^2 \tag{A.21}$$

Therefore, the derivation of the differential cross section comes down to a problem for the derivation of the scattering amplitude $f(\theta)$.

Back to Equation (A.8), it can be re-written as follows:

$$(\boldsymbol{\nabla}^2 + k^2)\varphi(\boldsymbol{r}) = U(r)\varphi(\boldsymbol{r}) \tag{A.22}$$

Where k and $U(r)$ are defined as follows:

$$k = \frac{2mE}{\hbar^2} \tag{A.23}$$

$$U(r) = \frac{2m\ \ (r)}{\hbar^2} \tag{A.24}$$

In order to solve the differential equation (A.22), the Green function $G(\boldsymbol{r})$ is introduced that satisfies the following equation:

$$(\boldsymbol{\nabla}^2 + k^2)G(\boldsymbol{r}) = \delta(\boldsymbol{r}) \tag{A.25}$$

Solving the differential equation (A.22) under a boundary condition (A.12) comes down to solving the following integral equation:

$$\varphi(\boldsymbol{r}) = \varphi_0(\boldsymbol{r}) + \int d^3r \;\; G(\boldsymbol{r} - \boldsymbol{r}\;)U(r\;)\varphi(\boldsymbol{r}\;) \quad , \tag{A.26}$$

where $\varphi_0(\boldsymbol{r})$ is the plane wave function e^{ikz} that satisfies $(\boldsymbol{\nabla}^2 + k^2)\varphi_0(\boldsymbol{r}) = 0$. Equation (A.26) can be proved by operating $(\boldsymbol{\nabla}^2 + k^2)$ from the left on both sides of Equation (A.26). The solution of Equation (A.25) for the Green function is

$$G_\pm(\boldsymbol{r}) = -\frac{1}{4\pi}\frac{e^{\pm ikr}}{r} \tag{A.27}$$

where $G_+(\boldsymbol{r})$ is the radially outward spherical wave and $G_-(\boldsymbol{r})$ is the radially inward spherical wave. To satisfy the boundary condition (A.12), the outward spherical wave $G_+(\boldsymbol{r})$ should be chosen. Then the integral equation (A.26) becomes

$$\begin{aligned} \varphi^+(\boldsymbol{r}) &= e^{ikz} + \int d^3r \;\; G_+(\boldsymbol{r} - \boldsymbol{r}\;)U(r\;)\varphi(\boldsymbol{r}\;) \\ &= e^{ikz} - \frac{1}{4\pi}\int d^3r \;\; \frac{e^{ik|r-r\prime|}}{|\boldsymbol{r} - \boldsymbol{r}\;|}U(r\;)\varphi^+(\boldsymbol{r}) \end{aligned} \tag{A.28}$$

$G_+(\boldsymbol{r} - \boldsymbol{r}\;)$ can be approximated as follows at $r \to \infty$ and by assuming $r \gg r$.

$$|\boldsymbol{r} - \boldsymbol{r}\;| = r - \boldsymbol{e}_r \cdot \boldsymbol{r} \; + O\left(\frac{r}{r}\right) \tag{A.29}$$

$$\therefore k|\boldsymbol{r} - \boldsymbol{r}\;| = kr - \boldsymbol{k} \cdot \boldsymbol{r} \; + O\left(k\frac{r}{r}\right) \tag{A.30}$$

$$\frac{1}{|\boldsymbol{r} - \boldsymbol{r}\;|} = \frac{1}{r} + O\left(\frac{r}{r^2}\right) \tag{A.31}$$

$$\therefore \;\; G_+(\boldsymbol{r} - \boldsymbol{r}\;) \overset{r\to\infty}{\longrightarrow} -\frac{1}{4\pi}\frac{e^{ikr}}{r}e^{-i\boldsymbol{k}\cdot\boldsymbol{r}\prime} \tag{A.32}$$

Substituting Equation (A.32) for $G_+(\boldsymbol{r}-\boldsymbol{r}\ )$ in Equation (A.28) gives

$$\begin{aligned}\varphi^+(\boldsymbol{r}) &= e^{ikz} + \int d^3r'\, G_+(\boldsymbol{r}-\boldsymbol{r}')U(r')\varphi(\boldsymbol{r}') \\ &\overset{r\to\infty}{\longrightarrow} e^{ikz} - \frac{1}{4\pi}\frac{e^{ikr}}{r}\int d^3r\ e^{-i\boldsymbol{k}\cdot\boldsymbol{r}'}U(r\ )\varphi^+(\boldsymbol{r})\end{aligned} \tag{A.33}$$

By comparing Equation (A.33) with (A.12), the scattering amplitude $f(\theta)$ can be obtained as follows:

$$f(\theta) = -\frac{m}{2\pi\hbar^2}\int d^3r\ e^{-i\boldsymbol{k}\cdot\boldsymbol{r}'}\ \ (r\ )\varphi^+(\boldsymbol{r}) \tag{A.34}$$

Since the scattering amplitude $f(\theta)$ in Equation (A.34) contains unknown function $\varphi^+(\boldsymbol{r})$, it cannot simply be used for the calculation of the differential cross section. In such a case, perturbation method is useful to approximate the unknown function $\varphi^+(\boldsymbol{r})$. Suppose $\boldsymbol{k}_i = k\boldsymbol{e}_z$, $\varphi^+(\boldsymbol{r})$ can be expanded as follows by the perturbation method starting with the 0th order approximation $\varphi_0(\boldsymbol{r}) = e^{ikz} = e^{i\boldsymbol{k}_i\cdot\boldsymbol{r}}$.

$$\begin{aligned}\varphi^+(\boldsymbol{r}) &= e^{i\boldsymbol{k}_i\cdot\boldsymbol{r}} \\ &\quad + \int d^3r'\, G_+(\boldsymbol{r}-\boldsymbol{r}')U(r')e^{i\boldsymbol{k}_i\cdot\boldsymbol{r}'} \\ &\quad + \int d^3r' \int d^3r'\ \ G_+(\boldsymbol{r}-\boldsymbol{r}')U(r')e^{i\boldsymbol{k}_i\cdot\boldsymbol{r}'}\, G_+(\boldsymbol{r}'-\boldsymbol{r}'\ )U(r'\ )e^{i\boldsymbol{k}_i\cdot\boldsymbol{r}''} \\ &\quad + \cdots\end{aligned} \tag{A.35}$$

Substituting Equation (A.35) for $\varphi^+(\boldsymbol{r})$ in Equation (A.34) gives

$$\begin{aligned}f(\theta) &= -\frac{m}{2\pi\hbar^2}\int d^3r\ e^{-i\boldsymbol{k}\cdot\boldsymbol{r}'}\ \ (r\ )e^{i\boldsymbol{k}_i\cdot\boldsymbol{r}'} \\ &\quad - \frac{m}{2\pi\hbar^2}\int d^3r\ \int d^3r'\ e^{-i\boldsymbol{k}\cdot\boldsymbol{r}'}\ \ (r\ )G_+(\boldsymbol{r}-\boldsymbol{r}')U(r')e^{i\boldsymbol{k}_i\cdot\boldsymbol{r}''} \\ &\quad + \cdots\end{aligned} \tag{A.36}$$

Using the first term in Equation (A.36) is called the Born approximation expressed as follows:

$$f(\theta) = -\frac{m}{2\pi\hbar^2}\int d^3r\ e^{-i\boldsymbol{K}\cdot\boldsymbol{r}'}\ \ (r\ ) \quad , \qquad \text{(A.37)}$$

where $\boldsymbol{K} = \boldsymbol{k} - \boldsymbol{k}_i$ (Figure A.1). Assuming that the potential $\ (r)$ is the central force field, Equation (A.36) becomes

$$\begin{aligned} f(\theta) &= -\frac{m}{2\pi\hbar^2}\int_0^\infty \ (r) r^2 dr \int_0^{2\pi} d\phi \int_0^{\pi} e^{-iKr\cos\vartheta}\sin\vartheta\, d\vartheta \\ &= -\frac{2m}{\hbar^2}\int_0^\infty \ (r) r \frac{\sin\ \ r}{\ } dr \end{aligned} \qquad \text{(A.38)}$$

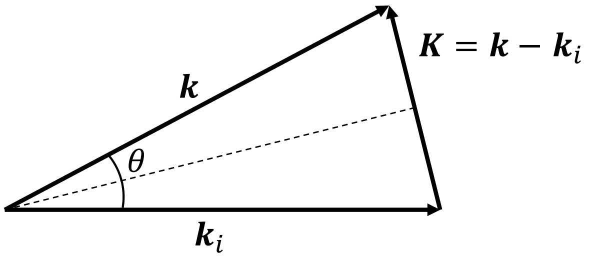

Figure A.1 Illustration of the scattering angle θ and $\boldsymbol{k}$ vectors.

The differential cross section $d\sigma/d\Omega = |f(\theta)|^2$ by the Born approximation can be expressed as follows:

$$\frac{d\sigma}{d\Omega} = \frac{4m^2}{\hbar^4}\left|\int_0^\infty \ (r) r \frac{\sin\ \ r}{\ } dr\right|^2 \qquad \text{(A.39)}$$

Assuming that the incident particle is a proton, the screened Coulomb potential can be expressed as follows:

$$\ (r) = \frac{Z{q_e}^2}{4\pi\varepsilon_0}\frac{e^{-r/a}}{r} \quad , \qquad \text{(A.40)}$$

where Z is the atomic number of the target particle, q_e is the elementary charge, ε_0 is the vacuum permittivity, and a is the Fermi radius of the target particle. This screened Coulomb potential represents the screening of the nuclear charge by atomic electrons around it. Substituting the screened Coulomb potential for $\quad(r)$ in Equation (A.38) gives

$$\begin{aligned} f(\theta) &= -\frac{2m}{\hbar^2}\frac{Zq_e{}^2}{4\pi\varepsilon_0}\int_0^\infty e^{-r/a}\frac{\sin\quad r}{\quad}\,dr \\ &= -\frac{2m}{\hbar^2}\frac{Zq_e{}^2}{4\pi\varepsilon_0}\frac{1}{2}\int_0^\infty\left(e^{-\left(\frac{1}{a}-iK\right)r} - e^{-\left(\frac{1}{a}+iK\right)r}\right)dr \\ &= -\frac{2m}{\hbar^2}\frac{Zq_e{}^2}{4\pi\varepsilon_0}\frac{1}{\left(\frac{1}{a}\right)^2 + \quad{}^2} \end{aligned} \tag{A.41}$$

Since $\quad = 2k\sin(\theta/2)$ (Figure A.1), Equation (A.41) becomes

$$\begin{aligned} f(\theta) &= -\frac{2m}{\hbar^2}\frac{Zq_e{}^2}{4\pi\varepsilon_0}\frac{1}{\left(\frac{1}{a}\right)^2 + \quad{}^2} \\ &= -\frac{2m}{\hbar^2}\frac{Zq_e{}^2}{4\pi\varepsilon_0}\frac{1}{\left(\frac{1}{a}\right)^2 + 4k^2\sin^2\frac{\theta}{2}} \\ &= -\frac{Zq_e{}^2}{4\pi\varepsilon_0}\frac{1}{4}\frac{2m}{\hbar^2k^2}\frac{1}{\left(\frac{1}{2ka}\right)^2 + \sin^2\frac{\theta}{2}} \end{aligned} \tag{A.42}$$

Since $\hbar^2k^2/2m$ is the energy of the incident particle E, Equation (A.42) becomes

$$\begin{aligned} f(\theta) &= -\frac{Zq_e{}^2}{4\pi\varepsilon_0}\frac{1}{4}\frac{2m}{\hbar^2k^2}\frac{1}{\left(\frac{1}{2ka}\right)^2 + \sin^2\frac{\theta}{2}} \\ &= -\frac{Zq_e{}^2}{4\pi\varepsilon_0}\frac{1}{4E}\frac{1}{\left(\frac{1}{2ka}\right)^2 + \sin^2\frac{\theta}{2}} \end{aligned} \tag{A.43}$$

Using the definition of the de Broglie wavelength $\lambda = h/p = 2\pi/k$, Equation (A.43) becomes

$$\begin{aligned} f(\theta) &= -\frac{Zq_e{}^2}{4\pi\varepsilon_0}\frac{1}{4E}\frac{1}{\left(\frac{1}{2ka}\right)^2 + \sin^2\frac{\theta}{2}} \\ &= -\frac{Zq_e{}^2}{4\pi\varepsilon_0}\frac{1}{4E}\frac{1}{\frac{1}{4}\left(\frac{\lambda}{2\pi a}\right)^2 + \frac{1}{2}(1-\cos\theta)} \quad , \\ &= -\frac{Zq_e}{8\pi\varepsilon_0 E_{\mathrm{eV}}}\left(\frac{1}{1-\cos\theta+2\eta}\right) \end{aligned} \tag{A.44}$$

where E_{eV} is the incident particle energy in the unit of eV, and η is the screening parameter defined as follows:

$$\eta = \frac{1}{4}\left(\frac{\lambda}{2\pi a}\right)^2 \tag{A.45}$$

The screened parameter η has been modified by Nigam et al. (1959) as follows:

$$\eta = \frac{1}{4}\left(1.12\frac{\lambda}{2\pi a}\right)^2 \tag{A.46}$$

Finally, the differential cross section, called the screened Rutherford cross section, can be expressed as follows:

$$\frac{d\sigma}{d\Omega} = |f(\theta)|^2 = \left(\frac{Zq_e}{8\pi\varepsilon_0 E_{\mathrm{eV}}}\right)^2\left(\frac{1}{1-\cos\theta+2\eta}\right)^2 \tag{A.47}$$

We referred to Igi and Kawai (1994) for the derivation of the differential cross section with some modifications for the scattering of protons under the screened Coulomb potential.

Appendix B

Particle fluxes converted from trajectories

Examples of the particle fluxes converted from the trajectories of particles and mean cosine pitch angles are shown in Figures B.1-B.5. Figures B.1 and B.2 show the results for the primary electrons and secondary electrons due to precipitation of incident 100 keV electrons, respectively. Figures B.3, B.4, and B.5 shows the results for the primary protons, hydrogen atoms, and secondary electrons due to the precipitation of incident 1 MeV protons, respectively.

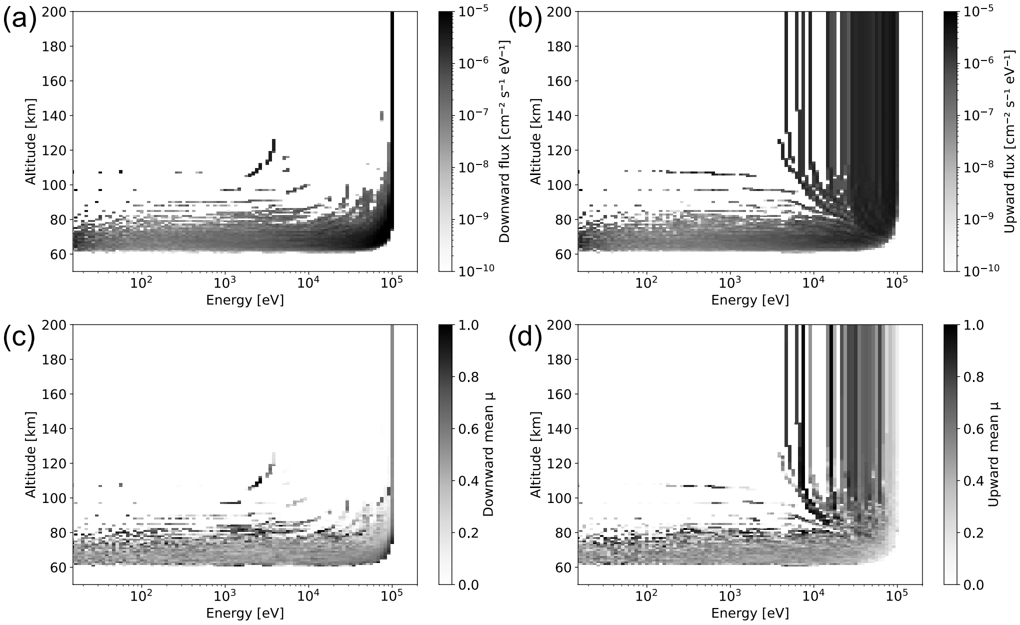

Figure B.1 (a, b) Downward and upward fluxes of primary electrons converted from the particles’ trajectories (using Equation (2.9) and (2.8)) due to the precipitation of incident 100 keV electrons, respectively. (c, d) Mean cosine pitch angles of downward and upward primary electrons (using Equation (2.11) and (2.10)) due to the precipitation of incident 100 keV electrons, respectively.

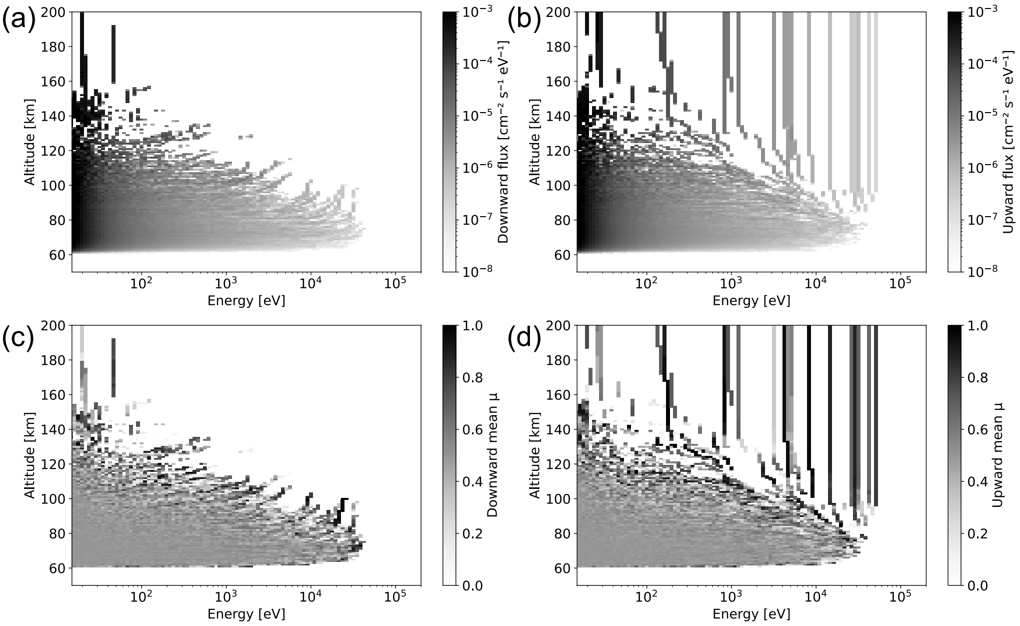

Figure B.2 Same as Figure B.1, but for secondary electrons due to precipitation of incident 100 keV electrons.

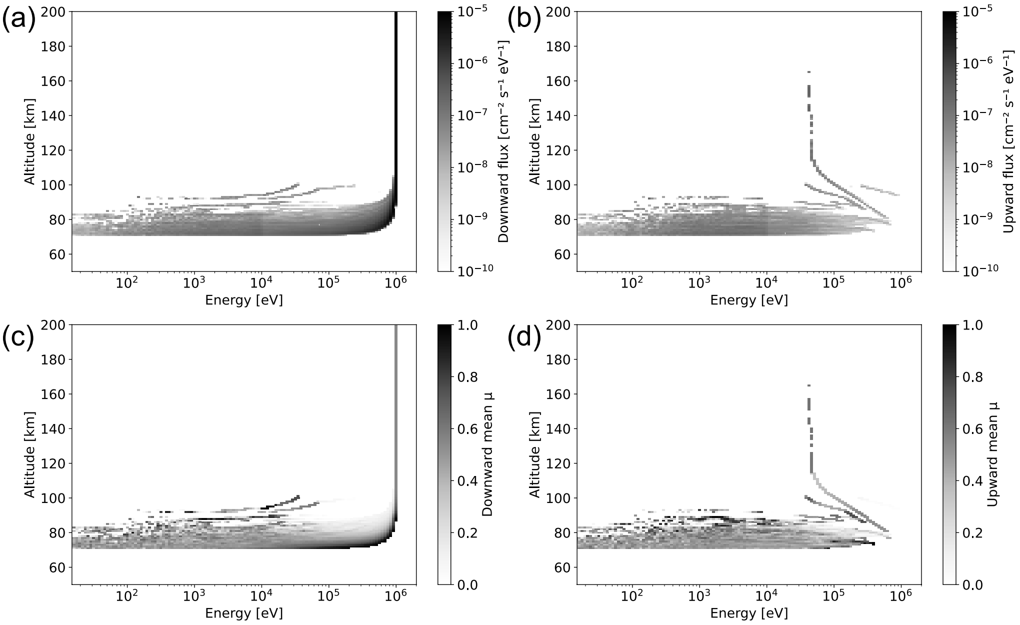

Figure B.3 Same as Figure B.1, but for primary protons due to precipitation of incident 1 MeV protons.

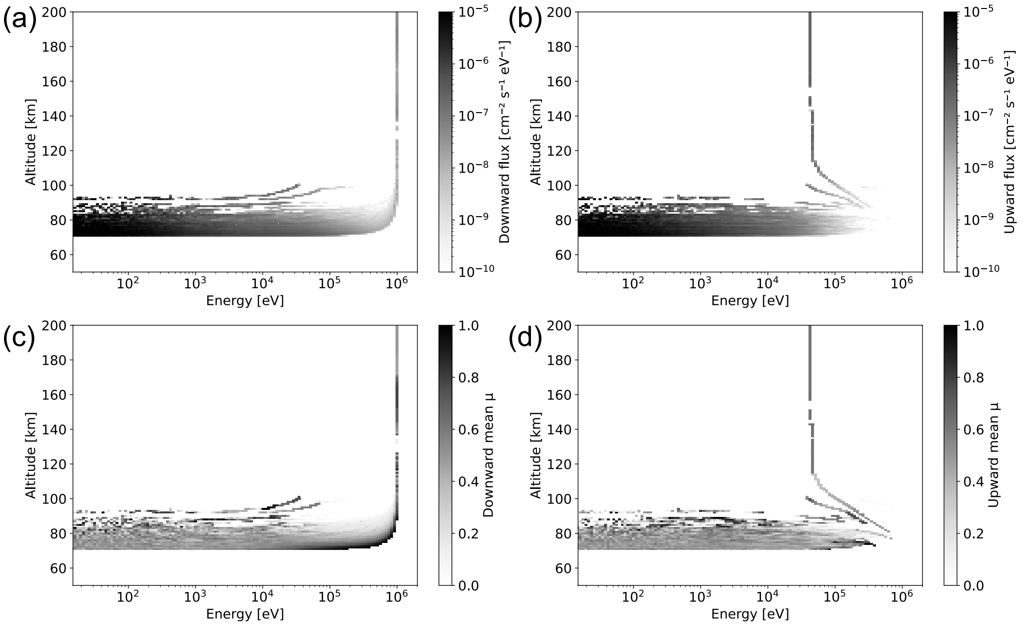

Figure B.4 Same as Figure B.1, but for hydrogen atoms due to precipitation of incident 1 MeV protons.

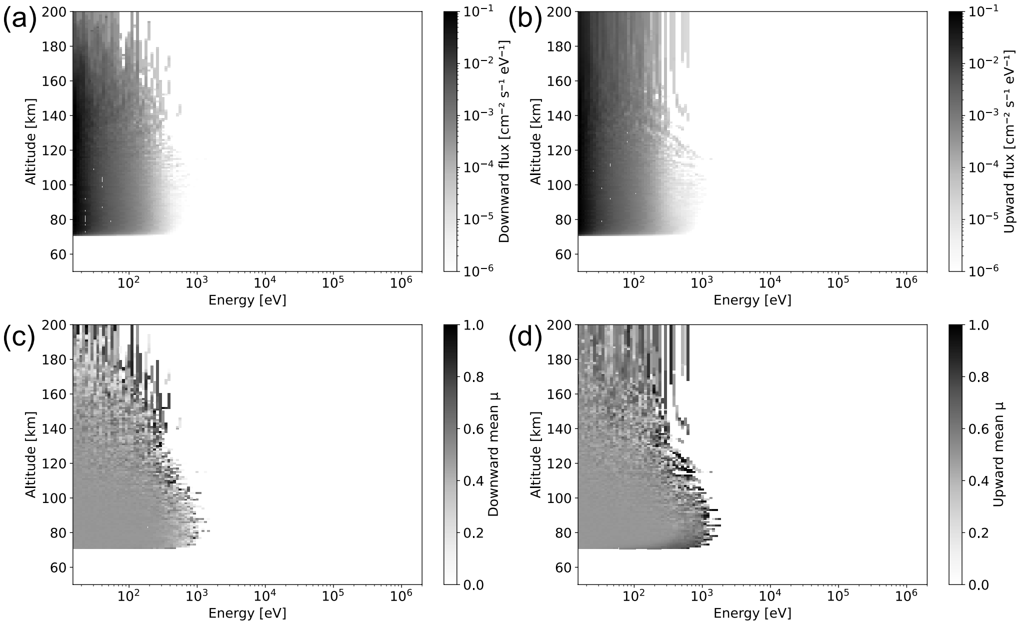

Figure B.5 Same as Figure B.1, but for secondary electrons due to precipitation of incident 1 MeV protons.

Appendix C

Absorption and dissociation cross sections

The absorption and the dissociation cross sections used in PROTEUS for the application to the Martian atmosphere are listed in Table C.1 and displayed in Figures C.1 and C.2.

Table C.1 List of cross sections and quantum yields implemented into PROTEUS.

	Species or reactions	Wavelength range	References
σ^a	CO_2 (absorption)	0.1254-138.8869 nm	Huestis and Berkowitz (2011)[a]
		138.8913 - 212.7660 nm	Schmidt et al. (2013)
ϕ	$CO_2 + h\nu \rightarrow CO + O$	138.8913 - 212.7660 nm	(Assumed to be 1.0)
σ^d	$CO_2 + h\nu \rightarrow CO + O(^1D)$	0.1 - 138 nm	Huebner and Mukherjee (2015)[b]
σ^a	$^{13}CO_2$ (absorption)	138.8913 - 212.7660nm	Schmidt et al. (2013)
σ^a	O_2 (absorption)	0.99 - 43.5 nm	Huffman (1969)[a]
		49.043646 - 103.066357 nm	Holland et al. (1993)[a]
		103.62 - 107.74 nm	Lee (1955)[a]
		108.75 - 114.95 nm	Ogawa and Ogawa (1975)[a]
		115 - 130.02 nm	Lu et al. (2010)[a]
		130.04 - 175.24 nm	Yoshino et al. (2005)[a]
		175.4 - 204 nm	Minschwaner et al. (1992)[a]
		193 - 245 nm	Yoshino et al. (1992)[a]
ϕ	$O_2 + h\nu \rightarrow O + O$	103 - 242 nm	Burkholder et al. (2015)
ϕ	$O_2 + h\nu \rightarrow O + O(^1D)$	103 - 175 nm	Burkholder et al. (2015)

Table C.1 - *Continued*

	Species or reactions	Wavelength range	References
σ^a	H_2O (absorption)	6.2 - 59.04 nm	Chan et al. (1993)[a]
		60.01 - 114.58 nm	Gürtler et al. (1977)[a]
		114.80 - 120.35 nm	Mota et al. (2005)[a]
		120.38 - 139.99 nm	Yoshino et al. (1996, 1997)[a]
		140.00 - 196.00 nm	Chung et al. (2001)[a]
		196.031 - 230.413 nm	Ranjan et al. (2020)[a]
ϕ	$H_2O + h\nu \rightarrow H + OH$	105 nm -	Burkholder et al. (2015)
ϕ	$H_2O + h\nu \rightarrow H_2 + O(^1D)$	105 - 145 nm	Burkholder et al. (2015)
σ^a	O_3 (absorption)	0.06 - 210 nm	Huebner and Mukherjee (2015)[b]
		213.330 - 1100 nm	Gorshelev et al. (2014)
			Serdyuchenko et al. (2014)
ϕ	$O_3 + h\nu \rightarrow O_2 + O(^1D)$	220 - 340 nm	Matsumi et al. (2002)[a]
ϕ	$O_3 + h\nu \rightarrow O_2 + O$	220 - 340 nm	(Assumed to be $1 - \phi(O_3 \rightarrow O(^1D))$)
σ^a	HO_2 (absorption)	190 - 260 nm	Burkholder et al. (2015)
ϕ	$HO_2 + h\nu \rightarrow OH + O$	190 - 260 nm	Burkholder et al. (2015)
σ^a	H_2O_2 (absorption)	121.33 - 189.70 nm	Schürgers and Welge (1968)[a]
		190.00 - 255.00 nm	Burkholder et al. (2015)
ϕ	$H_2O_2 + h\nu \rightarrow HO_2 + H$	121 - 230 nm	Burkholder et al. (2015)
ϕ	$H_2O_2 + h\nu \rightarrow OH + OH$	121 - 340 nm	Burkholder et al. (2015)
σ^a	OH (absorption)	0.06 - 282.3 nm	Huebner and Mukherjee (2015)[b]
σ^d	$OH + h\nu \rightarrow H + O$	124.5 - 261.65 nm	Huebner and Mukherjee (2015)[b]
σ^d	$OH + h\nu \rightarrow H + O(^1D)$	93 - 511.4 nm	Huebner and Mukherjee (2015)[b]
σ^a	H_2 (absorption)	0.1 - 110.86 nm	Huebner and Mukherjee (2015)[b]
σ^d	$H_2 + h\nu \rightarrow H + H$	84.48 - 110.86 nm	Huebner and Mukherjee (2015)[b]
σ^a	N_2 (absorption)	0.1 - 103.8 nm	Huebner and Mukherjee (2015)[b]
σ^d	$N_2 + h\nu \rightarrow N + N$	51.96 - 103.8 nm	Huebner and Mukherjee (2015)[b]
σ^a	NO (absorption)	0.1 - 191 nm	Huebner and Mukherjee (2015)[b]
σ^d	$NO + h\nu \rightarrow N + O$	0.1 - 191 nm	Huebner and Mukherjee (2015)[b]

Table C.1 - *Continued*

	Species or reactions	Wavelength range	References
σ^a	NO_2 (absorption)	0.06 - 238 nm	Huebner and Mukherjee (2015)[b]
		238.08219 - 666.57808 nm	Vandaele et al. (1998)[a]
σ^d	$NO_2 + hv \rightarrow NO + O(^1D)$	108 - 243.88 nm	Huebner and Mukherjee (2015)[b]
ϕ	$NO_2 + hv \rightarrow NO + O$	108 - 238 nm	Huebner and Mukherjee (2015)[b]
		239 - 300 nm	(Assumed to be 1)
		300 - 422 nm	Burkholder et al. (2015)
σ^a	NO_3 (absorption)	400 - 691 nm	Wayne et al. (1991)[a]
ϕ	$NO_3 + hv \rightarrow NO_2 + O$	400 - 640 nm	Johnston et al. (1996)[a]
ϕ	$NO_3 + hv \rightarrow NO + O_2$	586 - 640 nm	Johnston et al. (1996)[a]
σ^a	N_2O (absorption)	16.8 - 59.0 nm	Hitchcock et al. (1980)[a]
		60.0 - 99.9 nm	Cook et al. (1968)[a]
		108.20 - 122.18 nm	Zelikoff et al. (1953)[a]
		122.25 - 172.88 nm	Rabalais et al. (1971)[a]
		173 - 210 nm	Selwyn et al. (1977)[a]
ϕ	$N_2O + hv \rightarrow N_2 + O(^1D)$	140 - 230 nm	Burkholder et al. (2015)
σ^a	N_2O_5 (absorption)	152 - 198 nm	Osborne et al. (2000)[a]
		200 - 260 nm	Burkholder et al. (2015)
		260 - 410 nm	Burkholder et al. (2015)
ϕ	$N_2O_5 + hv \rightarrow NO_3 + NO_2$	248 - 410 nm	Burkholder et al. (2015)
ϕ	$N_2O_5 + hv \rightarrow NO_3 + NO + O$	152 - 289 nm	Burkholder et al. (2015)
σ^a	HNO_2 (absorption)	184 - 396 nm	Burkholder et al. (2015)
ϕ	$HNO_2 + hv \rightarrow NO + OH$	All	Burkholder et al. (2015)
σ^a	HNO_3 (absorption)	192 - 350 nm	Burkholder et al. (2015)
ϕ	$HNO_3 + hv \rightarrow HNO_2 + O$	193 - 260 nm	Estimated[c]
ϕ	$HNO_3 + hv \rightarrow HNO_2 + O(^1D)$	193 - 222 nm	Estimated[c]
ϕ	$HNO_3 + hv \rightarrow OH + NO_2$	193 - 350 nm	Estimated[c]

Table C.1 - *Continued*

	Species or reactions	Wavelength range	References
σ^a	HO_2NO_2 (absorption)	190 - 280 nm	Burkholder et al. (2015)
		280 - 350 nm	Burkholder et al. (2015)
ϕ	$HO_2NO_2 + hv \rightarrow HO_2 + NO_2$	190 - 350 nm	Burkholder et al. (2015)
ϕ	$HO_2NO_2 + hv \rightarrow OH + NO_3$	190 - 350 nm	Burkholder et al. (2015)
σ^a	H_2CO (absorption)	224.56 - 376 nm	Meller and Moortgat (2000)[a]
ϕ	$H_2CO + hv \rightarrow H_2 + CO$	250 - 360 nm	Burkholder et al. (2015)
ϕ	$H_2CO + hv \rightarrow H + HCO$	250 - 360 nm	Burkholder et al. (2015)

σ^a: Absorption cross section, σ^d: dissociation cross section, ϕ: quantum yield, [a]: data files are taken from The MPI-Mainz UV/VIS Spectral Atlas (Keller-Rudek et al., 2013), [b]: data files are taken from PHIDRATES (Huebner and Mukherjee, 2015), [c]: quantum yields for each photolysis reaction of HNO_3 were estimated by quantum yield of each product (OH, O, and O(^{1}D)) obtained by Johnston et al. (1974), Turnipseed et al. (1992), and Margitan and Watson (1982).

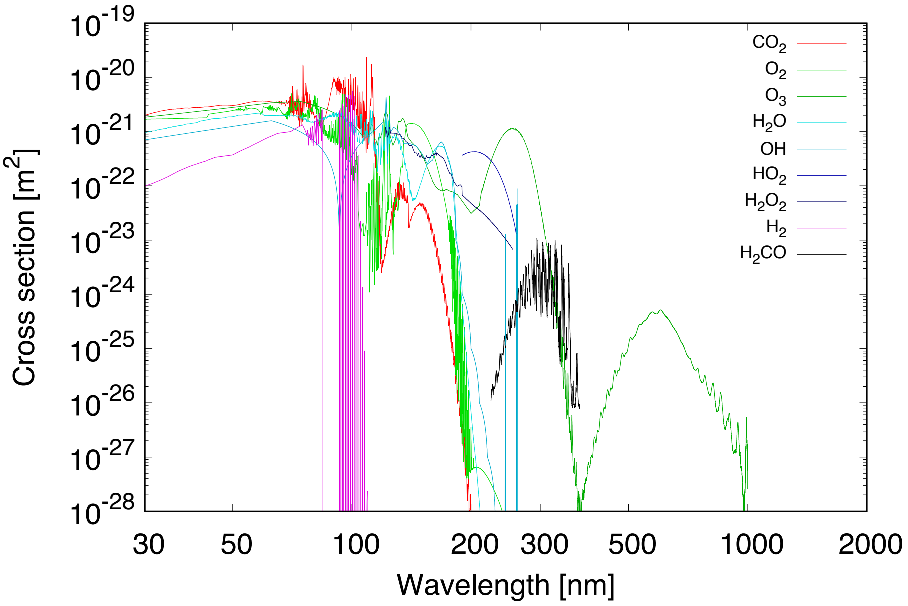

Figure C.1 Absorption cross sections for C-, H-, and O-baring species implemented into PROTEUS. The neutral temperature is set to 210 K to calculate cross sections.

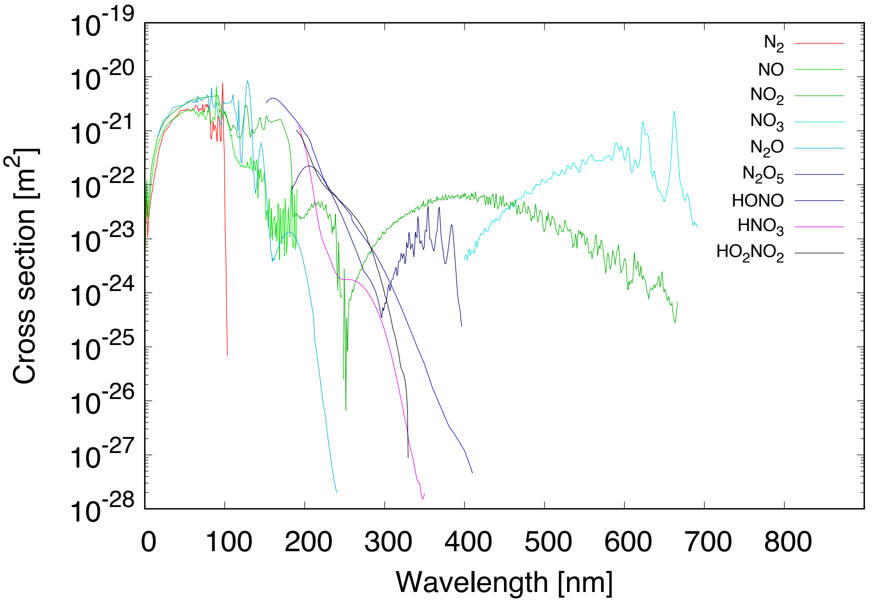

Figure C.2 Absorption cross sections for nitrogen-related species implemented into PROTEUS. The neutral temperature is set to 210 K to calculate cross sections.

Appendix D

Cubed sphere grid

Generation of the Nth order cubed sphere grid begins with the cube dividing each edge into N edges (Figure D.1a). The vertices on the original cubic grid are then projected onto a spherical surface (Figure D.1b) to become a cubed sphere grid (Figure D.1c). Each edge of the original cube is non-uniformly divided in order to make the surface area of cells uniform when projected onto the spherical surface, which will be explained later.

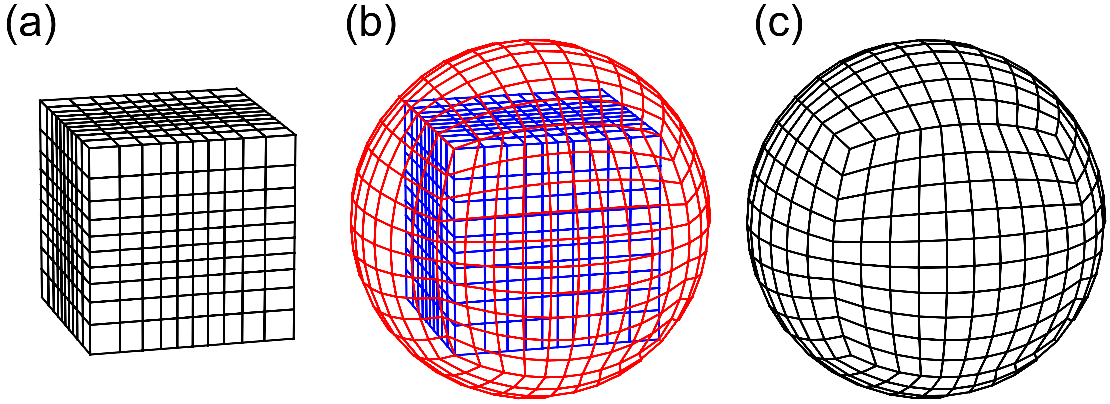

Figure D.1 Generation of a 10th order cubed sphere grid.

The localization method, a method for identifying the grid index at a particle's position, is easy for the cubed sphere grid. Since the cubed sphere grid is generated by projecting a cubic grid onto a spherical surface, the particle location can easily be identified by projecting the particle's position (red dot in Figure D.2) onto the original cubic grid (blue dot in Figure D.2).

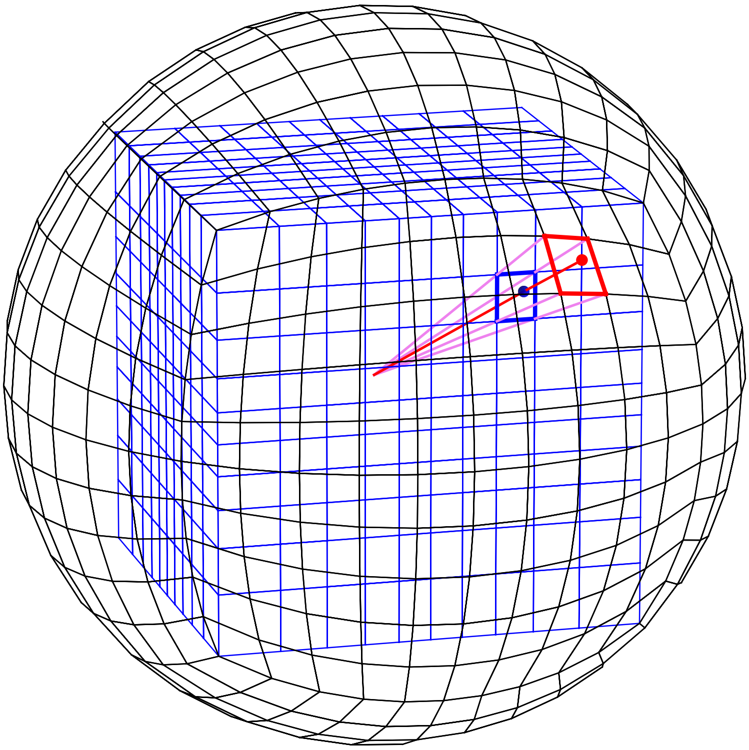

Figure D.2 Illustration of the localization method.

The definition of indices of cells and vertices of the cubed sphere grid is defined as follows. First, we named the square faces of the original cube "Square 1" to "Square 6", and divided each square into $\mathrm{N}\times\mathrm{N}$ cells (Figure D.3). Then we define the group of vertices as 'A' to 'F' on the faces of "Square 1" to "Square 6", respectively, not to overlap each other. The index of each cell is defined sequentially from "Square 1" to "Square 6". Indices of cells in "Square 1" are $1 \sim \mathrm{N}^2$, those in "Square 2" are $\mathrm{N}^2 + 1 \sim 2\mathrm{N}^2$, those in "Square 3" are $2\mathrm{N}^2 + 1 \sim 3\mathrm{N}^2$, those in "Square 4" are $3\mathrm{N}^2 + 1 \sim 4\mathrm{N}^2$, those in "Square 5" are $4\mathrm{N}^2 + 1 \sim 5\mathrm{N}^2$, and those in "Square 6" are $5\mathrm{N}^2 + 1 \sim \ \mathrm{N}^2$. The vertices of the original cube are named as "a" to "h" in order to make the relative position of faces easy to read.

The center of the original cube locates at $(x, y, z) = (0,0,0)$, and the cube has a $2/\sqrt{3}$ length for each edge. The definition of indices of vertices, the position of each vertex, and the localization method will be described for each face as follows.

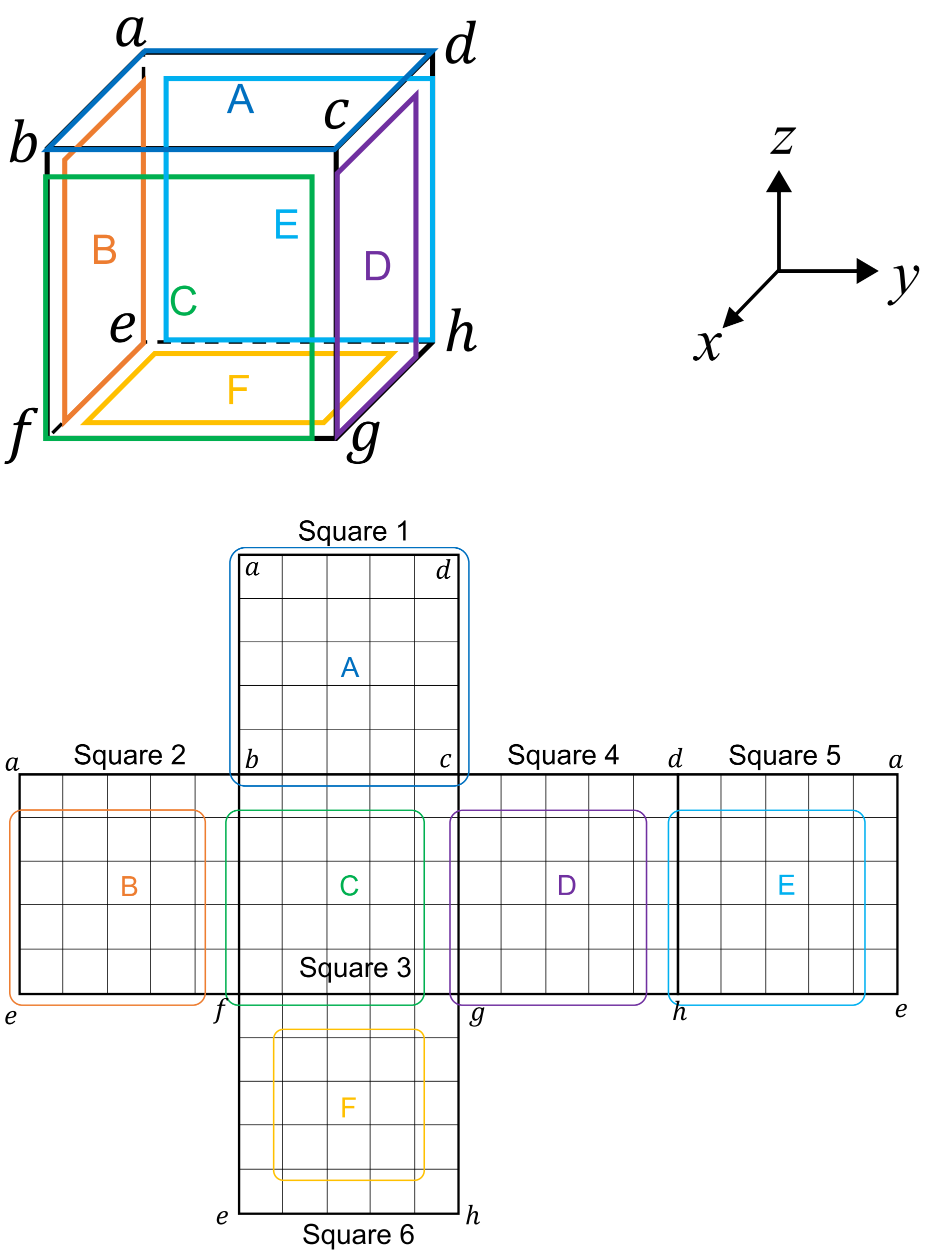

Figure D.3 Illustration of the definition of the faces of the original cube and the group of vertices on each face.

Positions of the vertices of the original cube are defined as follows:

$$
\begin{aligned}
a &= \left(-\frac{1}{\sqrt{3}}, -\frac{1}{\sqrt{3}}, \frac{1}{\sqrt{3}}\right) \\
b &= \left(\frac{1}{\sqrt{3}}, -\frac{1}{\sqrt{3}}, \frac{1}{\sqrt{3}}\right) \\
c &= \left(\frac{1}{\sqrt{3}}, \frac{1}{\sqrt{3}}, \frac{1}{\sqrt{3}}\right) \\
d &= \left(-\frac{1}{\sqrt{3}}, \frac{1}{\sqrt{3}}, \frac{1}{\sqrt{3}}\right) \\
e &= \left(-\frac{1}{\sqrt{3}}, -\frac{1}{\sqrt{3}}, -\frac{1}{\sqrt{3}}\right) \\
f &= \left(\frac{1}{\sqrt{3}}, -\frac{1}{\sqrt{3}}, -\frac{1}{\sqrt{3}}\right) \\
g &= \left(\frac{1}{\sqrt{3}}, \frac{1}{\sqrt{3}}, -\frac{1}{\sqrt{3}}\right) \\
h &= \left(-\frac{1}{\sqrt{3}}, \frac{1}{\sqrt{3}}, -\frac{1}{\sqrt{3}}\right)
\end{aligned}
$$

(a) Cell indices – Square 1

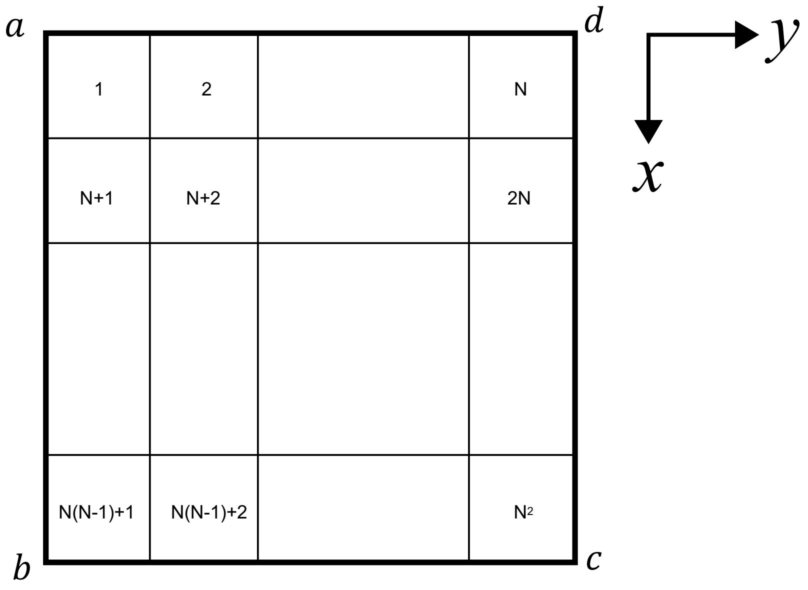

(b) Vertex indices – Square 1

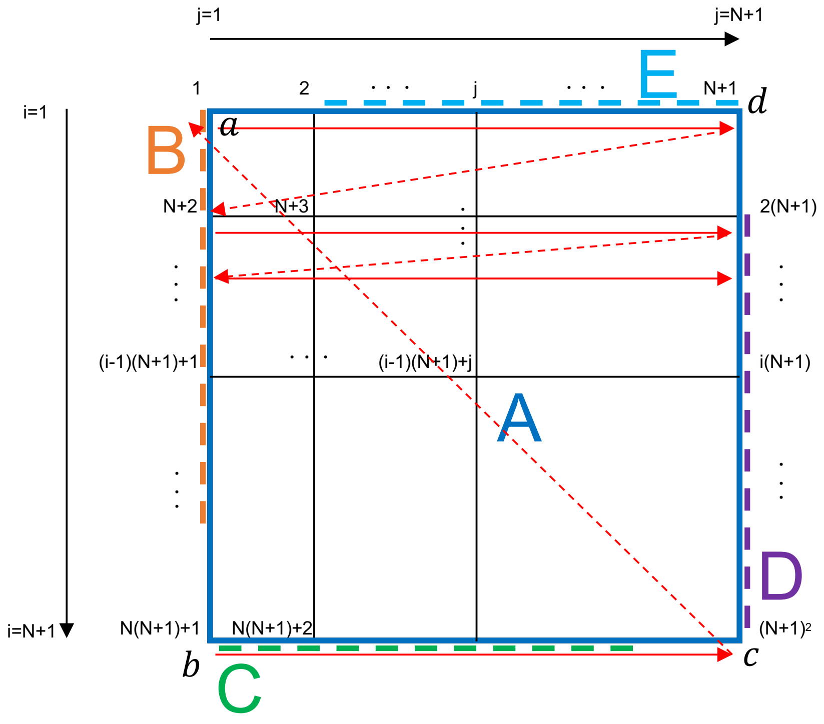

Figure D.4 (a, b) Illustration of the definition of indices of each cell and each vertex on the face “Square 1”, respectively.

"Square 1"

The face "Square 1" consists only of the vertex group "A". The indices of vertices are defined as "1~(N+1)^2" as illustrated in Figure D.4. The index of the vertex group "A" starts at (i, j)=(1,1), and the index of vertex increases from the point (i, j)=(1,1) to (1,N+1), and then move to the next line of i from the point (i, j)=(2,1) to (2,N+1). The index of the vertex group "A" finishes at the point (i, j)=(N+1,N+1).

The position of each vertex (x_i, y_j, z) on the original cube is defined as follows:

$$x_i = \frac{1}{\sqrt{3}} \tan\left(\frac{2\alpha}{\mathrm{N}}\left(i - 1 - \frac{\mathrm{N}}{2}\right)\right) / \tan\alpha \quad , \tag{D.1.1}$$

$$y_j = \frac{1}{\sqrt{3}} \tan\left(\frac{2\alpha}{\mathrm{N}}\left(j - 1 - \frac{\mathrm{N}}{2}\right)\right) / \tan\alpha \quad , \tag{D.1.2}$$

$$z = \frac{1}{\sqrt{3}} \quad , \tag{D.1.3}$$

where i=1~N+1 and j=1~N+1 are illustrated in Figure D.4, and α is a parameter as a function of N to adjust the surface area of each cell uniform, which will be explained later. A particle can be regarded as on one of the cells in "Square 1" when the particle's position (x, y, z) satisfies all of the following conditions:

$$\begin{cases} z \geq x, & z \geq -x \\ z \geq y, & z \geq -y \end{cases} \tag{D.1.4}$$

By solving an inverse problem of the above definition of the position of each vertex, the index of the cell in which the particle exists can be identified as follows:

$$\mathrm{cell\ index} = j + (i - 1)\mathrm{N} \quad , \tag{D.1.5}$$

$$i = \left\lfloor \frac{\mathrm{N}}{2} + 1 + \frac{\mathrm{N}}{2\alpha} \arctan\left(\sqrt{3}\tilde{x} \tan\alpha\right) \right\rfloor \quad , \tag{D.1.6}$$

$$j = \left\lfloor \frac{\mathrm{N}}{2} + 1 + \frac{\mathrm{N}}{2\alpha} \arctan\left(\sqrt{3}\tilde{y} \tan\alpha\right) \right\rfloor \quad , \tag{D.1.7}$$

where $\lfloor a \rfloor$ is the floor function defined by the greatest integer less than or equal to a, and $(\tilde{x}, \tilde{y})$ is the position of the particle (x, y) after projected onto the face "Square 1". When i=N+1 and j=N+1 in Equations (D.1.6) and (D.1.7), i and j are defined as N as exceptions, respectively.

(a) Cell indices – Square 2

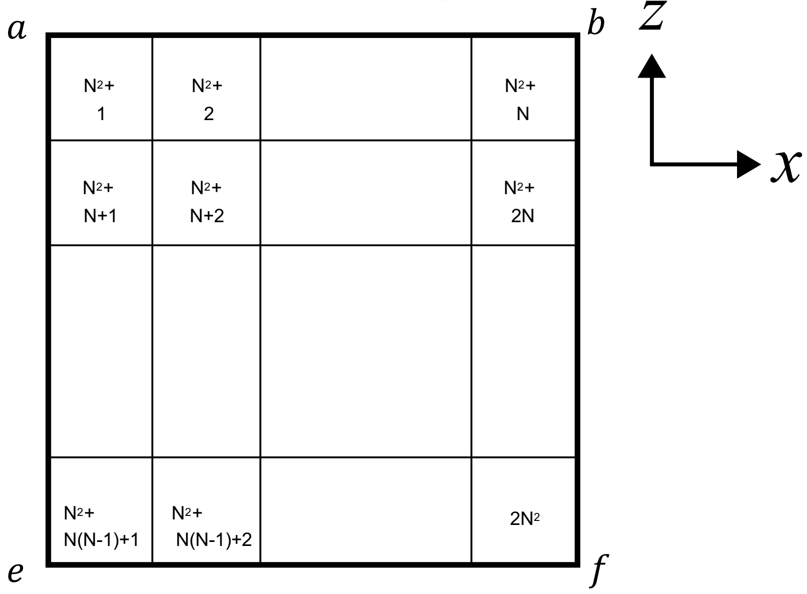

(b) Vertex indices – Square 2

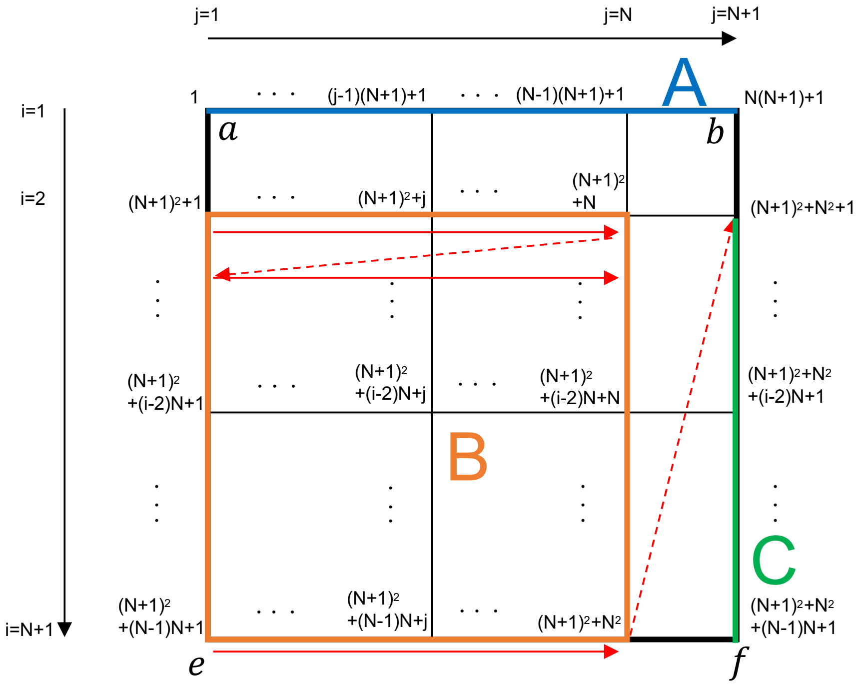

Figure D.5 Same as Figure D.4, but for “Square 2”.

“Square 2”

The face “Square 2” consists of the vertex group “A”, “B” and “C”. The indices of vertex group “B” are defined as “$(\mathrm{N}+1)^2+1 \sim (\mathrm{N}+1)^2+\mathrm{N}^2$” as illustrated in Figure D.5. The index of the vertex group “B” starts at (i,j)=(2,1), and the index of vertex increases from the point (i,j)=(2,1) to (2,N), and then move to the next line of i from the point (i,j)=(3,1) to (3,N). The index of the vertex group “B” finishes at the point (i,j)=(N+1,N).

The position of each vertex (x_j, y, z_i) on the original cube is defined as follows:

$$x_j = \frac{1}{\sqrt{3}} \tan\left(\frac{2\alpha}{\mathrm{N}}\left(j-1-\frac{\mathrm{N}}{2}\right)\right) \Big/ \tan\alpha \tag{D.2.1}$$

$$y = -\frac{1}{\sqrt{3}} \tag{D.2.2}$$

$$z_i = \frac{1}{\sqrt{3}} \tan\left(\frac{2\alpha}{\mathrm{N}}\left(\frac{\mathrm{N}}{2}-i+1\right)\right) \Big/ \tan\alpha \tag{D.2.3}$$

A particle can be regarded as on one of the cells in “Square 2” when the particle’s position (x,y,z) satisfies all of the following conditions:

$$\begin{cases} -y \geq x, & -y \geq -x \\ -y \geq z, & -y \geq -z \end{cases} \tag{D.2.4}$$

By solving an inverse problem of the above definition of the position of each vertex, the index of the cell in which the particle exists can be identified as follows:

$$\text{cell index} = j + (i-1)\mathrm{N} + \mathrm{N}^2 \quad , \tag{D.2.5}$$

$$i = \left\lfloor \frac{\mathrm{N}}{2} + 1 - \frac{\mathrm{N}}{2\alpha} \arctan\left(\sqrt{3}z \tan\alpha\right) \right\rfloor \quad , \tag{D.2.6}$$

$$j = \left\lfloor \frac{\mathrm{N}}{2} + 1 + \frac{\mathrm{N}}{2\alpha} \arctan\left(\sqrt{3}\tilde{x} \tan\alpha\right) \right\rfloor \quad , \tag{D.2.7}$$

where $(z, \tilde{x})$ is the position of the particle (z, x) after projected onto the face “Square 2”. When i=N+1 and j=N+1 in Equations (D.2.6) and (D.2.7), i and j are defined as N as exceptions, respectively.

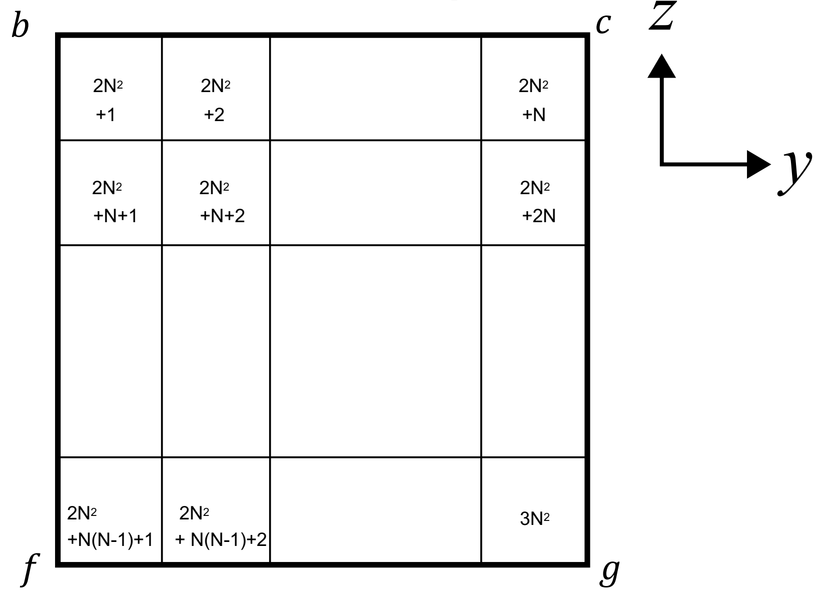

(a) Cell indices – Square 3

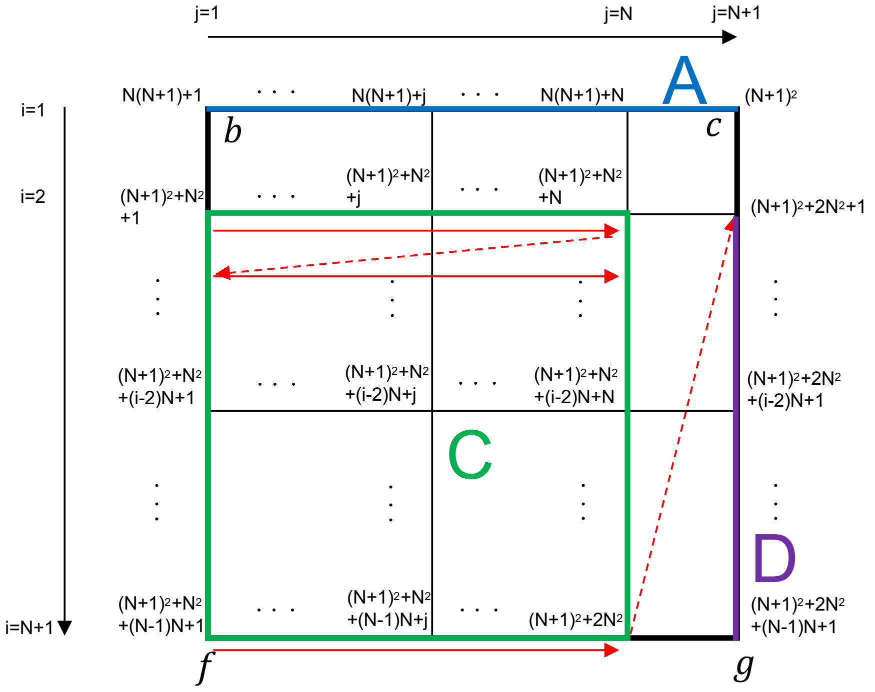

(b) Vertex indices – Square 3

Figure D.6 Same as Figure D.4, but for “Square 3”.

“Square 3”

The face “Square 3” consists of the vertex group “A”, “C” and “D”. The indices of vertex group “C” are defined as “$(\mathrm{N}+1)^2+\mathrm{N}^2+1$~$(\mathrm{N}+1)^2+2\mathrm{N}^2$” as illustrated in Figure D.6. The index of the vertex group “C” starts at (i, j)=(2,1), and the index of vertex increases from the point (i, j)=(2,1) to (2,N), and then move to the next line of i from the point (i, j)=(3,1) to (3,N). The index of the vertex group “C” finishes at the point (i, j)=(N+1,N).

The position of each vertex (x, y_j, z_i) on the original cube is defined as follows:

$$x = \frac{1}{\sqrt{3}} \tag{D.3.1}$$

$$y_j = \frac{1}{\sqrt{3}} \tan\left(\frac{2\alpha}{\mathrm{N}}\left(j-1-\frac{\mathrm{N}}{2}\right)\right) \Big/ \tan\alpha \tag{D.3.2}$$

$$z_i = \frac{1}{\sqrt{3}} \tan\left(\frac{2\alpha}{\mathrm{N}}\left(\frac{\mathrm{N}}{2}-i+1\right)\right) \Big/ \tan\alpha \tag{D.3.3}$$

A particle can be regarded as on one of the cells in “Square 3” when the particle’s position (x, y, z) satisfies all of the following conditions:

$$\begin{cases} x \geq z, \quad x \geq -z \\ x \geq y, \quad x \geq -y \end{cases} \tag{D.3.4}$$

By solving an inverse problem of the above definition of the position of each vertex, the index of the cell in which the particle exists can be identified as follows:

$$\text{cell index} = j + (i-1)\mathrm{N} + 2\mathrm{N}^2 \quad , \tag{D.3.5}$$

$$i = \left\lfloor \frac{\mathrm{N}}{2} + 1 - \frac{\mathrm{N}}{2\alpha} \arctan\left(\sqrt{3}z \tan\alpha\right) \right\rfloor \quad , \tag{D.3.6}$$

$$j = \left\lfloor \frac{\mathrm{N}}{2} + 1 + \frac{\mathrm{N}}{2\alpha} \arctan\left(\sqrt{3}\tilde{y} \tan\alpha\right) \right\rfloor \quad , \tag{D.3.7}$$

where $(\tilde{y}, z)$ is the position of the particle (y, z) after projected onto the face “Square 3”. When i=N+1 and j=N+1 in Equations (D.3.6) and (D.3.7), i and j are defined as N as exceptions, respectively.

(a) Cell indices – Square 4

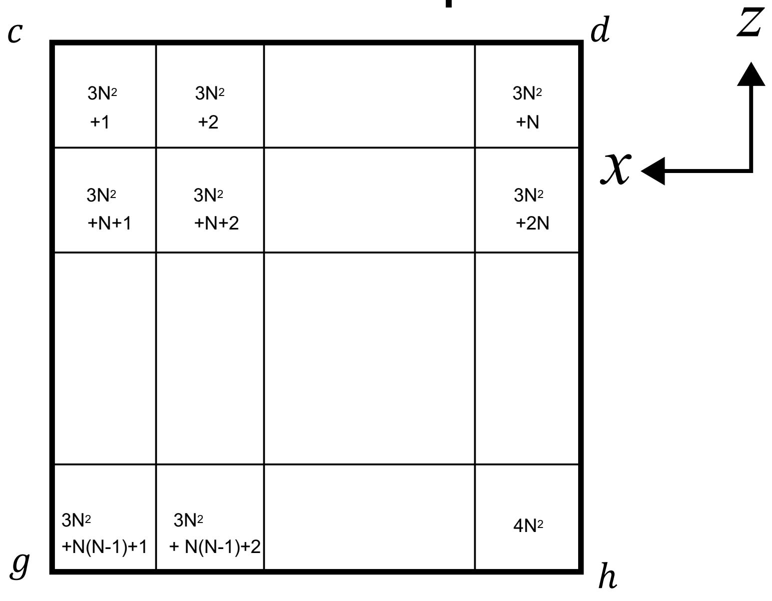

(b) Vertex indices – Square 4

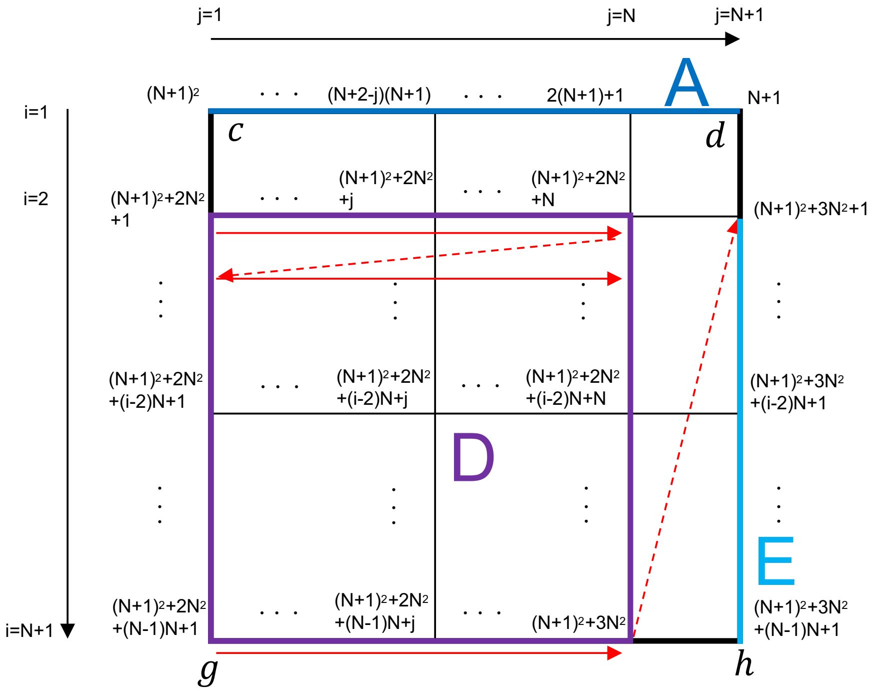

Figure D.7 Same as Figure D.4, but for “Square 4”.

"Square 4"

The face "Square 4" consists of the vertex group "A", "D" and "E". The indices of vertex group "D" are defined as "$(N+1)^2+2N^2+1$~$(N+1)^2+3N^2$" as illustrated in Figure D.7. The index of the vertex group "D" starts at (i, j)=(2,1), and the index of vertex increases from the point (i, j)=(2,1) to (2,N), and then move to the next line of i from the point (i, j)=(3,1) to (3,N). The index of the vertex group "D" finishes at the point (i, j)=(N+1,N).

The position of each vertex (x_j, y, z_i) on the original cube is defined as follows:

$$x = \frac{1}{\sqrt{3}} \tan\left(\frac{2\alpha}{\mathrm{N}}\left(\frac{\mathrm{N}}{2} - j + 1\right)\right) \Big/ \tan\alpha \tag{D.4.1}$$

$$y_j = \frac{1}{\sqrt{3}} \tag{D.4.2}$$

$$z_i = \frac{1}{\sqrt{3}} \tan\left(\frac{2\alpha}{\mathrm{N}}\left(\frac{\mathrm{N}}{2} - i + 1\right)\right) \Big/ \tan\alpha \tag{D.4.3}$$

A particle can be regarded as on one of the cells in "Square 4" when the particle's position (x, y, z) satisfies all of the following conditions:

$$\begin{cases} y \geq x, \ \ y \geq -x \\ y \geq z, \ \ y \geq -z \end{cases} \tag{D.4.4}$$

By solving an inverse problem of the above definition of the position of each vertex, the index of the cell in which the particle exists can be identified as follows:

$$\text{cell index} = j + (i-1)\mathrm{N} + 3\mathrm{N}^2 \quad , \tag{D.4.5}$$

$$i = \left\lfloor \frac{\mathrm{N}}{2} + 1 - \frac{\mathrm{N}}{2\alpha} \arctan\left(\sqrt{3}z \tan\alpha\right) \right\rfloor \quad , \tag{D.4.6}$$

$$j = \left\lfloor \frac{\mathrm{N}}{2} + 1 - \frac{\mathrm{N}}{2\alpha} \arctan\left(\sqrt{3}\tilde{x} \tan\alpha\right) \right\rfloor \quad , \tag{D.4.7}$$

where $(z, \tilde{x})$ is the position of the particle (z, x) after projected onto the face "Square 4". When i=N+1 and j=N+1 in Equations (D.4.6) and (D.4.7), i and j are defined as N as exceptions, respectively.

(a) Cell indices – Square 5

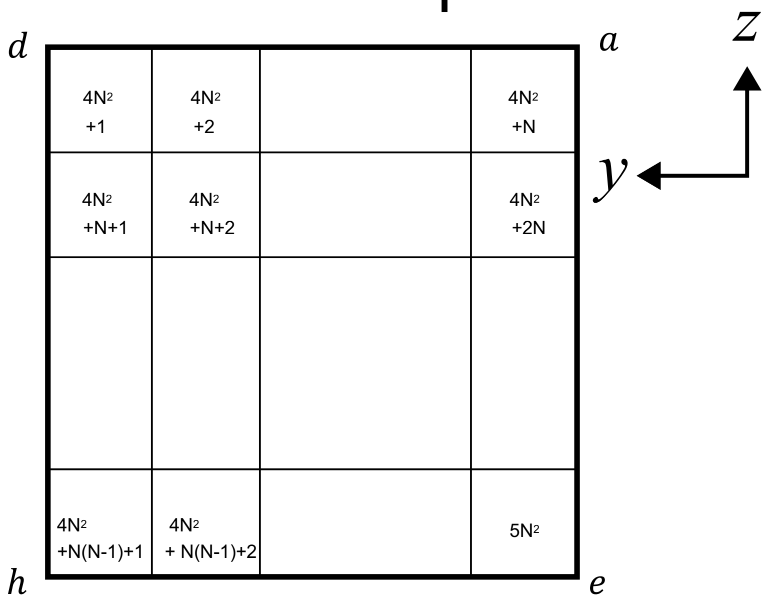

(b) Vertex indices – Square 5

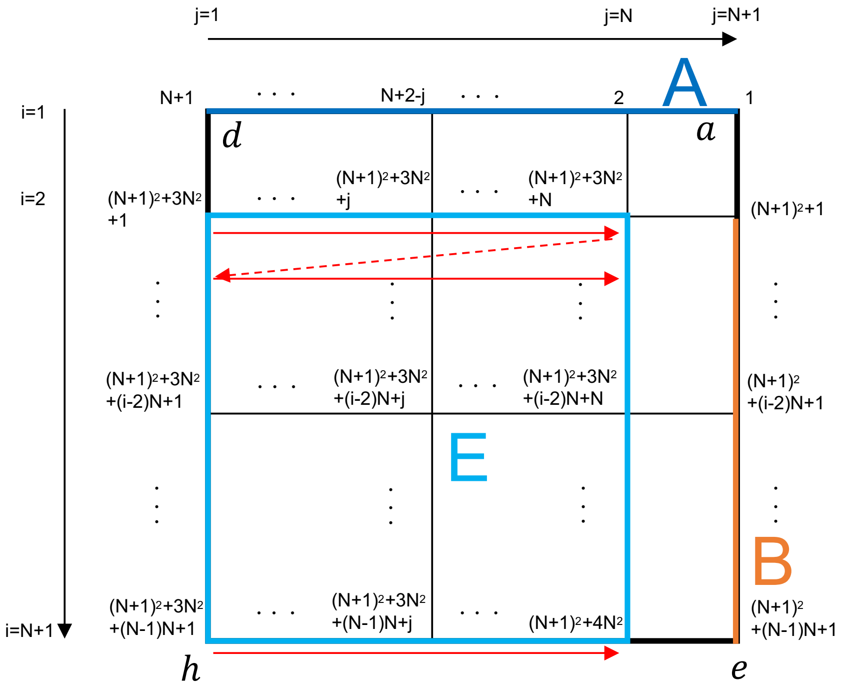

Figure D.8 Same as Figure D.4, but for “Square 5”.

“Square 5”

The face “Square 5” consists of the vertex group “A”, “E” and “B”. The indices of vertex group “E” are defined as “(N+1)^2+3N^2+1~(N+1)^2+4N^2” as illustrated in Figure D.8. The index of the vertex group “E” starts at (i, j)=(2,1), and the index of vertex increases from the point (i, j)=(2,1) to (2,N), and then move to the next line of i from the point (i, j)=(3,1) to (3,N). The index of the vertex group “E” finishes at the point (i, j)=(N+1,N).

The position of each vertex (x, y_j, z_i) on the original cube is defined as follows:

$$x = -\frac{1}{\sqrt{3}} \tag{D.5.1}$$

$$y_j = \frac{1}{\sqrt{3}} \tan\left(\frac{2\alpha}{\mathrm{N}}\left(\frac{\mathrm{N}}{2} - j + 1\right)\right) / \tan\alpha \tag{D.5.2}$$

$$z_i = \frac{1}{\sqrt{3}} \tan\left(\frac{2\alpha}{\mathrm{N}}\left(\frac{\mathrm{N}}{2} - i + 1\right)\right) / \tan\alpha \tag{D.5.3}$$

A particle can be regarded as on one of the cells in “Square 5” when the particle’s position (x, y, z) satisfies all of the following conditions:

$$\begin{cases} -x \geq z, & -x \geq -z \\ -x \geq y, & -x \geq -y \end{cases} \tag{D.5.4}$$

By solving an inverse problem of the above definition of the position of each vertex, the index of the cell in which the particle exists can be identified as follows:

$$\text{cell index} = j + (i-1)\mathrm{N} + 4\mathrm{N}^2 \quad , \tag{D.5.5}$$

$$i = \left\lfloor \frac{\mathrm{N}}{2} + 1 - \frac{\mathrm{N}}{2\alpha}\arctan\left(\sqrt{3}z\tan\alpha\right)\right\rfloor \quad , \tag{D.5.6}$$

$$j = \left\lfloor \frac{\mathrm{N}}{2} + 1 - \frac{\mathrm{N}}{2\alpha}\arctan\left(\sqrt{3}\tilde{y}\tan\alpha\right)\right\rfloor \quad , \tag{D.5.7}$$

where $(\tilde{y}, z)$ is the position of the particle (y, z) after projected onto the face “Square 5”. When i=N+1 and j=N+1 in Equations (D.5.6) and (D.5.7), i and j are defined as N as exceptions, respectively.

(a) Cell indices – Square 6

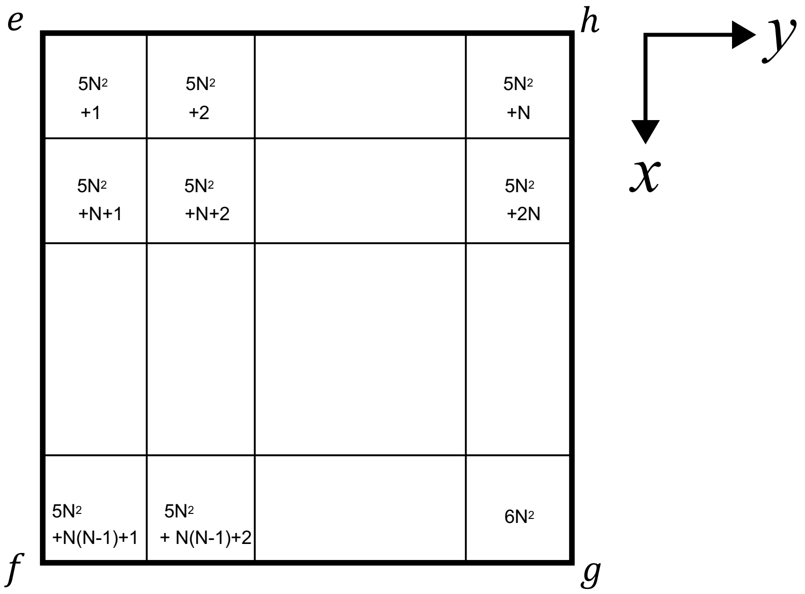

(b) Vertex indices – Square 6

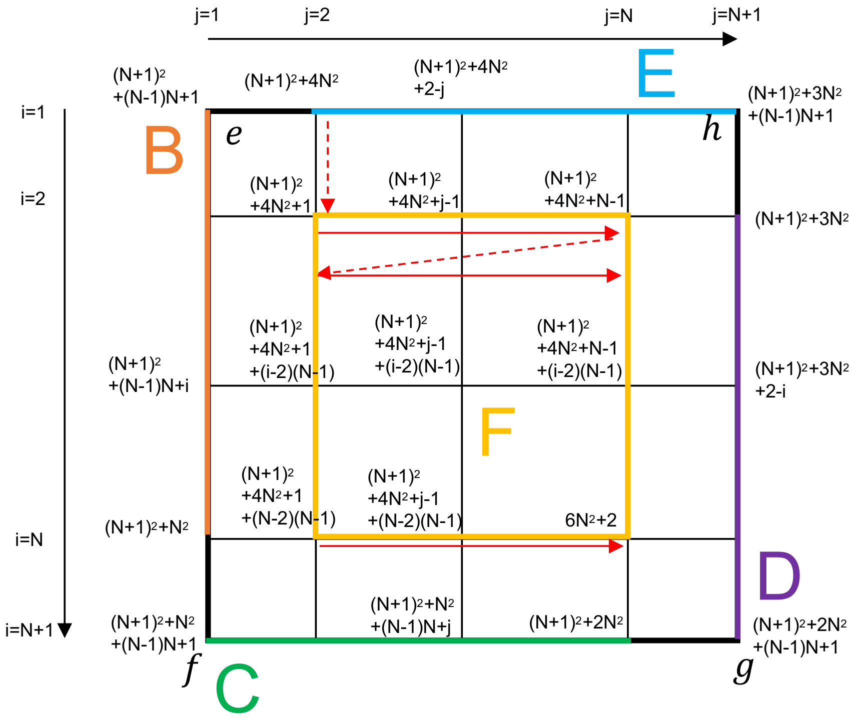

Figure D.9 Same as Figure D.4, but for “Square 6”.

"Square 6"

The face "Square 6" consists of the vertex group "B", "C", "D", "E" and "F". The indices of vertex group "F" are defined as "$(\mathrm{N}+1)^2+4\mathrm{N}^2+1$~$(\mathrm{N}+1)^2+4\mathrm{N}^2+(\mathrm{N}-1)^2$ ($=6\mathrm{N}^2+2$)" as illustrated in Figure D.9. The index of the vertex group "F" starts at (i,j)=(2,2), and the index of vertex increases from the point (i,j)=(2,2) to (2,N), and then move to the next line of i from the point (i,j)=(3,2) to (3,N). The index of the vertex group "F" finishes at the point (i,j)=(N,N).

The position of each vertex (x_i, y_j, z) on the original cube is defined as follows:

$$x_i = \frac{1}{\sqrt{3}} \tan\left(\frac{2\alpha}{\mathrm{N}}\left(i-1-\frac{\mathrm{N}}{2}\right)\right) / \tan\alpha \qquad \text{(D.6.1)}$$

$$y_j = \frac{1}{\sqrt{3}} \tan\left(\frac{2\alpha}{\mathrm{N}}\left(j-1-\frac{\mathrm{N}}{2}\right)\right) / \tan\alpha \qquad \text{(D.6.2)}$$

$$z = -\frac{1}{\sqrt{3}} \qquad \text{(D.6.3)}$$

A particle can be regarded as on one of the cells in "Square 6" when the particle's position (x, y, z) satisfies all of the following conditions:

$$\begin{cases} -z \geq x, & -z \geq -x \\ -z \geq y, & -z \geq -y \end{cases} \qquad \text{(D.6.4)}$$

By solving an inverse problem of the above definition of the position of each vertex, the index of the cell in which the particle exists can be identified as follows:

$$\text{cell index} = j + (i-1)\mathrm{N} + 5\mathrm{N}^2 \quad , \qquad \text{(D.6.5)}$$

$$i = \left\lfloor \frac{\mathrm{N}}{2} + 1 + \frac{\mathrm{N}}{2\alpha} \arctan\left(\sqrt{3}\tilde{x} \tan\alpha\right) \right\rfloor \quad , \qquad \text{(D.6.6)}$$

$$j = \left\lfloor \frac{\mathrm{N}}{2} + 1 + \frac{\mathrm{N}}{2\alpha} \arctan\left(\sqrt{3}\tilde{y} \tan\alpha\right) \right\rfloor \quad , \qquad \text{(D.6.7)}$$

where $(\tilde{x}, \tilde{y})$ is the position of the particle (x, y) after projected onto the face "Square 6". When i=N+1 and j=N+1 in Equations (D.6.6) and (D.6.7), i and j are defined as N as exceptions, respectively.

As mentioned before, each edge of the original cube was divided non-uniformly in order to make the surface area of individual cells nearly uniform. We divided each edge by weighting tangent function to achieve this objective. The parameter α appeared in the equation of the position of vertices and the localization method was defined as follows:

$$\alpha = \frac{\pi}{4}\eta \quad , \tag{D.7}$$

where η is an adjusting parameter that achieves the minimum deviation of the surface area from the mean value. We investigated η for several Nth order cubed sphere grids (Figure D.10).

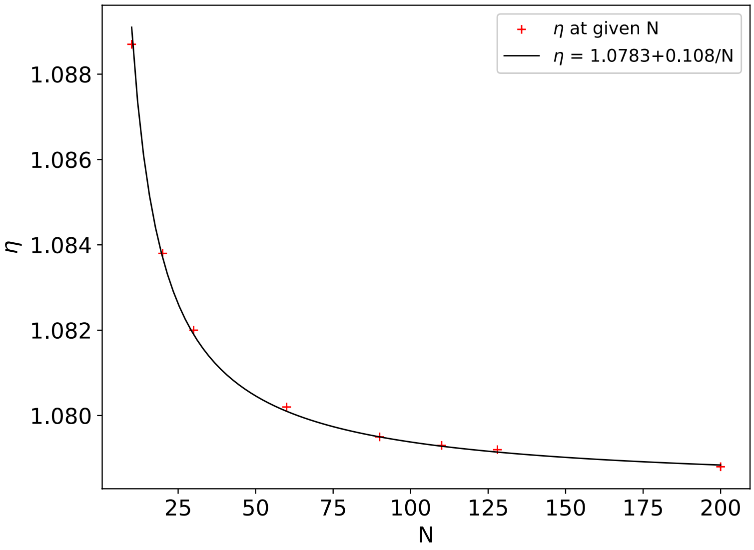

Figure D.10 The red dots represent the adjusting parameter η that satisfies the minimum deviation of the surface area of cells of Nth order cubed sphere grid. The black curve is the fitting result.

We found that η can be fitted by a following equation as a function of N.

$$\eta = 1.0783 + \frac{0.108}{\mathrm{N}} \tag{D.8}$$

As a comparison, the ratio of the maximum surface area of the cell to the minimum surface area of the cells, and the deviation of the surface area of the cells from the mean value for several dividing methods are shown in Figure D.11. If each edge of the original cube is divided uniformly in length, the ratio of the maximum surface area of the cells to the minimum is larger than 5 when N=100. Dividing each edge uniformly in angle improves the discrepancy, however, the ratio is still larger than 2 when N=100. Our dividing method using the tangent function further improves the discrepancy of the surface area of the cells, the ratio of the maximum to the minimum is around 1.23 when N=100 and the deviation of the surface area of the cells from the mean is smaller than 14% when N=100. This method also makes the discrepancy of the length between the adjacent vertices equal, and the ratio of the maximum length to the minimum length is 1.6 when N=100.

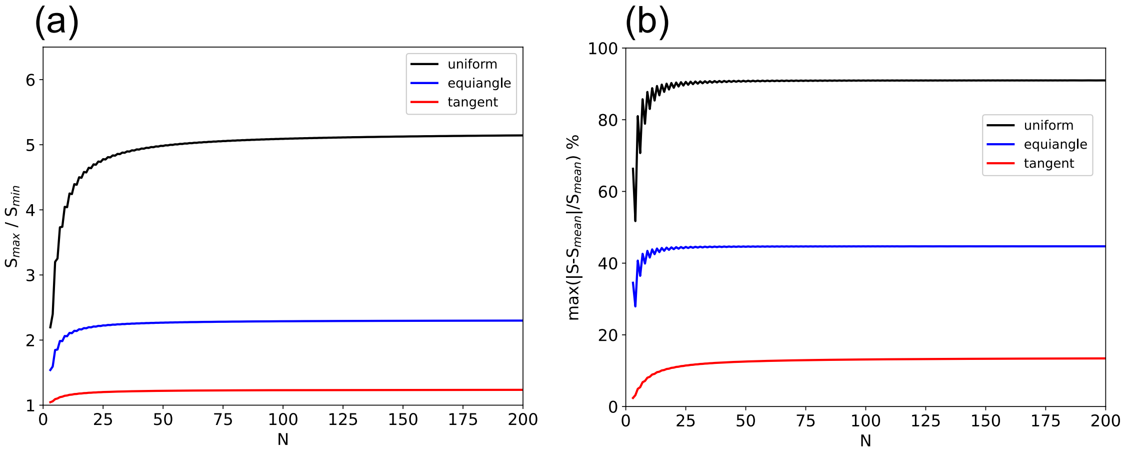

Figure D.11 (a) The ratio of the maximum surface area of cell to the minimum surface area of the cells. (b) The deviation of the surface area of the cells from the mean value. The black, blue and red lines are the cases when each edge of the original cube is divided uniformly in length, uniformly in angle, and weighted by a tangent function, respectively.

Appendix E

List of chemical reactions

Chemical reactions used in Chapter 6 are listed in Table E.1.

Table E.1 List of chemical reactions used in Chapter 6.

Reactions			Rate [cm^3/s]	Reference
$CO_2 + p^*$	$\rightarrow$	$CO_2^+ + e^- + p^*$		
$N_2 + p^*$	$\rightarrow$	$N_2^+ + e^- + p^*$		
$N_2 + p^*$	$\rightarrow$	$N^+ + e^- + p^*$		
$N_2 + p^*$	$\rightarrow$	$N + p^*$		
$N_2 + p^*$	$\rightarrow$	$N(^2D) + p^*$		
CO_2	$\rightarrow$	$CO_2^+ + e^-$	0.5×10^{-17}	cosmic ray MC01
CO_2	$\rightarrow$	$O^+(^4S) + e^-$	$0.1 \times 0.5 \times 10^{-17}$	cosmic ray MC01
N_2	$\rightarrow$	$N_2^+ + e^-$	0.5×10^{-17}	cosmic ray MC01
N_2	$\rightarrow$	$N + N(^2D)$	0.5×10^{-17}	cosmic ray MC01
$CO_2 + h\nu$	$\rightarrow$	$CO_2^+ + e^-$		
$CO_2 + h\nu$	$\rightarrow$	$CO^+ + e^- + O$		
$CO_2 + h\nu$	$\rightarrow$	$O^+(^4S) + e^- + CO$		
$CO_2 + h\nu$	$\rightarrow$	$C^+ + e^- + O_2$		
$O_2 + h\nu$	$\rightarrow$	$O_2^+ + e^-$		
$O_2 + h\nu$	$\rightarrow$	$O^+(^4S) + e^- + O$		
$O + h\nu$	$\rightarrow$	$O^+(^4S) + e^-$		
$O + h\nu$	$\rightarrow$	$O^+(^2D) + e^-$		
$O + h\nu$	$\rightarrow$	$O^+(^2P) + e^-$		
$CO + h\nu$	$\rightarrow$	$CO^+ + e^-$		
$CO + h\nu$	$\rightarrow$	$O^+(^4S) + e^- + C$		
$CO + h\nu$	$\rightarrow$	$C^+ + e^- + O$		
$N_2 + h\nu$	$\rightarrow$	$N_2^+ + e^-$		
$N_2 + h\nu$	$\rightarrow$	$N^+ + e^- + N$		

Table E.1 -*Continued*

Reactions			Rate [cm^3/s]	Reference
$CO_2 + h\nu$	$\rightarrow$	$CO + O$		
$CO_2 + h\nu$	$\rightarrow$	$CO + O(^1D)$		
$H_2O + h\nu$	$\rightarrow$	$H + OH$		
$H_2O + h\nu$	$\rightarrow$	$H_2 + O(^1D)$		
$O_3 + h\nu$	$\rightarrow$	$O_2 + O$		
$O_3 + h\nu$	$\rightarrow$	$O_2 + O(^1D)$		
$O_2 + h\nu$	$\rightarrow$	$O + O$		
$O_2 + h\nu$	$\rightarrow$	$O + O(^1D)$		
$H_2 + h\nu$	$\rightarrow$	$H + H$		
$OH + h\nu$	$\rightarrow$	$O + H$		
$OH + h\nu$	$\rightarrow$	$O(^1D) + H$		
$HO_2 + h\nu$	$\rightarrow$	$OH + O$		
$H_2O_2 + h\nu$	$\rightarrow$	$OH + OH$		
$H_2O_2 + h\nu$	$\rightarrow$	$HO_2 + H$		
$H_2O_2 + h\nu$	$\rightarrow$	$H_2O + O(^1D)$		
$N_2 + h\nu$	$\rightarrow$	$N + N(^2D)$		
$NO + h\nu$	$\rightarrow$	$N + O$		
$NO_2 + h\nu$	$\rightarrow$	$NO + O$		
$NO_2 + h\nu$	$\rightarrow$	$NO + O(^1D)$		
$NO_3 + h\nu$	$\rightarrow$	$NO + O_2$		
$NO_3 + h\nu$	$\rightarrow$	$NO_2 + O$		
$N_2O + h\nu$	$\rightarrow$	$N_2 + O(^1D)$		
$N_2O_5 + h\nu$	$\rightarrow$	$NO_3 + NO + O$		
$N_2O_5 + h\nu$	$\rightarrow$	$NO_3 + NO_2$		
$HONO + h\nu$	$\rightarrow$	$OH + NO$		
$HNO_3 + h\nu$	$\rightarrow$	$OH + NO_2$		
$HNO_3 + h\nu$	$\rightarrow$	$HONO + O$		
$HNO_3 + h\nu$	$\rightarrow$	$HONO + O(^1D)$		
$HO_2NO_2 + h\nu$	$\rightarrow$	$OH + NO_3$		
$HO_2NO_2 + h\nu$	$\rightarrow$	$HO_2 + NO_2$		
$H_2CO + h\nu$	$\rightarrow$	$HCO + H$		
$H_2CO + h\nu$	$\rightarrow$	$CO + H_2$		
$H_2CO + h\nu$	$\rightarrow$	$CO + H + H$		

Table E.1 -*Continued*

Reactions			Rate [cm^3/s]	Reference
$CO_2^+ + O$	$\rightarrow$	$CO + O_2^+$	1.64×10^{-10}	FS01
$CO_2^+ + O$	$\rightarrow$	$CO_2 + O^+(^4S)$	9.60×10^{-11}	FS01
$CO_2^+ + O_2$	$\rightarrow$	$CO_2 + O_2^+$	$5.50 \times 10^{-11} \times (300/T_i)^{0.82}$ for T = ∼ 1500 [K]	
			$1.50 \times 10^{-11} \times (1500/T_i)^{-0.75}$ for T = 1500 ∼ [K]	FS01
$CO_2^+ + NO$	$\rightarrow$	$NO^+ + CO_2$	1.23×10^{-10}	FS01
$CO_2^+ + N$	$\rightarrow$	$NO + CO^+$	3.40×10^{-10}	FS01
$CO_2^+ + N(^2D)$	$\rightarrow$	$N^+ + CO_2$	2.00×10^{-10}	FS01
$CO^+ + O$	$\rightarrow$	$CO + O^+(^4S)$	1.40×10^{-10}	FS01
$CO^+ + NO$	$\rightarrow$	$CO + NO^+$	4.20×10^{-10}	FS01
$CO^+ + O_2$	$\rightarrow$	$O_2^+ + CO$	$1.50 \times 10^{-10} \times (300/T_i)^{1.1}$	FS01
$CO^+ + CO_2$	$\rightarrow$	$CO_2^+ + CO$	1.10×10^{-9}	FS01
$CO^+ + N$	$\rightarrow$	$NO^+ + C$	8.20×10^{-11}	FS01
$O_2^+ + N$	$\rightarrow$	$NO^+ + O$	1.00×10^{-10}	FS01
$O_2^+ + N(^2D)$	$\rightarrow$	$NO^+ + O$	1.80×10^{-10}	FS01
$O_2^+ + N(^2D)$	$\rightarrow$	$N^+ + O_2$	8.65×10^{-11}	FS01
$O_2^+ + NO$	$\rightarrow$	$NO^+ + O_2$	4.50×10^{-10}	FS01
$O_2^+ + C$	$\rightarrow$	$CO^+ + O$	5.00×10^{-11}	FS01
$O_2^+ + C$	$\rightarrow$	$C^+ + O_2$	5.00×10^{-11}	FS01
$O_2^+ + N_2$	$\rightarrow$	$NO^+ + NO$	1.00×10^{-15}	FS01
$N_2^+ + N$	$\rightarrow$	$N^+ + N_2$	1.00×10^{-11}	FS01
$N_2^+ + CO_2$	$\rightarrow$	$N_2 + CO_2^+$	$9.00 \times 10^{-10} \times (300/T_i)^{0.23}$	FS01
$N_2^+ + CO$	$\rightarrow$	$N_2 + CO^+$	7.60×10^{-11}	FS01
$N_2^+ + O_2$	$\rightarrow$	$N_2 + O_2^+$	$5.10 \times 10^{-11} \times (300/T_i)^{1.16}$ for T = ∼ 1000[K]	
			$1.26 \times 10^{-11} \times (1000/T_i)^{-0.67}$ for T = 1000 ∼ 2000[K]	
			2.39×10^{-11} for T = 2000 ∼ [K]	FS01
$N_2^+ + O$	$\rightarrow$	$NO^+ + N(^2D)$	$1.33 \times 10^{-10} \times (300/T_i)^{0.44}$ for T = ∼ 1500[K]	
			$6.55 \times 10^{-11} \times (1500/T_i)^{-0.2}$ for T = 1500 ∼ [K]	FS01
$N_2^+ + O$	$\rightarrow$	$O^+(^4S) + N_2$	$7.00 \times 10^{-12} \times (300/T_i)^{0.23}$ for T = ∼ 1500[K]	
			$4.83 \times 10^{-12} \times (1500/T_i)^{-0.41}$ for T = 1500 ∼ [K]	FS01
$N_2^+ + NO$	$\rightarrow$	$N_2 + NO^+$	3.60×10^{-10}	FS01
$N^+ + CO_2$	$\rightarrow$	$CO^+ + NO$	2.02×10^{-10}	FS01
$N^+ + CO_2$	$\rightarrow$	$N + CO_2^+$	9.18×10^{-10}	FS01
$N^+ + NO$	$\rightarrow$	$N + NO^+$	$4.72 \times 10^{-10} \times (300/T_i)^{0.24}$	FS01
$N^+ + NO$	$\rightarrow$	$N_2^+ + O$	$8.33 \times 10^{-11} \times (300/T_i)^{0.24}$	FS01
$N^+ + CO$	$\rightarrow$	$NO^+ + C$	$6.16 \times 10^{-11} \times (300/T_i)^{0.5}$	FS01
$N^+ + CO$	$\rightarrow$	$CO^+ + N$	$4.93 \times 10^{-10} \times (300/T_i)^{0.5}$	FS01
$N^+ + CO$	$\rightarrow$	$C^+ + NO$	$5.60 \times 10^{-12} \times (300/T_i)^{0.5}$	FS01
$N^+ + O_2$	$\rightarrow$	$O_2^+ + N$	$2.02 \times 10^{-10} \times (300/T_i)^{-0.45}$ for T = ∼ 1000 [K]	
			3.49×10^{-10} for T = 1000 ∼ [K]	FS01
$N^+ + O_2$	$\rightarrow$	$O_2^+ + N(^2D)$	$8.65 \times 10^{-11} \times (300/T_i)^{-0.45}$ for T = ∼ 1000[K]	
			1.49×10^{-10} for T = 1000 ∼ [K]	FS01
$N^+ + O_2$	$\rightarrow$	$NO^+ + O$	$4.32 \times 10^{-11} \times (300/T_i)^{-0.45}$ for T = ∼ 1000[K]	
			7.47×10^{-11} for T = 1000 ∼ [K]	FS01
$N^+ + O_2$	$\rightarrow$	$NO^+ + O(^1D)$	$1.75 \times 10^{-10} \times (300/T_i)^{-0.45}$ for T = ∼ 1000[K]	
			3.02×10^{-10} for T = 1000 ∼ [K]	FS01
$N^+ + O_2$	$\rightarrow$	$O^+(^4S) + NO$	$4.34 \times 10^{-11} \times (300/T_i)^{-0.45}$ for T = ∼ 1000[K]	
			7.53×10^{-11} for T = 1000 ∼ [K]	FS01
$N^+ + O$	$\rightarrow$	$N + O^+(^4S)$	2.20×10^{-12}	FS01

Table E.1 -*Continued*

Reactions			Rate [cm^3/s]	Reference
$O^+(^4S) + O_2$	$\rightarrow$	$O + {O_2}^+$	$1.60 \times 10^{-11} \times (300/T_i)^{0.52}$ for T = $\sim$ 900[K]	
			$9.00 \times 10^{-12} \times (900/T_i)^{-0.92}$ for T = 900 $\sim$ [K]	FS01
$O^+(^4S) + NO$	$\rightarrow$	$NO^+ + O$	$7.00 \times 10^{-13} \times (300/T_i)^{0.66}$ for T = $\sim$ 300[K]	
			$7.00 \times 10^{-13} \times (300/T_i)^{-0.87}$ for T = 300 $\sim$ [K]	FS01
$O^+(^4S) + CO_2$	$\rightarrow$	${O_2}^+ + CO$	1.10×10^{-9} for T = $\sim$ 800[K]	
			$1.10 \times 10^{-9} \times (800/T_i)^{0.39}$ for T = 800 $\sim$ [K]	FS01
$O^+(^4S) + N_2$	$\rightarrow$	$NO^+ + N$	$1.20 \times 10^{-12} \times (300/T_i)^{0.45}$ for T = $\sim$ 1000 [K]	
			$7.00 \times 10^{-13} \times (1000/T_i)^{-2.12}$ for T = 1000 $\sim$ [K]	FS01
$O^+(^4S) + N(^2D)$	$\rightarrow$	$N^+ + O$	1.30×10^{-10}	FS01
$O^+(^4S) + C$	$\rightarrow$	$C^+ + O$	1.00×10^{-10}	FS01
$O^+(^2D) + CO_2$	$\rightarrow$	${O_2}^+ + CO$	6.00×10^{-11}	FS01
$O^+(^2D) + CO_2$	$\rightarrow$	${CO_2}^+ + O$	1.00×10^{-9}	FS01
$O^+(^2D) + CO$	$\rightarrow$	$CO^+ + O$	1.30×10^{-9}	FS01
$O^+(^2D) + O_2$	$\rightarrow$	${O_2}^+ + O$	7.00×10^{-10}	FS01
$O^+(^2D) + NO$	$\rightarrow$	$NO^+ + O$	1.20×10^{-9}	FS01
$O^+(^2D) + O$	$\rightarrow$	$O^+(^4S) + O$	1.00×10^{-11}	FS01
$O^+(^2D) + N_2$	$\rightarrow$	${N_2}^+ + O$	$5.70 \times 10^{-10} \times \exp(-400/T_i)$	FS01
$O^+(^2D) + N$	$\rightarrow$	$N^+ + O$	1.50×10^{-10}	FS01
$O^+(^2D) + e^-$	$\rightarrow$	$O^+(^4S) + e^-$	$6.03 \times 10^{-8} \times (300/T_e)^{0.5}$	FS01
$O^+(^2P) + CO_2$	$\rightarrow$	$CO + {O_2}^+$	6.00×10^{-11}	FS01
$O^+(^2P) + CO_2$	$\rightarrow$	${CO_2}^+ + O$	1.00×10^{-9}	FS01
$O^+(^2P) + CO$	$\rightarrow$	$CO^+ + O$	1.30×10^{-9}	FS01
$O^+(^2P) + O_2$	$\rightarrow$	$O^+(^4S) + O_2$	1.30×10^{-10}	FS01
$O^+(^2P) + O_2$	$\rightarrow$	${O_2}^+ + O$	1.30×10^{-10}	FS01
$O^+(^2P) + O$	$\rightarrow$	$O^+(^2D) + O$	5.20×10^{-10}	FS01
$O^+(^2P) + N_2$	$\rightarrow$	$O^+(^4S) + N_2$	$6.20 \times 10^{-10} \times \exp(-340/T_i)$	FS01
$O^+(^2P) + N$	$\rightarrow$	$O^+(^4S) + N(^2D)$	1.00×10^{-11}	FS01
$O^+(^2P) + NO$	$\rightarrow$	$NO^+ + O$	1.20×10^{-9}	FS01
$O^+(^2P) + e^-$	$\rightarrow$	$O^+(^4S) + e^-$	$3.03 \times 10^{-8} \times (300/T_e)^{0.5}$	FS01
$O^+(^2P) + e^-$	$\rightarrow$	$O^+(^2D) + e^-$	$1.84 \times 10^{-7} \times (300/T_e)^{0.5}$	FS01
$C^+ + CO_2$	$\rightarrow$	$CO^+ + CO$	1.10×10^{-9}	FS01
$C^+ + NO$	$\rightarrow$	$NO^+ + C$	$7.50 \times 10^{-10} \times (300/T_i)^{0.2}$	FS01
$C^+ + O_2$	$\rightarrow$	$O^+(^4S) + CO$	5.22×10^{-10}	FS01
$C^+ + O_2$	$\rightarrow$	$CO^+ + O$	3.48×10^{-10}	FS01
$C^+ + H_2$	$\rightarrow$	$CH^+ + H$	$7.40 \times 10^{-10} \times \exp(-4538/T_i)$	FS01
$H^+ + O$	$\rightarrow$	$O^+(^4S) + H$	3.75×10^{-10}	SN09
$N(^2D) + CO$	$\rightarrow$	$N + CO$	1.90×10^{-12}	FS01
$N(^2D) + O_2$	$\rightarrow$	$NO + O(^1D)$	$9.70 \times 10^{-12} \times \exp(-185/T_n)$	FS01
$N(^2D) + H_2$	$\rightarrow$	$NH + H$	$4.20 \times 10^{-11} \times \exp(-880/T_n)$	FS01
$N(^2D) + e^-$	$\rightarrow$	$N + e^-$	$3.86 \times 10^{-10} \times (300/T_e)^{-0.81}$	FS01
$N(^2P) + CO_2$	$\rightarrow$	$N(^2D) + CO_2$	2.00×10^{-15}	FS01
$N(^2P) + CO$	$\rightarrow$	$N(^2D) + CO$	6.00×10^{-15}	FS01
$N(^2P) + O_2$	$\rightarrow$	$NO + O$	$1.03 \times 10^{-12} \times \exp(-60/T_n)$	FS01
$N(^2P) + O_2$	$\rightarrow$	$NO + O(^1D)$	$1.03 \times 10^{-12} \times \exp(-60/T_n)$	FS01
$N(^2P) + O_2$	$\rightarrow$	$NO + O(^1S)$	$1.03 \times 10^{-12} \times \exp(-60/T_n)$	FS01
$N(^2P) + O$	$\rightarrow$	$N(^2D) + O$	1.70×10^{-11}	FS01

Table E.1 -*Continued*

Reactions			Rate [cm^3/s]	Reference
$N(^2P) + NO$	→	$N(^2D) + NO$	2.90×10^{-11}	FS01
$N(^2P) + N_2$	→	$N(^2D) + N_2$	5.00×10^{-17}	FS01
$N(^2P) + N$	→	$N(^2D) + N$	6.20×10^{-13}	FS01
$N(^2P) + H_2$	→	$N(^2D) + H_2$	2.50×10^{-15}	FS01
$N(^2P) + e^-$	→	$N + e^-$	$2.04 \times 10^{-10} \times (300/T_e)^{-0.85}$	FS01
$N(^2P) + e^-$	→	$N(^2D) + e^-$	9.50×10^{-9}	FS01
$C + CO_2$	→	$CO + CO$	$7.62 \times 10^{-14} \times (300/T_n)^{-0.5} \times \exp(-3480/T_n)$	FS01
$C + NO$	→	$CN + O$	$7.50 \times 10^{-11} \times (300/T_n)^{0.16}$	FS01
$C + NO$	→	$CO + N$	$7.50 \times 10^{-11} \times (300/T_n)^{0.16}$	FS01
$C + O_2$	→	$CO + O$	$4.90 \times 10^{-11} \times (300/T_n)^{0.32}$	FS01
$O(^1D) + CO$	→	$O + CO$	3.60×10^{-11}	FS01
$O(^1D) + O$	→	$O + O$	$6.47 \times 10^{-12} \times (300/T_n)^{-0.14}$	FS01
$O(^1D) + e^-$	→	$O + e^-$	$2.87 \times 10^{-10} \times (300/T_e)^{-0.91}$	FS01
$O(^1S) + CO_2$	→	$O(^1D) + CO_2$	$2.02 \times 10^{-11} \times \exp(-1327/T_n)$	FS01
$O(^1S) + CO_2$	→	$O + CO_2$	$1.19 \times 10^{-11} \times \exp(-1327/T_n)$	FS01
$O(^1S) + O_2$	→	$O(^1D) + O_2$	$1.36 \times 10^{-12} \times \exp(-815/T_n)$	FS01
$O(^1S) + O_2$	→	$O + O_2$	$3.04 \times 10^{-12} \times \exp(-815/T_n)$	FS01
$O(^1S) + O$	→	$O(^1D) + O$	0.00	FS01
$O(^1S) + N_2$	→	$O(^1D) + N_2$	5.00×10^{-17}	FS01
$O(^1S) + CO$	→	$O(^1D) + CO$	$7.40 \times 10^{-14} \times \exp(-961/T_n)$	FS01
$O(^1S) + H_2$	→	$O(^1D) + H_2$	2.86×10^{-16}	FS01
$O(^1S) + e^-$	→	$O(^1D) + e^-$	8.50×10^{-9}	FS01
$O(^1S) + e^-$	→	$O + e^-$	$1.56 \times 10^{-10} \times (300/T_e)^{-0.94}$	FS01
${CO_2}^+ + e^-$	→	$CO + O$	$3.50 \times 10^{-7} \times (300/T_e)^{0.5}$	FS01
$CO^+ + e^-$	→	$C + O$	$1.80 \times 10^{-7} \times (300/T_e)^{0.55}$	FS01
$CO^+ + e^-$	→	$C + O(^1D)$	$0.25 \times 10^{-7} \times (300/T_e)^{0.55}$	FS01
$CO^+ + e^-$	→	$C(^1D) + O$	$0.70 \times 10^{-7} \times (300/T_e)^{0.55}$	FS01
${O_2}^+ + e^-$	→	$O + O$	$0.39 \times 10^{-7} \times (300/T_e)^{0.70}$ for T = ~ 1200 [K]	
			$1.48 \times 10^{-8} \times (1200/T_e)^{0.56}$ for T = 1200 ~ [K]	FS01
${O_2}^+ + e^-$	→	$O + O(^1D)$	$0.86 \times 10^{-7} \times (300/T_e)^{0.70}$ for T = ~ 1200 [K]	
			$3.25 \times 10^{-8} \times (1200/T_e)^{0.56}$ for T = 1200 ~ [K]	FS01
${O_2}^+ + e^-$	→	$O(^1D) + O(^1D)$	$6.05 \times 10^{-8} \times (300/T_e)^{0.70}$ for T = ~ 1200 [K]	
			$2.29 \times 10^{-8} \times (1200/T_e)^{0.56}$ for T = 1200 ~ [K]	FS01
${O_2}^+ + e^-$	→	$O(^1D) + O(^1S)$	$9.75 \times 10^{-9} \times (300/T_e)^{0.70}$ for T = ~ 1200 [K]	
			$3.69 \times 10^{-9} \times (1200/T_e)^{0.56}$ for T = 1200 ~ [K]	FS01
${N_2}^+ + e^-$	→	$N + N(^2D)$	$1.01 \times 10^{-7} \times (300/T_e)^{0.39}$	FS01
${N_2}^+ + e^-$	→	$N(^2D) + N(^2D)$	$1.01 \times 10^{-7} \times (300/T_e)^{0.39}$	FS01
${N_2}^+ + e^-$	→	$N + N(^2P)$	$1.76 \times 10^{-8} \times (300/T_e)^{0.39}$	FS01
$NO^+ + e^-$	→	$N(^2D) + O$	$3.40 \times 10^{-7} \times (300/T_e)^{0.5}$	FS01
$NO^+ + e^-$	→	$N + O$	$0.60 \times 10^{-7} \times (300/T_e)^{0.5}$	FS01
$O^+(^2D)$	→	$O^+(^4S) + h\nu$	4.85×10^{-5}	FS01
$O^+(^2P)$	→	$O^+(^2D) + h\nu$	1.71×10^{-1}	FS01
$O^+(^2P)$	→	$O^+(^4S) + h\nu$	4.8×10^{-2}	FS01
$N(^2D)$	→	$N + h\nu$	1.07×10^{-5}	FS01
$N(^2P)$	→	$N(^2D) + h\nu$	7.9×10^{-2}	FS01
$N(^2P)$	→	$N + h\nu$	5.0×10^{-3}	FS01
$O(^1D)$	→	$O + h\nu$	9.3×10^{-3}	FS01
$O(^1S)$	→	$O(^1D) + h\nu$	1.06	FS01
$O(^1S)$	→	$O + h\nu$	4.5×10^{-2}	FS01
$OH^+ + CO$	→	$CO^+ + OH$	3.55×10^{-10}	M20
$OH^+ + O$	→	${O_2}^+ + H$	7.1×10^{-10}	M20
$OH^+ + NO$	→	$NO^+ + OH$	3.59×10^{-10}	M20
$OH^+ + O_2$	→	${O_2}^+ + OH$	3.8×10^{-10}	M20
$OH^+ + e^-$	→	$O + H$	$3.75 \times 10^{-8} \times (300/T_e)^{0.5}$	M20
$O^+(^4S) + H_2O$	→	$H_2O^+ + O$	2.60×10^{-9}	A93

Table E.1 -*Continued*

Reactions			Rate [cm^3/s]	Reference
$CO_2{}^+ + CO_2 + M$	→	$CO_2{}^+(CO_2) + M$	2.5×10^{-28}	MC01
$CO_2{}^+(CO_2) + O_2$	→	$O_2{}^+ + CO_2 + CO_2$	1.53×10^{-10}	MC01
$CO_2{}^+(CO_2) + O_2$	→	$O_2{}^+(CO_2) + CO_2$	2.7×10^{-11}	MC01
$O_2{}^+ + CO_2 + M$	→	$O_2{}^+(CO_2) + M$	1.7×10^{-29}	MC01
$O_2{}^+(CO_2) + CO_2$	→	$O_2{}^+ + CO_2 + CO_2$	2.4×10^{-13}	MC01
$O_2{}^+(CO_2) + H_2O$	→	$O_2{}^+(H_2O) + CO_2$	1.1×10^{-9}	MC01
$e^- + O$	→	$O^- + h\nu$	1.3×10^{-15}	MC01
$e^- + O_2 + M$	→	$O_2{}^- + M + h\nu$	$2.0 \times 10^{-31} \times (T_n/300)^{1.} \times \exp(-600/T_n)$	MC01
$e^- + O_3$	→	$O^- + O_2$	$9.1 \times 10^{-12} \times (T_n/300)^{-1.46}$	MC01
$O_2{}^- + CO_2 + M$	→	$CO_4{}^- + M$	1.3×10^{-29}	MC01
$N_2{}^+ + N_2 + M$	→	$N_4{}^+ + M$	$6.8 \times 10^{-29} \times (300/T_n)^{2.23}$	
			$\times$ (1-0.00824$\times(300/T_n)^{0.89}$	P14
$N_4{}^+ + M$	→	$N_2{}^+ + N_2 + M$	$6.5 \times 10^{-5} \times (300/T_n)^{3.23}$	
			$\times$(1-0.00824$\times(300/T_n)^{0.89} \times \exp(-1300/T_n)$	P14
$N_4{}^+ + O_2$	→	$O_2{}^+ + 2N_2$	1.5×10^{-10}	P14
$N_4{}^+ + CO_2$	→	$CO_2{}^+ + 2N_2$	7.0×10^{-10}	P14
$N_4{}^+ + H_2O$	→	$H_2O^+ + 2N_2$	3.0×10^{-10}	P14
$NO^+(H_2O) + M$	→	$NO^+ + H_2O + M$	$3.5 \times 10^{-4} \times (300/T_n)^{3.837} \times \exp(-9316/T_n)$	P14
$N_4{}^+ + e^-$	→	$2N_2$	$2.6 \times 10^{-6} \times (300/T_n)^{5.} \times \exp(-3872/T_n)$	V16
$O_2{}^+ + O_2 + M$	→	$O_4{}^+ + M$	$4.0 \times 10^{-30} \times (300/T_n)^{2.93}$	V16
$O_2{}^+ + H_2O + M$	→	$O_2{}^+(H_2O) + M$	2.8×10^{-28}	V16
$O_4{}^+ + H_2O$	→	$O_2{}^+(H_2O) + O_2$	1.7×10^{-9}	V16
$O_4{}^+ + O$	→	$O_2{}^+ + O_3$	3.0×10^{-10}	V16
$O_2{}^+(H_2O) + H_2O$	→	$H_3O^+(OH) + O_2$	9.0×10^{-10}	V16
$O_2{}^+(H_2O) + H_2O$	→	$H^+(H_2O) + OH + O_2$	2.4×10^{-10}	V16
$H_3O^+(OH) + H_2O$	→	$H^+(H_2O)_2 + OH$	2.0×10^{-9}	V16
$H^+(H_2O) + H_2O + M$	→	$H^+(H_2O)_2 + M$	$4.6 \times 10^{-27} \times (300/T_n)^{4.}$	V16
$H^+(H_2O)_2 + M$	→	$H^+(H_2O) + H_2O + M$	$2.5 \times 10^{-2} \times (300/T_n)^{5.} \times \exp(-15900/T_n)$	V16
$H^+(H_2O)_2 + H_2O + M$	→	$H^+(H_2O)_3 + M$	$2.3 \times 10^{-27} \times (300/T_n)^{7.5}$	V16
$H^+(H_2O)_3 + M$	→	$H^+(H_2O)_2 + H_2O + M$	$2.6 \times 10^{-3} \times (300/T_n)^{8.5} \times \exp(-10272/T_n)$	V16
$H^+(H_2O)_3 + H_2O + M$	→	$H^+(H_2O)_4 + M$	$3.6 \times 10^{-27} \times (300/T_n)^{8.1}$	V16
$H^+(H_2O)_4 + M$	→	$H^+(H_2O)_3 + H_2O + M$	$1.5 \times 10^{-1} \times (300/T_n)^{9.1} \times \exp(-9000/T_n)$	V16
$H^+(H_2O)_4 + H_2O + M$	→	$H^+(H_2O)_5 + M$	$4.6 \times 10^{-28} \times (300/T_n)^{1.}$	V16
$H^+(H_2O)_5 + M$	→	$H^+(H_2O)_4 + H_2O + M$	$1.7 \times 10^{-3} \times (300/T_n)^{1.} \times \exp(-6400/T_n)$	V16
$O_4{}^+ + e^-$	→	$2O_2$	$4.2 \times 10^{-6} \times (300/T_n)^{0.5}$	V16
$O_2{}^+(H_2O) + e^-$	→	$O_2 + H_2O$	2.0×10^{-6}	V16
$H_3O^+(OH) + e^-$	→	$OH + H + H_2O$	1.5×10^{-6}	V16
$H^+(H_2O) + e^-$	→	$H + H_2O$	$6.3 \times 10^{-7} \times (300/T_n)^{0.5}$	V16
$H^+(H_2O)_2 + e^-$	→	$H + 2H_2O$	$2.5 \times 10^{-6} \times (300/T_n)^{0.1}$	V16
$H^+(H_2O)_3 + e^-$	→	$H + 3H_2O$	$2.48 \times 10^{-6} \times (300/T_n)^{0.76}$	V16
$H^+(H_2O)_4 + e^-$	→	$H + 4H_2O$	3.6×10^{-6}	V16
$H^+(H_2O)_5 + e^-$	→	$H + 5H_2O$	5.0×10^{-6}	V16
$O_2{}^+(H_2O)$	→	$O_2{}^+ + H_2O$	0.42	V16

Table E.1 -*Continued*

Reactions			Rate [cm^3/s]	Reference
$NO^+ + N_2 + M$	→	$NO^+(N_2) + M$	$3.0 \times 10^{-31} \times (300/T_n)^{4.3}$	V16
$NO^+ + CO_2 + M$	→	$NO^+(CO_2) + M$	$1.4 \times 10^{-29} \times (300/T_n)^{4.}$	V16
$NO^+ + H_2O + M$	→	$NO^+(H_2O) + M$	$1.35 \times 10^{-28} \times (300/T_n)^{2.83}$	V16
$NO^+(N_2) + CO_2$	→	$NO^+(CO_2) + N_2$	1.0×10^{-9}	V16
$NO^+(N_2) + H_2O$	→	$NO^+(H_2O) + M$	1.0×10^{-9}	V16
$NO^+(N_2) + M$	→	$NO^+ + N_2 + M$	$1.5 \times 10^{-8} \times (300/T_n)^{4.3} \times \exp(-2093/T_n)$	V16
$NO^+(CO_2) + H_2O$	→	$NO^+(H_2O) + CO_2$	1.0×10^{-9}	V16
$NO^+(CO_2) + M$	→	$NO^+ + CO_2 + M$	$3.4 \times 10^{-7} \times (300/T_n)^{5.} \times \exp(-3872/T_n)$	V16
$NO^+(H_2O) + HO_2$	→	$H^+(H_2O) + NO_3$	0.5×10^{-9}	V16
$NO^+(H_2O) + OH$	→	$H^+(H_2O) + NO_2$	1.0×10^{-10}	V16
$NO^+(H_2O) + H$	→	$H^+(H_2O) + NO$	7.0×10^{-12}	V16
$NO^+(H_2O) + H_2O + M$	→	$NO^+(H_2O)_2 + M$	$1.0 \times 10^{-27} \times (308/T_n)^{4.7}$	V16
$NO^+(H_2O)_2 + H_2O + M$	→	$NO^+(H_2O)_3 + M$	$1.0 \times 10^{-27} \times (308/T_n)^{4.7}$	V16
$NO^+(H_2O)_3 + H_2O$	→	$H^+(H_2O)_3 + HONO$	7.0×10^{-11}	V16
$H^+(H_2O)_4 + N_2O_5$	→	$H^+(H_2O)_3(HNO_3) + HNO_3$	4.0×10^{-12}	V16
$H^+(H_2O)_5 + N_2O_5$	→	$H^+(H_2O)_4(HNO_3) + HNO_3$	7.0×10^{-12}	V16
$H^+(H_2O)_3(HNO_3) + H_2O$	→	$H^+(H_2O)_4 + HNO_3$	1.0×10^{-9}	V16
$H^+(H_2O)_4(HNO_3) + H_2O$	→	$H^+(H_2O)_5 + HNO_3$	1.0×10^{-9}	V16
$NO^+(N_2) + e^-$	→	$NO + N_2$	$1.4 \times 10^{-6} \times (300/T_n)^{0.4}$	V16
$NO^+(CO_2) + e^-$	→	$NO + CO_2$	1.5×10^{-6}	V16
$NO^+(H_2O) + e^-$	→	$NO + H_2O$	1.5×10^{-6}	V16
$NO^+(H_2O)_2 + e^-$	→	$NO + 2H_2O$	2.0×10^{-6}	V16
$NO^+(H_2O)_3 + e^-$	→	$NO + 3H_2O$	2.0×10^{-6}	V16

Table E.1 -*Continued*

Reactions			Rate [cm^3/s]	Reference
$O^- + O_3$	$\rightarrow$	$O_3^- + O$	8.0×10^{-10}	V16
$O^- + CO_2 + M$	$\rightarrow$	$CO_3^- + M$	2.0×10^{-28}	V16
$O_2^- + O$	$\rightarrow$	$O^- + O_2$	1.5×10^{-10}	V16
$O_2^- + O_3$	$\rightarrow$	$O_3^- + O_2$	7.8×10^{-10}	V16
$O_2^- + O_2 + M$	$\rightarrow$	$O_4^- + M$	3.4×10^{-31}	V16
$O_3^- + O$	$\rightarrow$	$O_2^- + O_2$	2.5×10^{-10}	V16
$O_3^- + CO_2$	$\rightarrow$	$CO_3^- + O_2$	5.5×10^{-10}	V16
$O_4^- + O$	$\rightarrow$	$O_3^- + O_2$	4.0×10^{-10}	V16
$O_4^- + CO_2$	$\rightarrow$	$CO_4^- + O_2$	4.3×10^{-10}	V16
$CO_3^- + O$	$\rightarrow$	$O_2^- + CO_2$	1.1×10^{-10}	V16
$CO_3^- + O_2$	$\rightarrow$	$O_3^- + CO_2$	6.0×10^{-15}	V16
$CO_3^- + H_2O + M$	$\rightarrow$	$CO_3^-(H_2O) + M$	1.0×10^{-28}	V16
$CO_4^- + O_3$	$\rightarrow$	$O_3^- + O_2 + CO_2$	1.3×10^{-10}	V16
$CO_4^- + O$	$\rightarrow$	$CO_3^- + O_2 + CO_2$	1.4×10^{-10}	V16
$CO_3^-(H_2O) + M$	$\rightarrow$	$CO_3^- + H_2O + M$	$7.2 \times 10^{-4} \times (300/T_n) \times \exp(-7050/T_n)$	V16
$CO_3^-(H_2O) + H_2O + M$	$\rightarrow$	$CO_3^-(H_2O)_2 + M$	1.0×10^{-28}	V16
$CO_3^-(H_2O)_2 + M$	$\rightarrow$	$CO_3^-(H_2O) + H_2O + M$	$6.5 \times 10^{-3} \times (300/T_n) \times \exp(-6800/T_n)$	V16
$O^- + O$	$\rightarrow$	$O_2 + e^-$	1.9×10^{-10}	V16
$O_2^- + O$	$\rightarrow$	$O_3 + e^-$	1.5×10^{-10}	V16
$O_3^- + O$	$\rightarrow$	$2O_2 + e^-$	1.0×10^{-10}	V16
$O_3^- + O_3$	$\rightarrow$	$3O_2 + e^-$	1.0×10^{-10}	V16
O^-	$\rightarrow$	$O + e^-$	1.4	V16
O_2^-	$\rightarrow$	$O_2 + e^-$	0.38	V16
O_3^-	$\rightarrow$	$O_3 + e^-$	4.7×10^{-2}	V16
O_3^-	$\rightarrow$	$O^- + O_2$	0.47	V16
O_4^-	$\rightarrow$	$O_2^- + O_2$	0.24	V16
CO_3^-	$\rightarrow$	$O^- + CO_2$	0.15	V16
CO_4^-	$\rightarrow$	$O_2^- + CO_2$	6.2×10^{-3}	V16
$CO_3^-(H_2O)$	$\rightarrow$	$CO_3^- + H_2O$	0.6	V16

Table E.1 -*Continued*

Reactions			Rate [cm^3/s]	Reference
$O^- + NO_2$	$\rightarrow$	$NO_2^- + O$	1.0×10^{-9}	V16
$O^- + HNO_3$	$\rightarrow$	$NO_3^- + OH$	3.6×10^{-9}	V16
$O_2^- + NO_2$	$\rightarrow$	$NO_2^- + O_2$	7.0×10^{-10}	V16
$O_2^- + HNO_3$	$\rightarrow$	$NO_3^- + HO_2$	2.9×10^{-9}	V16
$O_3^- + NO$	$\rightarrow$	$NO_3^- + O$	$1.05 \times 10^{-12} \times (300/T_n)^{2.15}$	V16
$O_3^- + NO_2$	$\rightarrow$	$NO_3^- + O_2$	$2.50 \times 10^{-11} \times (300/T_n)^{0.79}$	V16
$O_3^- + NO_2$	$\rightarrow$	$NO_2^- + O_3$	$7.5 \times 10^{-11} \times (300/T_n)^{0.79}$	V16
$O_3^- + NO$	$\rightarrow$	$NO_2^- + O_2$	$1.05 \times 10^{-12} \times (300/T_n)^{2.15}$	V16
$CO_3^- + NO$	$\rightarrow$	$NO_2^- + CO_2$	$1.3 \times 10^{-11} \times (300/T_n)^{1.64}$	V16
$CO_3^- + NO_2$	$\rightarrow$	$NO_3^- + CO_2$	$3.3 \times 10^{-11} \times (300/T_n)^{2.38}$	V16
$CO_3^- + HNO_3$	$\rightarrow$	$NO_3^- + CO_2 + OH$	3.51×10^{-10}	V16
$NO_2^- + H$	$\rightarrow$	$OH^- + NO$	3.0×10^{-10}	V16
$NO_2^- + NO_2$	$\rightarrow$	$NO_3^- + NO$	2.0×10^{-13}	V16
$NO_2^- + O_3$	$\rightarrow$	$NO_3^- + O_2$	1.2×10^{-10}	V16
$NO_2^- + H_2O + M$	$\rightarrow$	$NO_2^-(H_2O) + M$	1.6×10^{-28}	V16
$NO_2^- + HNO_3$	$\rightarrow$	$NO_3^- + HONO$	1.6×10^{-9}	V16
$NO_3^- + O$	$\rightarrow$	$NO_2^- + O_2$	0.5×10^{-11}	V16
$NO_3^- + O_3$	$\rightarrow$	$NO_2^- + 2O_2$	1.0×10^{-13}	V16
$NO_3^- + H_2O + M$	$\rightarrow$	$NO_3^-(H_2O) + M$	1.6×10^{-28}	V16
$NO_3^- + HNO_3 + M$	$\rightarrow$	$NO_3^-(HNO_3) + M$	1.45×10^{-26}	V16
$CO_3^-(H_2O) + NO$	$\rightarrow$	$NO_2^- + H_2O + CO_2$	3.5×10^{-12}	V16
$CO_3^-(H_2O) + NO_2$	$\rightarrow$	$NO_3^- + H_2O + CO_2$	4.0×10^{-11}	V16
$CO_3^-(H_2O) + NO_2$	$\rightarrow$	$NO_3^-(H_2O) + CO_2$	4.0×10^{-11}	V16
$CO_3^-(H_2O) + NO$	$\rightarrow$	$NO_2^-(H_2O) + CO_2$	3.5×10^{-12}	V16
$NO_2^-(H_2O) + M$	$\rightarrow$	$NO_2^- + H_2O + M$	$5.7 \times 10^{-4} \times (300/T_n) \times \exp(-7600/T_n)$	V16
$NO_3^-(H_2O) + H_2O + M$	$\rightarrow$	$NO_3^-(H_2O)_2 + M$	1.6×10^{-28}	V16
$NO_3^-(H_2O) + N_2O_5$	$\rightarrow$	$NO_3^-(HNO_3) + HNO_3$	7.0×10^{-10}	V16
$NO_3^-(H_2O) + HNO_3$	$\rightarrow$	$NO_3^-(HNO_3) + H_2O$	1.6×10^{-9}	V16
$NO_3^-(H_2O) + M$	$\rightarrow$	$NO_3^- + H_2O + M$	$1.0 \times 10^{-3} \times (300/T_n) \times \exp(-7300/T_n)$	V16
$NO_3^-(H_2O)_2 + M$	$\rightarrow$	$NO_3^-(H_2O) + H_2O + M$	$1.5 \times 10^{-2} \times (300/T_n) \times \exp(-7150/T_n)$	V16
$NO_3^-(H_2O)_2 + N_2O_5$	$\rightarrow$	$NO_3^-(HNO_3) + HNO_3 + H_2O$	7.0×10^{-10}	V16
$NO_3^-(HNO_3) + M$	$\rightarrow$	$NO_3^- + HNO_3 + M$	$6.0 \times 10^{-3} \times (300/T_n) \times \exp(-13130/T_n)$	V16
$O^- + NO$	$\rightarrow$	$NO_2 + e^-$	$3.1 \times 10^{-10} \times (300/T_n)^{0.83}$	V16
NO_2^-	$\rightarrow$	$NO_2 + e^-$	8.0×10^{-4}	V16
NO_3^-	$\rightarrow$	$NO_3 + e^-$	5.2×10^{-2}	V16

Table E.1 -*Continued*

Reactions			Rate [cm^3/s]	Reference
$H^+(H_2O)_4 + CO_3^-$	→	$H + 4H_2O + O + CO_2$	$6.0 \times 10^{-8} \times (300/T_n)^{0.5}$	V16
$H^+(H_2O)_4 + O_2^-$	→	$H + 4H_2O + O_2$	$6.0 \times 10^{-8} \times (300/T_n)^{0.5}$	V16
$H^+(H_2O)_4 + CO_4^-$	→	$H + 4H_2O + O_2 + CO_2$	$6.0 \times 10^{-8} \times (300/T_n)^{0.5}$	V16
$H^+(H_2O)_4 + CO_3^-(H_2O)_2$	→	$H + 6H_2O + O + CO_2$	$6.0 \times 10^{-8} \times (300/T_n)^{0.5}$	V16
$H^+(H_2O)_4 + CO_3^-(H_2O)$	→	$H + 5H_2O + O + CO_2$	$6.0 \times 10^{-8} \times (300/T_n)^{0.5}$	V16
$H^+(H_2O)_5 + CO_3^-$	→	$H + 5H_2O + O + CO_2$	$6.0 \times 10^{-8} \times (300/T_n)^{0.5}$	V16
$H^+(H_2O)_5 + O_2^-$	→	$H + 5H_2O + O_2$	$6.0 \times 10^{-8} \times (300/T_n)^{0.5}$	V16
$H^+(H_2O)_5 + CO_4^-$	→	$H + 5H_2O + O_2 + CO_2$	$6.0 \times 10^{-8} \times (300/T_n)^{0.5}$	V16
$H^+(H_2O)_5 + CO_3^-(H_2O)_2$	→	$H + 7H_2O + O + CO_2$	$6.0 \times 10^{-8} \times (300/T_n)^{0.5}$	V16
$H^+(H_2O)_5 + CO_3^-(H_2O)$	→	$H + 6H_2O + O + CO_2$	$6.0 \times 10^{-8} \times (300/T_n)^{0.5}$	V16
$H^+(H_2O)_3 + CO_3^-$	→	$H + 3H_2O + O + CO_2$	$6.0 \times 10^{-8} \times (300/T_n)^{0.5}$	V16
$H^+(H_2O)_3 + O_2^-$	→	$H + 3H_2O + O_2$	$6.0 \times 10^{-8} \times (300/T_n)^{0.5}$	V16
$H^+(H_2O)_3 + CO_4^-$	→	$H + 3H_2O + O_2 + CO_2$	$6.0 \times 10^{-8} \times (300/T_n)^{0.5}$	V16
$H^+(H_2O)_3 + CO_3^-(H_2O)_2$	→	$H + 5H_2O + O + CO_2$	$6.0 \times 10^{-8} \times (300/T_n)^{0.5}$	V16
$H^+(H_2O)_3 + CO_3^-(H_2O)$	→	$H + 4H_2O + O + CO_2$	$6.0 \times 10^{-8} \times (300/T_n)^{0.5}$	V16
$O_2^+ + CO_3^-$	→	$O_2 + O + CO_2$	$6.0 \times 10^{-8} \times (300/T_n)^{0.5}$	V16
$O_2^+ + O_2^-$	→	$2O_2$	$6.0 \times 10^{-8} \times (300/T_n)^{0.5}$	V16
$O_2^+ + CO_4^-$	→	$2O_2 + CO_2$	$6.0 \times 10^{-8} \times (300/T_n)^{0.5}$	V16
$O_2^+ + CO_3^-(H_2O)_2$	→	$O_2 + O + 2H_2O + CO_2$	$6.0 \times 10^{-8} \times (300/T_n)^{0.5}$	V16
$O_2^+ + CO_3^-(H_2O)$	→	$O_2 + O + H_2O + CO_2$	$6.0 \times 10^{-8} \times (300/T_n)^{0.5}$	V16
$H^+(H_2O)_4 + CO_3^- + M$	→	$H + 4H_2O + O + CO_2 + M$	$1.25 \times 10^{-25} \times (300/T_n)^{4.}$	V16
$H^+(H_2O)_5 + CO_3^- + M$	→	$H + 5H_2O + O + CO_2 + M$	$1.25 \times 10^{-25} \times (300/T_n)^{4.}$	V16
$H^+(H_2O)_4 + CO_3^-(H_2O)_2 + M$	→	$H + 6H_2O + O + CO_2 + M$	$1.25 \times 10^{-25} \times (300/T_n)^{4.}$	V16
$H^+(H_2O)_5 + CO_3^-(H_2O)_2 + M$	→	$H + 7H_2O + O + CO_2 + M$	$1.25 \times 10^{-25} \times (300/T_n)^{4.}$	V16
$H^+(H_2O)_4 + CO_3^-(H_2O) + M$	→	$H + 5H_2O + O + CO_2 + M$	$1.25 \times 10^{-25} \times (300/T_n)^{4.}$	V16
$H^+(H_2O)_5 + CO_3^-(H_2O) + M$	→	$H + 6H_2O + O + CO_2 + M$	$1.25 \times 10^{-25} \times (300/T_n)^{4.}$	V16
$H^+(H_2O)_4 + NO_3^-(HNO_3)$	→	$2HNO_3 + 4H_2O$	$6.0 \times 10^{-8} \times (300/T_n)^{0.5}$	V16
$H^+(H_2O)_4 + NO_3^-$	→	$HNO_3 + 4H_2O$	$6.0 \times 10^{-8} \times (300/T_n)^{0.5}$	V16
$H^+(H_2O)_4 + NO_3^-(H_2O)$	→	$H + 5H_2O + NO_3$	$6.0 \times 10^{-8} \times (300/T_n)^{0.5}$	V16
$H^+(H_2O)_4 + NO_2^-(H_2O)$	→	$H + 5H_2O + NO_2$	$6.0 \times 10^{-8} \times (300/T_n)^{0.5}$	V16
$H^+(H_2O)_4 + NO_3^-(H_2O)_2$	→	$H + 6H_2O + NO_3$	$6.0 \times 10^{-8} \times (300/T_n)^{0.5}$	V16
$H^+(H_2O)_4 + NO_2^-$	→	$H + 4H_2O + NO_2$	$6.0 \times 10^{-8} \times (300/T_n)^{0.5}$	V16
$H^+(H_2O)_5 + NO_3^-(HNO_3)$	→	$2HNO_3 + 5H_2O$	$6.0 \times 10^{-8} \times (300/T_n)^{0.5}$	V16
$H^+(H_2O)_5 + NO_3^-$	→	$HNO_3 + 5H_2O$	$6.0 \times 10^{-8} \times (300/T_n)^{0.5}$	V16
$H^+(H_2O)_5 + NO_3^-(H_2O)$	→	$H + 6H_2O + NO_3$	$6.0 \times 10^{-8} \times (300/T_n)^{0.5}$	V16
$H^+(H_2O)_5 + NO_2^-(H_2O)$	→	$H + 6H_2O + NO_2$	$6.0 \times 10^{-8} \times (300/T_n)^{0.5}$	V16
$H^+(H_2O)_5 + NO_3^-(H_2O)_2$	→	$H + 7H_2O + NO_3$	$6.0 \times 10^{-8} \times (300/T_n)^{0.5}$	V16
$H^+(H_2O)_5 + NO_2^-$	→	$H + 5H_2O + NO_2$	$6.0 \times 10^{-8} \times (300/T_n)^{0.5}$	V16
$H^+(H_2O)_3 + NO_3^-(HNO_3)$	→	$2HNO_3 + 3H_2O$	$6.0 \times 10^{-8} \times (300/T_n)^{0.5}$	V16
$H^+(H_2O)_3 + NO_3^-$	→	$HNO_3 + 3H_2O$	$6.0 \times 10^{-8} \times (300/T_n)^{0.5}$	V16
$H^+(H_2O)_3 + NO_3^-(H_2O)$	→	$H + 4H_2O + NO_3$	$6.0 \times 10^{-8} \times (300/T_n)^{0.5}$	V16
$H^+(H_2O)_3 + NO_2^-(H_2O)$	→	$H + 4H_2O + NO_2$	$6.0 \times 10^{-8} \times (300/T_n)^{0.5}$	V16
$H^+(H_2O)_3 + NO_3^-(H_2O)_2$	→	$H + 5H_2O + NO_3$	$6.0 \times 10^{-8} \times (300/T_n)^{0.5}$	V16
$H^+(H_2O)_3 + NO_2^-$	→	$H + 3H_2O + NO_2$	$6.0 \times 10^{-8} \times (300/T_n)^{0.5}$	V16
$NO^+(H_2O) + NO_3^-(HNO_3)$	→	$NO + H_2O + NO_3 + HNO_3$	$6.0 \times 10^{-8} \times (300/T_n)^{0.5}$	V16
$NO^+(H_2O) + CO_3^-$	→	$NO + H_2O + O + CO_2$	$6.0 \times 10^{-8} \times (300/T_n)^{0.5}$	V16
$NO^+(H_2O) + NO_3^-$	→	$NO + H_2O + NO_3$	$6.0 \times 10^{-8} \times (300/T_n)^{0.5}$	V16
$NO^+(H_2O) + HCO_3^-$	→	$NO + H_2O + OH + CO_2$	$6.0 \times 10^{-8} \times (300/T_n)^{0.5}$	V16
$NO^+(H_2O) + O_2^-$	→	$NO + H_2O + O_2$	$6.0 \times 10^{-8} \times (300/T_n)^{0.5}$	V16
$NO^+(H_2O) + CO_4^-$	→	$NO + H_2O + O_2 + CO_2$	$6.0 \times 10^{-8} \times (300/T_n)^{0.5}$	V16
$NO^+(H_2O) + NO_3^-(H_2O)$	→	$NO + 2H_2O + NO_3$	$6.0 \times 10^{-8} \times (300/T_n)^{0.5}$	V16
$NO^+(H_2O) + CO_3^-(H_2O)_2$	→	$NO + 3H_2O + O + CO_2$	$6.0 \times 10^{-8} \times (300/T_n)^{0.5}$	V16
$NO^+(H_2O) + CO_3^-(H_2O)$	→	$NO + 2H_2O + O + CO_2$	$6.0 \times 10^{-8} \times (300/T_n)^{0.5}$	V16
$NO^+(H_2O) + NO_2^-(H_2O)$	→	$NO + 2H_2O + NO_2$	$6.0 \times 10^{-8} \times (300/T_n)^{0.5}$	V16
$NO^+(H_2O) + NO_3^-(H_2O)_2$	→	$NO + 3H_2O + NO_3$	$6.0 \times 10^{-8} \times (300/T_n)^{0.5}$	V16
$NO^+(H_2O) + NO_2^-$	→	$NO + H_2O + NO_2$	$6.0 \times 10^{-8} \times (300/T_n)^{0.5}$	V16

Table E.1 -*Continued*

Reactions			Rate [cm^3/s]	Reference
$NO^+(H_2O)_2 + NO_3^-(HNO_3)$	→	$NO + 2H_2O + NO_3 + HNO_3$	$6.0 \times 10^{-8} \times (300/T_n)^{0.5}$	V16
$NO^+(H_2O)_2 + CO_3^-$	→	$NO + 2H_2O + O + CO_2$	$6.0 \times 10^{-8} \times (300/T_n)^{0.5}$	V16
$NO^+(H_2O)_2 + NO_3^-$	→	$NO + 2H_2O + NO_3$	$6.0 \times 10^{-8} \times (300/T_n)^{0.5}$	V16
$NO^+(H_2O)_2 + HCO_3^-$	→	$NO + 2H_2O + OH + CO_2$	$6.0 \times 10^{-8} \times (300/T_n)^{0.5}$	V16
$NO^+(H_2O)_2 + O_2^-$	→	$NO + 2H_2O + O_2$	$6.0 \times 10^{-8} \times (300/T_n)^{0.5}$	V16
$NO^+(H_2O)_2 + CO_4^-$	→	$NO + 2H_2O + O_2 + CO_2$	$6.0 \times 10^{-8} \times (300/T_n)^{0.5}$	V16
$NO^+(H_2O)_2 + NO_3^-(H_2O)$	→	$NO + 3H_2O + NO_3$	$6.0 \times 10^{-8} \times (300/T_n)^{0.5}$	V16
$NO^+(H_2O)_2 + CO_3^-(H_2O)_2$	→	$NO + 4H_2O + O + CO_2$	$6.0 \times 10^{-8} \times (300/T_n)^{0.5}$	V16
$NO^+(H_2O)_2 + CO_3^-(H_2O)$	→	$NO + 3H_2O + O + CO_2$	$6.0 \times 10^{-8} \times (300/T_n)^{0.5}$	V16
$NO^+(H_2O)_2 + NO_2^-(H_2O)$	→	$NO + 3H_2O + NO_2$	$6.0 \times 10^{-8} \times (300/T_n)^{0.5}$	V16
$NO^+(H_2O)_2 + NO_3^-(H_2O)_2$	→	$NO + 4H_2O + NO_3$	$6.0 \times 10^{-8} \times (300/T_n)^{0.5}$	V16
$NO^+(H_2O)_2 + NO_2^-$	→	$NO + 2H_2O + NO_2$	$6.0 \times 10^{-8} \times (300/T_n)^{0.5}$	V16
$NO^+ + NO_3^-(HNO_3)$	→	$NO + NO_3 + HNO_3$	$6.0 \times 10^{-8} \times (300/T_n)^{0.5}$	V16
$NO^+ + CO_3^-$	→	$NO + O + CO_2$	$6.0 \times 10^{-8} \times (300/T_n)^{0.5}$	V16
$NO^+ + NO_3^-$	→	$NO + NO_3$	$6.0 \times 10^{-8} \times (300/T_n)^{0.5}$	V16
$NO^+ + HCO_3^-$	→	$NO + OH + CO_2$	$6.0 \times 10^{-8} \times (300/T_n)^{0.5}$	V16
$NO^+ + O_2^-$	→	$NO + O_2$	$6.0 \times 10^{-8} \times (300/T_n)^{0.5}$	V16
$NO^+ + CO_4^-$	→	$NO + O_2 + CO_2$	$6.0 \times 10^{-8} \times (300/T_n)^{0.5}$	V16
$NO^+ + NO_3^-(H_2O)$	→	$NO + H_2O + NO_3$	$6.0 \times 10^{-8} \times (300/T_n)^{0.5}$	V16
$NO^+ + CO_3^-(H_2O)_2$	→	$NO + 2H_2O + O + CO_2$	$6.0 \times 10^{-8} \times (300/T_n)^{0.5}$	V16
$NO^+ + CO_3^-(H_2O)$	→	$NO + H_2O + O + CO_2$	$6.0 \times 10^{-8} \times (300/T_n)^{0.5}$	V16
$NO^+ + NO_2^-(H_2O)$	→	$NO + H_2O + NO_2$	$6.0 \times 10^{-8} \times (300/T_n)^{0.5}$	V16
$NO^+ + NO_3^-(H_2O)_2$	→	$NO + 2H_2O + NO_3$	$6.0 \times 10^{-8} \times (300/T_n)^{0.5}$	V16
$NO^+ + NO_2^-$	→	$NO + NO_2$	$6.0 \times 10^{-8} \times (300/T_n)^{0.5}$	V16
$O_2^+ + NO_3^-(HNO_3)$	→	$O_2 + NO_3 + HNO_3$	$6.0 \times 10^{-8} \times (300/T_n)^{0.5}$	V16
$O_2^+ + NO_3^-$	→	$O_2 + NO_3$	$6.0 \times 10^{-8} \times (300/T_n)^{0.5}$	V16
$O_2^+ + NO_3^-(H_2O)$	→	$O_2 + H_2O + NO_3$	$6.0 \times 10^{-8} \times (300/T_n)^{0.5}$	V16
$O_2^+ + NO_2^-(H_2O)$	→	$O_2 + H_2O + NO_2$	$6.0 \times 10^{-8} \times (300/T_n)^{0.5}$	V16
$O_2^+ + NO_3^-(H_2O)_2$	→	$O_2 + 2H_2O + NO_3$	$6.0 \times 10^{-8} \times (300/T_n)^{0.5}$	V16
$O_2^+ + NO_2^-$	→	$O_2 + NO_2$	$6.0 \times 10^{-8} \times (300/T_n)^{0.5}$	V16
$H^+(H_2O)_4 + NO_3^- + M$	→	$HNO_3 + 4H_2O + M$	$1.25 \times 10^{-25} \times (300/T_n)^{4.}$	V16
$H^+(H_2O)_5 + NO_3^- + M$	→	$HNO_3 + 5H_2O + M$	$1.25 \times 10^{-25} \times (300/T_n)^{4.}$	V16
$H^+(H_2O)_4 + NO_3^-(HNO_3) + M$	→	$2HNO_3 + 4H_2O + M$	$1.25 \times 10^{-25} \times (300/T_n)^{4.}$	V16
$H^+(H_2O)_5 + NO_3^-(HNO_3) + M$	→	$2HNO_3 + 5H_2O + M$	$1.25 \times 10^{-25} \times (300/T_n)^{4.}$	V16
$H^+(H_2O)_4 + NO_3^-(H_2O) + M$	→	$H + 5H_2O + NO_3 + M$	$1.25 \times 10^{-25} \times (300/T_n)^{4.}$	V16
$H^+(H_2O)_5 + NO_3^-(H_2O) + M$	→	$H + 6H_2O + NO_3 + M$	$1.25 \times 10^{-25} \times (300/T_n)^{4.}$	V16

Table E.1 -*Continued*

Reactions			Rate [cm^3/s]	Reference
$O + O + M$	→	$O_2 + M$	$5.4 \times 10^{-33} \times (300/T_n)^{3.25}$	C17
$O + O_2 + N_2$	→	$O_3 + N_2$	$5.0 \times 10^{-35} \times \exp(724/T_n)$	C17
$O + O_2 + CO_2$	→	$O_3 + CO_2$	$1.5 \times 10^{-33} \times (300/T_n)^{2.4}$	C17
$O + O_3$	→	$O_2 + O_2$	$8.0 \times 10^{-12} \times \exp(-2060/T_n)$	C17
$O + CO + M$	→	$CO_2 + M$	$2.2 \times 10^{-33} \times \exp(-1780/T_n)$	C17
$O(^1D) + O_2$	→	$O + O_2$	$3.2 \times 10^{-11} \times \exp(70/T_n)$	C17
$O(^1D) + O_3$	→	$O_2 + O_2$	1.2×10^{-10}	C17
$O(^1D) + O_3$	→	$O + O + O_2$	1.2×10^{-10}	C17
$O(^1D) + H_2$	→	$H + OH$	1.2×10^{-10}	C17
$O(^1D) + CO_2$	→	$O + CO_2$	$7.5 \times 10^{-11} \times \exp(115/T_n)$	C17
$O(^1D) + H_2O$	→	$OH + OH$	$1.63 \times 10^{-10} \times \exp(60/T_n)$	C17
$H_2 + O$	→	$OH + H$	$6.34 \times 10^{-12} \times \exp(-4000/T_n)$	C17
$OH + H_2$	→	$H_2O + H$	$9.01 \times 10^{-13} \times \exp(-1526/T_n)$	C17
$H + H + CO_2$	→	$H_2 + CO_2$	$1.6 \times 10^{-32} \times (298/T_n)^{2.27}$	C17
$H + OH + CO_2$	→	$H_2O + CO_2$	$1.292 \times 10^{-30} \times (300/T_n)^{2.}$	C17
$H + HO_2$	→	$OH + OH$	7.2×10^{-11}	C17
$H + HO_2$	→	$H_2O + O(^1D)$	1.6×10^{-12}	C17
$H + HO_2$	→	$H_2 + O_2$	3.45×10^{-12}	C17
$H + H_2O_2$	→	$HO_2 + H_2$	$2.8 \times 10^{-12} \times \exp(-1890/T_n)$	C17
$H + H_2O_2$	→	$H_2O + OH$	$1.7 \times 10^{-11} \times \exp(-1800/T_n)$	C17
$H + O_2 + M$	→	$HO_2 + M$	$k_0 = 8.8 \times 10^{-32} \times (300/T_n)^{1.3}$	
			$k\infty = 7.5 \times 10^{-11} \times (300/T_n)^{-0.2}$	C17
$H + O_3$	→	$OH + O_2$	$1.4 \times 10^{-10} \times \exp(-470/T_n)$	C17
$O + OH$	→	$O_2 + H$	$1.8 \times 10^{-11} \times \exp(180/T_n)$	C17
$O + HO_2$	→	$OH + O_2$	$3.0 \times 10^{-11} \times \exp(200/T_n)$	C17
$O + H_2O_2$	→	$OH + HO_2$	$1.4 \times 10^{-12} \times \exp(-2000/T_n)$	C17
$OH + OH$	→	$H_2O + O$	1.8×10^{-12}	C17
$OH + OH + M$	→	$H_2O_2 + M$	$k_0 = 8.97 \times 10^{-31} \times (300/T_n)^{1.}$	
			$k\infty = 2.6 \times 10^{-11}$	C17
$OH + O_3$	→	$HO_2 + O_2$	$1.7 \times 10^{-12} \times \exp(-940/T_n)$	C17
$OH + HO_2$	→	$H_2O + O_2$	$4.8 \times 10^{-11} \times \exp(250/T_n)$	C17
$OH + H_2O_2$	→	$H_2O + HO_2$	1.8×10^{-12}	C17
$HO_2 + O_3$	→	$OH + O_2 + O_2$	$1.0 \times 10^{-14} \times \exp(-490/T_n)$	C17
$HO_2 + HO_2$	→	$H_2O_2 + O_2$	$3.0 \times 10^{-13} \times \exp(460/T_n)$	C17
$HO_2 + HO_2 + M$	→	$H_2O_2 + O_2 + M$	$4.2 \times 10^{-33} \times \exp(920/T_n)$	C17
$CO + OH + M$	→	$CO_2 + H + M$	$k_0M = 1.5 \times 10^{-13} \times (300/T_n)^{-0.6}$	
			$k\infty\ M = 2.1 \times 10^{9} \times (300/T_n)^{-6.1}$	C17
$CO + OH + M$	→	$HOCO + M$	$k_0 = 5.9 \times 10^{-33} \times (300/T_n)^{1.4}$	
			$k\infty = 1.1 \times 10^{-12} \times (300/T_n)^{-1.3}$	C17
$HOCO + O_2$	→	$HO_2 + CO_2$	2.0×10^{-12}	C17
${CO_2}^+ + H_2$	→	$CO_2 + H + H$	8.7×10^{-10}	C17

Table E.1 -*Continued*

Reactions			Rate $[cm^3/s]$	Reference
$N + O_2$	$\rightarrow$	$NO + O$	$1.5 \times 10^{-11} \times \exp(-3600/T_n)$	N94
$N + O_3$	$\rightarrow$	$NO + O_2$	1.0×10^{-16}	N94
$N + OH$	$\rightarrow$	$NO + H$	$3.8 \times 10^{-11} \times \exp(85/T_n)$	N94
$N + HO_2$	$\rightarrow$	$NO + OH$	2.2×10^{-11}	N94
$N + NO$	$\rightarrow$	$N_2 + O$	3.4×10^{-11}	N94
$N + NO_2$	$\rightarrow$	$N_2O + O$	3.0×10^{-12}	N94
$N(^2D) + O$	$\rightarrow$	$N + O$	6.9×10^{-13}	N94
$N(^2D) + CO_2$	$\rightarrow$	$NO + CO$	3.5×10^{-13}	N94
$N(^2D) + N_2$	$\rightarrow$	$N + N_2$	1.7×10^{-14}	N94
$N(^2D) + NO$	$\rightarrow$	$N_2 + O$	6.9×10^{-11}	N94
$O + NO + M$	$\rightarrow$	$NO_2 + M$	$k_0 = 1.2 \times 10^{-27} \times T_n{}^{-1.5}$	
			$k\,\infty = 3.0 \times 10^{-11}$	N94
$O + NO_2$	$\rightarrow$	$NO + O_2$	$6.5 \times 10^{-12} \times \exp(120/T_n)$	N94
$O + NO_2 + M$	$\rightarrow$	$NO_3 + M$	$k_0 = 2.0 \times 10^{-26} \times T_n{}^{-2.0}$	
			$k\,\infty = 2.2 \times 10^{-11}$	N94
$O + NO_3$	$\rightarrow$	$O_2 + NO_2$	1.0×10^{-11}	N94
$O + HO_2NO_2$	$\rightarrow$	$OH + NO_2 + O_2$	$7.8 \times 10^{-11} \times \exp(-3400/T_n)$	N94
$O(^1D) + N_2$	$\rightarrow$	$O + N_2$	$1.8 \times 10^{-11} \times \exp(110/T_n)$	N94
$O(^1D) + N_2 + M$	$\rightarrow$	$N_2O + M$	$2.8 \times 10^{-35} \times T_n{}^{-0.6}$	N94
$O(^1D) + N_2O$	$\rightarrow$	$2NO$	6.7×10^{-11}	N94
$O(^1D) + N_2O$	$\rightarrow$	$N_2 + O_2$	4.9×10^{-11}	N94
$NO + O_3$	$\rightarrow$	$NO_2 + O_2$	$2.0 \times 10^{-12} \times \exp(-1400/T_n)$	N94
$NO + HO_2$	$\rightarrow$	$NO_2 + OH$	$3.7 \times 10^{-12} \times \exp(240/T_n)$	N94
$NO + NO_3$	$\rightarrow$	$2NO_2$	$1.7 \times 10^{-11} \times \exp(150/T_n)$	N94
$H + NO_2$	$\rightarrow$	$OH + NO$	$2.2 \times 10^{-10} \times \exp(-182/T_n)$	N94
$H + NO_3$	$\rightarrow$	$OH + NO_2$	1.1×10^{-10}	N94
$OH + NO + M$	$\rightarrow$	$HONO + M$	$k_0 = 4.8 \times 10^{-24} \times T_n{}^{-2.6}$	
			$k\,\infty = 2.6 \times 10^{-10} \times T_n{}^{-0.5}$	N94
$OH + NO_2 + M$	$\rightarrow$	$HNO_3 + M$	$k_0 = 5.5 \times 10^{-22} \times T_n{}^{-3.2}$	
			$k\,\infty = 4.0 \times 10^{-8} \times T_n{}^{-1.3}$	N94
$OH + NO_3$	$\rightarrow$	$HO_2 + NO_2$	2.3×10^{-11}	N94
$OH + HONO$	$\rightarrow$	$H_2O + NO_2$	$1.8 \times 10^{-11} \times \exp(-390/T_n)$	N94
$OH + HNO_3$	$\rightarrow$	$H_2O + NO_3$	$7.2 \times 10^{-15} \times \exp(785/T_n)$	N94
$OH + HO_2NO_2$	$\rightarrow$	$H_2O + NO_2 + O_2$	$1.3 \times 10^{-12} \times \exp(380/T_n)$	N94
$HO_2 + NO_2 + M$	$\rightarrow$	$HO_2NO_2 + M$	$k_0 = 3.8 \times 10^{-23} \times T_n{}^{-3.2}$	
			$k\,\infty = 1.4 \times 10^{-8} \times T_n{}^{-1.4}$	N94
$HO_2 + NO_3$	$\rightarrow$	$O_2 + HNO_3$	9.2×10^{-13}	N94
$NO_2 + O_3$	$\rightarrow$	$NO_3 + O_2$	$1.2 \times 10^{-13} \times \exp(-2450/T_n)$	N94
$NO_2 + NO_3 + M$	$\rightarrow$	$N_2O_5 + M$	$k_0 = 2.5 \times 10^{-19} \times T_n{}^{-4.3}$	
			$k\,\infty = 2.6 \times 10^{-11} \times T_n{}^{-0.5}$	N94
$NO_2 + NO_3$	$\rightarrow$	$NO + NO_2 + O_2$	$8.2 \times 10^{-14} \times \exp(-1480/T_n)$	N94
$N + CO_2$	$\rightarrow$	$NO + CO$	1.0×10^{-19}	RK76
$H + CO + M$	$\rightarrow$	$HCO + M$	$2.0 \times 10^{-33} \times \exp(-850/T_n)$	P80
$H + HCO$	$\rightarrow$	$H_2 + CO$	3.0×10^{-10}	P80
$HCO + HCO$	$\rightarrow$	$H_2CO + CO$	6.3×10^{-11}	P80
$OH + HCO$	$\rightarrow$	$H_2O + CO$	5.0×10^{-11}	P80
$O + HCO$	$\rightarrow$	$H + CO_2$	1.0×10^{-10}	P80
$O + HCO$	$\rightarrow$	$OH + CO$	1.0×10^{-10}	P80
$O_2 + HCO$	$\rightarrow$	$HO_2 + CO$	5.0×10^{-12}	P80
$HO_2 + HCO$	$\rightarrow$	$H_2O_2 + CO$	1.0×10^{-11}	P80
$H + H_2CO$	$\rightarrow$	$H_2 + HCO$	$2.8 \times 10^{-11} \times \exp(-1540/T_n)$	P80
$OH + H_2CO$	$\rightarrow$	$H_2O + HCO$	$1.7 \times 10^{-11} \times \exp(-100/T_n)$	P80

MC01: Molina-Cuberos et al. (2001), FS01: Fox and Sung (2001), M20: Mukundan et al. (2020), A93: Anicich (1993), P14: Pavlov (2014), V16: Verronen et al. (2016), C17: Chaffin et al. (2017), N94: Nair et al. (1994), RK76: Rawlins and Kaufman (1976), P80: Pinto et al. (1980).

Bibliography

Acuña, M. H., Connerney, J. E. P., Wasilewski, P., Lin, R. P., Mitchell, D., Anderson, K. A., Carlson, C. W., McFadden, J., Rème, H., Mazelle, C., Vignes, D., Bauer, S. J., Cloutier, P., and Ness, N. F. (2001). Magnetic field of Mars: Summary of results from the aerobraking and mapping orbits, *J. Geophys. Res.*, 106(E10), 23403–23417, doi:10.1029/2000JE001404.

Adams, D., Luo, Y., Wong, M. L., Dunn, P., Christensen, M., Dong, C., Hu, R., and Yung, Y. (2021). Nitrogen Fixation at Early Mars, *Astrobiology*, 21:8, 968–980, doi:10.1089/ast.2020.2273.

Airapetian, V. S., Glocer, A., Gronoff, G., Hébrard, E., and Danchi, W. (2016). Prebiotic chemistry and atmospheric warming of early Earth by an active young Sun, *Nature Geoscience*, 9, 452–455, doi:10.1038/ngeo2719.

Amerstorfer, U. V., Gröller, H., Lichtenegger, H., Lammer, H., Tian, F., Noack, L., Scherf, M., Johnstone, C., Tu, L., and Guedel, M. (2017). Escape and evolution of Mars's CO_2 atmosphere: Influence of suprathermal atoms, *J. Geophys. Res. Planets*, 122, 1321–1337, doi:10.1002/2016JE005175.

Anicich, V. G. (1993). Evaluated bimolecular ion-molecule gas-phase kinetics of positive-ions for use in modeling planetary-atmospheres, cometary comae, and interstellar clouds, *J. Phys. Chem. Ref. Data*, 22, 1469–1569, doi:10.1063/1.555940.

Aoki, S., Daerden, F., Viscardy, S., Thomas, I. R., Erwin, J. T., Robert, S., et al. (2021). Annual appearance of hydrogen chloride on Mars and a striking similarity with the water vapor vertical distribution observed by TGO/NOMAD, *Geophys. Res. Lett.*, 48, e2021GL092506, doi:10.1029/2021GL092506.

Arney, G., Domagal-Goldman, S. D., Meadows, V. S., Wolf, E. T., Schwieterman, E., Charnay, B., Claire, M., Hébrard, E., and Trainer, M. G. (2016). The Pale Orange Dot: The Spectrum and Habitability of Hazy Archean Earth, *Astrobiology*, 16:11, 873–899 doi:10.1089/ast.2015.1422.

Avramenko, L. I., and V. M. Krasnen'kov, (1967). Reactions of nitrogen atoms. *Russ Chem Bull*, 16, 501–503, doi:10.1007/BF00905979.

Band, D., Matteson, J., Ford, L., Schaefer, B., Palmer, D., Teegarden, B., Cline, T., Briggs, M., Paciesas, W., Pendleton, G., Fishman, G., Kouveliotou, C., Meegan, C., Wilson, R., and Lestrade, P. (1993). BATSE Observations of Gamma-Ray Burst Spectra. I. Spectral Diversity, *Astrophysical Journal*, 413, 281, doi:10.1086/172995.

Basu, B., Jasperse, J. R., Robinson, R. M., Vondrak, R. R., and Evans, D. S. (1987). Linear transport theory of auroral proton precipitation: A comparison with observations, *J. Geophys. Res*., 92, 5920–5932, doi:10.1029/JA092iA06p05920.

Bertaux, J. L., Leblanc, F., Witasse, O., Quemerais, E., Lilensten, J., Stern, S. A., and Korablev, O. (2005). Discovery of an aurora on Mars, *Nature*, 435, 790–794, doi:10.1038/nature03603.

Bhardwaj, A., and Jain, S. K. (2009). Monte Carlo model of electron energy degradation in a CO_2 atmosphere, *J. Geophys. Res.*, 114, A11309, doi:10.1029/2009JA014298.

Bhardwaj, A., and Jain, S. K. (2013). CO Cameron band and CO_2^+ UV doublet emission in the dayglow of Venus: Role of CO in the Cameron band production, *J. Geophys. Res.: Space Physics*, 118, 3660–3671, doi:10.1002/jgra.50345.

Birch, M. J., and Bromage, B. J. I. (2022). Sunspot numbers and proton events in solar cycles 19 to 24, *Journal of Atmospheric and Solar-Terrestrial Physics*, 236, 105891, doi:10.1016/j.jastp.2022.105891.

Bisikalo, D. V., Shematovich, V. I., Gérard, J.-C., Hubert, B. (2017). Influence of crustal magnetic field on the Mars aurora electron flux and UV brightness, *Icarus*, 282, 127–135, doi:10.1016/j.icarus.2016.08.035.

Bornebusch, J. P., Wissing, J. M., and Kallenrode, M.-B. (2010). Solar particle precipitation into the polar atmosphere and their dependence on hemisphere and local time, *Advances in Space Research*, 45, 5, 632–637, doi:10.1016/j.asr.2009.11.008.

Brain, D. A., Halekas, J. S., Peticolas, L. M., Lin, R. P., Luhmann, J. G., Mitchell, D. L., et al. (2006). On the origin of aurorae on Mars, *Geophys. Res. Lett.*, 33, L01201, doi:10.1029/2005GL024782.

Brain, D. A., Lillis, R. J., Mitchell, D. L., Halekas, J. S., and Lin, R. P. (2007). Electron pitch angle distributions as indicators of magnetic field topology near Mars, *J. Geophys. Res.: Space Physics*, 112(A9), doi:10.1029/2007ja012435.

Breslow, R. (1959). On the mechanism of the formose reaction, *Tetrahedron Letters*, 1, 21, 22–26, doi:10.1016/S0040-4039(01)99487-0.

Brown, R., and Winkler, C. A. (1970). The chemical behaviour of active nitrogen, *Angew. Chem.*, 9, 181–254, doi:10.1002/anie.197001811.

Burkholder, J. B., Sander, S. P., Abbatt, J., Barker, J. R., Huie, R. E., Kolb, C. E., Kurylo, M. J., Orkin, V. L., Wilmouth, D. M., and Wine, P. H. (2015). Chemical Kinetics and Photochemical Data for Use in Atmospheric Studies, Evaluation No. 18, *JPL Publication 15-10*, Jet Propulsion Laboratory, Pasadena, http://jpldataeval.jpl.nasa.gov.

Burkholder, J. B., Sander, S. P., Abbatt, J., Barker, J. R., Cappa, C., Crounse, J. D., Dibble, T. S., Huie, R. E., Kolb, C. E., Kurylo, M. J., Orkin, V. L., Percival, C. J., Wilmouth, D. M., and Wine, P. H. (2019). Chemical Kinetics and Photochemical Data for Use in Atmospheric Studies, Evaluation No. 19, *JPL Publication 19-5*, Jet Propulsion Laboratory, Pasadena, http://jpldataeval.jpl.nasa.gov.

Butlerow, A. (1861). Formation synthétique d'une substance sucrée, *C. R. Acad. Sci,* 53, 145.

Cain, J. C., Ferguson, B. B., and Mozzoni, D. (2003). An n = 90 internal potential function of the Martian crustal magnetic field, *J. Geophys. Res.*, 108, 5008, doi:10.1029/2000JE001487, E2.

Cane, H. V., Reames, D. V., and von Rosenvinge, T. T. (1988). The role of interplanetary shocks in the longitude distribution of solar energetic particles, *J. Geophys. Res.*, 93:9555–9567, doi:10.1029/JA093iA09p09555.

Capetanakis, F. P., Sonderman, F., Hoser, S., and Stuhl, F. (1993). Temperature dependence of the quenching of O(^{1}S) by simple inorganic molecules, *J. Geophys. Res.*, 98, 7883–3887, doi:10.1063/1.464596.

Carr, M. (1987). Water on Mars, *Nature*, 326, 30–35, doi:10.1038/326030a0.

Catling, D. C., and Kasting, J. F. (2017). Atmospheric Evolution on Inhabitable Lifeless Worlds, *Cambridge, UK: Cambridge University Press*.

Chaffin, M. S., Deighan, J., Schneider, N. M., and Stewart, A. I. F. (2017). Elevated atmospheric escape of atomic hydrogen from Mars induced by high-altitude water, *Nature Geoscience*, 10, 174–178, doi:10.1038/ngeo2887.

Chan, W. F., Cooper, G., and Brion, C. E. (1993). The electronic spectrum of water in the discrete and continuum regions. Absolute optical oscillator strengths for photoabsorption (6-200 eV), *Chem. Phys.*, 178, 387–401, doi:10.1016/0301-0104(93)85078-M.

Chung, C.-Y., Chew, E. P., Cheng, B.-M., Bahou, M., and Lee, Y.-P. (2001). Temperature dependence of absorption cross-section of H_2O, HDO, and D_2O in the spectral region 140-193 nm, *Nuclear Instruments and Methods in Physics Research Section A: Accelerators, Spectrometers, Detectors and Associated Equipment*, 467–468, Part 2, 1572-1576, doi.org/10.1016/S0168-9002(01)00762-8.

Connerney, J. E. P., Acuña, M., Ness, N., Kletetschka, G., Mitchell, D., Lin, R., and Reme, H. (2005). Tectonic implications of Mars crustal magnetism, *Proceedings of the National Academy of Sciences*, 102, 14970–14975, doi:10.1073/pnas.0507469102.

Cook, G. R., Metzger, P. H., and Ogawa, M. (1968). Photoionization and absorption coefficients of N_2O, *J. Opt. Soc. Am.*, 58, 129–136, doi:10.1364/JOSA.58.000129.

Craddock, R. A., and Howard, A. D. (2002). The case for rainfall on a warm, wet early Mars, *J. Geophys. Res.*, 107(E11), 5111, doi:10.1029/2001JE001505.

Cravens, T. E., Hamil, O., Houston, S., Bougher, S., Ma, Y., Brain, D. and Ledvina, S. (2017). Estimates of ionospheric transport and ion loss at Mars, *Journal of Geophysical Research: Space Physics*, 122, doi:10.1002/2017JA024582.

Crutzen, P. J. (1970). The influence of nitrogen oxides on the atmospheric ozone content, *Quart .J. R. Meteorol. Soc.*, 96, 320–325, doi:10.1002/qj.49709640815.

Crutzen, P. J., Isaksen, I. S. A., and Reid, G. C. (1975). Solar proton events: Stratospheric sources of nitric oxide, *Science*, 189, 457, doi:10.1126/science.189.4201.457.

Damian, V., Sandu, A., Damian, M., Potra, F., and Carmichael, G. R. (2002). The kinetic preprocessor KPP - a software environment for solving chemical kinetics, *Computers & Chemical Engineering*, 26, 11, 1567–1579, doi:10.1016/S0098-1354(02)00128-X.

Deighan, J., Jain, S. K., Chaffin, M. S., Fang, X., Halekas, J. S., Clarke, J. T., et al. (2018). Discovery of proton aurora at Mars, *Nature Astronomy*, 2(10), 802–807, doi:10.1038/s41550-018-0538-5.

Desai, M., and Giacalone, J. (2016). Large gradual solar energetic particle events, *Living Rev. Sol. Phys*., 13, 3, doi:10.1007/s41116-016-0002-5.

Desai, M. I., Mason, G. M., Dayeh, M. A., Ebert, R. W., McComas, D. J., Li, G., Cohen, C. M. S., Mewaldt, R. A., Schwadron, N. A., and Smith, C. W. (2016). SPECTRAL PROPERTIES OF LARGE GRADUAL SOLAR ENERGETIC PARTICLE EVENTS. II. SYSTEMATIC Q/M DEPENDENCE OF HEAVY ION SPECTRAL BREAKS, *Astrophysical Journal*, 828, 106, doi:10.3847/0004-637X/828/2/106.

Desorgher, L., Flückiger, E. O., and Gurtner, M. (2006). The PLANETOCOSMICS Geant4 application, in *36th COSPAR Scientific Assembly*, 36, 2361.

Dotan, I., Hierl, P. M., Morris, R. A., and Viggiano, A. A. (1997). Rate constants for the reactions of N^+ and N_2^+ with O_2 as a function of temperature (300 - 1800 K), *Int. J. Mass Spectrom. Ion Proc.*, 167/168, 223–230, doi:10.1016/S0168-1176(97)00077-3.

Ehresmann, B., Hassler, D. M., Zeitlin, C., Guo, J., Wimmer-Schweingruber, R. F., Matthiä, D., et al. (2018). Energetic particle radiation environment observed by RAD on the surface of Mars during the September 2017 event, *Geophys. Res. Lett.*, 45, 5305–5311, doi:10.1029/2018GL077801.

Espley, J. R., Farrell, W. M., Brain, D. A., Morgan, D. D., Canor, B., Plaut, J. J., et al. (2007). Absorption of MARSIS radar signals: Solar energetic particles and the dayside ionosphere, *Geophys. Res. Lett.*, 34, L09101, doi:10.1029/2006GL028829.

Fang, X., Lummerzheim, D., and Jackman, C. H. (2013). Proton impact ionization and a fast calculation method, *J. Geophys. Res.: Space Physics*, 118, 5369–5378, doi:10.1002/jgra.50484.

Fernandez, A., Goumri, A., and Fontijn, A. (1998). Kinetics of the reactions of N(^{4}S) atoms with O_2 and CO_2 over wide temperature ranges, *J. Phys. Chem.*, 102, 168–172, doi:10.1021/jp972365k.

Forget, F., Montmessin, F., Bertaux, J. ‐ L., González-Galindo, F., Lebonnois, S., Quémerais, E., Reberac, A., Dimarells, E., and López-Valverde, M. A. (2009). Density and temperatures of the upper Martian atmosphere measured by stellar occultations with Mars Express SPICAM, *J. Geophys. Res.*, 114, E01004, doi:10.1029/2008JE003086.

Fox, J. L., and Dalgarno, A. (1979a). Ionization, luminosity, and heating of the upper atmosphere of Mars, *J. Geophys. Res.*, 84, 7315–7333, doi:10.1029/JA084jA12p07315.

Fox, J. L., and Dalgarno, A. (1979b), Electron energy deposition in carbon dioxide, *Planetary and Space Science*, 27, 4, 491–502, doi:10.1016/0032-0633(79)90126-0.

Fox, J. L., and Sung, K. Y. (2001). Solar activity variations of the Venus thermosphere/ionosphere, *J. Geophys. Res.*, 106(A10), 21305–21335, doi:10.1029/2001JA000069.

Gérard, J.-C., Soret. L., Libert, L., Lundin, R., Stiepen, A., Radioti, A., and Bertaux, J.-L. (2015). Concurrent observations of ultraviolet aurora and energetic electron precipitation with Mars Express, *J. Geophys. Res.: Space Physics*, 120, 6749–6765, doi:10.1002/2015JA021150.

Gérard, J.-C., Soret, L., Shematovich, V. I., Bisikalo, D. V., and Bougher, S. W. (2017). The Mars diffuse aurora: A model of ultraviolet and visible emissions, *Icarus*, 288, 284–294, doi:10.1016/j.icarus.2017.01.037.

Gérard, J.-C., Hubert, B., Ritter, B., Shematovich, V. I., and Bisikalo, D. V. (2019). Lyman-α emission in the Martian proton aurora: Line profile and role of horizontal induced magnetic field, *Icarus*, 321, 266–271, doi:10.1016/j.icarus.2018.11.013.

Gerdjikova, M. G., and Shepherd, G. G. (1987). Evaluation of auroral 5577 Å excitation processes using Intercosmos Bulgaria 1300 satellite measurements, *J. Geophys. Res*., 92(A4), 3367–3374, doi:10.1029/JA092iA04p03367.

Gopalswamy, N. (2018). Chapter 2 - Extreme Solar Eruptions and their Space Weather Consequences, in Buzulukova, N. (editor), *Extreme Events in Geospace*, 37–63, Elsevier, doi:10.1016/B978-0-12-812700-1.00002-9.

Gorshelev, V., Serdyuchenko, A., Weber, M., Chehade, W., and Burrows, J. P., (2014). High spectral resolution ozone absorption cross-sections – Part 1: Measurements, data analysis and comparison with previous measurements around 293 K, *Atmos. Meas. Tech*., 7, 609–624, 2014, doi.org/10.5194/amt-7-609-2014.

Gray, C., Kovac, S., Nordheim, T., Stemock, B., and DeColibus, D. (2021). The Venusian Oxygen Green Line - A Proton Aurora?, *Bulletin of the AAS*, 53(7). Retrieved from https://baas.aas.org/pub/2021n7i408p04.

Green, A. E. S., and Sawada, T. (1972). Ionization cross sections and secondary electron distributions, *Journal of Atmospheric and Terrestrial Physics*, 34, 10, 1719–1728, doi:10.1016/0021-9169(72)90031-1.

Gröller, H., Montmessin, F., Yelle, R. V., Lefèvre, F., Forget, F., Schneider, N. M., et al. (2018). MAVEN/IUVS stellar occultation measurements of Mars atmospheric structure and composition, *J. Geophys. Res.: Planets*, 123, 1449–1483, doi:10.1029/2017JE005466.

Guo, J., Zeitlin, C., Wimmer-Schweingruber, R. F., McDole, T., Kühl, P., Appel, J. C., Matthiä, D., Krauss, J., and Köhler, J. (2018). A Generalized Approach to Model the Spectra and Radiation Dose Rate of Solar Particle Events on the Surface of Mars, *Astrophysical Journal*, 155, 49, doi:10.3847/1538-3881/aaa085.

Gürtler, P., Saile, V., and Koch, E. E. (1977). Rydberg series in the absorption spectra of H_2O and D_2O in the vacuum ultraviolet, *Chem. Phys. Lett.*, 51, 386–391, doi:10.1016/0009-2614(77)80427-2.

Haider, S. A., Seth, S. P., Kallio, E., and Oyama, K. I. (2002). Solar EUV and electron-proton-hydrogen atom-produced ionosphere on Mars: Comparative studies of particle fluxes and ion production rates due to different processes, *Icarus*, 159(1), 18–30. doi:10.1006/icar.2002.6919.

Haider, S. A., Abdu, M. A., Batista, I. S., Sobral, J. H., Luan, X., Kallio, E., Maguire, W. C., Verigin, M. I., and Singh, V. (2009), D, E, and F layers in the daytime at high-latitude terminator ionosphere of Mars: Comparison with Earth's ionosphere using COSMIC data, *J. Geophys. Res*., 114, A03311, doi:10.1029/2008JA013709.

Haider, S. A., and Masoom, J. (2019). Modeling of Diffuse Aurora due to Precipitation of H^+ - H and SEP Electrons in the Nighttime Atmosphere of Mars: Monte Carlo Simulation and MAVEN Observation, *J. Geophys. Res.: Space Physics*, 124, 9566–9576, doi:10.1029/2019JA026688.

Hake, R. D. and Phelps, A. V. (1967), Momentum-Transfer and Inelastic-Collision Cross Sections for Electrons in O_2, CO, and CO_2, *Phys. Rev*., 158, 1, 70–84, doi:10.1103/PhysRev.158.70.

Harada, Y., Gurnett, D. A., Kopf, A. J., Halekas, J. S., Ruhunusiri, S., DiBraccio, G. A., et al. (2018). MARSIS observations of the Martian nightside ionosphere during the September 2017 solar event, *Geophysical Research Letters*, 45, 7960–7967, doi:10.1002/2018GL077622.

Hassler, D. M., Zeitlin, C., Ehresmann, B., Wimmer-Schweingruber, R. F., Guo, J., Matthiä, D., et al (2018). Space weather on the surface of Mars: Impact of the September 2017 events, *Space Weather*, 16, 1702–1708, doi:10.1029/2018SW001959.

Herran, C., Arqueros, F., and Campos, F. (1983). Lifetime of electronic states of CO_2^+, *Journal of Molecular Spectroscopy*, 97, 2, 244–247, doi.org/10.1016/0022-2852(83)90264-3.

Herron, J. T., and Huie, R. E. (1968). On the reaction of atomic nitrogen with carbon dioxide, *J. Phys. Chem.*, 72, 2235–2236, doi:10.1021/j100852a064.

Hitchcock, A. P., Brion, C. E., and van der Wiel, M. J. (1980). Absolute oscillator-strengths for valence-shell ionic photofragmentation of N_2O and CO_2 (8-75 eV), *Chem. Phys.*, 45, 461–478, doi:10.1016/0301-0104(80)87015-7.

Holland, D. M. P., Shaw, D. A., McSweeney, S. M., MacDonald, M. A., Hopkirk, A., Hayes, M. A. (1993). A study of the absolute photoabsorption, photoionization and photodissociation cross sections and the photoionization quantum efficiency of oxygen from the ionization threshold to 490 Å, *Chemical Physics*, 173, 2, 315–331, doi:10.1016/0301-0104(93)80148-3.

Huebner, W. F., Mukherjee, J. (2015). Photoionization and photodissociation rates in solar and blackbody radiation fields, *Planetary and Space Science*, doi:10.1016/j.pss.2014.11.022.

Huestis, D. L., and Berkowitz, J. (2011). Critical evaluation of the photoabsorption cross section of CO_2 from 0.125 to 201.6 nm at room temperature, *Advances in Geosciences*, 229–242, doi:10.1142/9789814355377_0018.

Huffman, R. E. (1969). Absorption cross-sections of atmospheric gases for use in aeronomy, *Canadian Journal of Chemistry*, 47 (10), 1823–1834 doi:10.1139/v69-298.

Hughes, A., Chaffin, M., Mierkiewicz, E., Deighan, J., Jain, S., Schneider, N., et al. (2019). Proton aurora on Mars: A dayside phenomenon pervasive in southern summer, *J. Geophys. Res.: Space Physics*, 124, 10533–10548. doi:10.1029/2019JA027140.

Hunten, D. M. (1973). The escape of light gases from planetary atmospheres, *Journal of the Atmospheric Sciences*, 30(8), 1481–1494, doi:10.1175/1520-0469(1973)030%3C1481:TEOLGF%3E2.0.CO;2.

Igi, K., and Kawai, H. (1994). 量子力学 II, 講談社サイエンティフィク.

Intriligator, D. S., and Smith, E. J. (1979). Mars in the solar wind, *J. Geophys. Res.*, 84(B14), 8427–8435, doi:10.1029/JB084iB14p08427.

Itikawa, Y. (2002). Cross sections for electron collisions with carbon dioxide, *J. Phys. Chem. Ref. Data*, 31, 749, doi:10.1063/1.1481879.

Itikawa, Y. (2006). Cross sections for electron collisions with nitrogen molecules, *J. Phys. Chem. Ref. Data*, 35, 31, doi:10.1063/1.1937426.

Itikawa, Y. (2009). Cross sections for electron collisions with oxygen molecules, *J. Phys. Chem. Ref. Data*, 38, 1, doi:10.1063/1.3025886.

Itikawa, Y. (2015). Cross sections for electron collisions with carbon monoxide, *J. Phys. Chem. Ref. Data*, 44, 013105, doi:10.1063/1.4913926.

Itikawa, Y., and Ichimura, A. (1990). Cross Sections for Collisions of Electrons and Photons with Atomic Oxygen, *Journal of Physical and Chemical Reference Data*, 19, 637–651, doi:10.1063/1.555857.

Jackman, C. H., Garvey, R. H., and Green, A. E. S. (1977). Electron impact on atmospheric gases, I. Updated cross sections, *J. Geophys. Res.*, 82(32), 5081–5090, doi:10.1029/JA082i032p05081.

Jackman, C. H., DeLand, M. T., Labow, G. J., Fleming, E. L., Weisenstein, D. K., Ko, M. K. W., Sinnhuber, M., and Russell, J. M. (2005). Neutral atmospheric influences of the solar proton events in October–November 2003, *J. Geophys. Res.*, 110, A09S27, doi:10.1029/2004JA010888.

Jakosky, B. M. (1991). Mars volatile evolution: Evidence from stable isotopes, *Icarus*, 94, 1, 14–31, doi:10.1016/0019-1035(91)90138-J.

Jakosky, B. M., and Jones, J. (1994). Evolution of water on Mars, *Nature*, 370, 328–329, doi:10.1038/370328a0.

Jakosky, B. M., Grebowsky, J. M., Luhmann, J. G., Connerney, J., Eparvier, F., Ergun, R., et al. (2015). MAVEN observations of the response of Mars to an interplanetary coronal mass ejection, *Science*, 350(6261), doi:10.1126/science.aad0210.

Jakosky, B. M., Slipski, M., Benna, M., Mahaffy, P., Elrod, M., Yelle, R., Stone, S., and Alsaeed, N. (2017). Mars' atmospheric history derived from upper-atmosphere measurements of ^{38}Ar/^{36}Ar, *Science*, 355(6332), 1408–1410, doi:10.1126/science.aai7721.

Johnston, H. S., Chang, S.-G., and Whitten, G. (1974). Photolysis of nitric acid vapor, *J. Phys. Chem.*, 78, 1–7, doi:10.1021/j100594a001.

Johnston, H. S., Davis, H. F., and Lee, Y. T. (1996). NO_3 photolysis product channels: Quantum yields from observed energy thresholds, *J. Phys. Chem.*, 100, 4713–4723, doi:10.1021/jp952692x.

Jolitz, R. D., Dong, C. F., Lee, C. O., Lillis, R. J., Brain, D. A., Curry, S. M., et al. (2017). A Monte Carlo model of crustal field influences on solar energetic particle precipitation into the Martian atmosphere, *J. Geophys. Res.: Space Physics*, 122, 5653–5669, doi:10.1002/2016JA023781.

Jolitz, R. D., Dong, C. F., Rahmati, A., Brain, D. A., Lee, C. O., Lillis, R. J., et al. (2021). Test particle model predictions of SEP electron transport and precipitation at Mars, *J. Geophys. Res.: Space Physics*, 126, e2021JA029132, doi:10.1029/2021JA029132.

Kallio, E., and Barabash, S. (2001). Atmospheric effects of precipitating energetic hydrogen atoms on the Martian atmosphere, *J. Geophys. Res.*, 106(A1), 165–177, doi:10.1029/2000JA002003.

Kamada, A., Kuroda, T., Kasaba, Y., Terada, N., Nakagawa, H., and Toriumi, K. (2020). A coupled atmosphere-hydrosphere global climate model of early Mars: A ‘cool and wet’ scenario for the formation of water channels, *Icarus*, 338, 113567, doi:10.1016/j.icarus.2019.113567.

Kamada, A., Kuroda, T., Kasaba, Y., Terada, N., and Nakagawa, H. (2021). Global climate and river transport simulations of early Mars around the Noachian and Hesperian boundary, *Icarus*, 368, 114618, doi:10.1016/j.icarus.2021.114618.

Kamada, A., Kuroda, T., Kodama, T., Kasaba, Y., and Terada, N. (2022). Evolution of ice sheets on early Mars with subglacial river systems, *Icarus*, 385, 115117, doi:10.1016/j.icarus.2022.115117.

Kasai, Y., H. Sagawa, T. Kuroda, T. Manabe, S. Ochiai, K. Kikuchi, T. Nishibori, P. Baron, J. Mendrok, P. Hartogh, D. Murtagh, J. Urban, F. Scheele, and U. Frisk (2012). Overview of the Martian atmospheric submillimetre sounder FIRE, *Planetary and Space Science*, 63–64, 62–82, doi:10.1016/j.pss.2011.10.013.

Kasting, J. F., Liu, S. C., and Donahue, T. M. (1979). Oxygen levels in the prebiological atmosphere, *J. Geophys. Res.*, 84(C6), 3097–3107, doi:10.1029/JC084iC06p03097.

Kataoka, R., Nakagawa, Y., and Sato, T. (2015). Radiation dose of aircrews during a solar proton event without ground-level enhancement, *Ann. Geophys.*, 33, 75–78, doi:10.5194/angeo-33-75-2015.

Kataoka, R. (2020). Extreme geomagnetic activities: a statistical study, *Earth Planets Space*, 72, 124, doi:10.1186/s40623-020-01261-8.

Keller-Rudek, H., Moortgat, G. K., Sander, R., and Sörensen, R. (2013). The MPI-Mainz UV/VIS spectral atlas of gaseous molecules of atmospheric interest, *Earth Syst. Sci. Data*, 5, 365–373, doi:10.5194/essd-5-365-2013.

Khayat, A. S. J., Smith, M. D., Wolff, M., Daerden, F., Neary, L., Patel, M. R., et al. (2021). ExoMars TGO/NOMADUVIS vertical profiles of ozone: 2. The high-altitude layers of atmospheric ozone, *Journal of Geophysical Research: Planets*, 126, e2021JE006834, doi:10.1029/2021JE006834.

Kim, Y. H., and Fox, J. L. (1994). The chemistry of hydrocarbon ions in the Jovian ionosphere, *Icarus*, 112, 310–325, doi:10.1006/ icar.1994.1186.

Kobayashi, K., Tsuchiya, M., Oshima, T. et al. (1990). Abiotic synthesis of amino acids and imidazole by proton irradiation of simulated primitive earth atmospheres, *Origins Life Evol. Biosphere*, 20, 99–109, doi:10.1007/BF01808270.

Koyama, S., Terada, N., Nakagawa, H., Kuroda, T., and Sekine, Y. (2021). Stability of atmospheric redox states of early Mars inferred from time response of the regulation of H and O losses, *Astrophysical Journal*, 912(2), 135, doi:10.3847/1538-4357/abf0ac.

Kozelov, B. V., and Ivanov, V. E. (1992). Monte Carlo calculation of proton-hydrogen atom transport in N_2, *Planetary and Space Science*, 40, 11, 1503–1511, doi:10.1016/0032-0633(92)90047-R.

Krasnopolsky, V. A. (1993). Photochemistry of the Martian atmosphere (mean conditions), *Icarus*, 101, 313–332, doi:10.1006/icar.1993.1027.

Krasnopolsky, V. A., (2009). A photochemical model of Titan's atmosphere and ionosphere, *Icarus*, 201, 1, 226–256, doi:10.1016/j.icarus.2008.12.038.

Krasnopolsky, V. A. (2012). A photochemical model for the Venus atmosphere at 47–112km, Icarus, 218, 1, 230–246, doi:10.1016/j.icarus.2011.11.012.

Krivolutsky, A. A., V’yushkova, T. Y., Cherepanova, L. A. et al. (2015). The three-dimensional photochemical model CHARM. Incorporation of solar activity, *Geomagn. Aeron.*, 55, 59–88, doi:10.1134/S0016793215010077.

Kumar, Y., Tiwari, N., Kumar, M., and Tomar, S. (2010). Total ionization cross-sections of atmospheric molecules due to electron impact, *Indian Journal of Pure & Applied Physics*, 48, 621–625.

Lanzerotti, L. J. (2017). Space Weather: Historical and Contemporary Perspectives, *Space Sci. Rev.*, 212, 1253–1270, doi:10.1007/s11214-017-0408-y.

Larson, D. E., Lillis, R. J., Lee, C. O., Dunn, P. A., Hatch, K., Robinson, M., et al. (2015). The MAVEN Solar Energetic Particle Investigation, *Space Sci. Rev.*, 195, 153–172, doi:10.1007/s11214-015-0218-z.

Lassettre, E. N., and Shiloff, J. C. (1965). Collision Cross ‐ Section Study of CO_2, *J. Chem. Phys.*, 43, 560–571 doi:10.1063/1.1696781.

Leblanc, F., Luhmann, J. G., Johnson, R. E., and Chassefiere, E., (2002). Some expected impacts of a solar energetic particle event at Mars, *J. Geophys. Res.*, 107(A5), doi:10.1029/2001JA900178.

Leblanc, F., Witasse, O., Lilensten, J., Frahm, R. A., Safaenili, A., Brain, D. A., et al. (2008). Observations of aurorae by SPICAM ultraviolet spectrograph on board Mars Express: Simultaneous ASPERA-3 and MARSIS measurements, *J. Geophys. Res.*, 113(A08311), doi:10.1029/2008JA013033.

Lebonnois, S., Quémerais, E., Montmessin, F., Lefèvre, F., Perrier, S., Bertaux, J.-L., and Forget, F. (2006). Vertical distribution of ozone on Mars as measured by SPICAM/Mars Express using stellar occultations, *J. Geophys. Res.*, 111, E09S05, doi:10.1029/2005JE002643.

Lee, P. (1955). Photodissociation and photoionization of oxygen (O_2) as inferred from measured absorption coefficients, *J. Opt. Soc. Am.*, 45, 703–709, doi:10.1364/JOSA.45.000703.

Lefèvre, F., Trokhimovskiy, A., Fedorova, A., Baggio, L., Lacombe, G., Määttänen, A., et al. (2021). Relationship between the ozone and water vapor columns on Mars as observed by SPICAM and calculated by a global climate model, *J. Geophys. Res.: Planets*, 126, e2021JE006838, doi:10.1029/2021JE006838.

Lester, M., Sanchez-Cano, B., Potts, D., Lillis, R., Cartacci, M., Bernardini, F., et al. (2022). The impact of energetic particles on the Martian ionosphere during a full solar cycle of radar observations: Radar blackouts, *J. Geophys. Res.: Space Physics*, 127, e2021JA029535, doi:10.1029/2021JA029535.

Lillis, R. J., Fillingim, M. O., and Brain, D. A. (2011). Three-dimensional structure of the Martian nightside ionosphere: Predicted rates of impact ionization from Mars Global Surveyor magnetometer and electron reflectometer measurements of precipitating electrons, *J. Geophys. Res.*, 116, A12317, doi:10.1029/2011JA016982.

Lillis, R. J., Lee, C. O., Larson, D., Luhmann, J. G., Halekas, J. S., Connerney, J. E. P., and Jakosky, B. M. (2016). Shadowing and anisotropy of solar energetic ions at Mars measured by MAVEN during the March 2015 solar storm, *J. Geophys. Res.: Space Physics*, 121, 2818–2829, doi:10.1002/2015JA022327.

Lillis, R. J., Deighan, J., Brain, D., Fillingim, M., Jain, S., Chaffin, M., et al. (2022). First synoptic images of FUV discrete aurora and discovery of sinuous aurora at Mars by EMM EMUS. *Geophys. Res. Lett.*, 49, e2022GL099820, doi:10.1029/2022GL099820.

Lingam, M., Dong, C., Fang, X., Jakosky, B., and Loeb, A. (2018). The Propitious Role of Solar Energetic Particles in the Origin of Life, *The Astrophysical Journal*, 853:10, doi:10.3847/1538-4357/aa9fef.

Lu, H.-C., Chen, K.-K., Chen, H.-F., Cheng, B.-M., and Ogilvie, J. F. (2010). Absorption cross section of molecular oxygen in the transition $E^3\Sigma_u^-$, v = 0 - $X^3\Sigma_g^-$, v = 0 at 38 K, *Astronom. Astrophys.*, 520, A19, 1–4, doi:10.1051/0004-6361/201013998.

Luhmann, J. G., Zeitlin, C., Turner, R., Brain, D. A., Delory, G., Lyon, J. G., and Boynton, W. (2007). Solar energetic particles in near-Mars space, *J. Geophys. Re*s., 112, E10001, doi:10.1029/2006JE002886.

Mahaffy, P. R., Webster, C. R., Atreya, S. K., Franz, H., Wong, M., Conrad, P. G., Harpold, D., Jones, J. J., Leshin, L. A., Manning, H., Owen, T., Pepin, R. O., Squyres, S., Trainer, M., and MSL Science Team (2013). Abundance and Isotopic Composition of Gases in the Martian Atmosphere from the Curiosity Rover, *Science*, 341, 6143, 263–266, doi:10.1126/science.1237966.

Mann, G. (2015). Energetic electrons generated during solar flares, *Journal of Plasma Physics*, 81(6), 475810601, doi:10.1017/S0022377815001166.

Margitan, J. J., and Watson, R. T. (1982). Kinetics of the reaction of hydroxyl radicals with nitric acid, *J. Phys. Chem.*, 1982, 86, 3819–3824, doi:10.1021/j100216a022.

Matsumi, Y., Comes, F. J., Hancock, G., Hofzumahaus, A., Hynes, A. J., Kawasaki, M., and Ravishankara, A. R. (2002). Quantum yields for production of $O(^1D)$ in the ultraviolet photolysis of ozone: Recommendation based on evaluation of laboratory data, *J. Geophys. Res.*, 107(D3), doi:10.1029/2001JD000510.

McConkey, J. W., and Latimer, I. D. (1965). Absolute cross sections for simultaneous ionization and excitation of N_2 by electron impact, *Proc. Phys. Soc.*, 86, 463, doi:10.1088/0370-1328/86/3/304.

McPeters, R. D., and Jackman, C. H. (1985). The response of ozone to solar proton events during solar cycle 21: The observations, *J. Geophys. Res.*, 90(D5), 7945–7954, doi:10.1029/JD090iD05p07945.

Meller, R., and Moortgat, G. K. (2000). Temperature dependence of the absorption cross sections of formaldehyde between 223 and 323 K in the wavelength range 225-375 nm, *J. Geophys. Res.*, 105(D6), 7089–7101, doi:10.1029/1999JD901074.

Mewaldt, R. A., Cohen, C. M. S., Labrador, A. W., Leske, R. A., Mason, G. M., Desai, M. I., Looper, M. D., Mazur, J. E., Selesnick, R. S., and Haggerty, D. K. (2005). Proton, helium, and electron spectra during the large solar particle events of October–November 2003, *J. Geophys. Res.*, 110, A09S18, doi:10.1029/2005JA011038.

Michel, F. C. (1971). Solar wind interaction with planetary atmospheres, *Rev. Geophys.*, 9(2), 427–435, doi:10.1029/RG009i002p00427.

Millour, E., Forget, F., Spiga, A., Vals, M., Zakharov, V., Montabone, et al. (2018). The Mars climate database (version 5.3), *From Mars express to ExoMars Scientific Workshop*, Madrid, Spain: ESA-ESAC.

Minschwaner, K., Anderson, G. P., Hall, L. A., and Yoshino, K. (1992). Polynomial coefficients for calculating O_2 Schumann-Runge cross sections at 0.5 cm^{-1} resolution, *J. Geophys. Res.*, 97(D9), 10103–10108, doi:10.1029/92JD00661.

Mitchell, D. L., Mazelle, C., Sauvaud, J.-A., Thocaven, J.-J., Rouzaud, J., Fedorov, A., et al. (2016). The MAVEN Solar Wind Electron Analyzer, *Space Sci. Rev.*, 200, 495–528, doi:10.1007/s11214-015-0232-1.

Molina-Cuberos, G. J., López-Moreno, J. J., Rodrigo, R., Lichtenegger, H., and Schwingenschuh, K. (2001). A model of the Martian ionosphere below 70 km, *Adv. Space Res.*, 27(11), 1801–1806, doi:10.1016/S0273-1177(01)00342-8.

Morgan, D. D., Gurnett, D. A., Kirchner, D. L., Huff, R. L., Brain, D. A., Boynton, W. V., et al. (2006). Solar control of radar wave absorption by the Martian ionosphere, *Geophysical Research Letters*, 33, L13202, doi:10.1029/2006GL026637.

Mota, R., Parafita, R., Giuliani, A., Hubin-Franskin, M.-J., Lourenço, J. M. C., Garcia, G., Hoffmann, S. V., Mason, M. J., Ribeiro, P. A., Raposo, M., and Limão-Vieira, P. (2005). Water VUV electronic state spectroscopy by synchrotron radiation, *Chem. Phys. Lett.*, 416, 152–159, doi:10.1016/j.cplett.2005.09.073.

Mukundan, V., Thampi, S. V., Bhardwaj, A., and Krishnaprasad, C. (2020). The dayside ionosphere of Mars: Comparing a one-dimensional photochemical model with MAVEN Deep Dip campaign observations, *Icarus*, 337, 113502, doi:10.1016/j.icarus.2019.113502.

Nair, H., Allen, M., Anbar, A. D., Yung, Y. L., and Clancy, R. T., (1994). A Photochemical Model of the Martian Atmosphere, *Icarus*, 111, 1, 124–150, doi:/10.1006/icar.1994.1137.

Nakamura, Y., Terada, N., Leblanc, F., Rahmati, A., Nakagawa, H., Sakai, S., et al. (2022a). Modeling of diffuse auroral emission at Mars: Contribution of MeV protons. *Journal of Geophysical Research: Space Physics*, 127, e2021JA029914, doi:10.1029/2021JA029914.

Nakamura, Y., Terada, K., Tao, C., Terada, N., Kasaba, Y., Leblanc, F., et al. (2022b). Effect of meteoric ions on ionospheric conductance at Jupiter. *Journal of Geophysical Research: Space Physics*, 127, e2022JA030312, doi:10.1029/2022JA030312.

Newman, J. H., Chen, Y. S., Smith, K. A., and Stebbings, R. F. (1986). Differential cross sections for scattering of 0.5-, 1.5-, and 5.0-keV hydrogen atoms by He, H_2, N_2, and O_2, *J. Geophys. Res.: Space Physics*, 91(A8), 8947–8954, doi:10.1029/JA091iA08p08947.

Nigam, B. P. and Sundaresan, M. K. and Wu, T.-Y. (1959). Theory of Multiple Scattering: Second Born Approximation and Corrections to Molière's Work, *Phys. Rev.*, 115, 3, 491–502, doi:10.1103/PhysRev.115.491.

Noël, S., and Prölss, G. W. (1993). Heating and radiation production by neutralized ring current particles, *J. Geophys. Res.*, 98(A10), 17317–17325, doi:10.1029/93JA01500.

Ogawa, S., and Ogawa, M. (1975). Absorption cross sections of $O_2(a^1\Delta_g)$ and $O_2(X^3\Sigma_g^-)$ in the region from 1087 to 1700 Å", *Can. J. Phys.*, 53, 1845–1852, doi:10.1139/p75-236.

Ono, T. (1993). Derivation of Energy Parameters of Precipitating Auroral Electrons by Using the Intensity Ratios of Auroral Emissions, *Journal of geomagnetism and geoelectricity*, 45, 6, 455–472, doi:10.5636/jgg.45.455.

Osborne, B. A., Marston, G., Kaminski, L., Jones, N. C., Gingell, J. M., Mason, N., Walker, I. C., Delwiche, J., and Hubin-Franskin, M.-J. (2000). Vacuum ultraviolet spectrum of dinitrogen pentoxide, *J. Quant. Spectrosc. Radiat. Transfer*, 64, 67–74, doi:10.1016/S0022-4073(99)00104-1.

Patel, B., Percivalle, C., Ritson, D. et al. (2015). Common origins of RNA, protein and lipid precursors in a cyanosulfidic protometabolism, *Nature Chem.*, 7, 301–307, doi:10.1038/nchem.2202.

Patel, M. R., Zarnecki, J. C., and Catling, D. C. (2002). Ultraviolet radiation on the surface of Mars and the Beagle 2 UV sensor, *Planetary and Space Science*, 50, 9, 915–927, doi:10.1016/S0032-0633(02)00067-3.

Patel, M. R., Sellers, G., Mason, J. P., Holmes, J. A., Brown, M. A. J., Lewis, S. R., et al. (2021). ExoMars TGO/NOMAD-UVIS vertical profiles of ozone: 1. Seasonal variation and comparison to water, *Journal of Geophysical Research: Planets*, 126, e2021JE006837, doi:10.1029/2021JE006837.

Paul, J., Fortuin, F., and Kelder, H. (1998). An ozone climatology based on ozonesonde and satellite measurements, *J. Geophys. Res.*, 103(D24), 31709–31734, doi:10.1029/1998JD200008.

Pavlov, A. V. (2014). Photochemistry of Ions at D-region Altitudes of the Ionosphere: A Review, *Surv. Geophys.*, 35:259–334, doi:10.1007/s10712-013-9253-z.

Piccialli, A., Vandaele, A. C., Trompet, L., Neary, L., Viscardy, S., Erwin, J. T., Määttänen, A., Daerden, F., Willame, Y., Robert, S., Aoki, S., Wilquet, V., Lefèvre, F., and Montmessin, F. (2021). Impact of gradients at the martian terminator on the retrieval of ozone from SPICAM/Mex, *Icarus*, 353, 113598, doi:10.1016/j.icarus.2019.113598.

Pinto J. P., Gladstone, G. R., and Yung, Y. L. (1980). Photochemical Production of Formaldehyde in Earth's Primitive Atmosphere, *Science*, 210, 4466, doi:10.1126/science.210.4466.183.

Porter, H. S., Jackman, C. H., and Green, A. E. S. (1976). Efficiencies for production of atomic nitrogen and oxygen by relativistic proton impact in air, *J. Chem. Phys.*, 65, 154 doi:10.1063/1.432812.

Porter, H. S., and Jump, F. W. (1978). Analytical total angular elastic electron impact cross sections for planetary atmospheres, *NASA Publ.*, CSC/TM.

Porter, H. S., Varosi, F., and Mayr, H. G. (1987). Iterative solution of the multistream electron transport equation: 1. Comparison with laboratory beam injection experiments, *J. Geophys. Res.*, 92(A6), 5933–5959, doi:10.1029/JA092iA06p05933.

Rabalais, J. W., McDonald, J. M., Scherr, V., and McGlynn, S. P. (1971). Electronic spectroscopy of isoelectronic molecules. II. Linear triatomic groupings containing sixteen valence electrons, *Chem. Rev.*, 71, 73–108, doi:10.1021/cr60269a004.

Randall, C. E., Harvey, V. L., Manney, G. L., Orsolini, Y., Codrescu, M., Sioris, C., Brohede, S., Haley, C. S., Gordley, L. L., Zawodny, J. M., Russell III, J. M. (2005). Stratospheric effects of energetic particle precipitation in 2003–2004, *Geophys. Res. Lett.*, 32, L05802, doi:10.1029/2004GL022003.

Ranjan, S., Schwieterman, E. W., Harman, C., Fateev, A., Sousa-Silva, C., Seager, S., and Hu, R. (2020). Photochemistry of anoxic abiotic habitable planet atmospheres: Impact of new H_2O cross-sections, *Astrophys. J.*, 896, 148, doi:10.3847/1538-4357/ab9363.

Rawlins, W. T., and Kaufman, F. (1976). The reaction of CO_2 with active nitrogen, *J. Chem. Phys.*, 64, 1128–1133, doi:10.1063/1.432300.

Reames, D. V. (1995). Solar energetic particles: a paradigm shift, *Rev. Geophys.*, 33(Suppl):585–589, doi:10.1029/95RG00188.

Reames, D. V. (1999). Particle acceleration at the Sun and in the heliosphere, *Space Science Reviews*, 90, 413–491, doi:10.1023/A:1005105831781.

Reames, D. V. (2021). Solar Energetic Particles, 2nd edition, Lec. Notes Phys., vol 978. *Springer, Cham.*, doi:10.1007/978-3-030-66402-2.

Rees, M. H. (1984). Excitation of O(^{1}S) and emission of 5577 Å radiation in aurora, *Planetary and Space Science*, 32, 3, 373–378, doi:10.1016/0032-0633(84)90171-5.

Reid, G. C., and Collins, C. (1959). Observations of abnormal VHF radio wave absorption at medium and high latitudes, *Journal of Atmospheric and Terrestrial Physics*, 14, 1–2, 63–81, doi:10.1016/0021-9169(59)90056-X.

Richards, P. G., Fennelly, J. A., and Torr, D. G. (1994). EUVAC: A solar EUV flux model for aeronomic calculations, *J. Geophys. Res*., 99(A5), 8981–8992, doi:10.1029/94JA00518.

Rieke, F. F. and Prepejchal, W. (1972). Ionization Cross Sections of Gaseous Atoms and Molecules for High-Energy Electrons and Positrons, *Phys. Rev. A*, 6, 4, 1507–1519, doi:10.1103/PhysRevA.6.1507.

Ritter, B., Gérard, J.-C., Hubert, B., Rodriguez, L., and Montmessin, F. (2018). Observations of the proton aurora on Mars with SPICAM on board Mars Express, *Geophys. Res. Lett.*, 45, 612–619, doi:10.1002/ 2017GL076235.

Ronchi, C., Iacono, R., and Paolucci, P. S. (1996). The “Cubed Sphere”: A New Method for the Solution of Partial Differential Equations in Spherical Geometry, *Journal of Computational Physics*, 124, 1, 93–114, doi:10.1006/jcph.1996.0047.

Rudd, M. E., DuBois, R. D., Toburen, L. H., Ratcliffe, C. A., and Goffe, T. V. (1983). Cross sections for ionization of gases by 5-4000-keV protons and for electron capture by 5-150-keV protons, *Phys. Rev. A*, 28, 6, 3244–3257, doi:10.1103/PhysRevA.28.3244.

Rusch, D. W., Gérard, J.-C., Solomon, S., Crutzen, P. J., Reid, G. C. (1981). The effect of particle precipitation events on the neutral and ion chemistry of the middle atmosphere—I. Odd nitrogen, *Planetary and Space Science*, 29, 7, 767–774, doi:10.1016/0032-0633(81)90048-9.

Russell, C. T., Yu, Z. J., and Kivelson, M. G. (2001). The rotation period of Jupiter, *Geophys. Res. Lett*., 28 (10): 1911–1912, doi:10.1029/2001GL012917.

Sánchez-Cano, B., Blelly, P.-L., Lester, M., Witasse, O., Cartacci, M., Orosei, R., et al. (2019). Origin of the extended Mars radar blackout of September 2017, *Journal of Geophysical Research: Space Physics*, 124, 4556–4568, doi:10.1029/2018JA026403.

Sánchez-Cano, B., Lester, M., Andrews, D. J. et al. (2021). Mars' plasma system. Scientific potential of coordinated multipoint missions: "The next generation", *Experimental Astronomy*, doi:10.1007/s10686-021-09790-0.

Sandford. B. P. (1961). Enhancement of Night-Sky Molecular Nitrogen Emission in Polar Cap Absorption Events, *Nature*, 190, 245–246, doi:10.1038/190245a0.

Sandford, B. P. (1962). Polar-glow aurora in polar cap absorption events, *Journal of Atmospheric and Terrestrial Physics*, 24, 3, 155–171, doi:10.1016/0021-9169(62)90240-4.

Sandford, B. P. (1963). Optical studies of particle bombardment in polar cap absorption events, *Planetary and Space Science*, 10, 195–213, doi:10.1016/0032-0633(63)90017-5.

Sawada, T., Strickland, D. J., and Green, A. E. S. (1972), Electron energy deposition in CO_2, *J. Geophys. Res*., 77(25), 4812–4818, doi:10.1029/JA077i025p04812.

Schmidt, J. A., Johnson, M. S., and Schinke, R. (2013). Carbon dioxide photolysis from 150 to 210 nm: Singlet and triplet channel dynamics, UV-spectrum, and isotope effects, *Proceedings of the National Academy of Sciences*, 110(44), 17691–17696, doi:10.1073/pnas.1213083110.

Schneider, N. M., Deighan, J. I., Jain, S. K., Stiepen, A., Stewart, A. I. F., Larson, D. et al. (2015). Discovery of diffuse aurora on Mars, *Science*, 350, 6261, doi:10.1126/science.aad0313.

Schneider, N. M., Jain, S. K., Deighan, J., Nasr, C. R., Brain, D. A., Larson, D., et al. (2018). Global aurora on Mars during the September 2017 space weather event, *Geophys. Res. Lett.*, 45, 7391–7398, doi:10.1029/2018GL077772.

Schneider, N. M., Milby, Z., Jain, S. K., Gérard, J.-C., Soret, L., Brain, D. A., et al. (2021). Discrete aurora on Mars: Insights into their distribution and activity from MAVEN/ IUVS observations, *J. Geophys. Res.: Space Physics*, 126, e2021JA029428, doi:10.1029/2021JA029428.

Schunk, R. W., and Nagy, A. F. (2009). *Ionospheres, 2nd edition*, Cambridge University Press.

Schürgers, M., and Welge, K. H. (1968). Absorptions koeffizient von H_2O_2 und N_2H_4 zwischen 1200 und 2000 Å, *Z. Naturforsch.*, 23a, 1508–1510, doi:10.1515/zna-1968-1011.

Scott, G. B. I., Fairley, D. A., Milligan, D. B., Freeman, C. G., and McEwan, M. J. (1999). Gas phase reactions of some positive ions with atomic and molecular oxygen and nitric oxide at 300 K, *J. Phys. Chem. A*, 103, 7470–7473, doi:10.1021/jp9913719.

Selwyn, G., Podolske, J., and Johnston, H. S. (1977). Nitrous oxide ultraviolet absorption spectrum at stratospheric temperatures, *Geophys. Res. Lett.*, 4, 427–430, doi:10.1029/GL004i010p00427.

Seppälä, A., Verronen, P. T., Kyrölä, E., Hassinen, S., Backman, L., Hauchecorne, A., Bertaux, J. L., and Fussen, D. (2004). Solar proton events of October–November 2003: Ozone depletion in the Northern Hemisphere polar winter as seen by GOMOS/Envisat, *Geophys. Res. Lett.*, 31, L19107, doi:10.1029/2004GL021042.

Serdyuchenko, A., Gorshelev, V., Weber, M., Chehade, W., and Burrows, J. P. (2014). High spectral resolution ozone absorption cross-sections – Part 2: Temperature dependence, *Atmos. Meas. Tech.*, 7, 625–636, doi:10.5194/amt-7-625-2014.

Sheel, V., Haider, S. A., Withers, P., Kozarev, K., Jun, I., Kang, S., Gronoff, G., and Simon Wedlund, C. (2012). Numerical simulation of the effects of a solar energetic particle event on the ionosphere of Mars, *J. Geophys. Res.*, 117, A05312, doi:10.1029/2011JA017455.

Shibayama, T., Maehara, H., Notsu, S., Notsu, Y., Nagao, T., Honda, S., Ishii, T. T., Nogami, D., and Shibata, K. (2013). SUPERFLARES ON SOLAR-TYPE STARS OBSERVED WITH KEPLER. I. STATISTICAL PROPERTIES OF SUPERFLARES, *The Astrophysical Journal*, 209:5, doi:10.1088/0067-0049/209/1/5.

Shirai, T., Tabata, T., and Tawara, H. (2001). Analytic cross sections for electron collisions with CO, CO_2, and H_2O relevant to edge plasma impurities, *Atom. Data Nucl. Data Tables*, 79, 143–184, doi:10.1006/adnd.2001.0866.

Shute, G. G., Robson, D., McKenna, V. R., and Berztiss, A. T. (1962). Elastic scattering of protons by carbon, *Nuclear Physics*, 37, 535–553, doi:10.1016/0029-5582(62)90289-4.

Simmons, D., and Henriksen, K. (1995). Polar-glow aurora observed from Spitsbergen, *Polar Record*, 31(178), 315–326, doi:10.1017/S0032247400013863.

Solomon, S., Rusch, D. W., Gérard, J.-C., Reid, G. C., and Crutzen, P. J. (1981). The effect of particle precipitation events on the neutral and ion chemistry of the middle atmosphere: II. Odd hydrogen, *Planetary and Space Science*, 29, 8, 885–893, doi:10.1016/0032-0633(81)90078-7.

Solomon, S. C. (2001). Auroral particle transport using Monte Carlo and hybrid methods, *J. Geophys. Res.*, 106(A1), 107–116, doi:10.1029/2000JA002011.

Soret, L., Gérard, J.-C., Libert, L., Shematovich, V. I., Bisikalo, D. V., Stiepen, A., and Bertaux, J.-L. (2016). SPICAM observations and modeling of Mars aurorae, *Icarus*, 264, 398–406, doi:10.1016/j.icarus.2015.09.023.

Soret, L., Gérard, J.-C., Schneider, N., Jain, S., Milby, Z., Ritter, B., et al. (2021). Discrete aurora on Mars: Spectral properties, vertical profiles, and electron energies. *J. Geophys. Res.: Space Physics*, 126, e2021JA029495, doi:10.1029/2021JA029495.

Strickland, D. J., and Green, A. E. S. (1969). Electron impact cross sections for CO_2, *J. Geophys. Res.*, 74(26), 6415–6424, doi:10.1029/JA074i026p06415.

Swartz, W. E., Nisbet, J. S., and Green, A. E. S. (1971). Analytic expression for the energy-transfer rate from photoelectrons to thermal-electrons, *J. Geophys. Res.*, 76(34), 8425–8426, doi:10.1029/JA076i034p08425.

Takeuchi, Y., Furukawa, Y., Kobayashi, T., Sekine, T., Terada, N., and Kakegawa, T. (2020). Impact-induced amino acid formation on Hadean Earth and Noachian Mars, *Scientific Reports*, 10, 9220, doi:10.1038/s41598-020-66112-8.

Terada, N., Kulikov, Y. N., Lammer, H., Lichtenegger, H. I. M., Tanaka, T., Shinagawa, H., and Zhang, T. (2009). Atmosphere and water loss from early Mars under extreme solar wind and extreme ultraviolet conditions, *Astrobiology*, 9(1), 55–70, doi:10.1089/ast.2008.0250.

Troe, J. (2005). Temperature and pressure dependence of ion − molecule association and dissociation reactions: the $N_2^+ + N_2$ (+ M) ⇔ N_4^+ (+ M) reaction, *Phys. Chem. Chem. Phys*., 7, 1560–1567, doi:10.1039/B417945P.

Tsurutani, B. T., Gonzalez, W. D., Tang, F., Akasofu, S. I., and Smith, E. J. (1988), Origin of interplanetary southward magnetic fields responsible for major magnetic storms near solar maximum (1978–1979), *J. Geophys. Res*., 93(A8), 8519–8531, doi:10.1029/JA093iA08p08519.

Turnipseed, A. A., Vaghjiani, G. L., Thompson, J. E., and Ravishankara, A. R. (1992). Photodissociation of HNO_3 at 193, 222, and 248 nm: Products and quantum yields, *J. Chem. Phys*., 1992, 96, 5887–5895, doi:10.1063/1.462685.

Vahedi, V., and Surrendra, M. (1995). A Monte Carlo collision model for the particle-in-cell method: applications to argon and oxygen discharges, *Computer Physics Communications*, 87, 1–2, 179–198, doi:10.1016/0010-4655(94)00171-W.

Vandaele, A. C., Hermans, C., Simon, P. C., Carleer, M., Colins, R., Fally, S., Mérienne, M. F., Jenouvrier, A., and Coquart, B. (1998). Measurements of the NO_2 absorption cross-sections from 42000 cm-1 to 10000 cm-1 (238-1000 nm) at 220 K and 294 K, *J. Quant. Spectrosc. Radiat. Transfer*, 59, 171–184, doi:10.1016/S0022-4073(97)00168-4.

Vandaele, A. C., Neefs, E., Drummond, R., Thomas, I. R., Daerden, F., Lopez-Moreno, J.-J., et al. (2015). Science objectives and performances of NOMAD, a spectrometer suite for the ExoMars TGO mission, *Planetary and Space Science*, 119, 233–249, doi:10.1016/j.pss.2015.10.003.

Vandaele, A. C., Lopez-Moreno, J. J., Patel, M. R. et al. (2018). NOMAD, an Integrated Suite of Three Spectrometers for the ExoMars Trace Gas Mission: Technical Description, Science Objectives and Expected Performance, *Space Sci. Rev.*, 214, 80, doi:10.1007/s11214-018-0517-2.

Verkhoglyadova, O. P., Wang, S., Mlynczak, M. G., Hunt, L. A., and Zank, G. P. (2015), Effects of two large solar energetic particle events on middle atmosphere nighttime odd hydrogen and ozone content: Aura/MLS and TIMED/SABER measurements, *J. Geophys. Res. Space Physics*, 120, 12–29, doi:10.1002/2014JA020609.

Verronen, P. T., Andersson, M. E., Marsh, D. R., Kovács, T., and Plane, J. M. C. (2016), WACCM-D—Whole Atmosphere Community Climate Model with D-region ion chemistry, *J. Adv. Model. Earth Syst.*, 8, 954–975, doi:10.1002/2015MS000592.

Wayne, R. P., Barnes, I., Burrows, J. P., Canosa-Mas, C. E., Hjorth, J., Le Bras, G., Moortgat, G.K., Perner, D., Poulet, G., Restelli, G., and Sidebottom, H. (1991). The nitrate radical: Physics, chemistry, and the atmosphere, *Atmos. Environ.*, 25A, 1–203, doi:10.1016/0960-1686(91)90192-A.

Williams, D. (2021). Mars Fact Sheet, *NASA Goddard Space Flight Center*, retrieved on 16 October 2022.

Withers, P., Felici, M., Mendillo, M. et al. (2020). The MAVEN Radio Occultation Science Experiment (ROSE). *Space Sci. Rev.*, 216, 61, doi:10.1007/s11214-020-00687-6.

Withers, P., Felici, M., Mendillo, M., Vogt, M. F., Barbinis, E., Kahan, D., et al. (2022). Observations of high densities at low altitudes in the nightside ionosphere of Mars by the MAVEN Radio Occultation Science Experiment (ROSE), *J. Geophys. Res.: Space Physics*, 127, e2022JA030737, doi:10.1029/2022JA030737.

Woods, T. N., Chamberlin, P. C., Harder, J. W., Hock, R. A., Snow, M., Eparvier, F. G., Fontenla, J., McClintock, W. E., and Richard, E. C. (2009). Solar Irradiance Reference Spectra (SIRS) for the 2008 Whole Heliosphere Interval (WHI), *Geophys. Res. Lett.*, 36, L01101, doi:10.1029/2008GL036373.

Yalcin, S., Gurler, O., Gultekin, A., and Gundogdu, O. (2006). An analytical expression for electron elastic scattering cross section from atoms and molecules in 1.0 keV to 1.0 MeV energy range, *Phys. Lett. A*, 356, 2, 138–145, doi:10.1016/j.physleta.2006.04.037.

Yoshida, N., Nakagawa, H., Aoki, S., Erwin, J., Vandaele, A. C., Daerden, F., et al. (2022). Variations in vertical CO/CO_2 profiles in the Martian mesosphere and lower thermosphere measured by the ExoMars TGO/NOMAD: Implications of variations in eddy diffusion coefficient, *Geophysical Research Letters*, 49, e2022GL098485, doi:10.1029/2022GL098485.

Yoshida, T., Aoki, S., Ueno, Y., Terada, N., Nakamura, Y., Shiobara, K., Yoshida, N., Nakagawa, H., Sakai, S., and Koyama, S. (2022). Strong depletion of ^{13}C in CO induced by photolysis of CO_2 in the Martian atmosphere calculated by a photochemical model, *Planetary Science Journal*, submitted.

Yoshino, K., Esmond, J. R., Cheung, A. S.-C, Freeman, D. E., and Parkinson, W. H. (1992). High resolution absorption cross sections in the transmission window region of the Schumann-Runge bands and Herzberg continuum of O_2, *Planetary and Space Science*, 40, 2–3, 185–192, doi:10.1016/0032-0633(92)90056-T.

Yoshino, K., Esmond, J. R., Parkinson, W. H., Ito, K., and Matsui, T. (1996). Absorption cross section measurements of water vapor in the wavelength region 120 to 188 nm, *Chem. Phys.*, 211, 387–391, doi:10.1016/0301-0104(96)00210-8.

Yoshino, K., Esmond, J. R., Parkinson, W. H., Ito, K., Matsui, T. (1997). Absorption cross section measurements of water vapor in the wavelength region 120 nm to 188 nm (Chem. Phys. 211 (1996) 387–391). *Chemical Physics*, 215, 429–430, doi:10.1016/s0301-0104(96)00381-3.

Yoshino, K., Parkinson, W. H., Ito, K., and Matsui, T. (2005). Absolute absorption cross-section measurements of Schumann-Runge continuum of O_2 at 90 and 295 K, *J. Mol. Spectrosc.*, 229, 238–243, doi:10.1016/j.jms.2004.08.020.

Zahnle, K., Claire, M. and Catling, D. (2006). The loss of mass-independent fractionation in sulfur due to a Palaeoproterozoic collapse of atmospheric methane, *Geobiology*, 4: 271–283, doi:10.1111/j.1472-4669.2006.00085.x.

Zelikoff, M., Watanabe, K., and Inn, E. C. Y. (1953). Absorption coefficients of gases in the vacuum ultraviolet. Part II. Nitrous oxide, *J. Chem. Phys.*, 21, 1643–1647, doi:10.1063/1.1698636.

GR Space Physics

RESEARCH ARTICLE
10.1029/2021JA029914

Modeling of Diffuse Auroral Emission at Mars: Contribution of [redacted]ns

[1]Graduate School of Science, Tohoku University, Sendai, Japan, [2]LATMOS/CNRS, Sorbonne Université, Paris, France, [3]Space Sciences Laboratory, University of California, Berkeley, CA, USA, [4]Planetary Plasma and Atmospheric Research Center, Graduate School of Science, Tohoku University, Sendai, Japan, [5]National Institute of Polar Research, Tokyo, Japan, [6]The Graduate University for Advanced Studies, SOKENDAI, Kanagawa, Japan

Key Points:

Supporting Information:

Correspondence to:

yuki.nakamura.r2@dc.tohoku.ac.jp

Citation:

https://doi.org/10.1029/2021JA029914

Abstract

1. Introduction

201

2015

8

2018

2019

2. Model Descripti

2.1. Monte Carlo Tran

1995

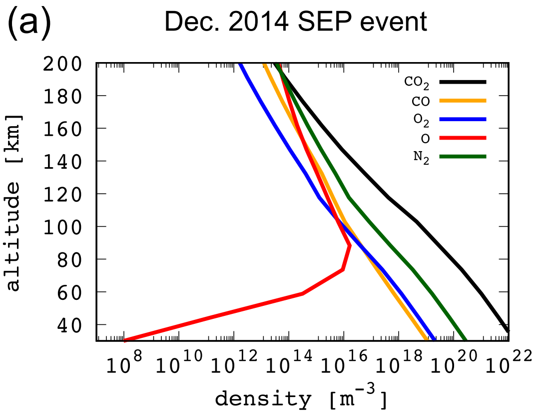

1

2.2. Collisional Cross Sections

2009

1977

2

2001

2001

2001

1962

2

1983

1987

2002

1983

2002

2001

2017

2001

1983

2.3. Energy Loss, Scattering Angle, and Secondary Electron Energy

2

2001

1993

2001

1977

1971

2.4. Method for Converting Particle Trajectories Into Flux

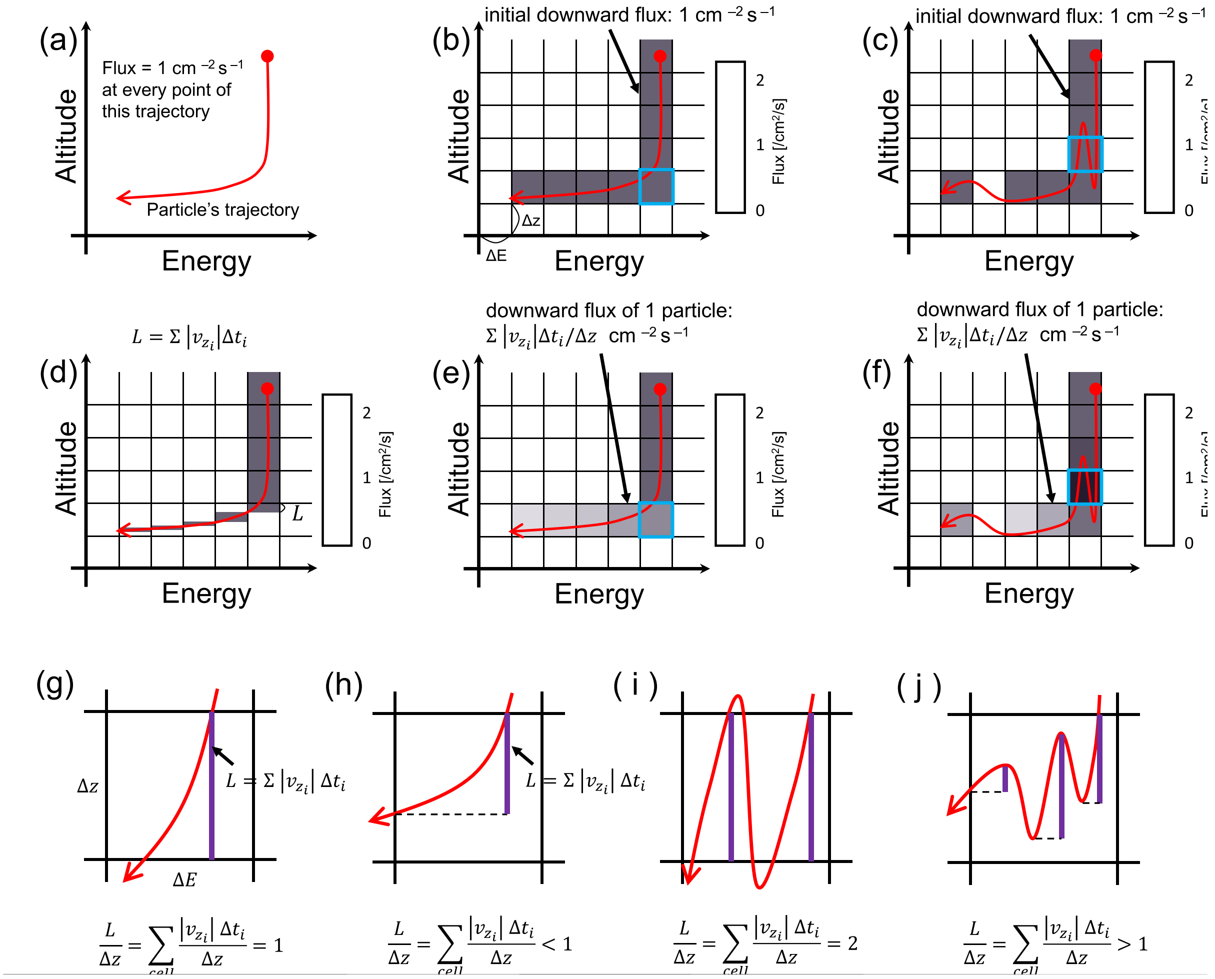
(a)
Altitude
Flux = 1 cm $^{-2}$ s $^{-1}$ at every point of this trajectory
Particle's trajectory
Energy
(b)
initial downward flux: 1 cm $^{-2}$ s $^{-1}$
Altitude
Δz
ΔE
Energy
Flux [/cm²/s]
0
1
2
(c)
initial downward flux: 1 cm $^{-2}$ s $^{-1}$
Altitude
Energy
0
1
2
(d)
$L = \Sigma |v_{z_i}| \Delta t_i$
Altitude
L
Energy
Flux [/cm²/s]
0
1
2
(e)
downward flux of 1 particle:
$\Sigma |v_{z_i}| \Delta t_i / \Delta z$ cm $^{-2}$ s $^{-1}$
Altitude
Energy
Flux [/cm²/s]
0
1
2
(f)
downward flux of 1 particle:
$\Sigma |v_{z_i}| \Delta t_i / \Delta z$ cm $^{-2}$ s $^{-1}$
Altitude
Energy
0
1
2
(g)
Δz
$L = \Sigma |v_{z_i}| \Delta t_i$
ΔE
$\frac{L}{\Delta z} = \sum_{cell} \frac{|v_{z_i}| \Delta t_i}{\Delta z} = 1$
(h)
$L = \Sigma |v_{z_i}| \Delta t_i$
$\frac{L}{\Delta z} = \sum_{cell} \frac{|v_{z_i}| \Delta t_i}{\Delta z} < 1$
(i)
$\frac{L}{\Delta z} = \sum_{cell} \frac{|v_{z_i}| \Delta t_i}{\Delta z} = 2$
(j)
$\frac{L}{\Delta z} = \sum_{cell} \frac{|v_{z_i}| \Delta t_i}{\Delta z} > 1$

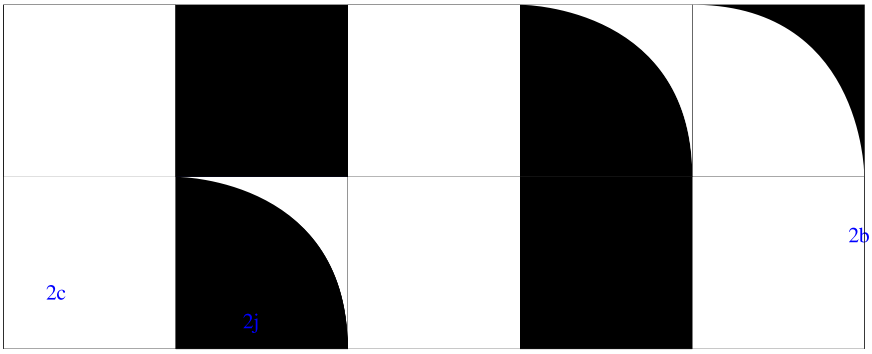
2c
2j
2b

2g

2e

2h

2i 2j

2e

2.5. Limb Intensity of CO_2^+ UVD

2013 1979 2019

3. Instruments

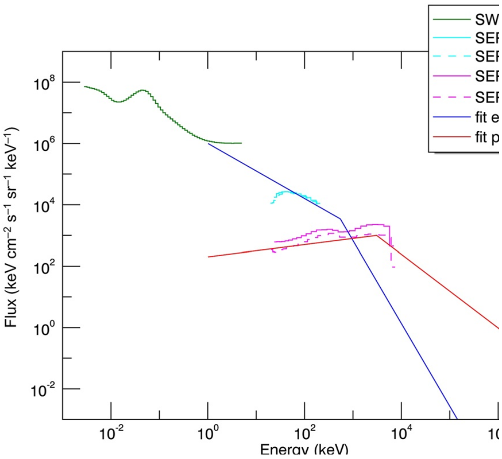

https://pds-ppi.igpp.ucla.edu/search/view/?f=yes&id=pds://PPI/

https://pds-ppi.igpp.ucla.edu/search/view/?f=yes&id=pds://PPI/maven.swea.

2015

3

2018

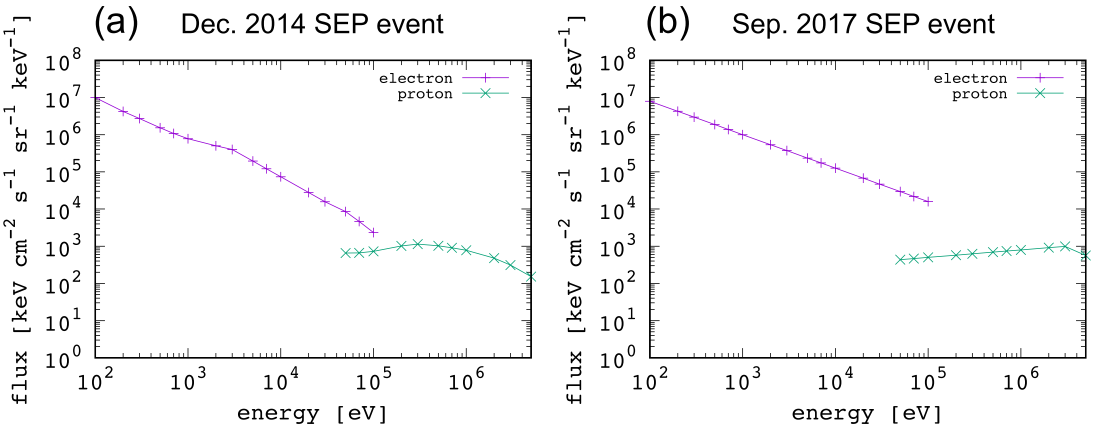

4. Results

4.1. Validation

2017

2017 1987

1987

1987

5

6

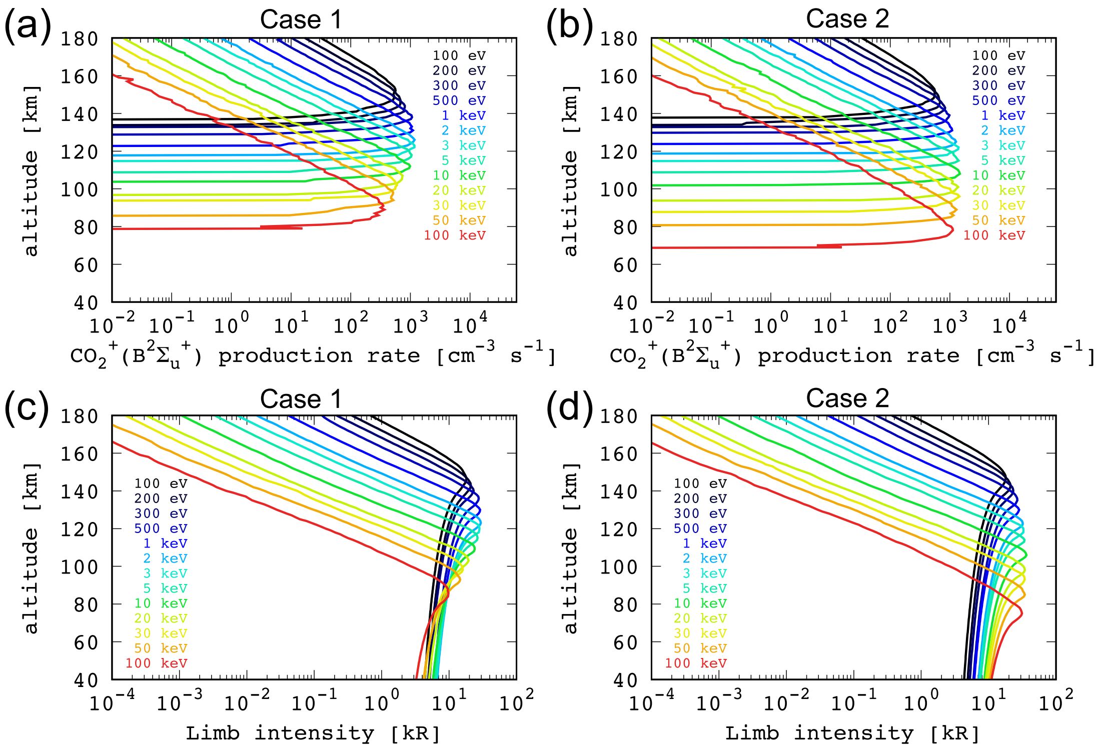

1987

2006

2001

2017

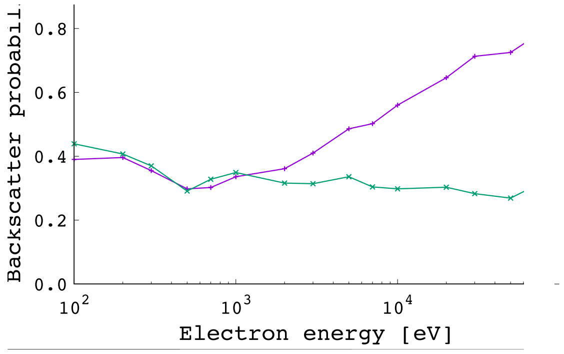

2 4

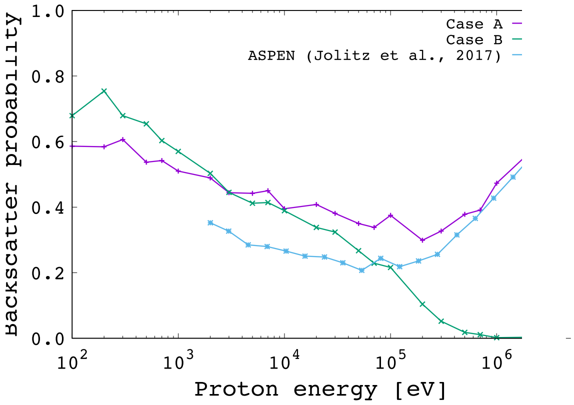

2 4

7

4.2. Production Rate of CO_2^+ ($B^2\Sigma_u^+$) During SEP Events

8

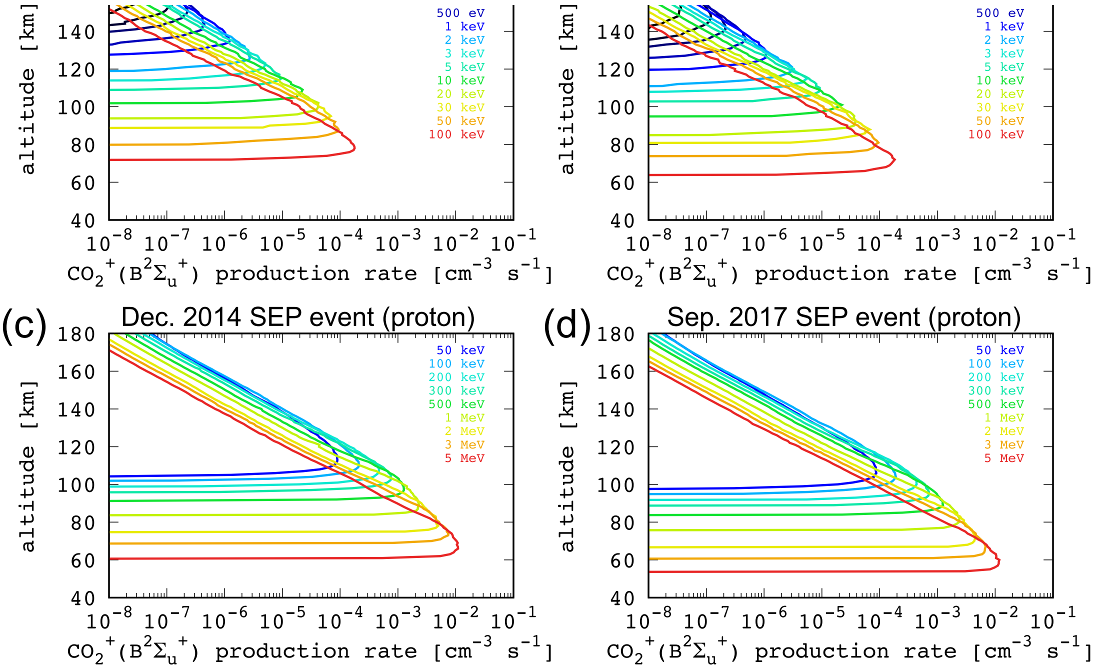

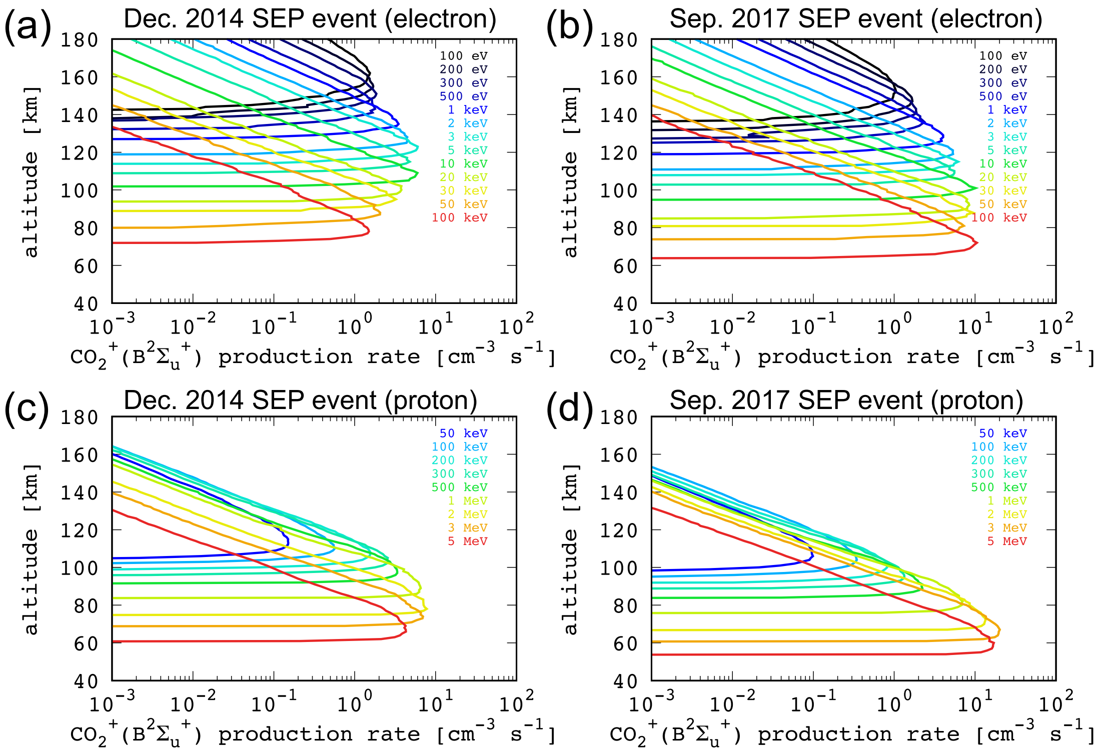

2017

2009

9

5

9c

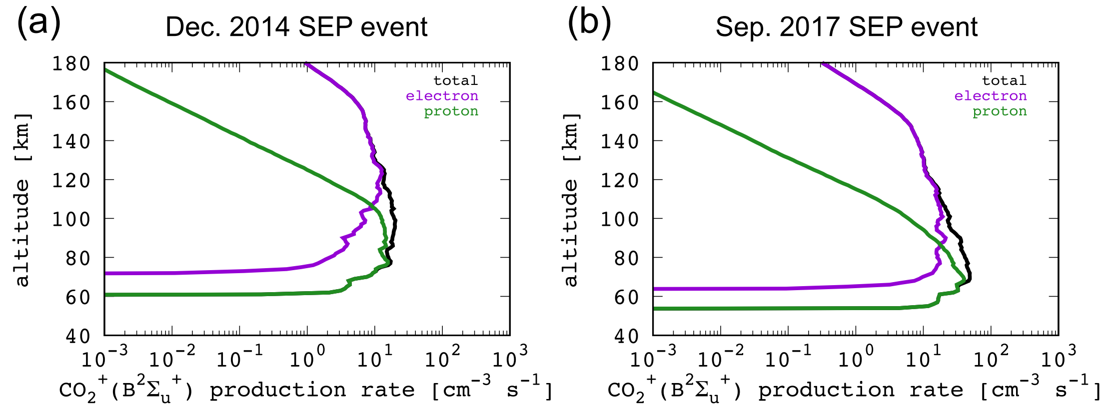

9

4.3. CO_2^+ UVD Limb Intensity Profiles During SEP Events

2.5

11

2017

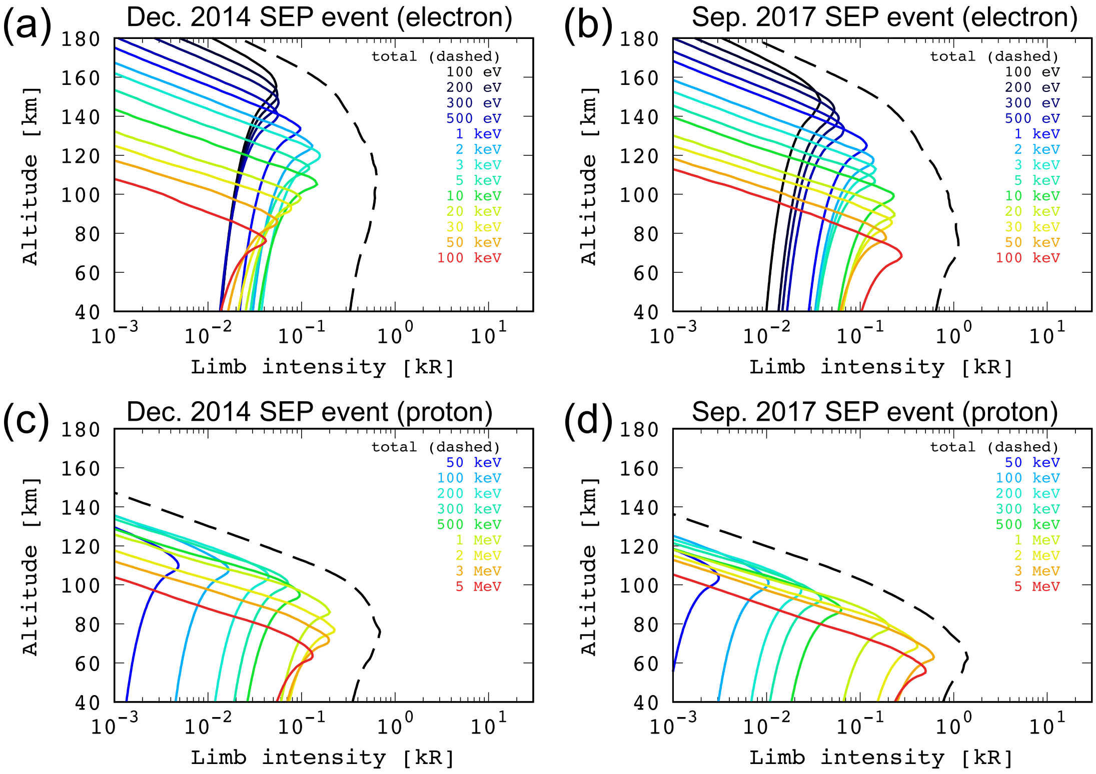
(a)
Dec. 2014 SEP event (electron)
(b)
Sep. 2017 SEP event (electron)
total (dashed)
100 eV
200 eV
300 eV
500 eV
1 keV
2 keV
3 keV
5 keV
10 keV
20 keV
30 keV
50 keV
100 keV
(c)
Dec. 2014 SEP event (proton)
(d)
Sep. 2017 SEP event (proton)
total (dashed)
50 keV
100 keV
200 keV
300 keV
500 keV
1 MeV
2 MeV
3 MeV
5 MeV
Altitude [km]
40
60
80
100
120
140
160
180
Limb intensity [kR]
10^{-3}
10^{-2}
10^{-1}
10^{0}
10^{1}

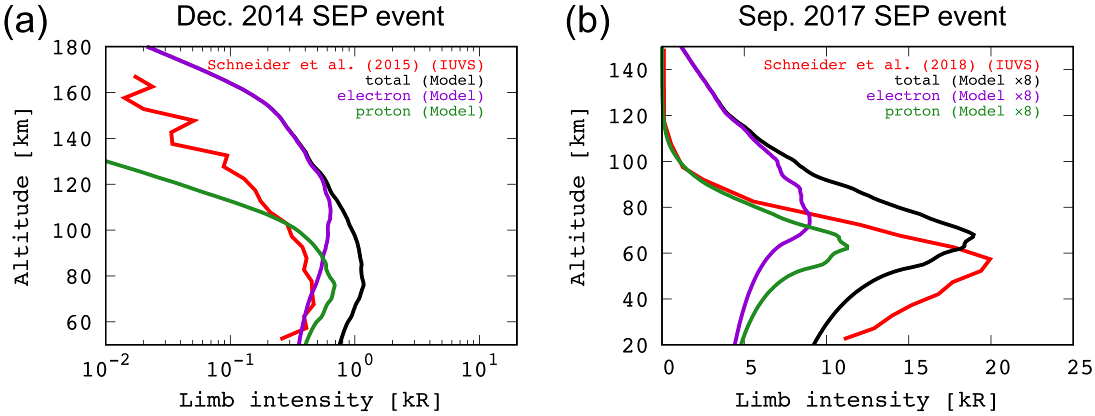
(a)
Dec. 2014 SEP event
Schneider et al. (2015) (IUVS)
total (Model)
electron (Model)
proton (Model)
Altitude [km]
60
80
100
120
140
160
180
Limb intensity [kR]
10^{-2}
10^{-1}
10^{0}
10^{1}
(b)
Sep. 2017 SEP event
Schneider et al. (2018) (IUVS)
total (Model ×8)
electron (Model ×8)
proton (Model ×8)
Altitude [km]
20
40
60
80
100
120
140
Limb intensity [kR]
0
5
10
15
20
25

12

5. Discussion

12

12

S1

3

13

14

2018

2006

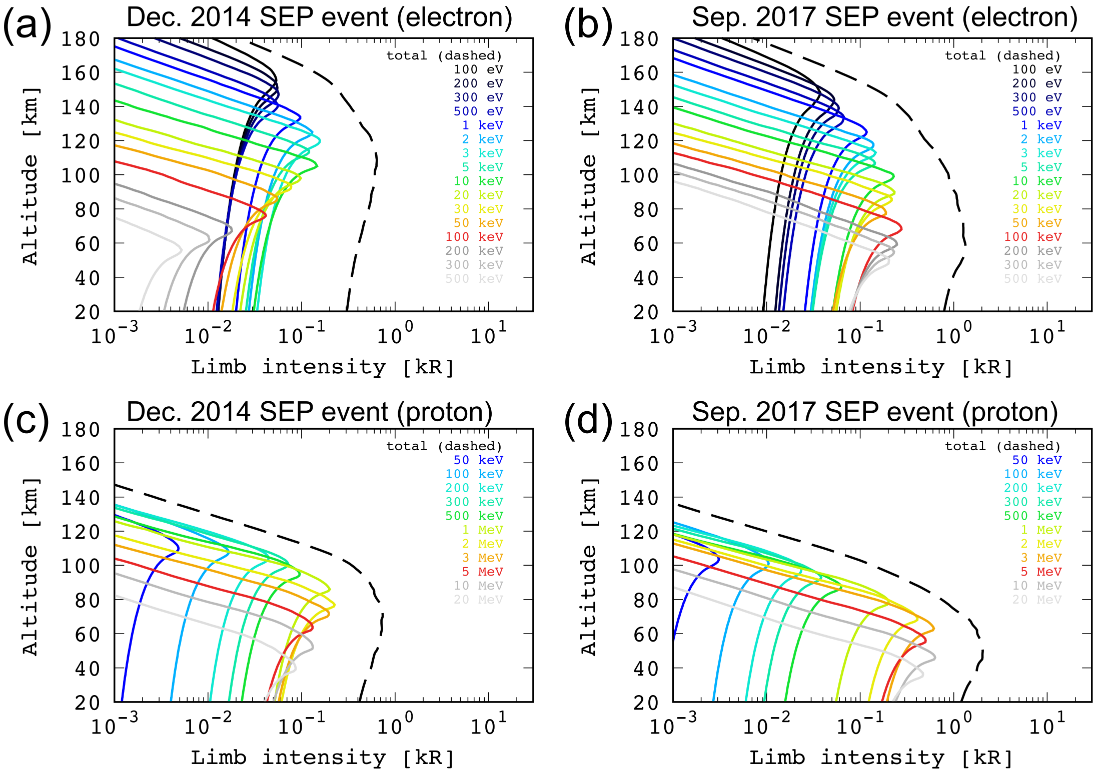
(a) Dec. 2014 SEP event (electron)
(b) Sep. 2017 SEP event (electron)
(c) Dec. 2014 SEP event (proton)
(d) Sep. 2017 SEP event (proton)
Altitude [km]
Limb intensity [kR]
180
160
140
120
100
80
60
40
20
10^{-3}
10^{-2}
10^{-1}
10^{0}
10^{1}
total (dashed)
100 eV
200 eV
300 eV
500 eV
1 keV
2 keV
3 keV
5 keV
10 keV
20 keV
30 keV
50 keV
100 keV
200 keV
300 keV
500 keV
50 keV
100 keV
200 keV
300 keV
500 keV
1 MeV
2 MeV
3 MeV
5 MeV
10 MeV
20 MeV

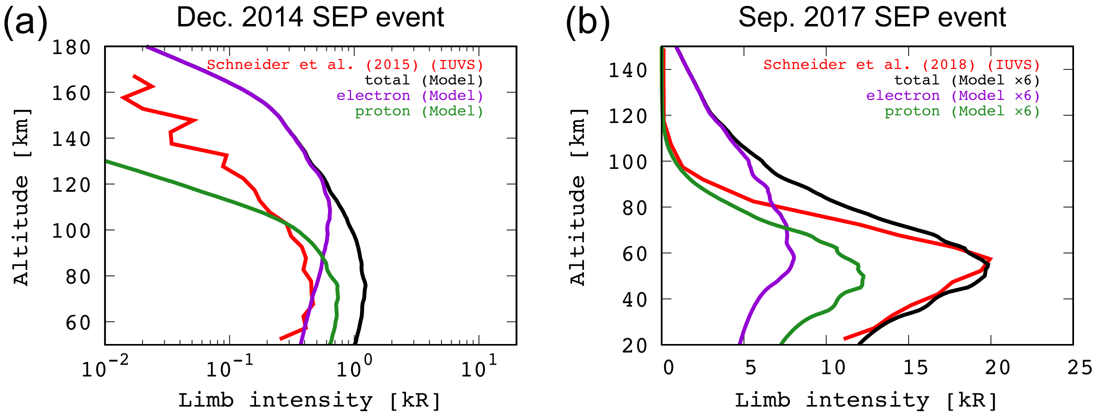
(a) Dec. 2014 SEP event
(b) Sep. 2017 SEP event
Altitude [km]
Limb intensity [kR]
180
160
140
120
100
80
60
40
20
10^{-2}
10^{-1}
10^{0}
10^{1}
0
5
10
15
20
25
Schneider et al. (2015) (IUVS)
total (Model)
electron (Model)
proton (Model)
Schneider et al. (2018) (IUVS)
total (Model ×6)
electron (Model ×6)
proton (Model ×6)

2018

2007

2016

6. Conclusions

2017 2019

2017 2001 2002

2018

2021

2015

Data Availability Statement

https://doi.org/10.5281/zenodo.5824669

Acknowledgments

References

https://doi.org/10.1029/JA092iA06p05920

https://doi.org/10.1038/nature03603

https://doi.org/10.1029/2009JA014298

https://doi.org/10.1002/jgra.50345

https://doi.org/10.1016/j.icarus.2016.08.035

https://doi.org/10.1029/2005GL024782

https://doi.org/10.1038/s41550-018-0538-5

https://doi.org/10.1002/jgra.50484

https://doi.org/10.1029/2008JE003086

https://doi.org/10.1029/JA084jA12p07315

https://doi.org/10.1016/j.icarus.2017.01.037

https://doi.org/10.1016/0021-9169(72)90031-1

https://doi.org/10.1029/2017JE005466

https://doi.org/10.1029/2019JA026688

https://doi.org/10.1006/icar.2002.6919

https://doi.org/10.1029/2019JA027140

https://doi.org/10.1063/1.1481879

https://doi.org/10.1063/1.1937426

https://doi.org/10.1063/1.3025886

https://doi.org/10.1063/1.4913926

https://doi.org/10.1029/JA082i032p05081

https://doi.org/10.1002/2016JA023781

https://doi.org/10.1029/2021JA029132

https://doi.org/10.1029/2000JA002003

https://doi.org/10.1016/0032-0633(92)90047-R

https://doi.org/10.1007/s11214-015-0218-z

https://doi.org/10.1029/2001JA900178

https://doi.org/10.1029/2005JE002643

https://doi.org/10.1029/2011JA016982

https://doi.org/10.1002/2015JA022327

https://doi.org/10.3847/1538-4357/aa9fef https://doi.org/10.1029/2006JE002886

https://doi.org/10.1007/s11214-015-0232-1

https://doi.org/10.1029/JA091iA08p08947

https://doi.org/10.1103/PhysRev.115.491

https://doi.org/10.1029/93JA01500

https://doi.org/10.1029/JA092iA06p05933

https://doi.org/10.1103/PhysRevA.6.1507

https://doi.org/10.1002/2017GL076235

https://doi.org/10.1103/PhysRevA.28.3244

https://doi.org/10.1126/science.aad0313

https://doi.org/10.1029/2018GL077772

https://doi.org/10.1016/0029-5582(62)90289-4

https://doi.org/10.1029/2000JA002011

https://doi.org/10.1029/JA076i034p08425

https://doi.org/10.1016/0010-4655(94)00171-W

https://doi.org/10.1016/j.physleta.2006.04.037

References From the Supporting Information

https://doi.org/10.1063/1.432812

Journal of Geophysical Research: Space Physics

Supporting Information for

Modeling of diffuse auroral emission at Mars: Contribution of MeV protons

Yuki Nakamura[1,2], Naoki Terada[1], Francois Leblanc[2], Ali Rahmati[3], Hiromu Nakagawa[1], Shotaro Sakai[1,4], Sayano Hiruba[1], Ryuho Kataoka[5,6], and Kiyoka Murase[5,6]

[1]Graduate School of Science, Tohoku University, Sendai, Japan, [2]LATMOS/CNRS, Sorbonne Université, Paris, France, [3]Space Sciences Laboratory, University of California, Berkeley, CA, USA, [4]Planetary Plasma and Atmospheric Research Center, Graduate School of Science, Tohoku Universtiy, Sendai, Japan, [5]National Institute of Polar Research, Tokyo, Japan, [6]The Graduate University for Advanced Studies, SOKENDAI, Kanagawa, Japan

Contents of this file

Figures S1 to S5
Text S1

Introduction

This supporting information provides additional details on the converted fluxes, the extrapolation of electron and proton fluxes, the extrapolation of ionization cross sections and the contributions of electrons and protons with energy above 100 keV and 5 MeV, respectively, to the CO_2^+ UVD emission profiles. Figure S1-S3 provide examples of particle fluxes converted from the particles' trajectories using the method described in equation (7) and (8), and mean cosine pitch angles. Figure S4 and S5 provide the comparison of the two method of calculating the production rate of CO_2^+ ($B^2\Sigma_u^+$): the method of counting the number of collisions and the method using the converted flux. Text S1 provides the details of the extrapolation of CO2 ionization cross sections due to impacting electrons above 100 keV, and protons above 5 MeV.

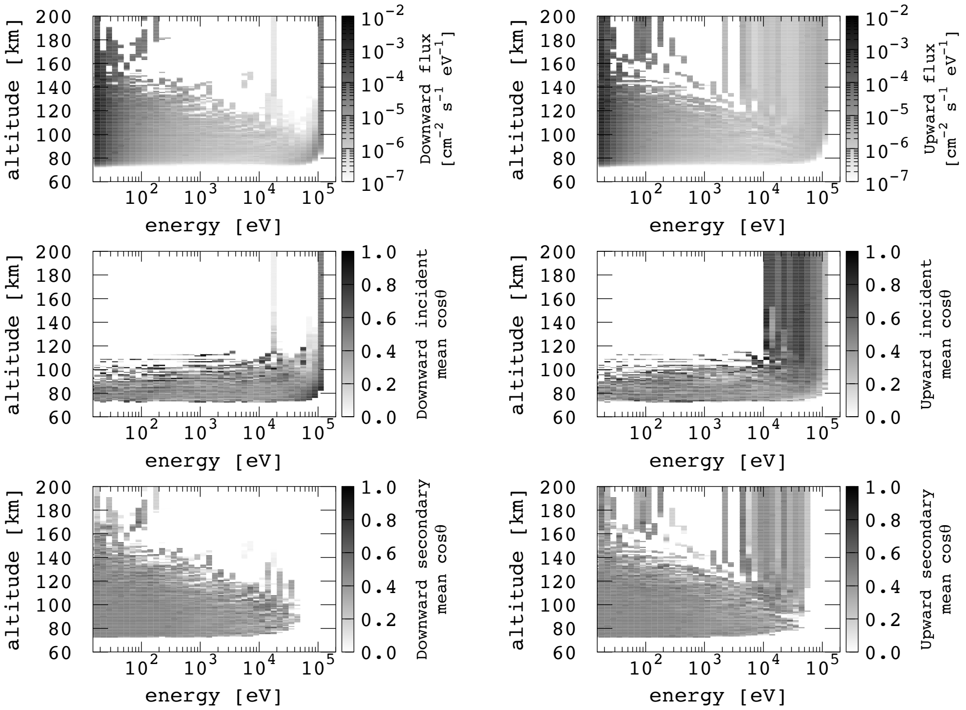

Figure S1. Electron flux converted from the particles' trajectories (using equation (7) and (8)) and mean cosine pitch angle (θ) due to the precipitation of 100 keV electrons.

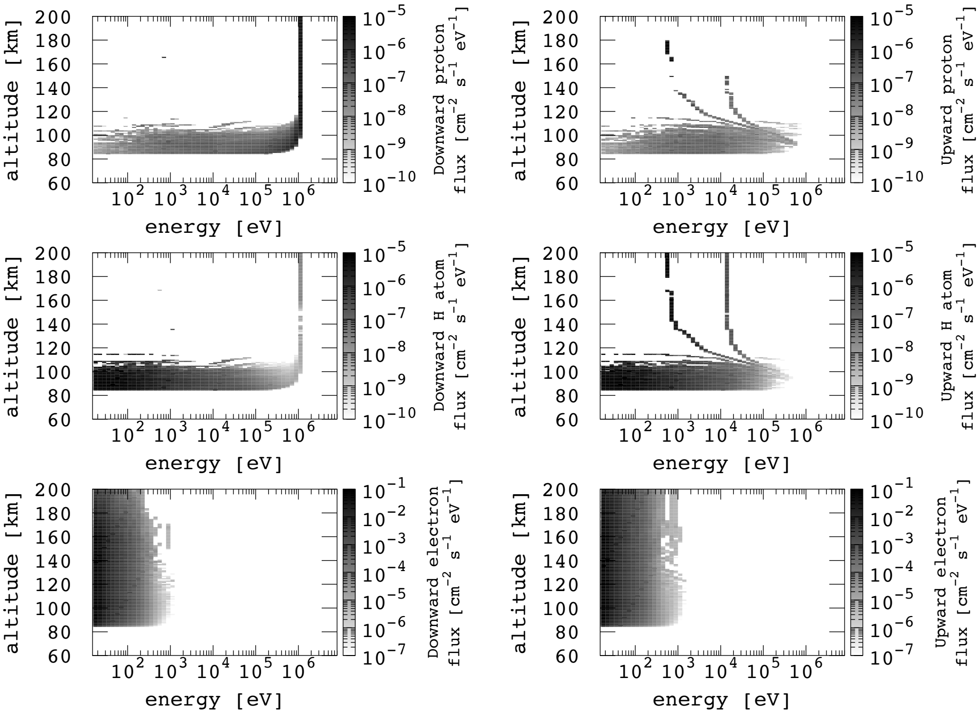

Figure S2. Converted fluxes of protons, hydrogen atoms and secondary electrons converted from the particles’ trajectories (using equation (7) and (8)) due to the precipitation of 1 MeV protons.

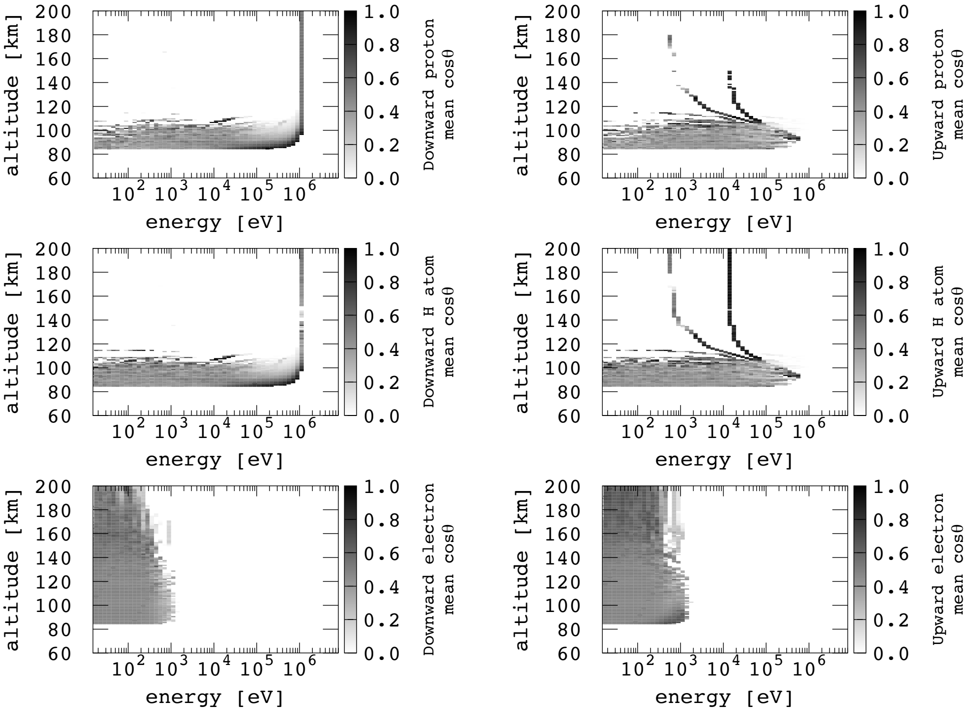

Figure S3. Mean cosine pitch angle (θ) of protons, hydrogen atoms and secondary electrons due to the precipitation of 1 MeV protons.

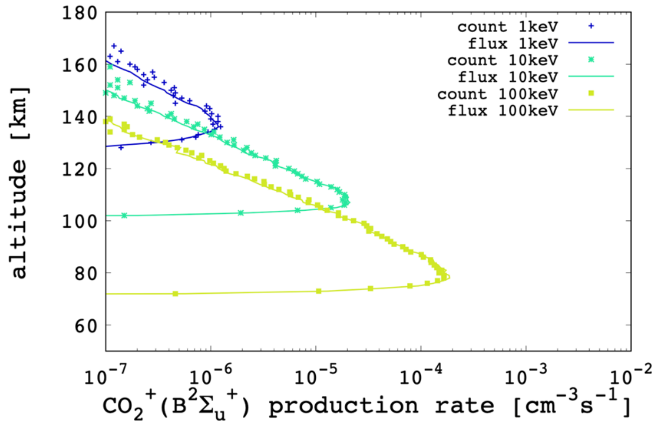

Figure S4. Comparison of the production rate of CO_2^+ ($B^2\Sigma_u^+$) calculated by using the method of counting (dotted) and the method using the flux, mean cosine pitch angle and neutral density (solid line) due to the precipitation of electrons at each incident energy.

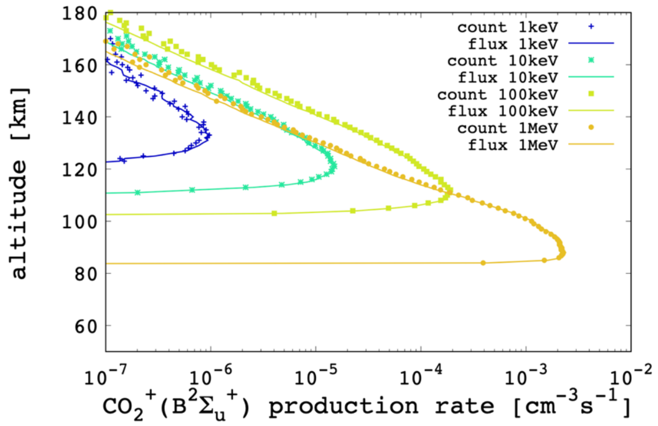

Figure S5. Comparison of the production rate of CO_2^+ ($B^2\Sigma_u^+$) calculated by using the method of counting (dotted) and the method using flux, mean cosine pitch angle and neutral density (solid line) due to the precipitation of protons at each incident energy.

Text S1.

The ionization collisional cross sections due to electron and proton impacts are extrapolated as follows. For electrons, the ionization cross section is known to exhibit the asymptotic relation up to 100 keV as $\sigma(E) \propto E^{-1}\ln(E)$, which is expected by the Born approximation, but deviates from this behavior above 100 keV (Rieke and Prepejchal, 1972). We used the ionization cross section of CO_2 due to electron impacts above 100 keV from Kumar et al. (2010), which agrees very well with the experimental cross section from Rieke and Prepejchal (1972). For protons, since the asymptotic relation of the ionization cross section holds even at around 100 MeV (Porter et al., 1976), we apply the ionization cross sections of Rudd et al. (1983) up to 20 MeV.

References in the Supporting Information

Rieke, Foster F. and Prepejchal, W. (1972). Ionization Cross Sections of Gaseous Atoms and Molecules for High-Energy Electrons and Positrons, Phys. Rev. A, 6, 4, 1507-1519, doi:10.1103/PhysRevA.6.1507.

Kumar, Y., Tiwari, N., Kumar, M., and Tomar, S. (2010). Total ionization cross-sections of atmospheric molecules due to electron impact, Indian Journal of Pure & Applied Physics, 48, 621-625.

Porter, H. S., Jackman, C. H., and Green, A. E. S. (1976). Efficiencies for production of atomic nitrogen and oxygen by relativistic proton impact in air, J. Chem. Phys., 65, 154 doi:10.1063/1.432812.

Rudd, M. E., DuBois, R. D., Toburen, L. H., Ratcliffe, C. A., and Goffe, T. V. (1983). Cross sections for ionization of gases by 5-4000-keV protons and for electron capture by 5-150-keV protons, Phys. Rev. A, 28, 6, 3244-3257, doi:10.1103/PhysRevA.28.3244.